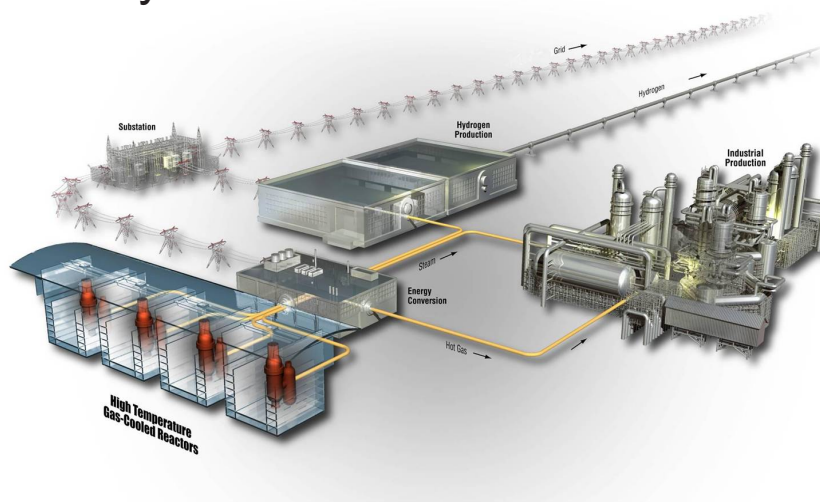# Summary Report on Solid-oxide Electrolysis Cell Testing and Development

J. E. O'Brien
X. Zhang
R. C. O'Brien
G. L. Hawkes
J. J. Hartvigsen
E. Elangovan
G. Tao
B. Yildiz
P. Singh
N. Petigny
S. Farmer

January 2012

Idaho National Laboratory

Summary Report on Solid-oxide Electrolysis Cell Testing and Development

J. E. O'Brien, X. Zhang, R. C. O'Brien, G. L. Hawkes (INL); J. J. Hartvigsen, E. Elangovan (Ceramatec, Inc.); G. Tao (MSRI), B. Yildiz (MIT); P. Singh (UConn); N. Petigny (St. Gobain); S. Farmer (NASA—GRC)

January 2012

**Idaho National Laboratory
Next Generation Nuclear Plant Project
Idaho Falls, Idaho 83415
http://www.inl.gov**

Next Generation Nuclear Plant Project

Summary Report on Solid-oxide Electrolysis Cell Testing and Development

INL/EXT-11-24261

January 2012

Approved by:

James E. O'Brien
Principal Investigator and Technical Director, High
Temperature Electrolysis

1/11/12
Date

Carl M. Stoots
Hydrogen Technical Reviewer

1/11/12
Date

David A. Petti
Director, Very High Temperature Gas Reactor
Technology Development Office

1-11-12
Date

Kimberly J. Armour   for
Quality Assurance

1/12/12
Date

Greg A. Gibbs
NGNP Project Director

1/12/12
Date

EXECUTIVE SUMMARY

Idaho National Laboratory (INL) has been researching the application of solid-oxide electrolysis cells (SOECs) for large-scale hydrogen production from steam over a temperature range of 800 to 900°C. From 2003 to 2009, this work was sponsored by the United States Department of Energy Nuclear Hydrogen Initiative, under the Office of Nuclear Energy. Starting in 2010, the high-temperature electrolysis (HTE) research program has been sponsored by the INL Next Generation Nuclear Plant Project. This report provides a summaryof program activities performed in Fiscal Year (FY) 2011 and the first quarter of FY-1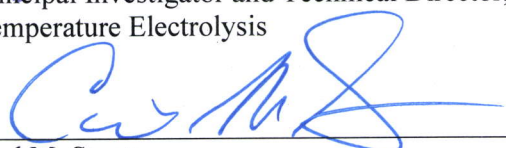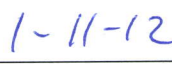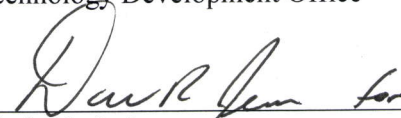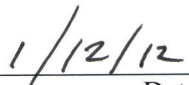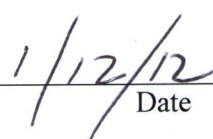2, with a focus on small-scale testing and cell development activities. HTE research priorities during this period have included the development and testing of SOEC and stack designs that exhibit high-efficiency initial performance and low, long-term degradation rates.

This report includes contributions from INL and five industry partners: Materials and Systems Research, Incorporated (MSRI); Versa Power Systems, Incorporated (VPS); Ceramatec, Incorporated; National Aeronautics and Space Administration—Glenn Research Center (NASA—GRC); and the St. Gobain Advanced Materials Division. These industry partners have developed SOEC cells and stacks for in-house testing in the electrolysis mode and independent testing at INL. Additional fundamental research and post-test physical examinations have been performed at two university partners: Massachusetts Institute of Technology (MIT) and the University of Connecticut. Summaries of these activities and test results are also presented in this report.

MSRI worked closely with INL as a subcontractor responsible for development and testing of advanced electrode-supported solid-oxide cells and stacks, optimized for operation in the electrolysis mode. MSRI also provided several stacks and single cells to INL for independent testing and characterization. Testing at both locations included several long-term (more than 1000 hours) stack durability tests. Test results were very favorable, with excellent initial performance and low degradation rates (less than 3%/khr). Based on the test results, and the development of an excellent working relationship, MSRI was selected as the supplier for cells and stacks for two major FY-12 program objectives: (1) demonstration of HTE at the 4-kW scale for 1000 hours using advanced technology cell and stack hardware, and (2) demonstration of pressurized operation of an HTE stack at a pressure of 1.5 MPa or higher.

VPS is a major developer of solid-oxide fuel cells and a member of the United States Department of Energy Solid State Energy Conversion Alliance. INL contracted with VPS in FY-10 for electrolysis testing activities performed at their research facility in Calgary, Alberta, Canada. Some of the test activities, including a stack test that ran for more than 4500 hours, extended into FY-11 and are therefore included in this report. VPS also examined the effects of constant current versus constant voltage operation. HTE test results performed at VPS were excellent. The stacks exhibited good initial performance and very low degradation rates (less than 1.5%/khr).

Ceramatec, Incorporated, continued to be an important contributor to the INL HTE Program during FY-11. Primary research objectives for FY-11 included continued refinement of the air-electrode material set to address various degradation mechanisms, development of an air-electrode-supported cell with a thin electrolyte, and development of a new double-doped electrolyte. Ceramatec also delivered several SOEC stacks to INL for testing and also performed their own in-house testing. One of the stacks was operated at INL for more than 2000 hours, with very stable long-term performance, even showing improved performance with time. However, because the cells are electrolyte-supported, the initial performance, measured in terms of area-specific resistance, is not as good as the performance of the electrode-supported cells such as those produced by MSRI.

INL established a contract with NASA—GRC in FY-10 to develop the NASA—GRC bi-supported cell and stack design for the electrolysis application. The electrode materials for these cells are infiltrated into a porous yytria-stabilized zirconia matrix bonded to either side of a thin, dense yytria-stabilized zirconia electrolyte. The NASA—GRC stack design combines multiple cells, separated by a thin, electronically-conductive ceramic interconnect rather than a metal interconnect. All-ceramic stacks have the potential to be especially durable with regard to multiple thermal cycles. NASA—GRC provided several button cells and single cells to INL for testing during FY-11. Unfortunately, the performance of these cells in the electrolysis mode was poor, and further development is needed.

INL established a Cooperative Research and Development Agreement (CRADA) with St. Gobain Advanced Materials in 2008. Under the CRADA, St. Gobain provides test articles (cells and stacks) to INL for testing in the electrolysis mode. The cells were fabricated by St. Gobain High-Performance Materials, and supplied to INL via the CRADA. The cell design was licensed by St. Gobain from the Jülich Institute for Energy Research. Several single cells were tested at INL during FY-11. Three types of cells, with different air electrodes, were tested. Performance of the St. Gobain single cells in the fuel cell mode was very stable. However, in the electrolysis mode, all three cell types exhibited serious air-electrode delamination issues. INL also tested two three-cell stacks provided by St. Gobain, based on the Jülich F design. Performance of these stacks was verified in the fuel cell mode, but as with the single cells, performance in the electrolysis mode was unacceptable.

INL also supported fundamental research and post-test physical examination activities at two universities via subcontract. The research focus of the MIT program during FY-11 was to evaluate the activity and stability of lanthanum strontium cobaltite as an oxygen-electrode material for SOECs. MIT used advanced diagnostic techniques and analysis to evaluate the surface and bulk properties of this material and implications for its use in solid-oxide cells.

The primary objective of the research performed at the University of Connecticut was to elucidate mechanisms of performance degradation observed in the high-temperature steam electrolysis cells. The specific focus during the first quarter of FY-11 was to investigate the root cause of delamination of the air electrodes at the electrode/electrolyte interface in SOECs. A correlation between anode delamination, morphology changes at the anode-electrolyte interface, and cell degradation rate was established. Additional degradation mechanisms such as interface compound formation and morphological changes under SOEC operating conditions were also examined. The role of chromium vaporization and transport was also evaluated.

Computational fluid dynamic studies of the coupled heat, mass, and momentum transfer, electrochemistry, and electric field effects were also supported at INL during FY-11. In this study, two three-dimensional computational fluid dynamic models were created to analyze high-temperature steam electrolysis in a planar cross-flow internally-manifolded solid-oxide electrolysis stack. The first model represents a stack of five cells that simulates the full geometry of several five-cell stack tests performed at INL and MSRI. The second model is for a single-cell stack as it would exist in a large stack, with symmetry boundary conditions on the top and bottom of the cell. Results of this study identified the effects of the geometry of the inlet and outlet flow passages on the flow, temperature, and voltage fields in the stack configuration.

ACKNOWLEDGMENTS

CONTENTS

FIGURES

TABLES

ACRONYMS

3-D	three-dimensional
AES	auger electron spectroscopy
AFM	atomic force microscopy
BEA	Battelle Energy Alliance, LLC
BET	absorption surface area measurement technique
CEM	controlled evaporation and mixing
CFD	computational fluid dynamics
CRADA	Cooperative Research and Development Agreement
CTE	coefficient of thermal expansion
DKKK	Daiichi Kigenso Kagaku Kogyo Co., Ltd.
DOE	Department of Energy
EIS	electrochemical impedance spectroscopy
FWHM	full width at half-maximum
FY	Fiscal Year
GDC	gadolinium-doped ceria
HastX	Hastelloy-X
HTE	high-temperature electrolysis
HTSE	high-temperature steam electrolysis
INL	Idaho National Laboratory
LCC	layer of Ca-doped $LaCrO3$
LCM	La-Ca-manganite
LCM50	$La_{0.5}Ca_{0.5}MnO_3$
LHV	lower heating value
LSC	$La_{1-x}Sr_xCoO_{3-\delta}$
LSCF	La-Sr-Co-Fe oxide
LSM	La-Sr manganite
MIT	Massachusetts Institute of Technology
MSRI	Materials and Systems Research, Incorporated
N/A	not applicable
NASA—GRC	National Aeronautics and Space Administration—Glenn Research Center
NGNP	Next Generation Nuclear Plant
OCV	open cell voltage
OER	oxygen evolution reaction

ORR	oxygen reduction reaction
P&ID	piping and instrumentation diagram
PLD	pulsed laser deposition
R&D	research and development
SDC	samarium-doped ceria
SECA	Solid State Energy Conversion Alliance
SEM	scanning electron microscopy
SOEC	solid-oxide electrolysis cell
SOFC	solid-oxide fuel cell
SSR	solid-state relay
TSC	tape casting, screen printing, and tunnel kiln for continuous co-firing
UConn	University of Connecticut
U.S.	United States
UT Austin	University of Texas at Austin
VPS	Versa Power Systems, Incorporated
XPS	x-ray photoelectron spectroscopy
XRD	x-ray diffraction
YSZ	yttria-stabilized zirconia

NOMENCLATURE

A	ampere, unit of electrical current
ac	alternating current
A/cm^2	ampere per square centimeter
A/m^2	amps per square meter
ASR	area-specific resistance, $\Omega\text{–}cm^2$
C	Coulomb, unit of charge
°C	degrees Celsius
cm	centimeter
cm^2	square centimeter
$\Omega\text{-}cm^2$	ohm per square centimeter
dc	direct current
eV	electron volt
F	Faraday number, 96487 C/mol
g/cc	grams per cubic centimeter
g/cm	grams per centimeter
g/cm^2	grams per square centimeter
ΔG_f	Gibbs energy of formation, J/mol
g/hr	grams per hour
$\Delta \dot{H}_2$	molar hydrogen production rate, mol/s
hr	hour
Hz	cycles per second (hertz)
i	current density, A/cm^2
I	current, A
in.	inch
J	Joule, unit of energy
$J\ cm^{-2}$	Joules per square centimeter
K	degrees Kelvin, unit of temperature, 0 K = -273°C
keV	kilo–electron–volt
kg	kilogram
kg/hr	kilogram per hour
khr	1000 hours
kW	kilowatt
kWe	kilowatt electric, unit of power

lb	pound
m	meter
μm	micronmeter or micron
ρ_M	standard-state molar density, mol/m³
m^2	square meter
mA/cm^2	milliampere per square centimeter
mbar	millibar
mil	0.0001 in.
min	minute
mm	millimeter
mol	gram-mole, 6.022×10^{23} atoms, electrons or molecules
mol%	mol percent
mol/m³	mole per cubic meter
MPa	megapascal
mV	millivolt
mV/khr	millivolts per 1000 hours
nA	nanoamp
NL and Nm^3	normal liters (or m^3) of a gas at 0°C and 1 atmosphere (101.3 kPa)
nm	nanometer
N_{O2prod}	number of oxygen equivalents
ns	nanosecond
OD	outside diameter
ohm	unit of electrical resistance, also written Ω
P	pressure, kPa
Pa	Pascal, unit of pressure
Po_2	oxygen partial pressure
ppm	parts per million
q"	heat flux, W/cm^2
Q	volumetric flow rate, sccm
Q_M	molar flow rate, mol/s
R_u	universal gas constant, J/mol·K
S	second, unit of time
s/cm	Siemens per centimeter
sccm	standard (0°C, 1 atmosphere) cubic centimeters per minute, unit of volumetric flow
slpm	standard liters per minute

T	temperature, K
T_{dp}	dew-point temperature
Torr	torr
U_{H2O}	steam utilization,%
V	volt, unit of electrical potential (voltage)
V/cell	volts per cell
V_{cell}	cell operating voltage, V
V_{OC}	open-cell voltage, V
Vdc	volts direct current
V_N	Nernst potential, V
vol%	volume percent
V_{tn}	thermal neutral voltage, V
W	watt
W/cm^2	watt per square centimeter
We	watt electric, unit of power
wt%	weight percent
y	mole fraction
y_{H2O}	mole fraction of steam
μ	micron

Summary Report on Solid-oxide Electrolysis Cell Testing and Development

1. INTRODUCTION

1.2 High-Temperature Electrolysis Program Overview

Idaho National Laboratory (INL) is performing research on high-temperature steam electrolysis (HTSE) for large-scale hydrogen production based on nuclear energy using solid-oxide electrolysis cells (SOECs). This work is funded by the INL Next Generation Nuclear Plant (NGNP) Project. A conceptual schematic depicting a high-temperature gas-cooled reactor coupled to an HTSE system is shown in Figure 1-1. The HTSE system produces hydrogen using the heat and electricity generated by a high-temperature nuclear reactor and power conversion unit. In this depiction, the primary helium coolant uses about 85% of the thermal energy output of the reactor to drive a gas-turbine Brayton power cycle, which provides the electrical energy required for the HTSE process. The remaining 15% of the reactor thermal energy is used to generate steam at about 800°C. Combining a high-efficiency power cycle with the direct use of nuclear process heat yields an overall thermal-to-hydrogen conversion efficiency of 50% or higher.
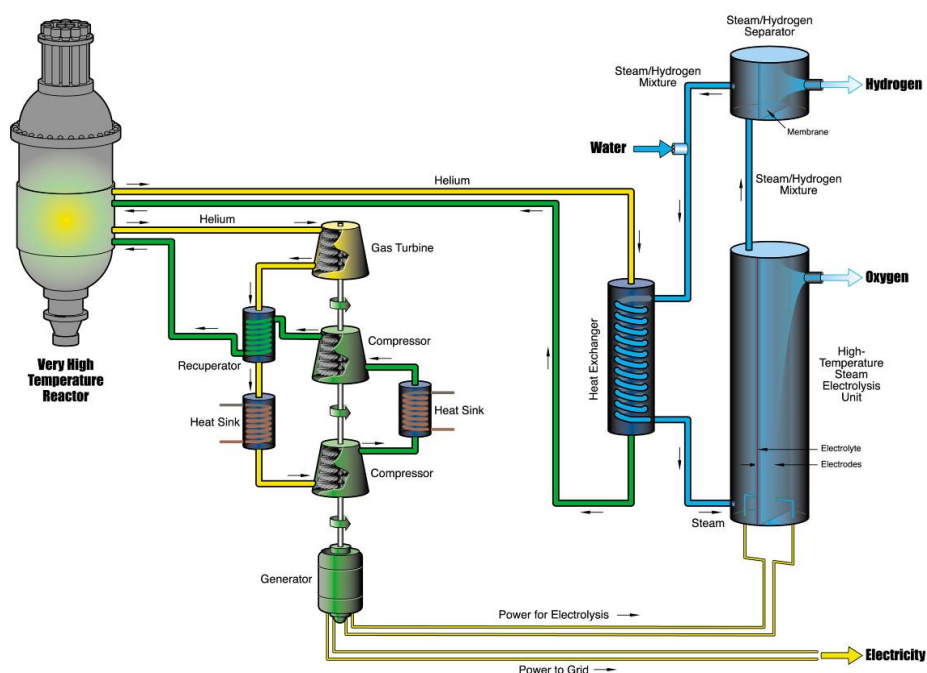
Figure 1-1. Schematic of high-temperature electrolysis (HTE) system coupled to advanced nuclear reactor.

The objective of the INL NGNP Project is to address the technical and scale-up issues associated with the implementation of SOEC technology for hydrogen production from steam. In the envisioned application, HTSE would be coupled to an advanced nuclear reactor for efficient, large-scale, nonfossil, nongreenhouse gas hydrogen production. The project supports a broad scope of activities, including small bench-scale experiments, larger-scale technology demonstrations, detailed computational fluid dynamic modeling, and system modeling. For this technology to be successful in a large industrial setting, several issues related to solid-oxide cells need to be resolved, including stack design optimization, identification

and evaluation of cell performance degradation parameters and processes, integrity and reliability of the SOEC stacks, lifetime prediction, and extension of the SOEC stacks. Significant progress has been made on these issues during 2011. This report summarizes the cell and stack testing and development activities performed in Fiscal Year (FY) 2011 and the first quarter of FY-12.

1.3 Fiscal Year 2011 Experimental Program Objectives

The highest priority objectives for FY-11were to continue testing and development of high-performance SOECs and demonstrate decreased long-term degradation rates. The approach included close collaboration with industry and university subcontractors and Cooperative Research and Development Agreement (CRADA) partners. Industry subcontracts were awarded to Ceramatec, Incorporated; Materials and Systems Research, Incorporated (MSRI); the National Aeronautics and Space Administration—Glenn Research Center (NASA—GRC); and Versa Power Systems, Incorporated (VPS). University subcontracts with the University of Connecticut, Massachusetts Institute of Technology, and University of Utah continued in FY-11. An ongoing CRADA continued with the St. Gobain Advanced Materials Division. INL continues to work toward development of a CRADA or other agreement with Topsoe Fuel Cell. Emphasis was placed on developing cells and stacks that are optimized for the electrolysis application. The most success was achieved with electrode-supported cells and stacks from MSRI and VPS. Based on results of INL independent testing and INL working relationship experience, MSRI was selected as the supplier for cells and stacks to meet the following Level-2 FY-12 milestones:

1. Demonstrate HTE at 4-kW scale for 1000 hours with advanced technology, internally-manifolded, electrode-supported cells.

2. Demonstrate pressurized operation of an HTE stack at 1.5 MPa or higher to advance the technology readiness level of HTSE to TRL5.

2 ADVANCED CELL AND STACK DEVELOPMENT ACTIVITIES— SUBCONTRACTORS AND COOPERATIVE RESEARCH AND DEVELOPMENT AGREEMENT PARTNERS

2.1 Materials and Systems Research, Incorporated

2.1.1 Background

Battelle Energy Alliance, LLC (BEA)/INL is continuing a research and development (R&D) project to develop an HTSE system for hydrogen production. The electrolysis system utilizes high-temperature process heat and electrical power to split hydrogen from steam using SOECs. An SOEC typically is comprised of an oxygen-ion conducting electrolyte membrane sandwiched between a fuel/steam electrode (negative electrode) and an oxygen electrode (positive electrode). With an externally applied voltage, steam on the fuel/steam electrode is split into hydrogen and oxygen ions that are further transported through the electrolyte membrane and reach the oxygen electrode, followed by oxygen formation by releasing electrons. To increase hydrogen production rates, individual SOECs are connected in series, parallel, or combination through interconnects and gas flow channels, forming stacks.

A key factor in developing a robust SOEC technology is to understand the degradation mechanisms and develop viable strategies to mitigate degradation. Like other types of electrochemical devices [i.e., solid-oxide fuel cells (SOFCs)], the SOEC encounters many possible degradation mechanisms associated with electrochemical processes, materials properties, construction, and operation. The degradation mechanisms generally can be catalogued into three groups, including the chemical/electrochemical degradation mechanisms (i.e., composition and phase segregation, electrode redox, electrolyte material stability, and Cr poisoning effects), structural degradation mechanisms (i.e., electrode material coarsening and interfacial delamination), and mechanical failure caused by thermal stress (i.e., cracks and warpage). In the last few years, MSRI has studied several possible chemical/electrochemical and structural degradation mechanisms in SOECs, and provided information aimed at reducing degradation in future SOECs. The objective of this project was to develop a promising, degradation-resistant SOEC technology consisting of MSRI's proprietary material compositions that had demonstrated high stability in laboratory tests.

2.1.2 Cell Materials Development for Lower Degradation Rate

By leveraging our established knowledge on cell material compositions and cell structures, MSRI has successfully fabricated planar, fuel electrode-supported SOECs using MSRI's state-of-the-art fabrication processes. Starting from the as-received commercial powders, NiO and yttria-stabilized zirconia (YSZ) were mixed with binders and solvents and ball-milled to form slurry, followed by casting over a precision surface with a doctor blade dispensing the slurry. The casting speed and gap between the blade and Mylar substrate were adjusted to control the flow. After drying in air, green tapes with a desired thickness were formed. The green tapes were then laser cut, followed by bisque firing in air. Graded negative-electrode functional layers comprising mixtures of NiO and 8YSZ at different ratios were applied by spray-coating, followed by air drying over a few hours. An YSZ-based electrolyte layer was applied by the same spray-coating technique. The multilayer structure was then co-sintered in air at elevated temperatures over a few hours. A $(La,Sr)(Co,Fe)O_{3-\delta}$-type perovskite-based positive-electrode interlayer and current collecting layer were screen printed, followed by firing in air at elevated temperatures.

To avoid possible chemical reactions (zirconates formation) or inter-diffusion reactions between La-Sr-Co-Fe oxide (LSCF) and YSZ during the firing process at elevated temperatures, a thin layer of samarium-doped ceria (SDC) was deposited as a barrier layer between the electrolyte and positive electrode. Typically, a completed cell had six distinct layers that included a Ni+YSZ-supporting substrate,

graded Ni+YSZ negative electrode interlayer, thin-film electrolyte, thin barrier layer, composite positive-electrode interlayer, and positive-electrode current collecting layer with a 100-cm^2 active area. Nonstack components necessary for SOEC stacks, including metallic interconnects, seal gaskets, and electrode dry contact aids, were also machined.

2.1.3 Fabrication and Testing of Planar, Fuel/Steam Electrode-supported Stacks

MSRI's state-of-the-art SOEC fabrication also involves cell quality control and inspection at every major process. To minimize possible cell variations among batches fabricated at different periods, a large batch of cells consisting of MSRI's advanced SOEC materials sets were made. Typically, cells were randomly selected from a pool of cells and assembled into a five-cell stack. In addition, all noncell repeat units for the construction of the stacks were identical, including dry contact aids, seal gaskets, and interconnects. Multiple five-cell stacks were tested using our standard testing protocol, specifically established for evaluating the SOEC degradation rate over a period of time.

In brief, a five-cell stack was preconditioned over 24 hours in a reducing atmosphere for curing seals and fuel-electrode substrates, followed by an SOFC baseline test and SOEC performance test. Compression load was applied externally to the stack to maintain the sealing. Both the SOFC and SOEC tests were performed in atmospheres with various steam compositions. The long-term degradation test in the hydrogen production mode (SOEC) was carried out immediately after the SOFC and SOEC characterization tests on the same day, and the corresponding data recording time was set to zero. Occasionally, the long-term test was also interrupted on schedule for an SOFC functional check.

Figure 2-1 through Figure 2-4 are typical performance characteristics of a five-cell stack tested at 800°C. This stack was one of twin stacks constructed with identical materials and components. Another five-cell stack was delivered to INL on January 10, 2011, for independent studies. Figure 2-1 shows the SOFC baseline test results with hydrogen as the fuel. Both the fuel and air utilizations were fixed at 40%. As shown in Figure 2-1, at 30.4 A, the stack generated 128.09 W of electricity at 4.205 V (or 0.841 V/cell). After the SOFC baseline test, the same stack was evaluated in the SOEC mode with the steam utilization fixed at 40%, as shown in Figure 2-2. The concentrations of steam carried by H_2 on the fuel electrode varied from 50 to 70%. At 20.3 A, the stack respectively consumed 104.48 and 102.44 W of power for the steam concentrations of 50 and 70%bal.H_2 for hydrogen production.
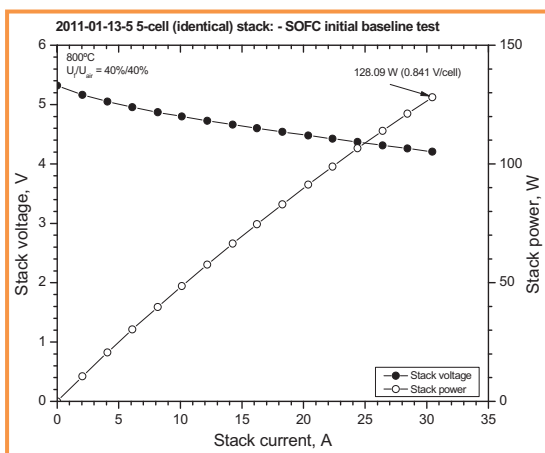
Figure 2-1. Performance characteristics of identical five-cell stack tested in SOFC mode as baseline. Hydrogen and air used as fuel and oxidant with both utilizations fixed at 40%.
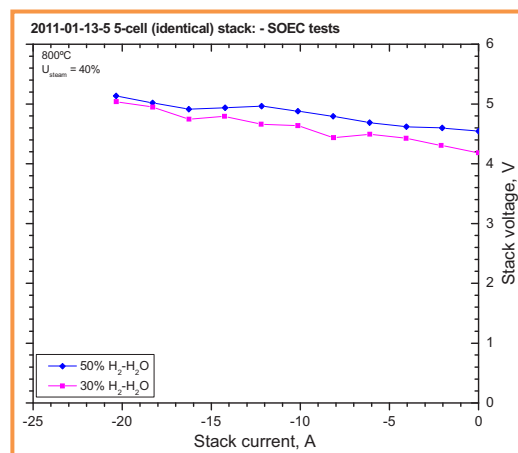
Figure 2-2. Performance characteristics of same five-cell stack tested in SOEC mode at 800°C. Concentrations of steam carried by H_2 varied from 50 to 70%.

4

Immediately after the aforementioned SOFC and SOEC tests, the long-term test in the hydrogen production mode was carried out on the same day to investigate the stack degradation over the time. The corresponding data recording time was also set to zero. Figure 2-3 shows the long-term test results over 1100 hours with 70%H_2O bal. H_2 as the fuel electrode gas. The steam utilization was fixed at 40%. Under a current control mode (by fixing the stack current at 20.3 A, or equivalent to 0.7074 standard liters of hydrogen per minute per stack production rate), this five-cell stack demonstrated a degradation rate less than 3%/khr. On day 32 (after 768 hours of continuous testing), the long-term test was interrupted for a scheduled operation in the SOFC mode (power generation mode) that served as a checkpoint for the stack functionality. As shown in Figure 2-4, the stack performed nearly as well as the initial test on day 1.
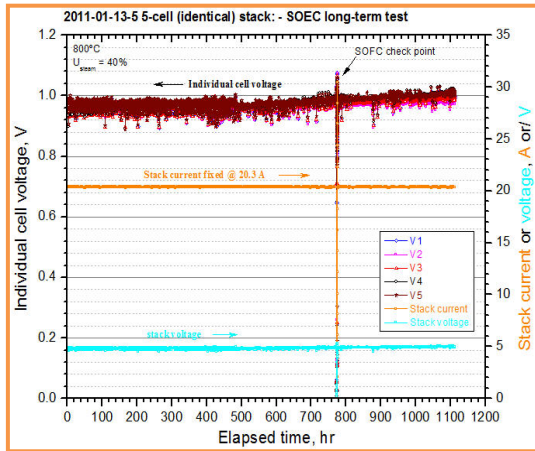
Figure 2-3. Long-term degradation test results of same identical five-cell stack in SOEC mode.
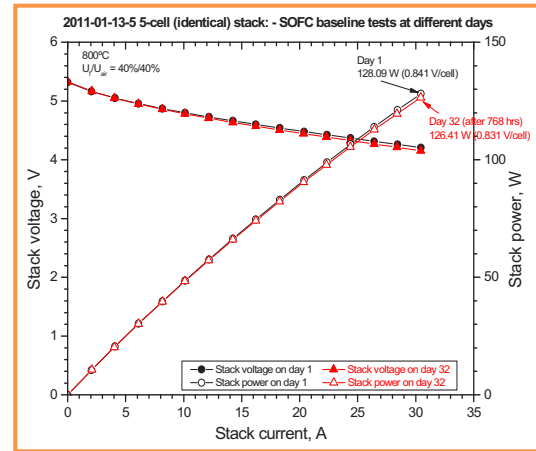
Figure 2-4. Five-cell stack functional checks in SOFC mode at different time.

To investigate the current density effects on the SOEC degradation rate, another five-cell stack was constructed, and currently is under evaluation in the SOEC mode. Implementing the same testing procedure as the stack discussed above, this five-cell stack was tested in the SOFC and SOEC modes first, immediately followed by the long-term test at 30 A. The corresponding steam flow rates were also adjusted to ensure the steam utilization was fixed at 40%. Air was used to sweep the oxygen on the positive electrode. Figure 2-5 shows the baseline SOFC test results. At 30 A, this five-cell stack generated 136 W of electricity at 4.53 V, or equivalent to a power density of 0.272 W/cm^2 at 0.9 V/cell. It is projected that at 3.5 V (0.7 V/cell) the stack will be capable of generating 265 W of electricity (0.53 W/cm^2). The fuel compositions effects on the stack performance were also investigated by varying the hydrogen composition from 100 to 50 vol% balanced with steam. The results are also shown in Figure 2-5. As expected, the SOFC performance dropped with low fuel compositions due to increased concentration polarization losses.
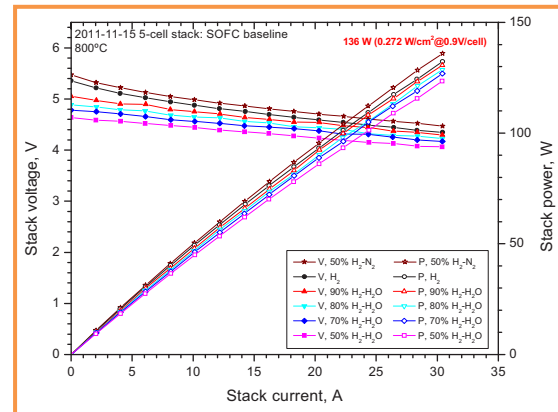
Figure 2-5. Performance characteristics of ongoing five-cell stack tested in SOFC mode as baseline. Fuel compositions varied from 100 to 50% hydrogen balanced with steam. Fuel and oxidant (air) utilizations fixed at 40%.

5

Similar studies were also performed to investigate the steam concentration effects on SOEC performance, as shown in

Figure 2-6. The same conclusion was obtained. Table 2-1 lists the stack area-specific resistance (ASR) at various gas compositions when the stack was operated in both the SOFC and SOEC modes.
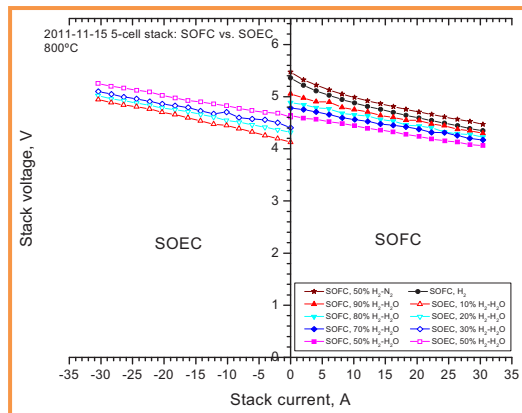
Figure 2-6. Performance characteristics of same stack tested in SOEC and SOFC modes at 800ºC. Steam concentrations carried by H$_2$ varied from 0 to 90%.

Table 2-1. Stack ASR at various gas compositions in both SOFC and SOEC modes.

	SOFC						SOEC			
Composition	50% H$_2$-N$_2$	H$_2$	90% H$_2$-H$_2$O	80% H$_2$-H$_2$O	70% H$_2$-H$_2$O	50% H$_2$-H$_2$O	50% H$_2$-H$_2$O	30% H$_2$-H$_2$O	20% H$_2$-H$_2$O	10% H$_2$-H$_2$O
ASR (Ω-cm^2)	0.608	0.622	0.482	0.44	0.402	0.389	0.415	0.426	0.458	0.53

After the SOFC and SOEC tests, the five-cell stack has been performing the long-term SOEC test at 30 A. Figure 2-7 is the up-to-date test result over 310 hours. Unfortunately, this stack suffered severe operation during the first weekend, when hydrogen (the carry gas to the fuel/steam electrode) was drained off. This potentially led to redox the Ni+YSZ-based fuel electrode. Evaluation is currently under way to either terminate the long-term test or continue it with a relatively low current (i.e., 20 A).
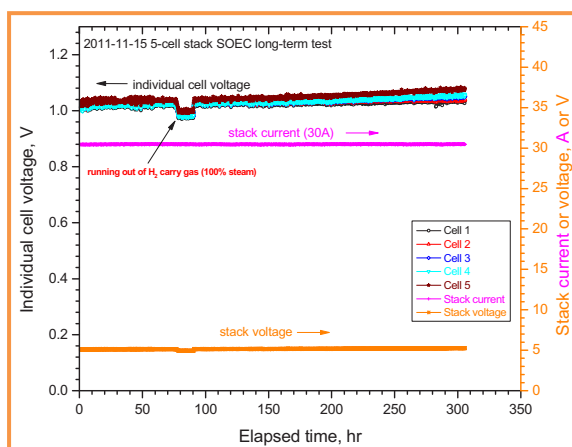
Figure 2-7. Long-term degradation test result of ongoing five-cell stack at 30 A.

To date, MSRI has successfully developed materials sets suitable for reversible SOFC/SOEC applications. Built with the advanced degradation-resistant SOEC technology, the voltage degradation rate was significantly reduced from the initial 30%/khr to less than 3%/khr at the five-cell stack level in the SOEC mode. Figure 2-8 summarizes our materials development progress towards SOEC degradation rate reduction over the past 3 years. It is our belief that proof-of-concept demonstration of the advanced degradation-resistant SOEC technology at a large scale will be necessary and immediate towards the potential adoption by fast growing markets.
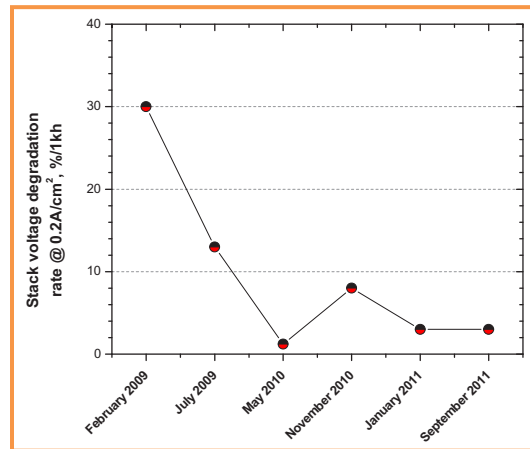
Figure 2-8. MSRI SOEC stack degradation study progress.

2.1.4 Fabrication and Delivery of Advanced Technology Stacks to Idaho National Laboratory for Independent Testing

MSRI has delivered five-cell stacks constructed with MSRI's advanced SOEC technologies to INL for independent evaluation. Three stacks were separately delivered to INL on January 10, 2011, July 10, 2011, and August 15, 2011. MSRI personnel were also present onsite and provided assistance during stack installation and testing. Additionally, MSRI delivered several single cells and necessary seal gaskets for supporting INL's activities.

2.2 Versa Power Systems, Incorporated

2.2.1 Background

BEA is continuing an R&D project to develop an HTSE system for hydrogen production. The project was supported during FY-10 by the INL NGNP Project. The system concept calls for high-temperature process heat and electrical power supplied to an HTSE system from a high-temperature nuclear reactor and power conversion unit. The basic electrolysis repeat unit consists of SOECs made from an oxygen-ion-conducting ceramic electrolyte with its attached electrodes (anode and cathode), interconnects, and gas flow channels and manifolds. The repeat units are assembled into multiple-cell stacks. VPS has been subcontracted by BEA to evaluate in-house developed SOEC technology in steady-state degradation. VPS will compare constant current to the constant voltage operation of a kWe-class stack operating as a steam electrolyzer.

VPS has completed execution of the agreed-upon scope of work, including one stack that operated over 2000 hours, and a second stack that has accumulated over 4500 hours of operation. Both stacks compare constant current to constant voltage operation, and were nominally sized at 1.4 kWe and 0.049 kg/hr of hydrogen production. The stacks produced 99 kg of hydrogen (theoretical) and 208 kg of hydrogen (theoretical), respectively, over the course of their testing.

A total of four stacks were built and tested over the course of this INL-sponsored effort, and a comparison was made between constant current and constant voltage operation. Given the low ASR of the proprietary VPS solid-oxide cells, they display good operating efficiencies. However, this also limits the current sensitivity of the cells, requiring significant current de-rating to accommodate modest degradation at a constant voltage. Constant voltage operation therefore results in significant apparent degradation at the system level, even if the degradation of the stack materials is minimal.

2.2.2 Stack Configuration

The stack architecture is a VPS standard 28-cell stack, with 121-cm^2 active area cells, running at 0.39 A/cm^2. Planar anode-supported cells with a 121-cm^2 active area will be used, with an electrode technology internally referred to as tape casting, screen printing, and tunnel kiln for continuous co-firing (TSC). In the fuel cell mode, this stack is designed to deliver 1 kWe or more under normal operating conditions. In electrolysis operation, the nominal power input to the stack is expected to be approximately 1.4 kWe, with a hydrogen production rate of approximately 50 g/hr. The operating temperature will be set to approximately 750°C. A VPS 28-cell stack of the type that will be used is shown in Figure 2-9.

Figure 2-9. 1-kWe VPS stack.

2.2.3 Stack Testing and Results

VPS has been developing a new family of SOFCs, generically termed by VPS as TSC3 cells. This is a third generation of cells fabricated via TSC (the process developed by VPS). These cells are being tested in both the fuel cell and electrolysis modes of operation, and are showing promising results. Some effort is under way to optimize the electrodes specifically for electrolysis operation as a part of parallel running projects at VPS.

The stacks built in this INL project are as follows:

1. Stack GT055296-0103 is a six-cell stack to validate a new anode flow media solution, developed under the United States (U.S.) Department of Energy (DOE) Solid State Energy Conversion Alliance (SECA) Program, and validated at the approximately 550-cm^2 active area level, but never previously implemented into small active area, 121 cm^2, cells. This stack has been running over 1600 hours so far, with a degradation rate less than half that of stack GT056019-0139.

2. Stack GT056019-0149 is the first 28-cell stack that incorporated the new anode flow media thought to be more suitable to electrolysis conditions. This stack was destroyed in a test stand failure after 800 hours of operation.

3. Stack GT056019-0150 is the second 28-cell stack that was built and run, in parallel to stack GT056019-0149, as a backup. It has accumulated 4650 hours of electrolysis hold to date, with degradation results reported herein.

4. Stack GT056019-0152 is the third 28-cell stack that was built, which replaced stack GT056019-0149 after it was destroyed in a test stand failure. It has accumulated 2300 hours of electrolysis hold, with degradation results reported below.

The test plan, and discussion of the first two stacks, stacks GT055296-0103 and GT056019-0149, was reported in a separate test plan document and the interim report, previously submitted to INL. Therefore, the following discussion focuses on the last two stacks, stacks GT056019-0150 and GT056019-0152.

2.2.4 Stack Electrical Configuration

To run the stack under both constant current and constant voltage electrolysis conditions, an additional voltage reference was needed, as shown to the right of Figure 2-10. This voltage reference serves to invert the polarity of the stack voltage feedback signal to the electronic load. Inversion is required because the load is designed for battery testing, where a drop in voltage should result in a drop in current, and vice versa. For electrolysis, the opposite reaction is required—if the test article voltage drops, current should be increased. The feedback also needs to be of positive polarity. Therefore, the solution was to use a stable laboratory power supply to provide a voltage V_{ref}, here chosen to be 60 V. The signal to the load bank becomes $V_{feedback} = V_{ref} - V_{stack}$, which has the characteristic of being a positive value for any foreseeable stack voltage and is such that $\Delta V_{feedback} = -\Delta V_{stack}$, as long as V_{ref} is constant. This is a workaround, allowing the use of the already installed load bank to run electrolysis conditions.
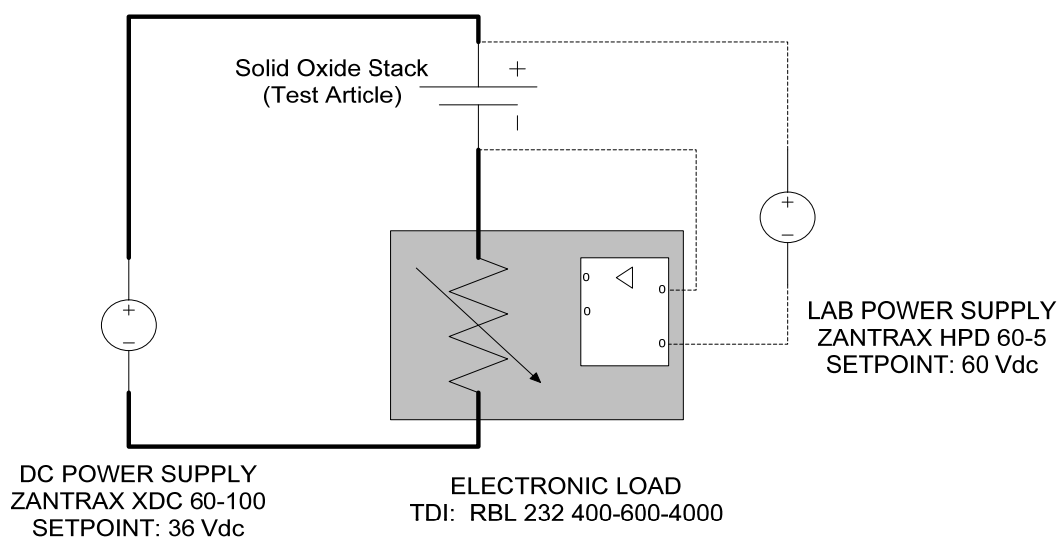
Figure 2-10. Electrical layout to allow constant stack voltage control in electrolysis.

A 60-V setpoint was chosen, somewhat arbitrarily, to give a control signal magnitude on the same order as the overall stack voltage, as well as to make the signal less sensitive to small variations in the reference supply output.

Although the power supplies, electronic load, and test stand data acquisition system are all electrically floating relative to ground, some voltage offset was visible on the top and bottom cell voltages, as read by the test stand, when the reference supply was put in-circuit. This suggests the electrical ground isolation of the test article is not perfect.

2.2.5 Stack GT056019-0150

2.2.5.1 Discussion

Stack GT056019-0150 was built and put into test in parallel with stack GT056019-0149 when the latter showed a weak cell layer, as reported in the interim report. The stack was installed into test stand

No. 1, the only other VPS test stand presently capable of running a "kW-class" (approximately 1.4 kWe actual in the fuel cell mode) electrolysis stack. Test stand No. 1 had been modified for preliminary electrolysis development, and does not have the same level of traceable calibration as was instituted for INL testing on stand No. 3.

This stack was built with an improved anode flow media technology that was developed under the U.S. DOE SECA Program for 550-cm^2 active area cells, and was showing performance and degradation advantages. The flow media was sized for the larger flows associated with the larger cells, so there was some uncertainty about operation at lower flow rates. While the oversized flow media would negatively impact the ability of these stacks to achieve higher fuel utilizations, it was anticipated that the impact would be small enough that it would not hinder stack operation under the electrolysis conditions of interest. This was validated on the stacks that were reported on in the interim report.

2.2.5.2   Test Overview

Stack GT056019-0150 is currently at 4650 hours of elapsed time into the electrolysis hold, after the stack's initial full thermal cycle (Figure 2-11). Two interruptions occurred over the course of the test as follows:

1. At 1540 hours of elapsed time, a local grid brownout caused the reference power supply to lose setpoint and drop to 0 V, resulting in an instantaneous stack unload. The stack was reloaded in the constant current mode to confirm that no damage had occurred and then switched again to constant voltage.

2. At 2101 hours of elapsed time, shortly into the second constant voltage hold, a solid-state relay (SSR) that powered the stack furnace failed, requiring a full thermal cycle to replace the SSR and restart the test.
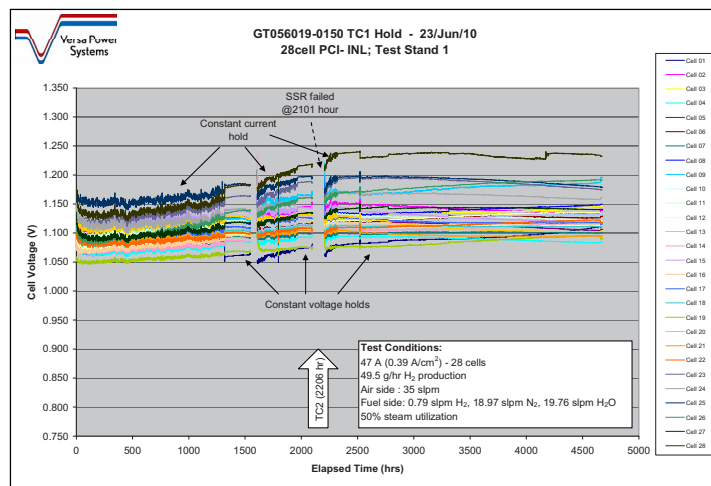
Figure 2-11. Stack GT056019-0150 electrolysis holds.

2.2.5.3   Constant Current Hold

Discarding the initial 50 hours as a stabilization period where performance is improving, stack GT056019-0150 demonstrated an average cell degradation rate of 15.3 mV/khr (1.4%/khr) over the constant current hold, from test hour 50 to hour 1320; at 0.39 A/cm^2, and 50% steam utilization. These results are shown in Figure 2-12.

10

Observations for the constant current hold period are as follows:

1. The voltage spread of 110 mV is quite large. One possible explanation is the incorporation of the new anode flow media, although more testing would be needed to confirm this was the cause of the wide voltage spread.

2. The degradation is relatively the same across all cells, there are no outliers over this time period. There does not appear to be any correlation between cell voltage and cell degradation (i.e., cells with high voltage, indicating less favorable conditions, are not degrading faster).
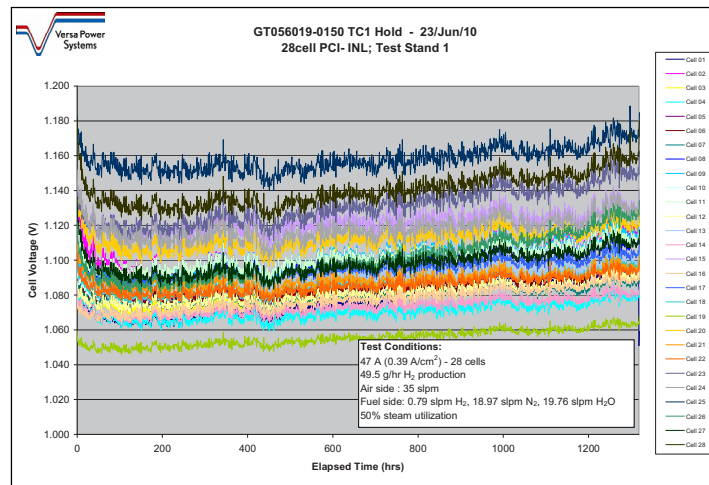
Figure 2-12. Stack GT056019-0150 constant current electrolysis hold.

2.2.5.4   Constant Voltage Hold

Figure 2-13 shows roughly 2300 hours of constant voltage hold. The main observations for the constant voltage hold period are as follows:

1. Comparing cell-to-cell, there are no significant outliers over this time period. While the stack has degraded overall, this is not being caused by individual cell layers, all cells are contributing to the overall degradation.

2. The average stack voltage is constant, controlled by the electronic load. The stack electrical current (hydrogen production) is degrading.

3. The voltage spread between cells is higher, about 160 mV, than for the original constant current hold. A close examination of Figure 2-11 suggests the following two causes:

    -   Data acquisition changes were triggered when the reference power supply was added at hour 1318, evidenced as an instant 30-mV decrease in reported cell No. 1 voltage and a 20-mV increase in reported cell No. 28 voltage, resulting in an overall reported voltage spread of 125 mV

    -   Some damage to cell layers occurring over the two unplanned transients resulted in the full 160-mV spread.

11
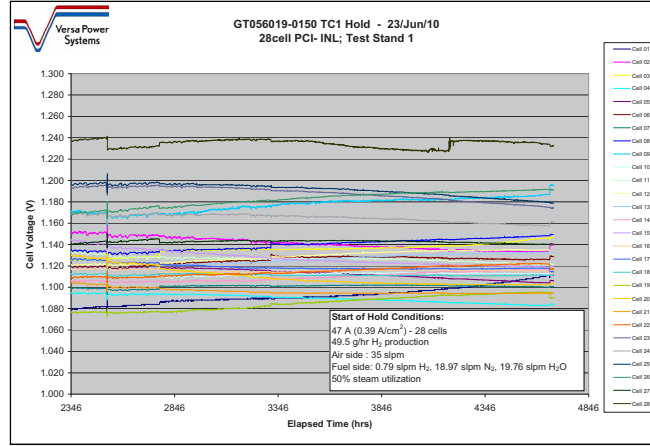
Figure 2-13. Stack GT056019-0150 constant voltage electrolysis hold.

2.2.5.5   *Degradation Rate Comparison*

A direct comparison of constant current degradation to constant voltage degradation is not necessarily simple; these are in many ways different operating strategies with little in common to form a basis for comparison. An approach is to examine the implications on an idealized system operating in each mode. Figure 2-14 shows this comparison by reporting lower heating value (LHV) efficiency of the stack, and hydrogen production rate, over the 4600 hours of operation to date.

LHV efficiency is calculated as:

$$\eta = \frac{\Delta H_{LHV_{H_2}} \dot{n}_{H_2}}{\overline{V}_{cell} I} = \frac{\Delta H_{LHV} \frac{I}{nF}}{\overline{V}_{cell} I} = \frac{\frac{\Delta H_{LHV}}{nF}}{\overline{V}_{cell}} = \frac{\frac{242 \, kJ/mol}{2*96485.34 \, C/mol}}{\overline{V}_{cell}} = \frac{1.254[V]}{\overline{V}_{cell}}$$

(2-1)
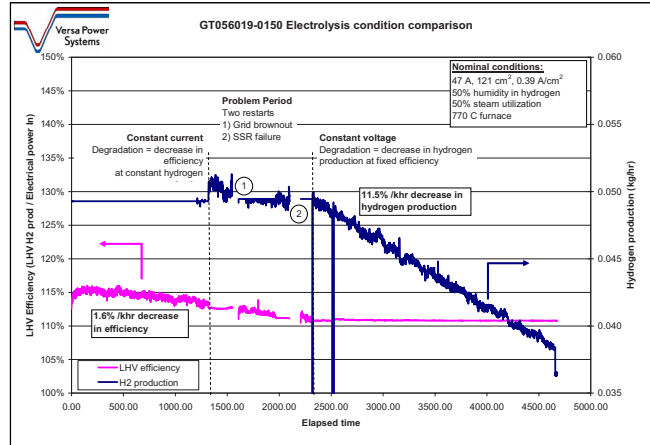
Figure 2-14. Stack GT056019-0150 electrolysis condition comparison.

The hydrogen production rate is calculated as:

$$\dot{m}_{H_2} = \frac{I}{nF}(MM)(\#cells) = I \frac{2.016 \, g/mol}{2*96485.34 \, C/mol} 28 = 1.05 * I[g/hr]$$

(2-2)

The calculated hydrogen production rate reflects the ion conduction implied by the imposed current, in practice the net hydrogen production of the stack will be lower through two mechanisms as follows:

1. Electrical leakage bypassing the electrolyte will consume current without generating hydrogen.

2. Gas leakage would result in loss of hydrogen (fuel leak-out) or reaction with oxygen and reversion to steam (oxidant leak-in).

No attempt was made to quantify these effects on this test.

With these calculations as a basis for comparison, an idealized system configured to run at constant current would produce hydrogen at a rate of 0.049 kg/hr, with an LHV efficiency that decreases by 1.6%/khr (left, Figure 2-14) based on VPS' cell material and selected operating conditions. Assuming that the degradation rate was stable over longer periods (for the purpose of discussion), this idealized system would operate for 19 months before reaching an arbitrary threshold of a 20% decrease in efficiency. During this time, the stack would always be endothermic, requiring an external heat source, so there is no danger of high in-stack temperatures. In addition, as the flows are constant, the system balance of plant is simpler, and could be well optimized for any given operating point.

In the constant voltage case, starting at approximately 2400 hours, the idealized system behaves quite differently. SOEC efficiency may be constant, but the output drops at a rate of 11.5%/khr. Assuming that this degradation rate is stable (and note that over 2300 hours it looks fairly linear), a similar arbitrary 20% degradation allowance would give a system lifetime of only 2.4 months, compared to 19 months for constant current. This degradation rate is also at constant gas flow rates, which might make sense from a balance-of-plant simplicity perspective, but it does mean that steam utilization is decreasing over time, requiring balance-of-plant setpoint changes as a function of time. The final drop in hydrogen production (far right, Figure 2-14) shows what occurs if the flows are adjusted to have the same steam utilization conditions as at the start of the constant voltage hold. This drop corresponds to a further 1.7%/khr drop in hydrogen production, implying an even shorter useful life of 2.0 months if flows are scaled with current.

It would be incorrect to blindly state that degradation is 8.4 times worse in constant voltage as in the constant current mode, because the degradations are measuring different quantities. In fact, the physical degradation in the constant voltage mode is likely the same or less than in constant current.

However, it is fair to say that a system configured to run constant current is likely to run significantly longer than a system configured to run constant voltage, unless there is some reason causing different degradation rates.

It is interesting to examine why the apparent degradation rate is higher when operating in the constant voltage mode. However, in this testing some confounding factors intrude as follows:

1. The two test interruptions may have increased the degradation rate between the two holds. This does not appear to be the case, but may nonetheless be present to a certain extent.

2. The constant voltage condition was run after the constant current condition, so if there is an acceleration of degradation with age, this might be impacting the results. Again, there is no clear evidence that this is occurring, but there may be some influence.

It is believed that the main reason for the difference can be directly attributed to the fuel cell performance. Figure 2-15 shows an example of a voltage current curve taken before and after significant degradation on an unrelated single-cell electrolysis test. If this degradation occurred in an idealized system running at constant current, starting from an arbitrary starting point of 0.34 A/cm^2 and 1.031 V, the impact would be an increase in cell voltage to 1.075 V, corresponding to a drop in LHV efficiency of 5%. The same degradation in constant voltage operation would correspond to a drop to 0.23 A/cm^2, a 32% decrease in hydrogen output.
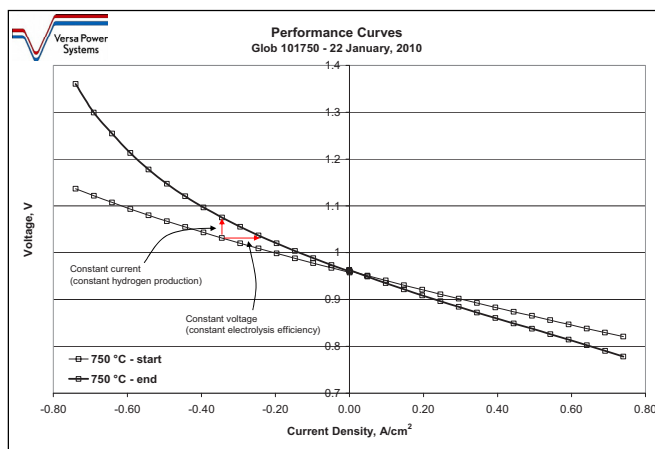
Figure 2-15. Example cell: 50% hydrogen, 50% steam voltage current curve, before and after degradation.

In other words, for a given amount of physical degradation, a system configured to run in the constant voltage mode will be impacted much less than a system configured to run in the constant current mode. The better the cell (the lower the intrinsic ASR) the more this will be true, so as cells improve as development proceeds, the relative discrepancy between constant current degradation and constant voltage degradation can be expected to increase.

In summary, stack GT056019-0150 has run 4675 hours in the electrolysis mode, and continues to display stability cell-to-cell. A comparison of constant current to constant voltage operating strategies shows the not-unexpected result of significantly higher rates of apparent degradation in the constant voltage mode. The difference in apparent degradation is a result of the stack impedance, and does not reflect a physical degradation of the stack. This highlights that system operating strategy can have an important impact on apparent stack lifetime. As materials improve, lowering the cell ASR, the challenges with operating at constant voltage will only increase.

2.2.6 Stack GT056019-0152

Stack GT056019-0152 was built late in the program to replace stack GT056019-0149 that was destroyed by a test stand failure. There was not time in the program to complete the full test protocol, but enough to get some initial data. The stack held for a total of 2049 hours with 1200 hours in the constant current mode and the balance at constant voltage. The stack also displayed a wide voltage spread, with general stability over the operating period (Figure 2-16). Cell No. 28 displayed abnormal behavior, starting with poor performance and improving with time. This is thought to be an indication of a problem with the new anode flow media, and improving electrical contact on that layer with time.

14
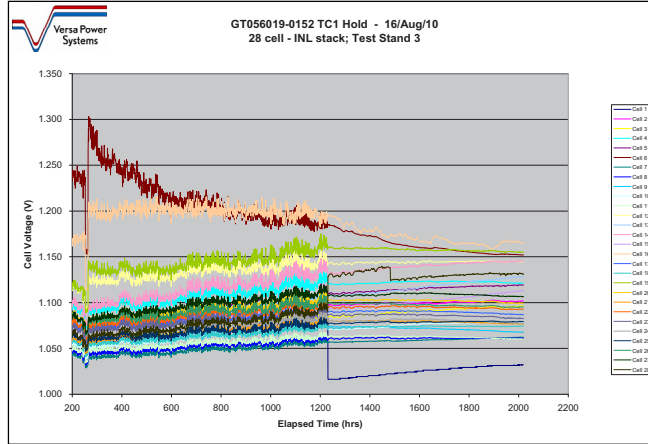
Figure 2-16. Stack GT056019-0152 electrolysis hold.

Following the same degradation assessment strategy as for stack GT056019-0150, the constant current degradation rate is 1.9%/khr reduction in LHV efficiency (Figure 2-17), and the constant voltage degradation is 7.6%/khr reduction in hydrogen output.
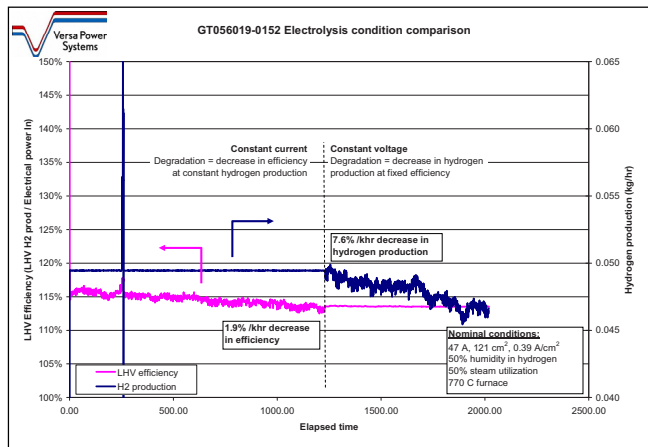
Figure 2-17. Stack GT056019-0152 electrolysis condition comparison.

Although the magnitudes are different, the conclusion is the same—system lifetime will likely be higher with a constant current operating strategy.

2.2.7 Summary

Three 28-cell stacks and a six-cell stack utilizing 121-cm^2 VPS cells have been built for the INL project. An improved anode flow media, developed under the U.S. DOE SECA Program, has been successfully demonstrated on these smaller stacks. In addition, the latest generation of cells (TSC3) has been incorporated.

The kW-class stacks (starting input power of 1.4 kWe) have been demonstrated for over 4500 hours (one stack), including periods under constant current control and constant voltage control. A second stack operated for over 2000 hours, also under both constant current and constant voltage control.

In both cases, the rate of degradation, as measured by system relevant variables (LHV efficiency and hydrogen production), are significantly higher for constant voltage operation. This is a direct consequence of the low ASR of these cells, which show little change in voltage for large changes in current. This does not reflect a physical degradation of the cell or stack materials, but is a consequence of stack impedance. With the expectation that cell performance will continue to improve with more development effort, voltage control is expected to become progressively less useful as a system control strategy.

2.2.8 Acknowledgements

1. Tony Wood and Hongpeng He have been leading the cell and cell materials development effort resulting in this new generation of cells.

2. Sofiane Benhaddad continues to find and evaluate new metals contributing to the overall lowering in degradation rates, as well as leading post-test analysis activities.

3. Thanks to Todd Machacek for taking time out from his regular duties to identify and install calibrated instrumentation for this testing.

4. Thanks to Cam Rankin for organizing the stack build effort, and designing and validating the modified anode flow field design integrated into these stacks.

5. Thanks to the wider team, including Ana Barros and Tahir Joia, for production help, and Marek Pozarski for test stand upgrades, stand failure analysis, and recommissioning.

2.3 Ceramatec, Incorporated

2.3.1 Background

Over the last 8 years, Ceramatec's R&D collaboration with INL in the area of HTE has resulted in a wealth of information regarding the performance and degradation of SOECs. Analysis of the cell and stack components, pre- and post-test, has shown several materials related first order causes for performance degradation. They are as follows:

1. Air electrode delamination.

2. Air-side bond layer compositional instability.

3. Cr evaporation from metal interconnect depositing on air bond layer and air electrode.

4. Seal leakage.

5. Potential electrolyte composition instability near the electrode interface.

6. Loss of mechanical contact by electrode sintering shrinkage and interconnect creep.

Significant changes to the materials addressing items 1 through 4 were implemented prior to the beginning of the current project year that resulted in lower degradation, of the order of 8%/khr measured at a constant voltage of 1.3 V/cell. The current project year focused on refining and/or modifying materials and processes to identify parameters that influence the degradation characteristics.

Additionally, performance improvement, having a direct effect on stack cost on a per kilowatt basis, has also been a focus of materials development area. To this end, a low level activity was conducted to fabricate thinner (target of less than or equal to 50 μ) electrolyte on a porous support to significantly lower the electrolyte contribution to cell resistance. The electrode, preferably the air electrode, was to be infiltrated into the pores. The infiltrated electrode would have the additional benefit of impeding macroscopic delamination from the electrolyte.

An alternate electrolyte composition targeting improved long-term stability was also investigated. The world-wide availability issues with ScO, used as the dopant in the current zirconia electrolyte, due to a shift in Chinese rare earth export policy, added certain urgency to this task. The alternative electrolyte composition evaluated was double-doped, 4 mol% Y_2O_3, 4 mol% Yb_2O_3 in ZrO_2 (i.e., oxide mol% basis) that was custom synthesized by our commercial vendor, Daiichi Kigenso Kagaku Kogyo Co., Ltd. (DKKK). A fuel cell test of 5 years in duration at Ceramatec in the early '90s showed that the 4Y4Yb composition was the most stable when tested in the fuel cell mode. This material was not commercially available and required in-house processing. However, it was expected that electrolyte stability of the 4Y4Yb-doped zirconia composition in the electrolysis mode would match that previously shown in the fuel cell mode. This composition was patented in 1967 by Franz Josef Rohr of Brown Boveri (Deutches Patentschrift 1671704, UK Patent 1,170,046). Ceramatec was working with ABB, Incorporated (Ulf Bossel, ABB, Incorporated, SOFC program director), at the time this material was being explored as an SOFC electrolyte.

Key activities in materials development over the past year are summarized below. Ceramatec's effort on these tasks was significantly augmented using nongovernment support.

2.3.2 Materials Development

2.3.2.1   Materials and Process Refinement

Several modifications to the composition of air electrode, underlayer, and firing conditions were initiated and many went through button-cell evaluation. As background, the standard set of materials used in an electrolysis cell consists of Sc-doped zirconia electrolyte, Ni-ceria fuel electrode, and La-Co-Fe oxide-based perovskite (of the type ABO_3) air electrode with a dopant on the La site. At high temperatures the A-site element (in this case La for example) has a tendency to react with zirconia to form an insulating phase while B-site elements (e.g., Co and Fe) tend to diffuse into zirconia without forming a new phase. Thus, it is common practice to add an underlayer of ceria before the air electrode is printed and fired. A high-conductivity perovskite (LaSrCoFe) is printed on top of the air electrode, and a Ni ink layer is printed on top of the fuel electrode as current distribution layers (also known as current collectors). More than 50 button cells were tested to evaluate these changes. A list of the button cells tested with a summary of their compositions and operating conditions is provided in Table 2-2.

2.3.2.2   Electrode Compositions

The modifications to the air electrode along with preliminary conclusions from the button-cell tests are as follows:

1. A-site deficient (nonstoichiometric A1-xBO3) with the objective of reducing the reaction driving force for A element forming an insulating phase. No significant change in initial performance noted, indicating that the interface reaction during fabrication is not significant with stoichiometric electrode composition. This may have been due to the presence of the ceria underlayer.

2. Single-step sintering of ceria underlayer and air electrode. No benefit seen in performance. The ASR was higher than standard.

3. Nonperovskite composition. The University of Texas at Austin (UT Austin) published results of their fuel cell testing using a nonperovskite air electrode that showed good performance. The composition tested was YBaCo3ZnO7 + Gd-doped ceria composite. This work was done with UT Austin permission. The button-cell performance was comparable to the current Ceramatec electrode only after catalyst infiltration, which is normally done for the Ceramatec electrode. As the long-term stability of the UT Austin electrode and its interaction with other components is not known, no further work was done.

Table 2-2. List of button cells tested in FY-11.

Build No.	Purpose	Electrolyte	Anode	Cathode	Fuel Cell OCV[1]	Fuel Cell ASR	HTE OCV	ELEC ASR
400								
401					1.050	1.030	0.970	1.630
402	A-site defient cathode	6ScZ	NMC70:30	ASD LPCF	0.950	1.120	0.910	1.310
403					1.000	0.590	0.920	0.610
404								
406	SDC underlayer	6ScZ	NMC70:30	ASD LPCF	1.050	0.660	0.960	0.720
407	on both electrodes				1.050	0.680	0.948	0.760
408								
410				YBCZ	0.990	0.920	0.940	0.740
411	UT Austin cell	6ScZ	NMC70:30	at 950C	0.970	0.690	0.920	1.020
412	evaluation			YBCZ	1.010	0.780	0.950	1.480
413				at 900C	1.050	0.600	0.950	0.600
415								
431	Fine (0.4 to 12 µm) carbon				1.060	1.150	0.970	1.300
432	added to	6ScZ	NMC70:30	std LPCF	1.040	0.620	0.960	1.000
433	LSCF bond layer				1.070	0.930	0.980	1.060
434					1.060	0.640	0.960	0.990
435								
436					1.050	0.860	0.980	0.970
437	SDC with 8Y addition				1.040	0.810	0.960	0.920
438	fired at 1350C	6ScZ	NMC70:30	std LPCF	1.000	0.740	0.920	0.870
439					1.000	0.970	0.940	1.130
440					1.040	0.830	0.960	0.900
445					1.016	0.730	0.960	0.800
446					N/A[1]	N/A	N/A	N/A
447	1400°C fired SDC	6ScZ	NMC70:30	std LPCF	0.990	0.590	0.928	0.610
455					1.020	0.750	0.950	0.880

Build No.	Purpose	Electrolyte	Anode	Cathode	Fuel Cell OCV[1]	Fuel Cell ASR	HTE OCV	ELEC ASR
456					1.020	0.620	0.930	0.680
459								
460					1.000	0.740	0.970	1.000
461	CTAB infiltration	6ScZ	NMC 70:30	std LPCF	1.030	0.850	0.970	1.200
473					1.030	0.900	0.940	0.990
474					1.020	0.650	0.970	0.930
475								
464					1.050	1.350	0.970	1.840
465	Cathode-SDC	6ScZ	NMC 70:30	std LPCF	1.020	0.940	0.935	1.020
466	co-sintered				1.070	1.000	0.980	1.180
467		6ScZ	cell fab 1106-6					
468	4Y4Yb electrolyte	4y4yb	NMC 70:30	std LPCF	1.030	1.540	0.940	1.070
469	evaluation				No data: cell cracked			
470					1.060	0.720	0.960	1.000
471					1.060	0.720	0.950	1.120
472	Urea infiltrate	6ScZ	NMC 70:30	std LPCF	0.970	1.230	0.940	0.870
462					1.040	1.170	0.940	1.270
463					1.020	1.040	0.960	1.160
482	High SA SDC (16m2/g)—				1.040	1.390	0.960	1.280
483	co-sintered with cathode	6ScZ	NMC 70:30	std LPCF	1.070	0.890	0.980	1.020
484								
485					1.030	0.670	0.950	0.900
486	High SA SDC (16m2/g)	6ScZ	NMC 70:30	std LPCF	1.020	0.450	0.930	0.510
487								
488	4Y4Yb electrolyte	4y4yb	NMC 70:30	std LPCF				
489	evaluation				cell cracked: no data			

Build No.	Purpose	Electrolyte	Anode	Cathode	Fuel Cell OCV[1]	Fuel Cell ASR	HTE OCV	ELEC ASR
490	Nitrate SDC				1.000	1.500	0.940	1.470
491	with CTAB	6ScZ	NMC 70:30	std LPCF	1.020	1.180	0.930	1.400
492	on both electrodes							
493								
494	Nitrate SDC				1.020	0.820	0.950	0.860
495	with CTAB	6ScZ	NMC 70:30	std LPCF	1.030	1.210	0.950	1.330
496	on cathode							
497								
502					1.070	0.790	0.960	1.690
503					1.030	0.590	0.950	0.890
509	5% CuO added	6ScZ	NMC 70:30	std LPCF				
510	SDC				1.050	0.770	0.960	0.770
511					1.030	1.230	0.960	1.000
512								
504					1.050	0.770	0.960	1.320
505					1.070	1.270	0.950	1.720
513	5% ZnO added	6ScZ	NMC 70:30	std LPCF	1.040	1.190	0.960	0.750
514	SDC				1.060	1.900	0.950	1.580
515								
516	High SA SDC (16m2/g)							
517	+	6ScZ	NMC 70:30	High SA SDC	1.050	0.890	0.960	0.680
518	High SA SDC added			added	1.050	1.340	0.950	1.250
519	cathode			std LPCF				

[1] OCV = open cell voltage
N/A = not applicable.

2.3.2.3   Adhesion

A new quality control test was instituted this year for pre-test evaluation of the adhesion of the air electrode layer. As noted before, air electrode delamination during testing was found to be a major source of performance degradation. The tape peel test was instituted for the sintered ceria underlayer, as well as after the air electrode was sintered on top of the ceria layer. It was found that the adhesion of the ceria layer and bi-layer varied for the standard process that was being used. Some process changes were implemented to improve the adhesion and button cells and some stacks were tested to understand the effect of these changes. More changes are in progress. These changes include the following:

1. Addition of YSZ to ceria. Passed the tape peel test. Long-term stability in button cells and a stack appeared to improve, but overall performance was lower than the standard ceria underlayer.

2. Increase in sintering temperature for ceria layer. Improved adhesion. The button cell showed very good stability and performance. Stack results were inconclusive.

3. Addition of sintering aid to ceria composition. Two different oxide additives were tried by mixing 5wt% into the ceria ink. Both showed improved adhesion. One additive showed good performance, but more tests are needed to evaluate long-term effects.

2.3.2.4   Porous Support with Infiltration

A thin electrolyte on a porous support layer would require infiltration of electrode material into the porous layer. Nitrates of precursor material are commonly infiltrated. However, the number of infiltration and firing to provide adequate loading may add to the time and cost of fabricating cells. One alternative is to use a surfactant to increase the loading per infiltration. The figures below show a comparison of standard nitrate infiltration versus surfactant-based infiltration. The latter shows better loading. For process development purposes, while the support layers were being developed, the catalyst infiltration process was evaluated on standard screen-printed electrodes. As the process for producing thin-film electrolytes on porous matures, the electrode infiltration process will be applied to convert the supported electrolyte structure to a complete cell.

2.3.2.5   New Electrolyte Material

Based on our prior experience with the 4Y4Yb electrolyte compositions and with processing of DKKK zirconia powders, we requested a custom sample lot of powder from DKKK who was open to the request as a result of the current unavailability of scandia. The custom lot of DKKK 4Y4Yb-doped zirconia had different particle morphology, size, and surface area than their 6ScSZ used by Ceramatec, requiring several slip formulation, casting, and sintering trials. Two problems were noted with this composition compared to the standard Sc-doped zirconia. The first is poor adhesion of the ceria underlayer. Increasing the surface area of ceria is one option that is being evaluated. The second problem is the mechanical strength. The original Rohr procedure shows addition of a small amount of alumina [as an organometallic (e.g., an alkoxide)] to the powder prior to tape formulation. We have implemented this step. It appears to improve the density and qualitative strength. Button cells will be evaluated soon. DKKK and Iwatani (the U.S. representative for DKKK) visited Ceramatec in November of 2011 and agreed to prepare another custom lot of 4Y4Yb with the alumina sintering aid and targeting the powder characteristics of their 6ScSZ. Powder specifications and sintering curves will also be provided.

2.3.3 Air-side Electrode Support

Previous work resulted in porous support tape that had shrinkages that were too high (30 to 40%) to match our dense tape (21%) and yielded badly warped or cracked parts. The porous layers were also too dense to be fully functional as an electrode at the thicknesses that were needed to act as a support. Based on that work it was decided to coarsen the starting YSZ material first to be used in the porous support. This should reduce the shrinkage and yield a more open structure.

Three powders were calcined at several different temperatures (1200 to 1550°C) to coarsen the particles and lower the surface area. These powders were DKKK HSY8, and 10ScSZ and Tosoh TZ8Y. The powder particle size distribution and surface area were measured. In addition to these powders, YSZ samples were also obtained from Unitec (UCM Group, United Kingdom and Germany) that had been precoarsened. After reviewing the data, powders with promising particle size distributions were pressed into pellets and fired to measure shrinkage and porosity. These pressed pellets showed acceptable microstructures for infiltration but most had very low shrinkage on the order of 5 to 12% with about 20 to 30% open porosity (Figure 2-18 and Figure 2-19).
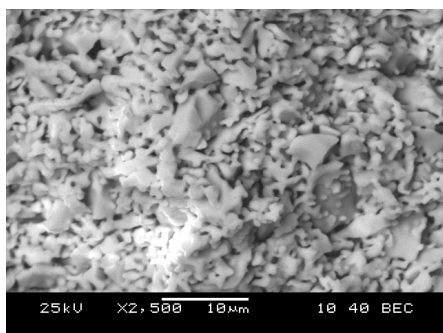
Figure 2-18. Unitec 3- to 5-µm pressed pellet.
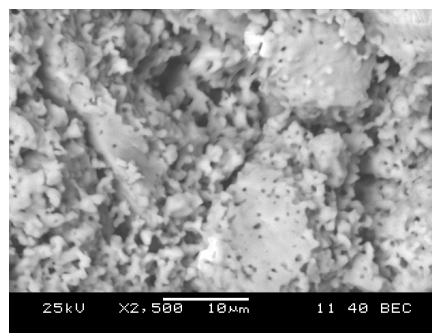
Figure 2-19. Unitec-325 mesh pressed pellet.

From the scanning electron microscopy (SEM) analysis and porosity data, three powders were selected for tape cast trials. They were the Unitec 3- to 5-µm and Unitec-325 material along with a calcined HSY8 material. Of these materials, the Unitec 3- to 5-µm powder cast the best. The others had particles that were too large and separated from the slip before and during the cast. After several unsuccessful casting trials, a Stokes settling analysis was performed to target the appropriate viscosity for the larger sized particles. Surprisingly, it predicted that the Unitec-325 cut powder could not be suspended in a slip of practical viscosity so focus was shifted to the Unitec 3- to 5-µm powder. The first Unitec 3- to 5-µm tape was made with conventional processing and milled too long so the particles/agglomerates were broken down and the tape fired too dense (Figure 2-20).
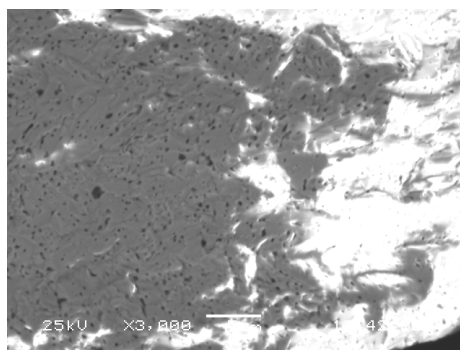
Figure 2-20. Unitec 3- to 5-µm milled tape.

After this result, more tapes were made with and without the performer using the Unitec 3- to 5-μm and 1400°C calcined HSY8 material. The slips made from these materials were not milled and they were only mixed on the acoustic mixer and cast. The resulting mixes had low viscosities and the tapes were cast thinner than desired. These fired to very fragile parts, but were sufficient for SEM analysis. Without the milling, the Unitec 3- to 5-μm powders looked very similar to the previously pressed pellets. There was also very little difference in the microstructure between the tape with pore former and the ones without except for very large pores scattered around in the tape with pore former (Figure 2-21 and Figure 2-22).
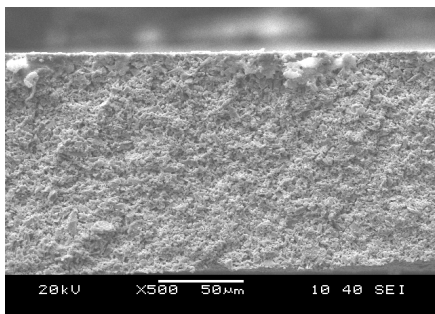
Figure 2-21. Unitec 3 to 5 μm without performer.
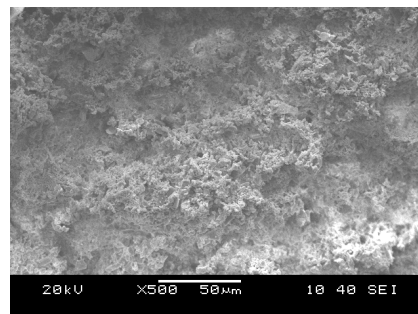
Figure 2-22. Unitec 3 to 5 μm with pore former (20%).

The shrinkage of these materials was not measureable since the cover plate used during firing constrained the parts and caused them to become badly misshaped. An additional cast of the Unitec 3- to 5- μm material without pore former was cast. Samples were fired and used for infiltration trials.

With the early trouble in tape casting, pellets were pressed and fired to evaluate the surface coating process over a bisqued substrate. Unrelated projects at Ceramatec have used this process successfully so work was started as a fallback to tape cast and lamination. These pellets were pressed from the Unitec 3- to 5- μm material and bisqued to either 1300 or 1350°C. The pellets were then coated with one of two dilute slips of a finer YSZ material and that material mixed with a coarse material, and then fired to 1250°C. After firing, the parts were coated with an even finer powder slip and fired to either 1350 or 1400°C. The resulting parts did not have dense coatings and had some large cracks in the dense layer scattered around due to high shrinkage of that layer (Figure 2-23 and Figure 2-24).
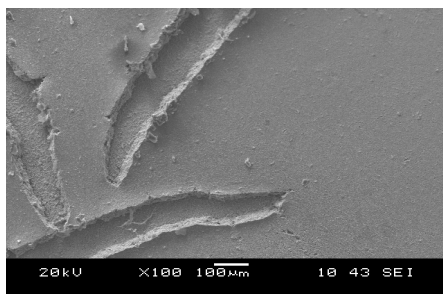
Figure 2-23. SEM surface image of coated pellet.
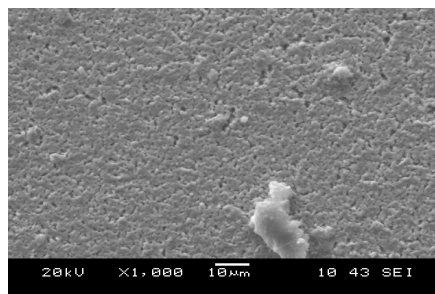
Figure 2-24. SEM image of coated pellet.

After talking with an engineer that utilizes this process, he suggested that our particle size distributions were not compatible for his process and proposed some targeted distributions that may work. Work was done to classify and create these desired distributions, and the starting pellets have been pressed and bisqued. After coating the pellets with the bond layer, it was noticed that some of the particles in the substrate powder were too large and that the bond and subsequent dense layers would not be able to close around these (Figure 2-25 and Figure 2-26).
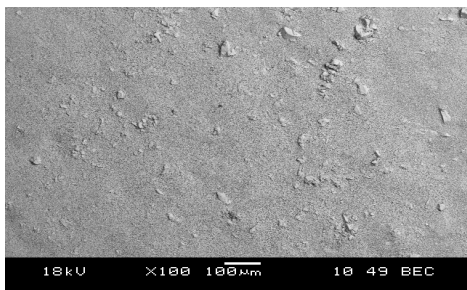
Figure 2-25. Surface of bond coat and protruding particles.
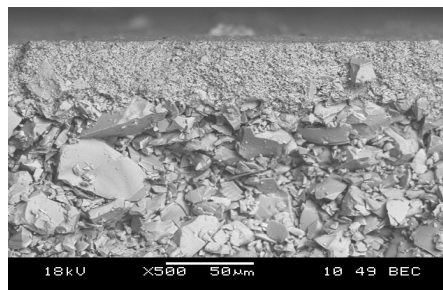
Figure 2-26. Cross section of substrate and bond coat.

Future substrates will be made from the same powder, but after screening out particles over 40 µm and then polishing the surface before coating using a 10-µm wheel. This should minimize the size of the particles that protrude through the bond coat from the support substrate.

2.3.4 Electrode Infiltration

Using fired button-cell-sized disks made from the Unitec 3- to 5- µm tape, an infiltration matrix was conducted. Variables evaluated were infiltration solution with and without dispersant, vacuum or heated infiltration, and using a predispersant or not. Most of the runs showed material buildup that was noticeable as a second phase using the SEM, but hard to see. (An EDAX scan should show material on all parts.) This made it difficult to draw a conclusion. Additional work needed to be done to improve infiltration loading and another matrix was planned. This evaluated using a different predispersant and different infiltration times at an elevated temperature along with multiple infiltration steps. After several additional trials it was found leaving the part in the solution at 60°C as the solvents were evaporated gave the best loading. Figure 2-27 through Figure 2-29 include SEM photomicrographs that show the before and after infiltration steps from the first matrix along with the improved loading from the second matrix.
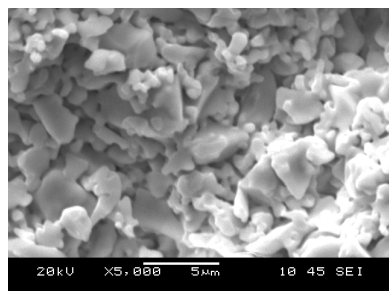
Figure 2-27. Unifiltrated porous sample.
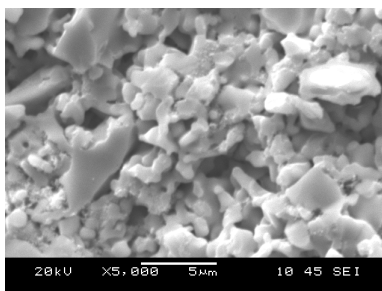
Figure 2-28. Infiltrated porous sample with hard-to-see loading.
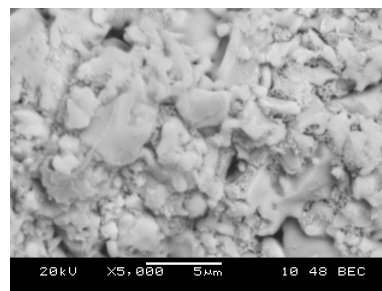
Figure 2-29. Improved infiltration loading with new procedure.

24

Alternate Electrolyte Material

Work has been going on to evaluate a replacement material for the Scandia-stabilized electrolyte material. A batch of 4Y4YbSZ was purchased and three batches of tape were cast. The first cast was more fragile than the current ScSZ material and the SEM showed large pores in the sintered parts that looked like poorly mixed tape (Figure 2-30). The subsequent tapes showed improved mixing of the slip. Sintering tests were run to ensure parts were being sintered at a high enough temperature. The tapes were sintered at 1400 and 1525°C. The density values at each temperature were very similar with the 1400°C parts at 6.26 g/cm and for the 1525°C parts it was 6.28 g/cm. Shrinkage was also very similar for both temperatures at around 21.15%. The SEM for this material shows only some very small and isolated pores comparable to the standard 6ScSZ electrolyte material (Figure 2-31 through Figure 2-33).
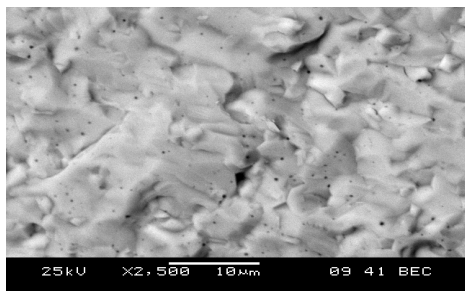
Figure 2-30. Sintered 4Y4Yb showing large pores.
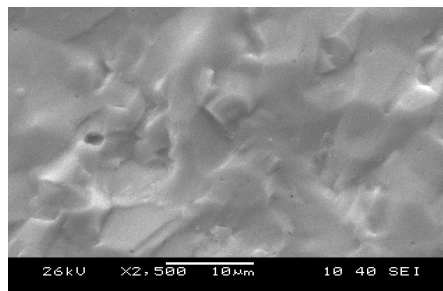
Figure 2-31. 4Y4Yb sintered at 1400°C.
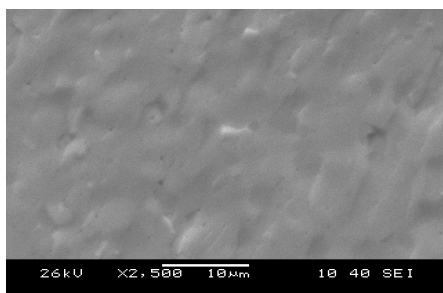
Figure 2-32. 4Y4Yb sintered at 1525°C.
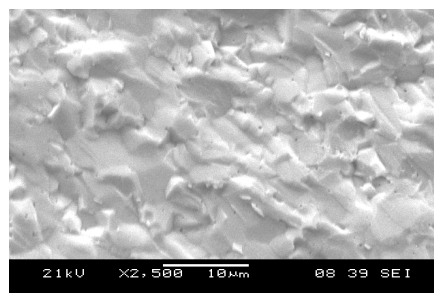
Figure 2-33. Standard 6ScES material sintered to 1400°C.

One remaining problem with these early 4Y4Yb electrolyte samples is that the underlayer does not bond well and the cathode and underlayer will peel off with adhesive tape. Several changes have been made in an effort to improve the underlayer adhesion. These include increasing the surface area of the underlayer material, varying the thickness of the underlayer, varying the firing temperature, and co-firing the underlayer and electrode materials. So far, the best adhering material was the co-fired material, but this material had high ASR in the button-cell testing. A thin cerium nitrate coating fired on the part followed by a printed SDC will be evaluated shortly. The air-side material without the underlayer does pass the peel test, but has not been evaluated in button-cell testing yet.

Due to the fragility and poor adhesion of the material, additions of a small amount of alumina are being evaluated. Two tapes have been cast and sintered at 1400°C for 6 hours. The sintered density on the tape batches were both higher than before the alumina addition with 6.35 g/cc and 6.31 g/cc. Shrinkage was also higher and was 22.3% and 23.6% for the two tapes. These tapes also had more overall binder, which could have increased the shrinkage, but other indications point to more complete sintering as the reason for higher shrinkage. The meeting with DKKK and Iwatani will result in a powder more suited to our electrolyte fabrication process.

2.3.5 Stack Fabrication and Testing

This work was funded by INL with substantial nongovernment cost share contributions.

Over the last year, Ceramatec has constructed and tested 15 SOEC stacks to help evaluate stack degradation and performance in the SOEC mode. Of the 15 stacks constructed, two were tested at INL. Some of the variables evaluated to improve degradation were air-side flow field material, air-side conductive coatings, thickness of separator plate material, air-side barrier material, getter material to clean inlet gasses, and inlet gas distribution. Most of these had a neutral effect on degradation and/or performance, with air-side flow field material and air-side coatings having a positive effect on performance and degradation.

A nonlinear degradation model and fitting procedure was applied to data from several stacks. The model expression was integrated to provide an extrapolated lifetime hydrogen production for the stack using the fitting parameters. Ceramatec's SOFC performance map methodology was revised to be applicable to SOEC operation. Techno-economic parameters were mapped into the operating space, showing conditions leading to a minimum cost of hydrogen for a given set of economic parameters.

A summary of the stacks that were constructed during September 1, 2010, through September 1, 2011, along with construction details and testing, is provided in the following subsections. References to anode and cathode retain the SOFC definition regardless of the mode of operation. Therefore, the electrolysis reaction electrode is referred to as the anode and the oxygen evolution electrode is referred to as the cathode.

2.3.5.1   Stacks 6FLEX515 and 6Metal516

Stacks 6FLEX515 and 6Metal516 were two six-cell stacks constructed to determine the effect of the Flexitallic edge seal material when compared to the standard SS441 edge rail material and to evaluate a higher fire condition during the metal treatment and coating processes. The cells were made from 6ScZ electrolyte and had standard electrode compositions synthesized using distilled water in place of demineralized water that had been used historically. The interconnects were constructed from standard SS441 separator plates with Hastelloy-X (HastX) air-side flow fields treated and coated at 1000°C with the CuMn followed by a 940°C firing of the Ag current distribution layer. The fuel-side flow fields were standard Ni alloy with Ni felt and Ni ink current distribution coatings.

These stacks were placed into a new dual position test stand where both could be tested at the same time. The initial ASR values in the SOFC mode were high and the OCV was low. The stacks were cooled down without SOEC testing.

When the stacks were removed and dismantled it was noticed that insufficient edge seal paste was used on the metal edge rails for stack 6Metal516 and that the Flexitallic edge rails were too thin to properly seal with the HastX flow fields in stack 6FLEX515. Also, the starting separator plates were too warped due to the higher temperature treatments. Both of these conditions allowed H_2 to move under the edge rails and decompose the air-side electrodes causing high ASR.

2.3.5.2   Stack 10Copasil517

Stack 10Copasil517 was constructed to evaluate a composite interconnect bond coat that performed well during the coupon testing. The cells and icons were the standard base materials used in stacks 6FLEX515 and 6Metal516, but the icons were treated and coated differently. The air-side coating for this stack had a high fire treatment and CuMn coating, but instead of using straight Ag, it was a composite of CuMn and Ag fired to 900°C. After firing, these parts were warped badly and went through a creep flattening run, but were still somewhat warped as assembled into the stack.

The SOFC mode ASR was 2.6 Ω-cm^2, and the SOEC mode ASR was 3.07 Ω-cm^2. The stack was left under load for one day and then cooled to evaluate why the initial performance was lower than expected. Upon dismantling, the icons were still too warped to make a proper seal and H$_2$ leaked under them and caused burning, which melted the Ag in the composite, which then pooled in localized regions.

2.3.5.3   Stack 7SOFC518

Stack 7SOFC518 was a seven-cell stack constructed to evaluate how our standard materials would degrade in SOFC testing. The stack was built with SS441 separator plates and HastX air-side flow field with the CuMn coating and Ag overlayers. The fuel-side flow fields were the standard Ni alloy and felt. Cells were made from the standard materials. The edge seals were Flexitallic material, but on the air side an additional thin mica material was used to make a good contact (this was based on poor contact of the air-side edge rails in stack 10Copasil517).

This stack had an initial ASR of about 2.0 Ω-cm^2 at 800°C with the bottom cell having an ASR of about 3.5 Ω-cm^2, which increased the overall stack ASR. This stack was placed under long-term load in the SOFC mode and it was stable until a breaker tripped allowing the oven to cool to 340°C with the stack under a constant current load. When it was reheated and placed back under load, the performance degraded some due to the thermal cycle. After about 4 hours of being back on test, the H$_2$ supply ran out and this killed the stack. The stack test history is shown in Figure 2-34.
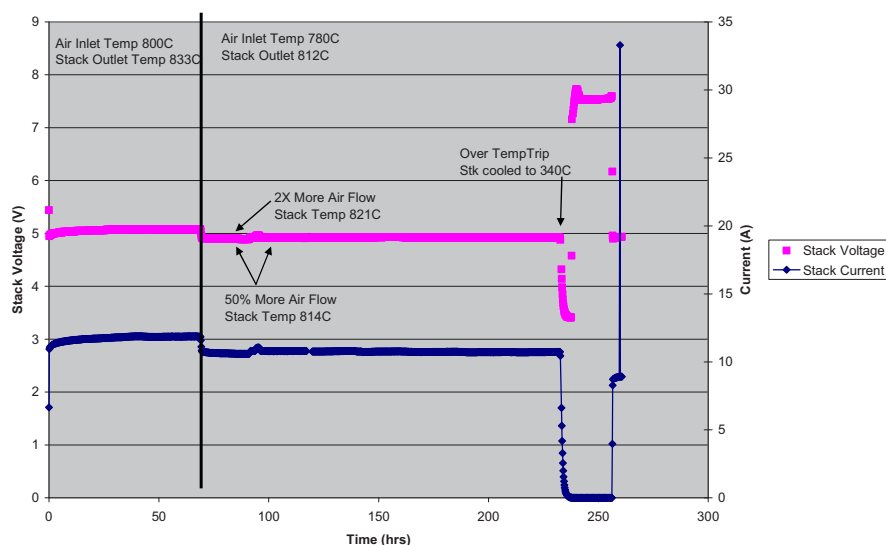
Figure 2-34. Stack 7SOFC518 performance history.

When stack 7SOFC518 was dismantled, it was seen that all of the hydrogen electrodes had oxidized and delaminated due to the H$_2$ supply failure.

2.3.5.4   Stack 519

Stack 519 was a 10-cell stack of identical construction of stack 518 that was also tested in the SOEC mode. This stack had an initial fuel cell performance at 800°C of 1.55 and 1.83 Ω-cm^2 in the SOEC mode at 800°C with an 80°C bubbler. The stack performance increased over the initial 30 hours and held steady for 90 hours. One theory for the low performance was that the inlet gas was not being fully saturated with water due to large holes drilled in the sparger. The inlet gas flow was doubled to pick up more steam and the performance increased 20%. The stack was left at this flow rate for long-term testing. The degradation rate was high, about 22%/khr for the last 400 hours. Most of the degradation came from the top cell,

which showed higher degrading from the start, and cell No. 6 that was worse than average (average was 10 to 12%/khr). When the stack was dismantled, cells No. 1, 6, and 10 were cracked and showed signs of cathode degradation. Also, all the cathodes have about the first two to three channels on each side delaminated from H_2 leakage past the edge rails adding to the degradation rate.

2.3.5.5   Stack 520

Stack 520 was a 10-cell stack following the same construction as stacks 519 and 518, except that the cell active area was reduced from 61 to 45 cm^2. This was to compensate for the air-side electrode delaminating under the first two to three channels resulting from H_2 leakage at the seal.

Initial performance in the SOFC mode was 1.15 Ω-cm^2 and in the SOEC mode it was 1.45 Ω-cm^2. The stack under long-term testing showed a degradation rate of 0%/khr based on initial performance to the point where the H_2 flow stopped (18%/khr from max power). When the stack came back on load, there was a 30% reduction of performance, but the degradation rate changed to 5.8%/khr until the power went out and the stack was taken off of load, cooled, and removed from the test stand. The stack test history is shown in Figure 2-35.
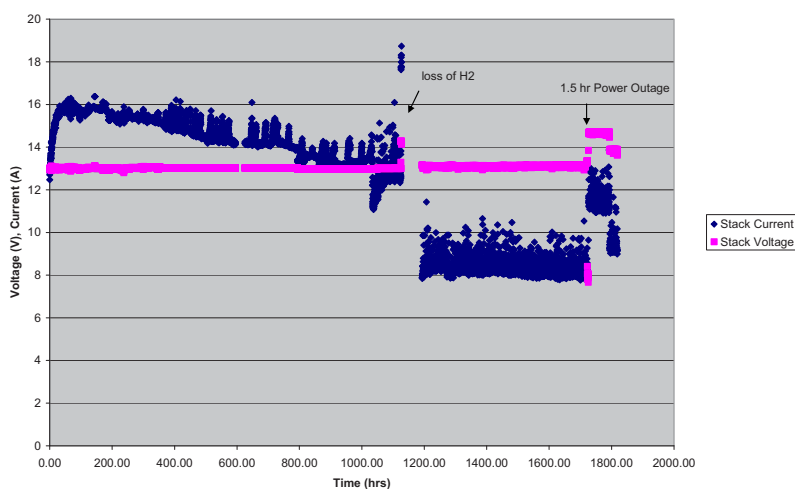
Figure 2-35. Stack 520 performance history.

A post-test disassembly of the stack showed that several of the cells had a delaminated anode likely due to the loss of H_2 and oxi/redox cycles on the anode. There was not any indication of the edge of the cathode delamination from H_2 leakage at the seal.

Air-side Delamination Problem

A photographic and observational log of the tested stack disassembly was kept in a series of PowerPoint files. These log files will be made available to the INL team as needed.

A trend observed in the post-test analysis of several stacks was cells with a delaminated air-side electrode that could not be explained by H_2 leakage from either seals or cracks. These cells contributed to the degradation rate in the stacks and the root cause needed to be understood. Peel testing of electrodes (using cellophane tape) prior to stack building was instituted and it was found that some of the cell batches had large percentages of cell area where the air-side electrode would peel off of the electrolyte at the underlayer interface. Looking at the history of the cells that delaminated in the stacks and that peeled before testing, it was noticed that the surface area of the underlayer material was lower than the cells that did not delaminate during stack testing. Not all of the cells peeled, which showed the fabrication process had moved to a condition where it was not robust. Work was instituted to improve adhesion.

Several variables were explored to resolve the issue of delamination. These included higher surface area underlayer powders, YSZ added composite underlayers, effect of underlayer thickness, and increased underlayer firing temperature. Reaction of the underlayer with the electrolyte potentially forming a second phase with a different expansion and high resistance also became a concern. Work was also initiated to evaluate lower temperature underlayer sintering to minimize reaction. Most of these trials were carried out on rejected full-sized parts. These test matrix parts were subjected to peel testing. Processes yielding improved adhesion were tested in button cells first then given good electrochemical performance the process was used to make full-size cells for stack testing.

2.3.5.6 *Stacks 5TKSP521 and 5TNSP522*

Stacks 5TKSP521 and 5TNSP522 were constructed together and tested in the same test stand to evaluate thin separator plates against thick separator plates. Previous stacks had thin separator plates and the parts were warped and may have caused leaks. The cells had the standard materials and the 45-cm^2 active area. All cells passed the tape peel test prior to assembly into a stack. The icon separator plates were SS441 with standard coatings, but in a change from recent tests, the air-side flow fields used an older stock of perforated SS441 parts that received the new coating processes. Edge rails on the fuel side were the same Flexitallic materials and thicknesses used in previous stacks, but the air side had a thin metal edge rail sandwiched between two thin Flexitallic rails.

Initial performance for these stacks in the fuel cell mode was 1.08 Ω-cm^2 for stack 5TKSP521 and 1.05 Ω-cm^2 for stack 5TNSP522. The degradation rate for stack 5TKSP521 from 500 to 3140 hours was 6.1%/khr and for stack 5TNSP522 it was 6.9%/khr. These rates were back into a range that had been seen before for similar materials leading to the conclusion that prescreening the cells for delamination may have helped reduce the degradation rate. Both of these stacks went through a couple of power outages while under constant voltage loads. The stack test history is shown in Figure 2-36 and Figure 2-37.
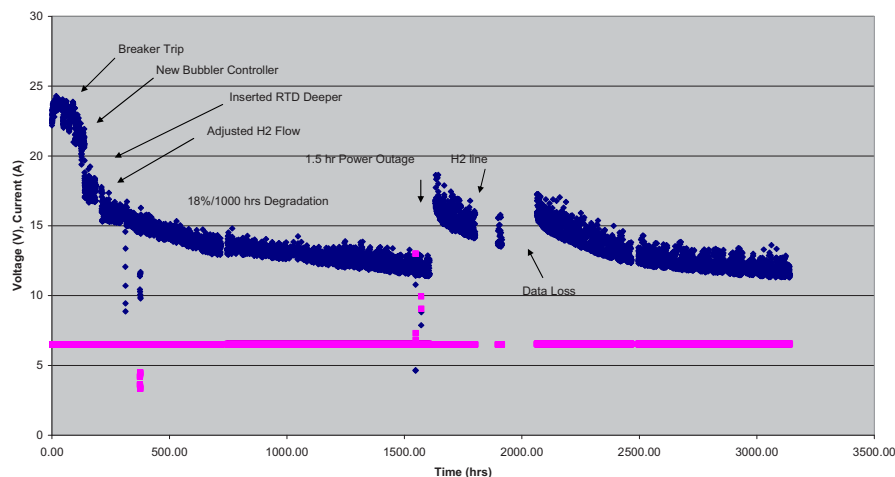
Figure 2-36. Stack 5TKSP521 performance history.
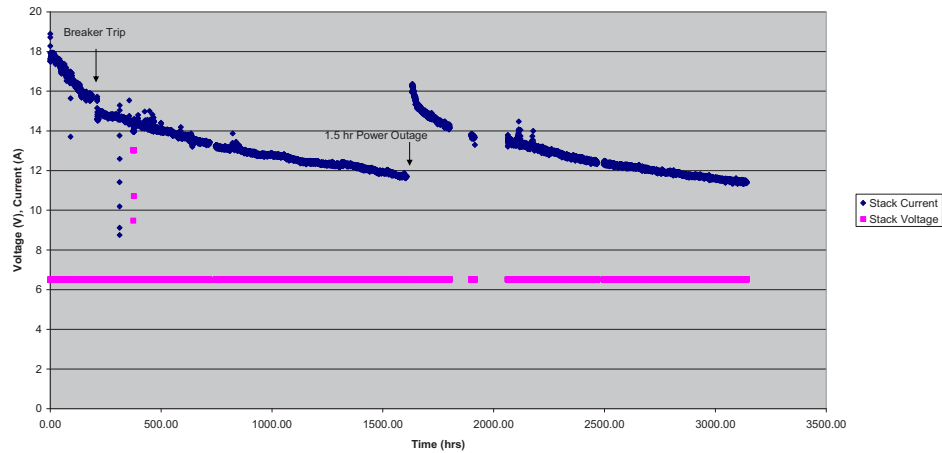
Figure 2-37. Stack 5TNSP522 performance history.

2.3.5.7   Stack 10INL523

Stack 10INL523 was a 10-cell stack built like stack 5TKSP521 with thick interconnects. The cells were prescreened for air-side delamination. This stack was installed at INL and the initial performance with an 80°C dew point was about 1.2 Ω-cm^2 at 800°C. This stack was placed on long-term load and tested at two different current densities that alternated every 120 hours or so. The lower current density had a lower degradation rate and was around 3.1%/khr. The stack test history is shown in Figure 2-38.
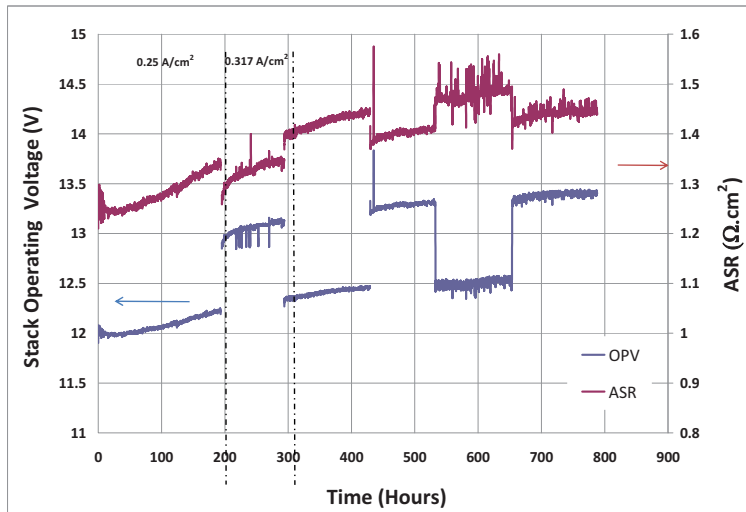
Figure 2-38. Stack 10INL523 performance history.

2.3.5.8   Stack 10CuB524

Stack 10CuB524 was a 10-cell stack that had Cu ink layer substituted in place of the Ni layer between the separator plate and fuel flow field. It also had a layer of Cu felt between the Ni flow field and the Cu printed layer on the separator plate. The Cu felt and ink layers were thicker than the standard Ni layers, so the edge rail thickness was adjusted to compensate. The stack retained the use of Ni felt between the Ni flow field and Ni ink layer printed on the anode. The air-side flow field was HastX instead of the SS441 that has been used in recent stacks. The cells were peel tested and made of two batches, one that was

standard process and another that had the underlayer fired on at a higher temperature to increase bonding to the electrolyte. These were alternated every other cell. Due to a trend where the poorest performing cell in each stack is either the top or bottom cell, a porous diffuser plate was included in the fuel inlet and air inlet manifolds. To fit this diffuser into the fuel manifold, the metal diffuser plate was removed and this porous plate was placed directly over the inlet port.

Initial testing of this stack showed low performance of 2.16 Ω-cm^2 in the SOEC mode at 800°C with an 80°C bubbler. The Cu addition should not have increased the resistance, so contact between the air-side flow field and cell was suspected (edge rail change may have been increased too much), as well as flow distribution from the diffuser plate. The spring force was increased, as well as the fuel flows, both with minimal positive effect. The stack also went through a few unplanned thermal cycles while under a constant voltage load. The stack slowly improved from about 500 hours to the thermal cycle at about 1500 hours. Following recovery from the thermal cycle at about 1650 hours onward, it was relatively stable operating around 11 A. As of mid-September of 2011, the stack was still on test, showing little to no difference between the degradation rate or performance of the cells fired at 1350 or 1400°C. The stack test history is shown in Figure 2-39 and Figure 2-40.
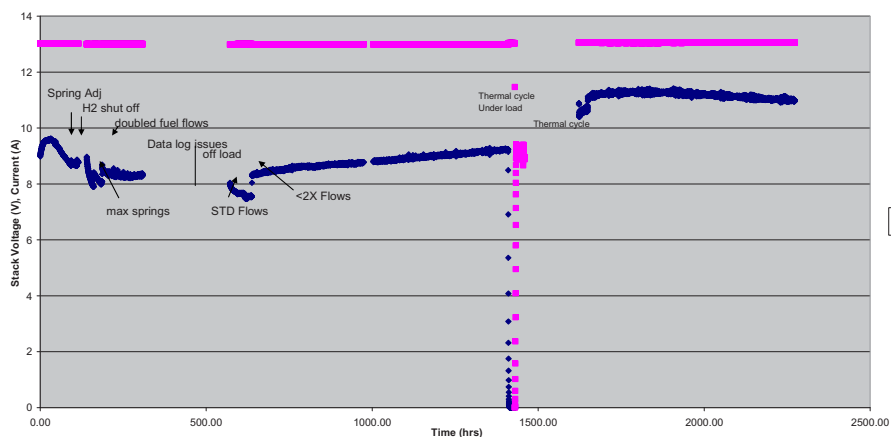
Figure 2-39. Stack 10CuB524 performance history.
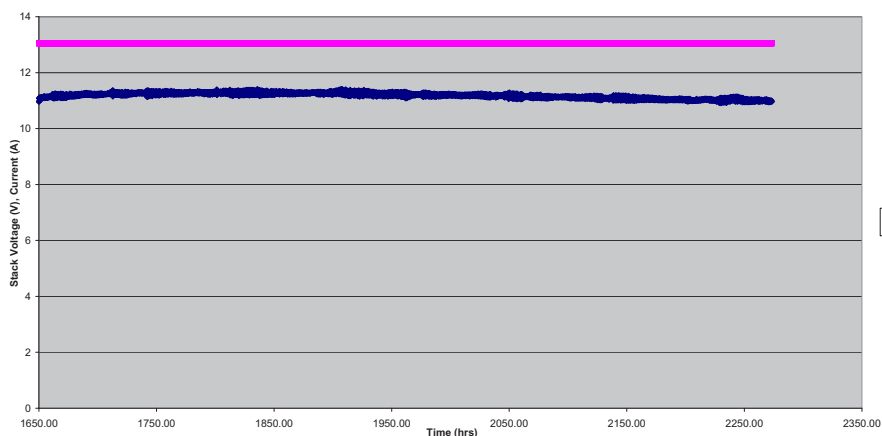
Figure 2-40. Stack 10CuB524 performance history following unplanned thermal cycle at 1600 hours.

31

2.3.5.9   Stack 5SDC8Y527

Stack 5SDC8Y527 was a five-cell stack that was made with SS441 interconnects and air-side flow fields. The icons had the standard CuMn and Ag coatings on the air side. The fuel side had the standard Ni alloy flow field and felt. The cells were made with a new composite underlayer that incorporated YSZ to increase bonding and they all passed the peel test.

ASR was 1.71 Ω-cm^2 in the SOEC mode at 800°C with an 83°C bubbler. The stack improved from 12 A to over 15.5 A after a day of being on test then began a slow degradation. This stack underwent two unplanned thermal cycles to low temperatures. The degradation rate after the second thermal cycle was high so the stack was cooled off after about 500 hours of total testing.

Post-mortem on the stack showed all cells had cracked, with the top cell having most of the air electrode delaminated due to H_2 leaking from the cracks. The end-of-life ASR on this cell was 16 Ω-cm^2 while the other four averaged about 2 Ω-cm^2. No doubt these cracks increased the degradation rate and likely happened because of the thermal cycles.

2.3.5.10   Stack 10INL528

Stack 10INL528 was constructed like stack 5SDC8Y527 and installed and tested at INL. This stack was operated for 1000 hours at a constant current density of 250 mA/cm^2. The stack voltage and ASR history is shown in Figure 2-41.
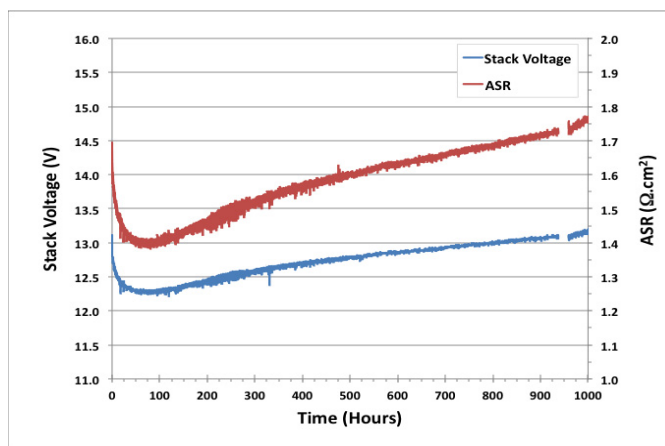
Figure 2-41. Stack 10INL528 performance history.

2.3.5.11   Stack 10RINL529

Stack 10RINL529 was a 10-cell stack built just like stack 10INL528 to evaluate stack operation between INL and Ceramatec. This stack had a high degradation rate and lower initial performance than its counterpart at INL. The stack initially experienced two unplanned thermal cycles (due to furnace and circuit breaker problems) before it was tested and another at approximately 100 hours. Cell No. 1 (top cell) was largely responsible for the high degradation rate. Upon post-mortem, cell No. 1 was cracked badly and the air-side electrode was mostly delaminated from H_2 leakage from the cracks. Two other cells were cracked, but did not show signs of much H_2 leakage. Cracks were likely formed during the quick thermal cycles. The stack test history is shown in Figure 2-42.
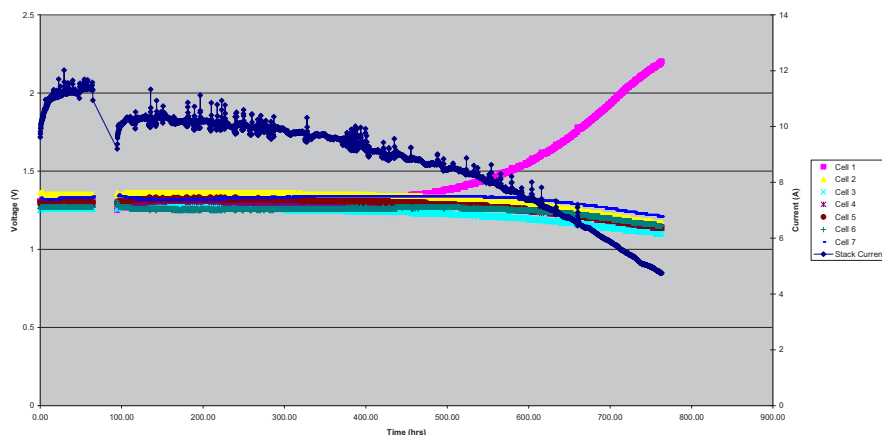
Figure 2-42. Stack 10RINL529 performance history.

2.3.5.12　*Stacks 5DIFF530 and 5XDIFF531*

Stacks 5DIFF530 and 5XDIFF531 were built to evaluate the effect of a diffuser plate in both fuel and air inlets. The worst performing cell is generally the top or bottom cell in the stack. One possible explanation is that the flow pattern in the manifold could be limiting the flow to the end cells relative to the core of the stack resulting in lower performance and higher degradation. A potential solution in such a scenario would be to install a porous diffuser plate to create a more one-dimensional velocity field approaching the flow field openings. Stack 5DIFF530 had the diffuser plate and stack 5XDIFF531 did not. A notable difference between how the diffuser plate was installed versus the one in stack 10CuB524 is that the standard metal diffuser plate in the inlet manifold was left intact and this porous plate was machined to fit the space between it and the stack. These stacks were constructed with SS441 icons and air-side flow fields with the standard treatments and CuMn and Ag coatings. Cells were all made with the higher fire (1400°C) underlayer and standard materials.

Initial SOEC performance for stack 5DIFF530 was 1.52 Ω-cm^2 and stack 5XDIFF531 was 1.41 Ω-cm^2 at 800°C with 80°C bubblers. These stacks are on long-term testing and the test history is shown in Figure 2-43 and Figure 2-44. There is much more noise in the current readings of stack 5DIFF530 compared to stack 5XDIFF531. However, this may be an indication of some instability in the bubbler system and unrelated to the diffuser plate. In any case, the diffuser plate did not improve the stack performance.
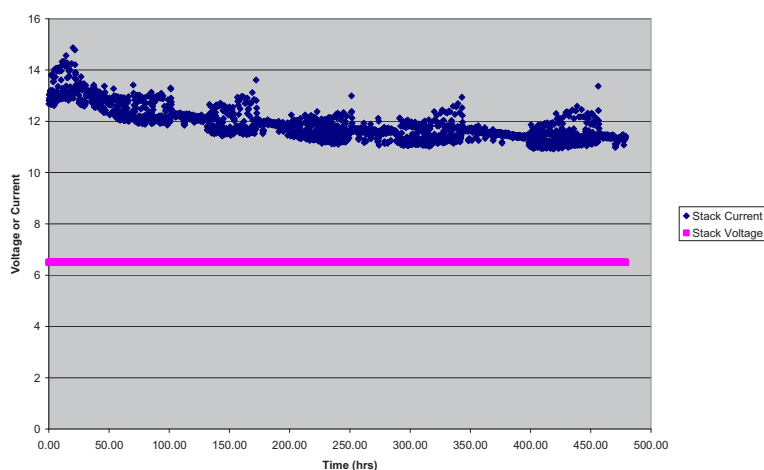
Figure 2-43. Stack 5DIFF530 performance history.

33
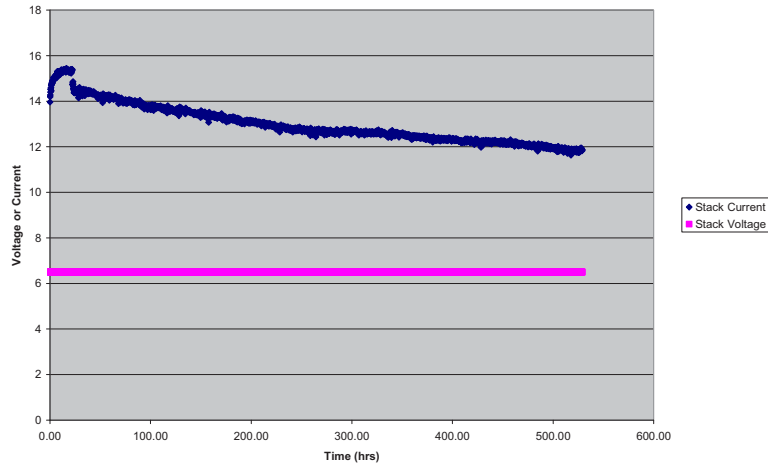
Figure 2-44. Stack 5XDIFF531 performance history.

2.3.6 Degradation Rate Analysis

It is customary to present degradation rates in units of %/khr. However, the same degradation behavior will yield different numerical values for %Voltage change at constant current compared with %Current change at constant voltage or %ASR change. Further, the degradation trajectory is clearly nonlinear, especially early in the test period. Often data from an initial "burn-in" period are not presented with lifetime results as the performance changes in the initial days or weeks of operation are not consistent with longer-term data. The degradation rate is also a function of current density over-potential at the stack operating point. The history data for stack 10INL523 are shown in Figure 2-45 and Figure 2-46. The degradation rate at 317 mA/cm^2 was 4.3%/khr (rate of increase in voltage at constant current), while the rate at 250 mA/cm^2 was 3.9%/khr. The initial two weeks of data were not used for these linear fits.
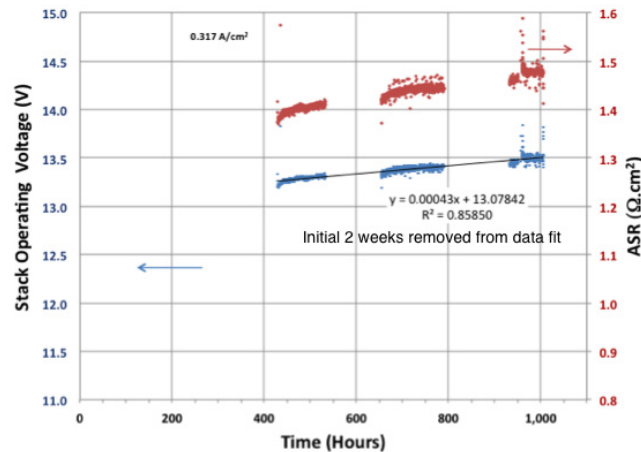
Figure 2-45. Linear fit of stack 10INL523 degradation at 317 mA/cm^2.

34
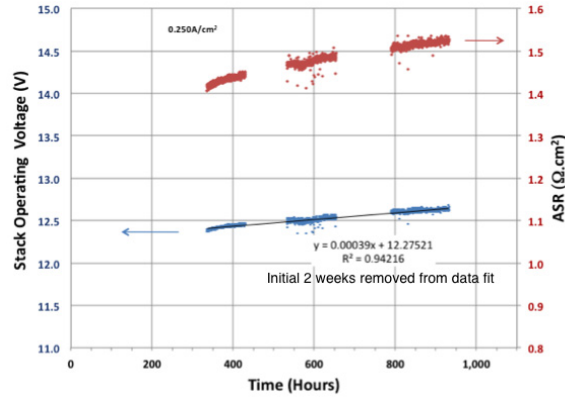
Figure 2-46. Linear fit of stack 10INL523 degradation at 250 mA/cm².

A diffusion limited degradation mechanism, such as describing oxide scale growth or cation inter-diffusion and interface reaction layer grow, leads to a parabolic rate law:

$$R''(t)=R0''*(1+sqrt(t/\tau)) \tag{2-3}$$

The variation of ASR with time requires an initial value of the ASR (R0") and a time for that value to double (τ). If the initial value of ASR is known or assumed, the value of τ can be determined from the slope of a linear regression of ((R''(t)-R0'')/R0'')^2. Alternatively, an optimizer routine can vary both R0" and τ to minimize the squared error of the model relative to the measured values of ASR. Having a value of tau enables one to account for degradation in the calculation of hydrogen production over a specified stack lifetime or period of operation. The reciprocal of the parabolic rate law can be integrated by defining the substitution variable U=1+sqrt(t/τ), resulting in a factor 2*(U-ln(U)-1)/(t/τ), which represents the average lifetime production rate relative to the initial hydrogen production rate.

The parabolic degradation rate fit of stack 10INL523 is shown in Figure 2-47. The periods of operation at 317 mA/cm² show a time to double initial ASR (τ) of about 13k hours while at 250 mA/cm² current density the value of τ increases to 20k hours. Stack 10INL528, which incorporated YSZ into the ceria interlayer to improve bonding, showed that τ had dropped to only 6100 hours indicating that the YSZ in the interlayer allows formation of a resistive La zirconate reaction layer at the cathode interface (Figure 2-48). Stack 9MiMx513, which was constructed in June of 2010 and operated for nearly 5100 hours (to January 20, 2011), showed a much lower degradation rate, with a τ reaching 36,500 hours (Figure 2-49). An overlay of mid-year stack test data, including stacks operating at the start of the reporting period, is shown in Figure 2-50.
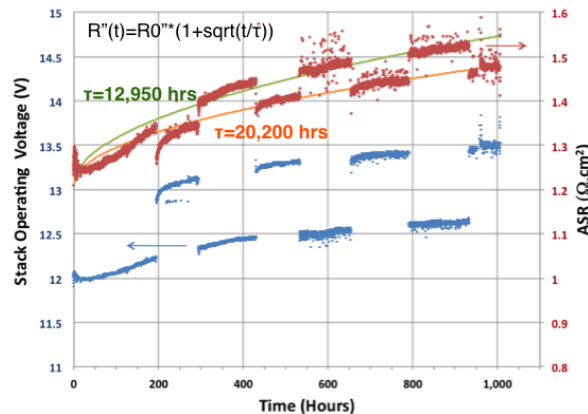
Figure 2-47. Parabolic rate fit of stack 10INL523.

35
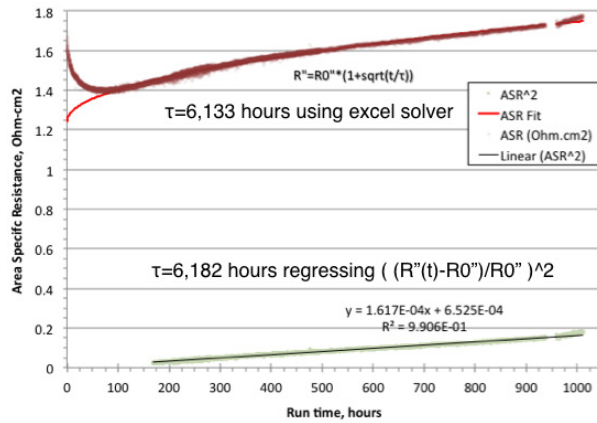
Figure 2-48. Parabolic rate fit of stack 10INL528.
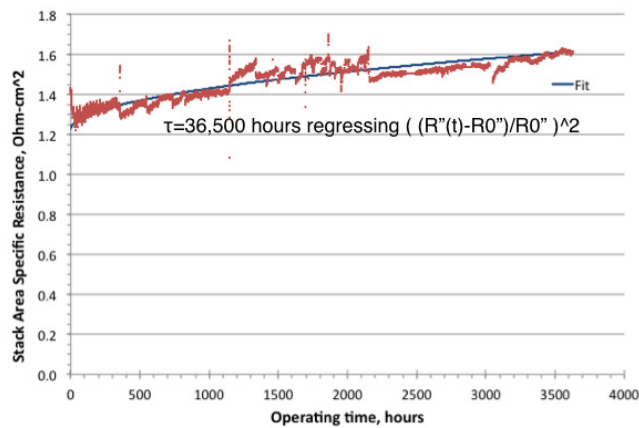
Figure 2-49. Stack 9MiMx513 parabolic degradation fit.
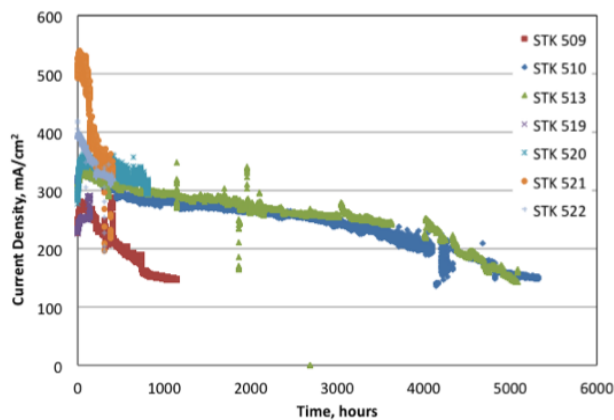
Figure 2-50. Summary of stack testing to mid-year 2011.

2.3.7   Solid-oxide Electrolysis Cell Performance Map

At a given value of ASR and operating temperature, which is usually materials limited, hydrogen or syngas production varies as a function of operating voltage and steam (or steam + CO_2) flow rate. A closed form parametric model of SOEC operation in the operating space of voltage and area-specific

36

reactant flow rates was developed following the methodology shown by Hartvigsen for SOFCs in the '90s. The calculated isolines of current density, power density, heat flux, reactant utilization and efficiency are shown in the operating space (Figure 2-51). In a similar fashion, cost contributions such as cost of electricity, CAPEX, insulation, recuperator, and process heat were also mapped into the operating space to generate a cost of hydrogen map (Figure 2-52). More details of the development of this analysis are provided in a PowerPoint format.
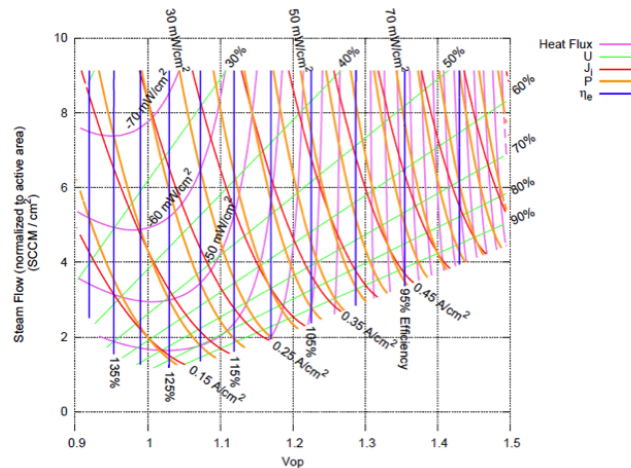
Figure 2-51. Example SOEC stack performance map.
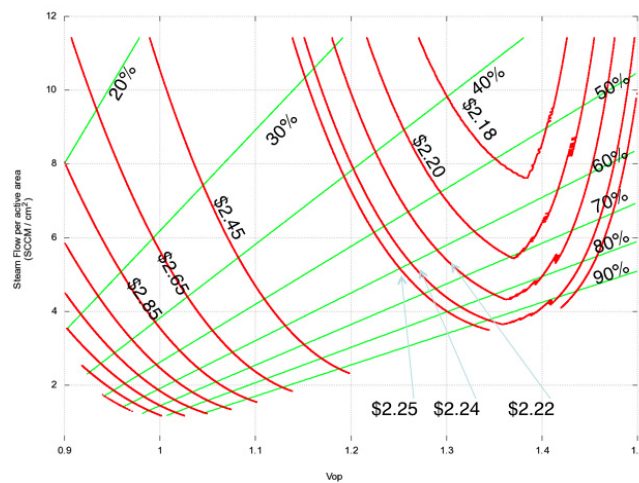
Figure 2-52. Example SOEC techno-economic map.

2.4   National Aeronautics and Space Administration— Glenn Research Center

2.4.1 Cell Design

The highest energy density configuration for a high-temperature fuel cell or electrolysis stack is the planar geometry. A repeat unit for a planar stack includes the cell itself (anode, cathode, and electrolyte), flow fields, and a gas-tight interconnect. Several basic cell designs have been developed, including electrolyte-supported, electrode-supported, and porous ceramic or metal substrate-supported cells. In an electrolyte-supported cell, the electrolyte layer is thicker than either of the electrodes and must have sufficient mechanical strength to withstand any stresses. However, as a result of the relatively thick electrolyte, ionic resistance across the electrolyte is large for this design. The best performing SOFC cells of recent design are the anode-supported cells in which the mechanical strength is provided by a thick (approximately 1.5 mm) layer of anode (usually Ni-YSZ cermet) material. Thin electrolyte and cathode layers are deposited on the anode material by screen printing or other techniques. The flow fields and interconnects for planar stacks must be electrically-conducting and are usually metallic, imposing an upper temperature limit to stack operation. NASA—GRC has developed an unconventional SOFC, called a bi-electrode-supported cell. The NASA—GRC cell is structurally symmetrical, with both electrodes supporting the thin electrolyte and containing microchannels for gas diffusion.

The electrodes are made by freeze casting—a modified tape casting technique that creates the many microchannels in the YSZ electrode green tape as shown in Figure 2-53. In freeze-casting, an aqueous or organic slip is cast across a freezing bed and micron-size ice crystals start to form at the Mylar side of the tape. The microcrystals increase in size and form continuous ice crystals that grow larger towards the top, creating a natural gradient in porosity in the green tape; the green tape is placed in a freeze dryer and the ice crystals are removed by sublimation in a vacuum, leaving the microchannels behind for gas flow. Enhancement of the microchannels is performed by laser etching. Symmetrical cells are fabricated by taking two green parts cut from the same piece of green freeze-cast tape, depositing a thin electrolyte layer between the tapes, and laminating the tapes together with the small pores facing each other, forming the YSZ tri-layer as shown in Figure 2-53. Cells 2.54 cm OD (1 in.) were prepared by firing the YSZ tri-layers at high temperature, followed by infiltration of the electrodes. Ni-nitrate was used for the SOFC anode and stoichiometric solutions of nitrates for the La-Sr ferrite cathode. Cells were allowed to dry/solidify prior to heat treatment for decomposition of the nitrates into metals or metal oxides, depending on the electrode. This infiltration procedure was performed multiple times on both the anode and cathode to achieve suitable electrodes. A total of 11 NASA—GRC button cells, based on the bi-electrode-supported cell technology, have been tested at INL to the end of FY-10. A summary of button-cell testing is provided in the FY-10 year-end report. These button cells were mounted to the end of a YSZ tube 1 in. OD using a high-temperature glass ceramic (Figure 2-54). A platinum wire was placed on both sides of the cell to read the voltage, then Ni mesh was used on the H_2 electrode and Ag mesh on the air electrode as current collectors; Au ink was used to attach the platinum wires for voltage measurement and the other leads to the cells.
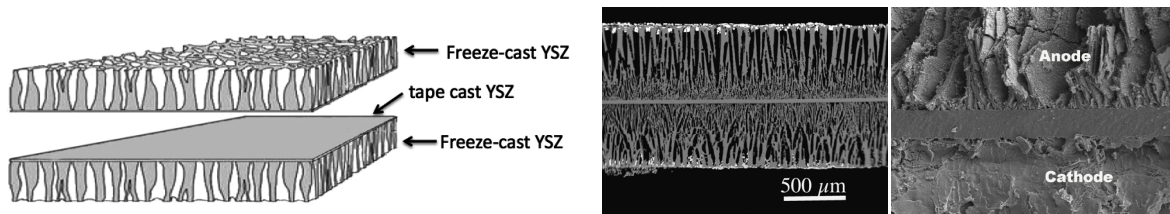
Figure 2-53. Layup (top) and cross-sections (bottom) of sintered cell showing thin YSZ (white) electrolyte in center and YSZ scaffolds/microchannels (black) formed by ice crystals during freeze castings.
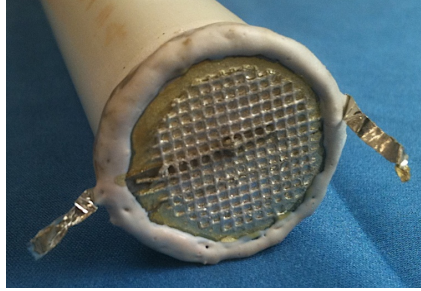
Figure 2-54. NASA—GRC button cell mounted on support tube.

The NASA—GRC stack design shown in Figure 2-55 combines multiple cells, separated by a thin ceramic interconnect rather than a metal interconnect. The stack is fabricated by coating the top and bottom of the green tri-layer cell with a thin layer of calcium-doped LaCrO3 (LCC) electronic conductor, producing a repeat unit as shown in Figure 2-56. A thin YSZ ink can be applied wet to form edge seals upon firing. This arrangement, with proper orientation of the anode and cathode scaffolds, creates the simple cross-flow geometry shown in Figure 2-56 and Figure 2-57. Given the iso-material design of the electrolyte and electrode scaffolds and an LCC interconnect with a coefficient of thermal expansion close to that of YSZ, cells can be laminated in the green state and co-sintered as one assembly, making the fabrication of the repeat unit relatively simple.[1] The all-ceramic fabrication makes it ideally suited to operate at higher temperatures, resulting in higher power density and efficiency.
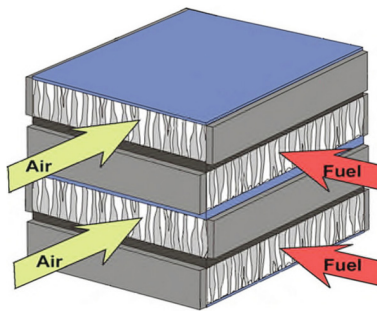
Figure 2-55. NASA—GRC cross-flow stack.
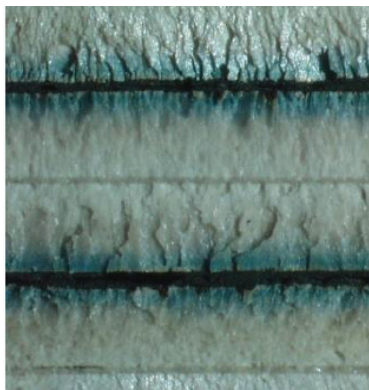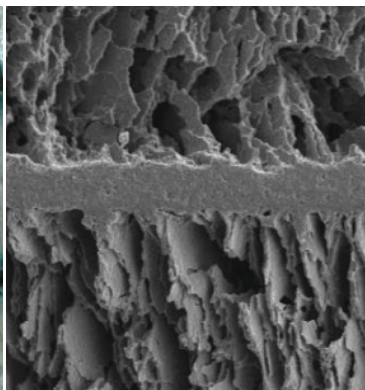
(a)   (b)

Figure 2-56. Multilayer stack of cells. (a) LCC interconnect (black), YSZ electrode support scaffold layer (500 μm), dense YSZ electrolyte (60 μm), and second YSZ electrode support scaffold. (b) 90-degree orientation of cross-flow design.

Figure 2-57. Gas inlet for NASA—GRC three-cell stack with edge seals.

Based on this cell technology and under contract to INL, NASA—GRC provided a total of four 5- × 5-cm single cells (three cells from batch No. 1 and one cell from batch No. 3), and a prototype 5- × 5-cm three-cell all-ceramic stack. Details of the experimental testing of these cells are provided below.

2.5   St. Gobain

INL established a CRADA with the St. Gobain Advanced Materials Division in 2008. Under the CRADA, St. Gobain provides test articles (cells and stacks) to INL for testing in the electrolysis mode. The individual cells are provided to INL via the CRADA. Since they are much more expensive to fabricate, the short stacks are provided to INL via procurement. INL provides test results to St. Gobain for their information and comment. St. Gobain is not currently doing any SOEC testing under this CRADA and will not be providing any reports to INL since there is no subcontract with them. This section provides a description of the cells and stacks provided by St. Gobain to INL for testing.

2.5.1 Single Electrode-Supported Cells

The focus of this activity is performance assessment of single electrode-supported cells operating in the electrolysis mode. Single-cell testing provides basic information on initial and long-term cell performance without the complications present in a stack configuration such as contact resistance interconnect corrosion, Cr migration, etc. In the fuel cell mode, anode-supported cells represent the state-of-the-art in terms of performance. Since the electrolyte generally represents the highest resistivity layer in the cell, decreasing its thickness can lead to significantly improved performance. The Ni cermet material (anode in the fuel cell mode, cathode in the electrolysis mode) has relatively high electronic conductivity and is therefore a logical choice for use as the mechanical support layer in electrode-supported cells. In an anode-supported SOFC, the anode is typically 1 to 1.5 mm thick, while the electrolyte can be as thin as 10 µm. Three types of single cells were provided during FY-11. The oxygen-side electrode material for the baseline cells is La-Sr manganite (LSM). Two other air electrode materials were also provided: modified LSM and LSCF. The air electrode layer is screen printed on the cells, with a thickness of about 90 µm. The cells were fabricated by St. Gobain High-Performance Materials, and supplied to INL via a CRADA agreement. The St. Gobain cell design has in turn been licensed from the Jülich Institute for Energy Research. Testing activities for the St. Gobain cells are limited to INL since INL does not have a subcontract with St. Gobain. A photograph of one of the single cells is provided in Figure 2-58. The green layer is the unreduced Ni cermet material. After reduction, the green NiO in this layer is converted to Ni metal and the layer color changes to silver gray. Typical layer dimensions for Ceramatec electrolyte-supported cells and St. Gobain/Jülich electrode-supported cells are presented in Table 2-3.
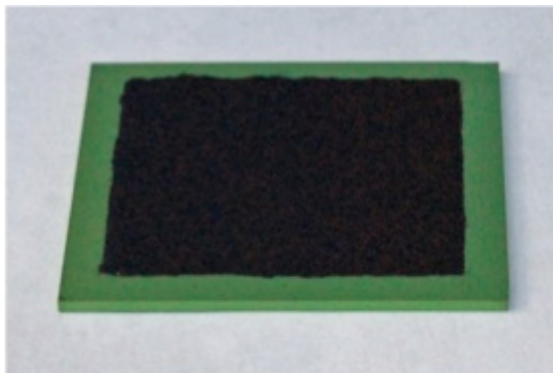
Figure 2-58. St. Gobain single electrode-supported cell.

Table 2-3. Layer thicknesses for electrolyte- and electrode-supported cells.

Typical Layer Thickness (µm)	Electrolyte-Supported Cell (Ceramatec)	Electrolyte-Supported Cell (Jülich)	Electrolyte-Supported Cell (MSRI)
Air/0_2 electrode	40	90	70
Electrolyte	160	10	10
H_2O/H_2 electrode	30	1500	700

During FY-11, INL completed a series of single-cell tests aimed at determining the effects of inlet steam content and current density on initial and long-term cell performance for cells operating both in the fuel cell and electrolysis modes. The single-cell test stand includes an electronic load, allowing operation in the fuel cell mode, as well as a power supply for the electrolysis mode. Diagnostics now also include electrochemical impedance spectroscopy (EIS) measurements. Interpretation of EIS results can help identify the individual phenomena responsible for overall cell ASR values. Individual contributions include ohmic resistances, activation, and concentration polarizations. Series EIS measurements obtained at several times over long-term tests can be interpreted to identify primary degradation mechanisms.

The single-cell test stand was redesigned during FY-11 to improve cell contact resistance and support higher current densities. A full description of the modified test stand is provided in Section 3.4.

2.5.2 10- × 10-cm Short Stacks

INL tested two three-cell short stacks from the St. Gobain Advanced Materials Division during FY-11. An exploded view of the stack is provided in Figure 2-59. The Jülich Institute for Energy Research developed this stack geometry, designated the F design. The stack includes three anode-supported cells with metallic frames and interconnect plates fabricated from ferritic stainless steel (Crofer22APU). The stack is internally manifolded with a counter-flow gas flow configuration and a "window frame" design. Each frame piece encloses a cell with a Ni mesh in contact with the steam-hydrogen electrode. Each interconnect includes grooves for air flow distribution. The cells are 1.5 mm thick with dimensions of 10×10 cm (80-cm^2 active area). The steam-hydrogen electrode (anode in the SOFC mode, cathode in the SOEC mode) material is Ni-zirconia (8YSZ) cermet. The air electrode is LSM with a Cr evaporation protective layer and a contact (or bond) layer to minimize contact resistance with the interconnect. The air electrode includes both a functional layer of LSM ($La_xSr_yMnO_{3-\delta}$) and 8YSZ plus a cathode layer of pure LSM. The stack is sealed with a glass-ceramic seal. It is designed to operate in the range of 750 to 800°C. The top and bottom metallic end plates include tabs for power connections. A full description of the INL tests of the St. Gobain three-cell stack is provided in Section 3.4.
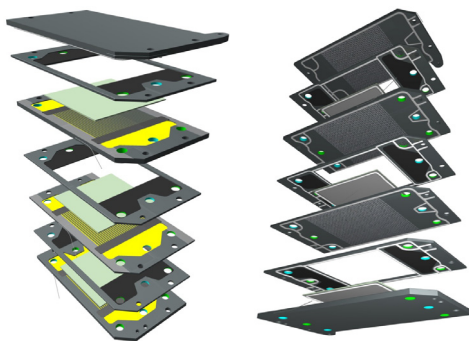
Figure 2-59. Exploded views of St. Gobain three-cell short stack.

2.6   References

1   T. Cable and S. Sofie, "A Symmetrical, Planar SOFC Design for NASA's High Specific Power
Density Requirements," *Journal of Power Sources*, Vol. 174, 2007, pp. 221–227.

3 ADVANCED CELL AND STACK TESTING PERFORMED AT IDAHO NATIONAL LABORATORY

3.1 Idaho National Laboratory High-Temperature Electrolysis Laboratory

3.1.1 General Information

A photograph of the INL HTE Laboratory, which is dedicated to small-scale experiments with single cells and small stacks, is shown in Figure 3-1. A comprehensive discussion of the INL high-temperature solid-oxide electrolysis bench-scale experiment is presented elsewhere.[1] A representative schematic of one of the test loops (test stand No. 6) shown in Figure 3-1 is presented in Figure 3-2. Primary components include gas supply cylinders, mass flow controllers, a heated water-bath humidifier, online dew-point sensors, temperature and pressure measurement instruments, a high-temperature furnace, and the SOEC. Nitrogen is used as an inert carrier gas. The use of a carrier gas allows for independent variation of both the partial pressures and flow rates of the inlet steam and hydrogen while operating near atmospheric pressure. Inlet flow rates of nitrogen, hydrogen, and air are established by means of precision mass flow controllers. Hydrogen is included in the inlet flow as a reducing gas to prevent oxidation of the Ni cermet electrode material. Air flow to the stack is supplied by the shop air system, after passing through a two-stage extractor/dryer unit. The cathode-side inlet gas mixture consisting of hydrogen and nitrogen is mixed with steam by means of a heated humidifier. The dew-point temperature of the nitrogen-hydrogen-steam gas mixture exiting the humidifier is monitored continuously using a precision dew-point sensor. All gas lines located downstream of the humidifier are heat-traced to prevent steam condensation.

Figure 3-1. INL HTE Laboratory.
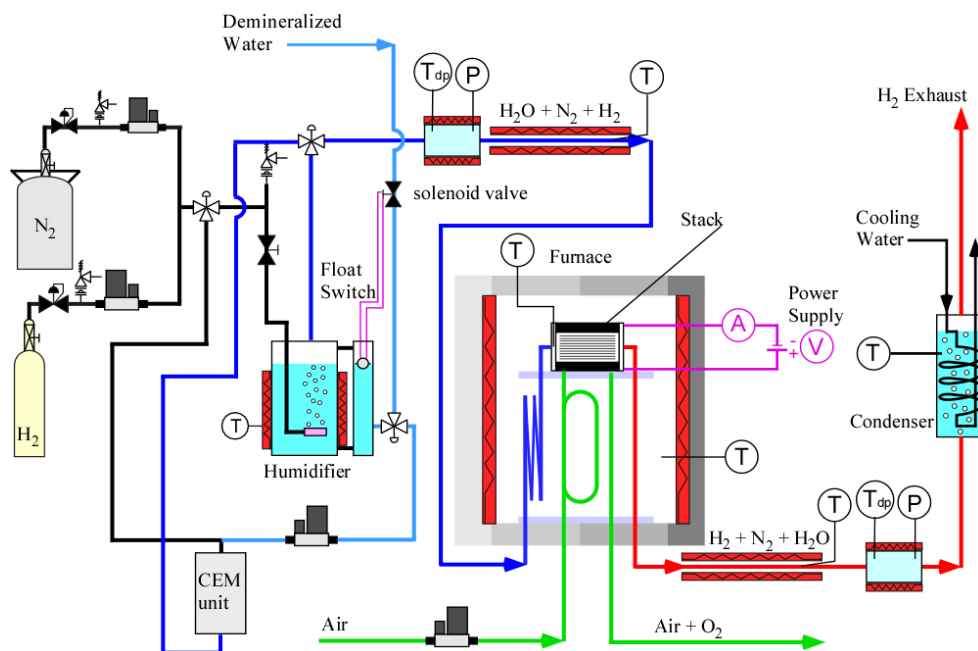
Figure 3-2. Process flow diagram for stack testing (test stand No. 6).

Downstream of the mass flow controllers, nitrogen is mixed with smaller flows of H_2. Hydrogen is included in the inlet flow as a reducing gas to prevent oxidation of the Ni cermet electrode material. The nitrogen-hydrogen gas mixture is mixed with steam by means of a heated humidifier. The humidifier water temperature is maintained at a constant setpoint value using computerized feedback control. The dew-point temperature of the nitrogen-hydrogen-steam gas mixture exiting the humidifier is monitored continuously using a precision dew-point sensor. Pressure is also measured at the dew-point measurement stations using absolute pressure transducers. Local stream pressure information is required to determine the mole fraction of steam in the gas mixture at the dew-point measurement station. Since the nitrogen and hydrogen flow rates are fixed by the mass flow controllers, and the steam partial pressure is fixed by the bath temperature, the complete inlet gas composition is precisely known at all times. All gas lines located downstream of the humidifier are heat-traced to prevent steam condensation. Gas line temperatures are monitored by thermocouples and controlled by computer-controlled power electronics.

The electrolysis product stream exiting the furnace is directed towards a second dew-point sensor and then to a condenser through a heat-traced line. The condenser removes most of the residual steam from the exhaust. The final exhaust stream is vented outside the laboratory through the roof. The rate of steam electrolysis is measured via two different, independent methods, which include the electrical current through the stack and measured change in the inlet and outlet steam concentration as measured by the online dew-point sensors.

Herring *et al.*[2] presented the progress of INL HTE research from small-scale bench testing to large-scale demonstration. INL has conducted experiments with the following cells/stacks:

1. Button-cell testing (approximately 1 W).

2. Stack testing (200 We–5 kWe)—electrode, electrolyte, and interconnect materials; flow channel materials and fabrication; intercell electrical contact cell and manifold sealing issues; and cell durability.

3. Integrated laboratory-scale testing (15 kWe)—all previous issues plus multiple-stack thermal management, heat recuperation, feedstock heating, and hydrogen.

3.1.2 New Laboratory Capabilities

3.1.2.1 Improved Single-Cell Apparatus

The aparatus used to test the single SOECs at INL was improved in FY-11 to provide better electrode-current collector contact and improve the current carrying capacity.

As illustrated in Figure 3-3 and Figure 3-4, a steam hydrogen mixture is supplied to the cell through a 1/4-in. inconel coiled tube into the inlet hole in the bottom of the HastX base plate. It then flows through a diverging flow channel milled into the HastX base plate and passes through a slot in the bottom of the alumina cell holder. The slots can be seen in Figure 3-2. An alumina felt gasket is used to seal the HastX base plate against the alumina cell holder. The flow then passes under the cell through a corrugated/perforated Ni flow field. The flow field establishes the gap for the steam/hydrogen flow channel under the cell while also serving as an electrical conductor. A 0.254-mm (0.010-in.) Ni foil underneath the flow field serves as a current collector. The Ni foil, flow field, and mesh are sized to fit into the inner square recess machined into the alumina cell holder. Alumina was selected as the cell holder and air flow distributor material to minimize the potential for Cr poisoning of the cell electrodes. The cell holder was machined in the bisque state and then fired. During firing, the bisque alumina shrinks by about 15%. This shrinkage must be taken into account when doing the machining such that the desired dimensions are achieved in the final dense alumina part.
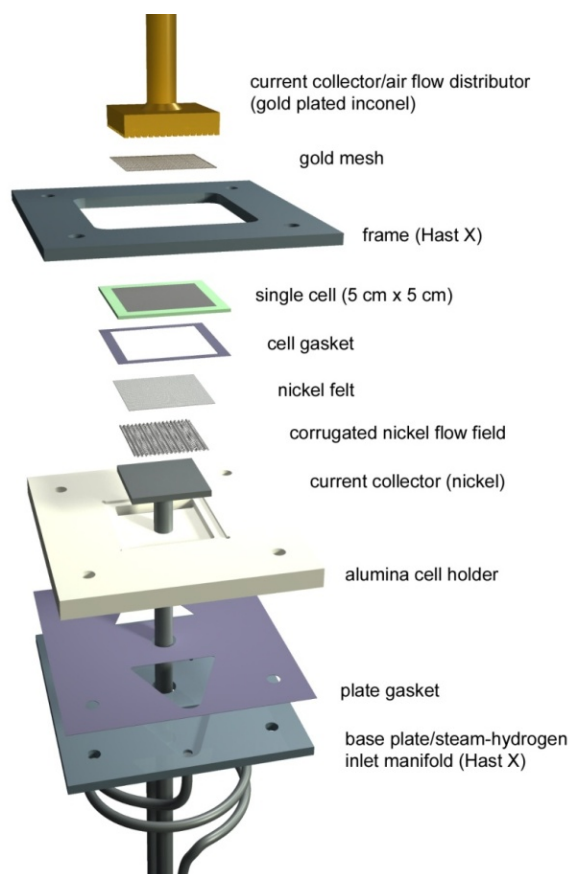
Figure 3-3. Exploded view of modified INL test fixture used to support and seal 5- × 5-cm single solid-oxide cells while providing steam flow and sweep gas flows.
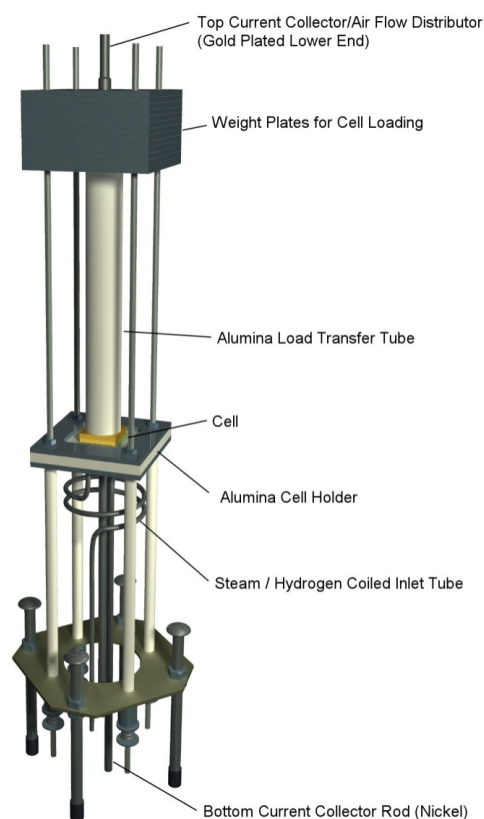
Figure 3-4. Overview of 5- × 5-cm cell test fixture and hot-zone apparatus.

A Ni plate welded to a solid inconel bus bar serves as the steam/hydrogen-side cell power supply/current collector. A separate wire is spot welded to the underside of the Ni plate to facilitate cell operational voltage measurements. The bus bar and voltage tap wire are insulated with alumina tubes and passed through a central hole in the bottom of the alumina cell holder, and in turn out of the furnace hot zone.

After passing along the bottom of the cell, the steam/hydrogen flow exits the alumina cell holder through a second slot, flows through a converging passage in the HastX base plate, and out through an 3/8-in. OD inconel outlet tube. The outlet tube is sized larger than the inlet tube to minimize back pressure on the cell seals to prevent leakage. The cell is placed on a recessed shelf milled into the alumina cell holder just above but in contact with the Ni mesh (see Figure 3-3). A Ni paste was used to enhance electrical contact between the Ni mesh and flow field foil. An alumina felt gasket is placed on the shelf underneath the cell to help with sealing. In addition, for sealing, an alumina-based ceramic paste (Aremco Products, Ceramabond 552) is distributed around the top outer edge of the cell to seal the gap between the cell and alumina cell holder.

On the air side of the cell, Au mesh is placed in contact with the air-side electrode. This Au mesh is held against the air-side electrode by a Au-plated current collector/air flow distributor fabricated from inconel plate. An earlier version of this air electrode/current collector was fabricated from a Ag/Pd alloy. This current collector caused an interaction with the air electrode material that led to corrosion and severe degradation. This experience was the motivation for the development of the Au-plated inconel air distributor/current collector.

Air is introduced to the top side of the cell through a Au-plated inconel inlet tube welded to the current collector/air flow distributor plate. The air inlet tube is double walled to serve its second purpose, which is the conduction of electrical current to/from the SOEC air-side electrode. The air flow distributor has an array of square protuberances milled into its surface (see Figure 3-5), creating a gap for air flow while also compressing the Au mesh against the air-side electrode. Several air outlet holes are distributed in the center of air flow distributor. After exiting the air flow distributor, the air impinges on the cathode side of the cell and flows radially outward through the array of protuberances. After sweeping the air-side electrode, the air exits into the furnace volume. An air-side electrode voltage tap wire, insulated by alumina tubing and beads, is spot welded to the air flow distributor and runs alongside the air inlet tube/current collector and out of the furnace hot zone for connection to the test stand data acquisition system.
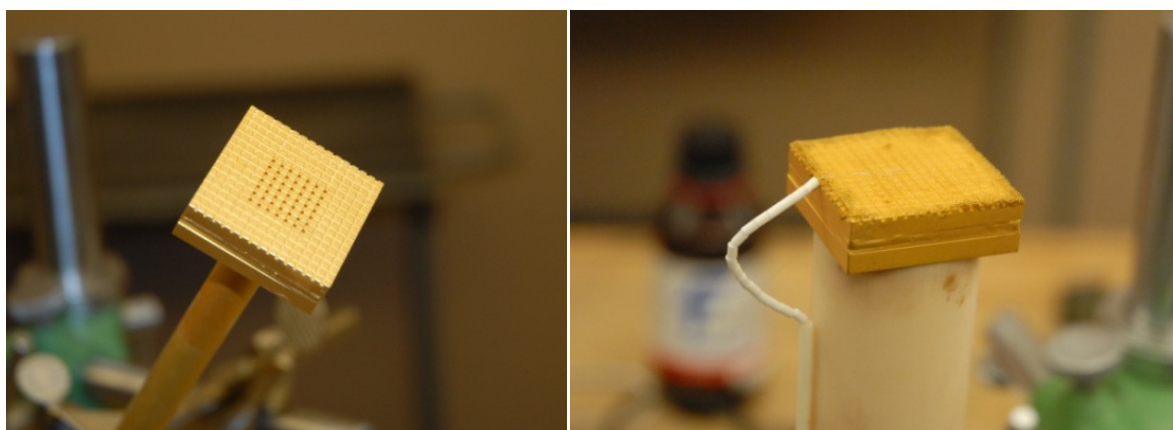
Figure 3-5. Underside of Au-plated air flow distributor/current collector. Left: Square milled protuberances and air outlet holes are visible. Right: Current collector/air flow distributor assembly prior to installation atop SOEC; Au mesh and insulated voltage tap wire are visible.

A fixed compressive load is applied to the entire cell stack up between the alumina cell holder and an alumina load tube/inconel pusher plate by means of weights, as shown in Figure 3-2. This load simultaneously compresses the cell against the Ni mesh, flow field, and foil on the bottom steam/hydrogen side of the cell and against the Au mesh on the air side. It also compresses the cell against the seal around the outer edge of the cell that rests on the shelf milled into the alumina cell holder. The HastX weight plates are held in alignment by the upper portion of threaded rods that extend upward from the base of the test fixture for this purpose. A fixed compressive load is independently applied between the HastX frame, alumina cell holder, and HastX base plate. This load is generated by the compression of four springs located under the test stand base support outside of the furnace. The springs are compressed a fixed amount that is determined by the height of underside spool pieces and tightening of a nut on the threaded rods. The threaded rods are fed through the alumina spacer tubes. These spacer tubes determine the height of the cell holder inside the furnace. The spring-generated load is intended to compress the seal between the cell holder and base plate. This seal was formed by alumina felt impregnated with alumina slurry. A nut is visible on the threaded rods in Figure 3-4 just above the HastX frame and below the weight plates. This nut represents the upper stop for this compressive load. The extension of the threaded rods above the nuts is for the purpose of aligning the weight plates. Note that the weight plates are floating above these nuts since they are resting on the HastX top plate.

A photograph of the test stand installed in the furnace base is provided in Figure 3-6. Note that the base support is located outside of the furnace hot zone. Holes were drilled in the bottom of the furnace for pass-through of the flow tubes, alumina spacer rods, power leads, and instrumentation.
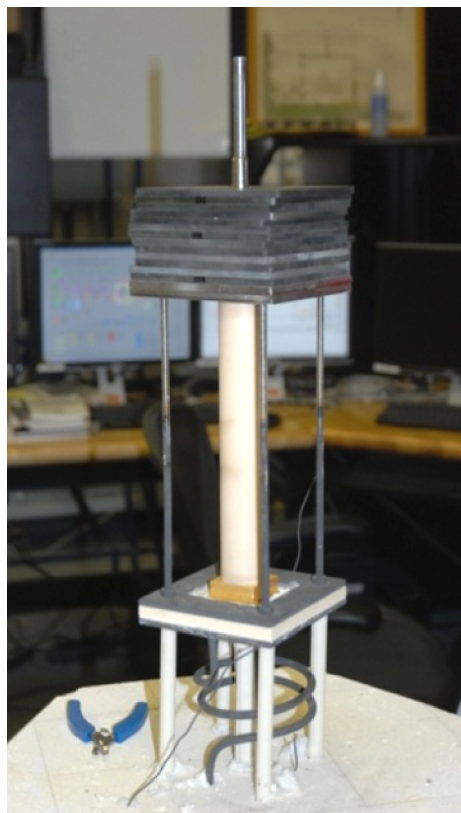
Figure 3-6. Test fixture on base plate of furnace. Note that base support outlined at bottom of Figure 3-2 is located outside furnace hot zone.

A process flow diagram for the experimental apparatus used for single-cell testing is presented in Figure 3-7. Primary components include gas supply cylinders, mass flow controllers, a heated water-bath humidifier, on-line dew-point sensors, temperature and pressure measurement, high-temperature furnace, and the SOEC. Nitrogen is used as an inert carrier gas. Inlet flow rates of nitrogen, hydrogen, and air are established by means of precision mass flow controllers. Hydrogen is included in the inlet flow as a reducing gas to prevent oxidation of the Ni cermet electrode material. Air flow to the cell is supplied by the shop air system, after passing through a two-stage extractor/dryer unit. The cathode-side inlet gas mixture, consisting of hydrogen and nitrogen, is mixed with steam by means of a heated humidifier. The dew-point temperature of the nitrogen/hydrogen/steam gas mixture exiting the humidifier is monitored continuously using a precision dew-point sensor. All gas lines located downstream of the humidifier are heat-traced to prevent steam condensation. Prior to the exhaust of process gases from the test apparatus, the gas stream is cooled via a bubbler condenser. The cooled exhaust product of hydrogen and nitrogen is vented to a stack on the facility roof; however, the product stream may optionally be compressed and stored for further experimentation such as reversed operation in the SOFC mode through reaction of SOEC products.
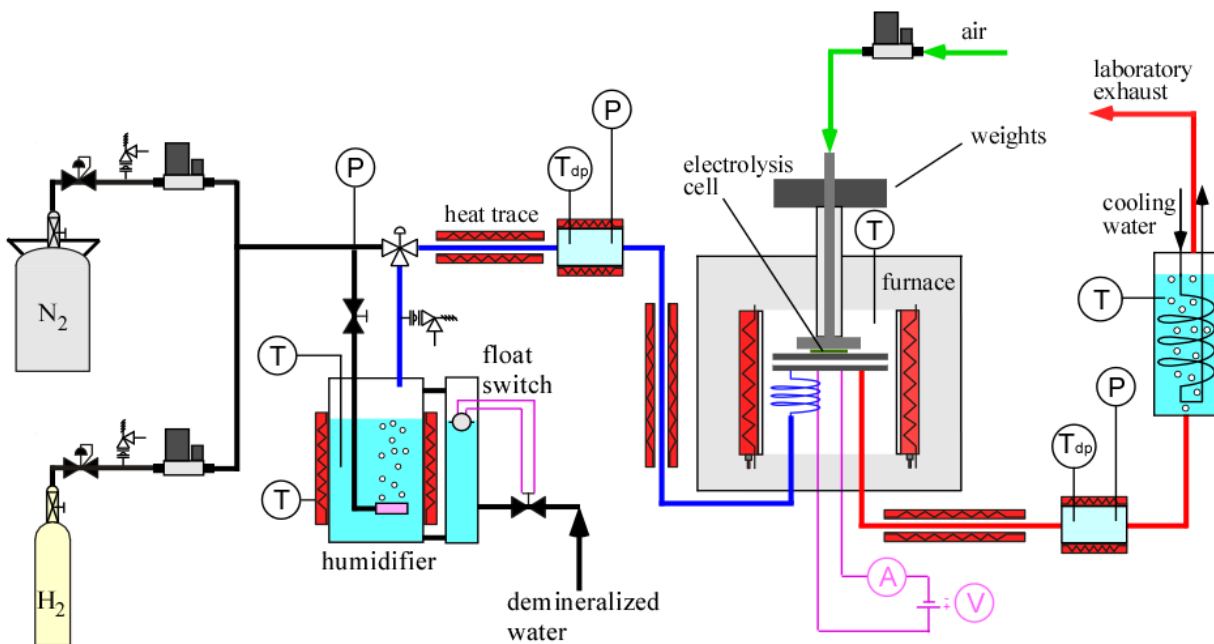
Figure 3-7. Process flow diagram for single-cell test apparatus.

Real-time test data are collected from in-line instrumentation within a National Instruments Labview™ based virtual instrument through an Agilent data acquisition unit. Control of the test apparatus temperature and process fluid controls is provided via a Measurement Computing™ USB DAC interface coupled to SSRs and mass flow controllers respectively. A Lambda™ power supply is used to provide electrical power to a stack while operated in the steam electrolysis mode. An Amrel electronic load is used as a power sink for operation of cells in the fuel cell mode. Switching between the power supply and electronic load is facilitated by a network of electronic relays housed within a switching box. Both the electronic load and power supply are controlled through the National Instruments Labview™ based virtual instrument, allowing for data acquisition and control of dc-potential sweeps for cell performance characterization.

3.1.2.2 Solid-oxide Electrolysis Cell Materials Fabrication and Powder Handling Capabilities

3.1.2.2.1 Powder Handling

In FY-11, the INL HTE Laboratory began establishing electrolytic and electrode powder processing capabilities that will allow for the preparation of materials for trial in advanced prototypic cell fabrication techniques. As part of this process, an inert-environment glovebox has been constructed to facilitate the safe handling of materials such as YSZ and NiO powders. Figure 3-8 is a photograph of the completed SOEC processing glovebox design. This glovebox was designed to be operated at less than atmospheric pressure with a cover gas of argon. All exhaust from the glovebox is vented through a high-efficiency particulate air filter and discharged to the outside via a facility vent line. Figure 3-9 illustrates the process control systems used to operate the glovebox. Commissioning of the SOEC powder handling glovebox is anticipated to be complete by Spring of 2012.

Figure 3-8. Constructed SOEC powder processing glovebox.
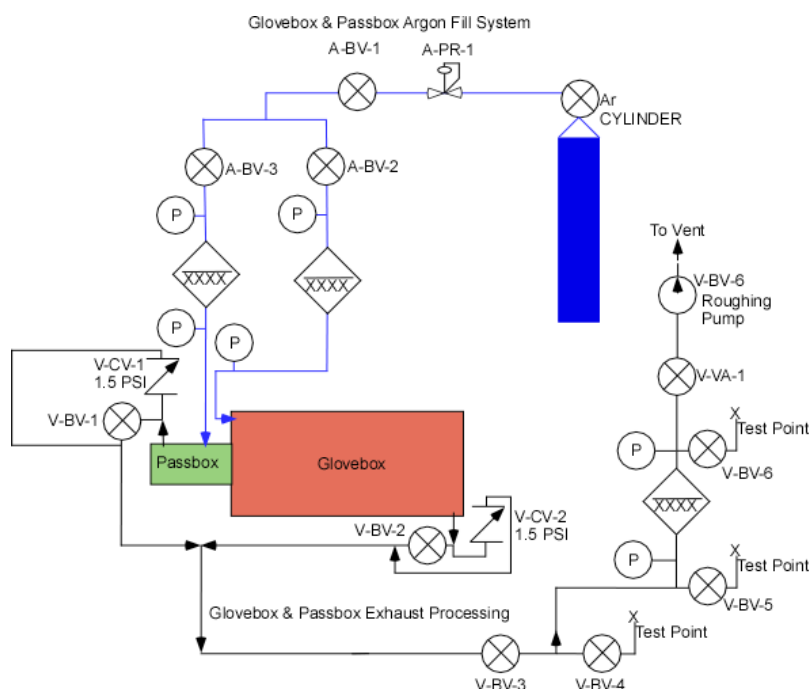
Figure 3-9. Process diagram for SOEC powder handling glovebox and its anticontamination passbox.

49

3.1.2.2.2 Powder Sintering Experiments

Several preliminary trials to sinter 8YSZ for electrolyte structure production were performed in FY-11 using a novel approach. This work is projected to lead to the generation of potentially patentable processes, the results of which will be presented in future peer-reviewed journals and conference proceedings.

3.1.2.3   Pressurized Test Apparatus Design

Design and fabrication activities are in progress for development of a new apparatus for pressurized testing of an HTE stack. Two views are shown in Figure 3-10. The apparatus includes a flanged 5-MPa pressure vessel that houses a high-temperature ceramic fiber heater, with the HTE stack located inside the heater hot zone. The flanged vessel also includes a pressurized cool zone above the heater. Mechanical compression of the stack will be accomplished using a spring-based system located in the cool zone. Cooling water lines will be welded to the outside of the vessel and flanges such that the vessel wall temperature will always be near room temperature, even when the hot zone is at 800°C. Initial stack heatup will occur at ambient pressure with the body of the pressure vessel lifted up to allow access to the spring tightening mechanism. After heatup, the pressure vessel body will be lowered and bolted in place to allow for system pressurization. Since the body and upper flanges of the pressure vessel are heavy (approximately 750 lb), the lifting will be accomplished using a motorized screw-driven system originally used to lift the furnace on the integrated laboratory-scale experiment, as shown in Figure 3-10(a). With the flanged vessel in the lifted position, full access to the test section is available.

(a)   (b)
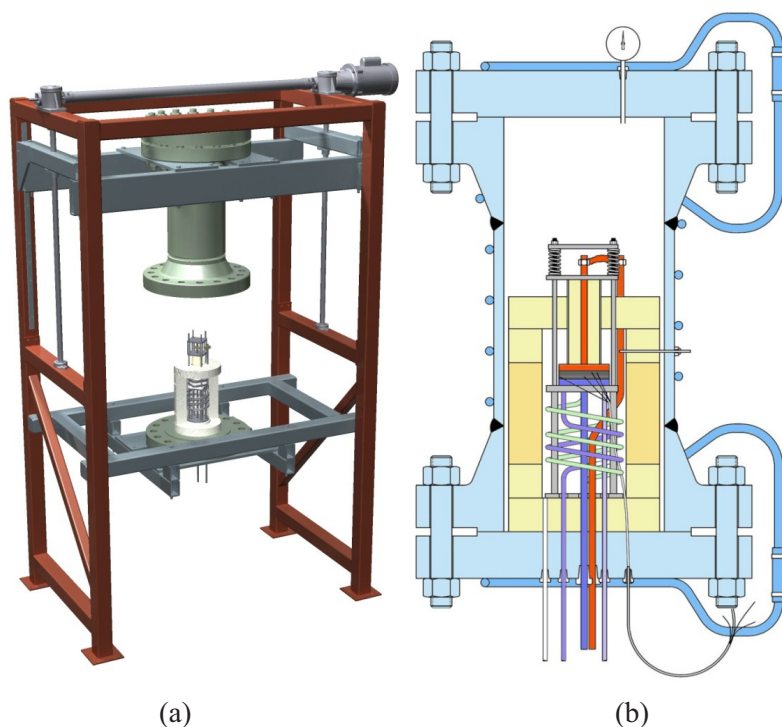
Figure 3-10. Pressurized system for HTE testing. (a) Lifting mechanism and frame. (b) Cross-section of pressure vessel internals.

A cross-sectional view of the pressure vessel and test section is shown in Figure 3-10(b). Vessel penetrations for flow inlet/outlet, power leads, and instrumentation are all through the bottom flange. Preheating of the inlet process gases is accomplished by coiled tubing located inside the hot zone.

A piping and instrumentation diagram (P&ID) for the pressurized test is shown in Figure 3-11. This P&ID shows the locations of the various process gases, mass flow controllers, pressure relief, water and steam supply, heat trace, condenser, drain lines, vents, and pressure controller. The system is designed to maintain equal pressure on both sides of the electrolysis cells, and in the vessel atmosphere. The vessel atmosphere is pressurized using nitrogen. Downstream of the vessel and stack, all process gases enter a single exhaust line to ensure pressure equalization.
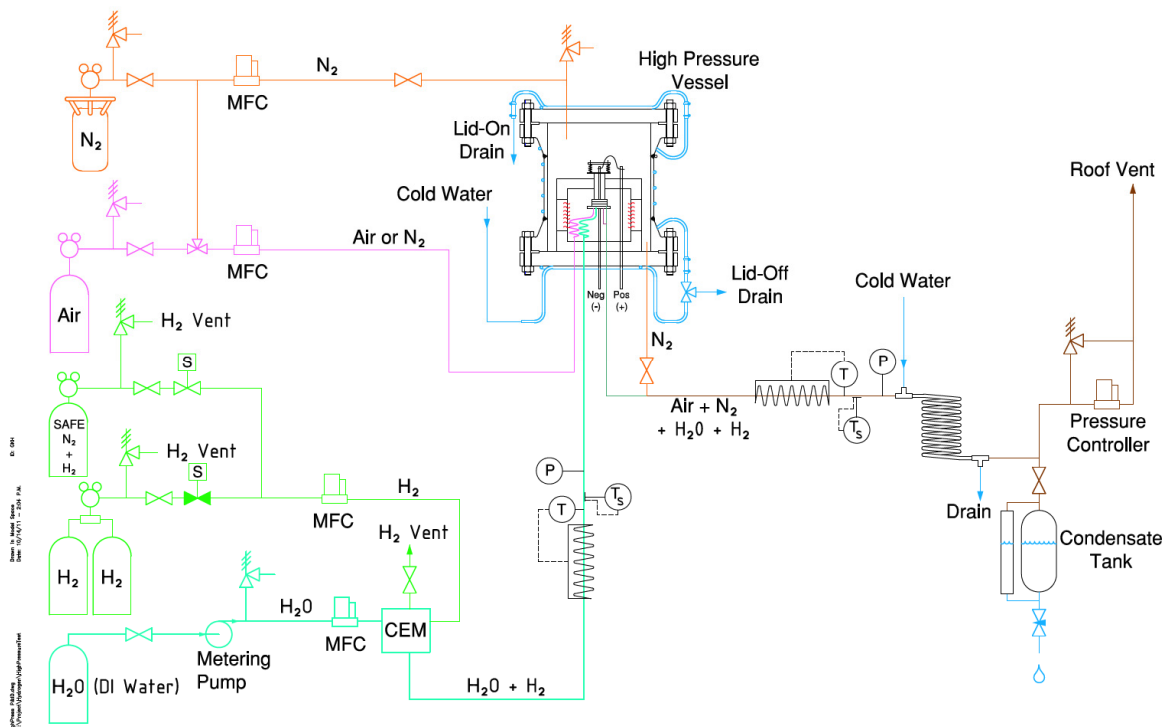
Figure 3-11. P&ID for HTE pressurized test.

3.1.2.4   4-kW Test Apparatus Design

Design activities are also in progress for modification of test stand No. 6 (Figure 3-12) to allow for HTE testing at the 4-kW scale. This test will require two 60-cell stacks operating in parallel. The two stacks will be located inside of the existing clamshell-style furnace [Figure 3-12(a)]. The stacks will be mounted on a common base manifold/current collector plate (Figure 3-13) that has been designed to uniformly distribute the process gas inlets and outlets to/from the two internally-manifolded stacks while minimizing the number of tubes required. Due to the high gas flow rates required for this test, two recuperative heat exchangers will be located underneath the furnace. The heat exchangers use a counter-flow tube-in-tube design. They are needed to preheat the low-temperature inlet gases by heat exchange with the hot exhaust gases. Further preheating of the inlet gases to the final operating temperature will be accomplished by means of coiled inconel tubing located inside the furnace [Figure 3-12(b)]. The two stacks are independently compressed using springs located above the furnace. The mechanical load is transferred to the stacks by an alumina tube. Each stack has its own current collector top plate.
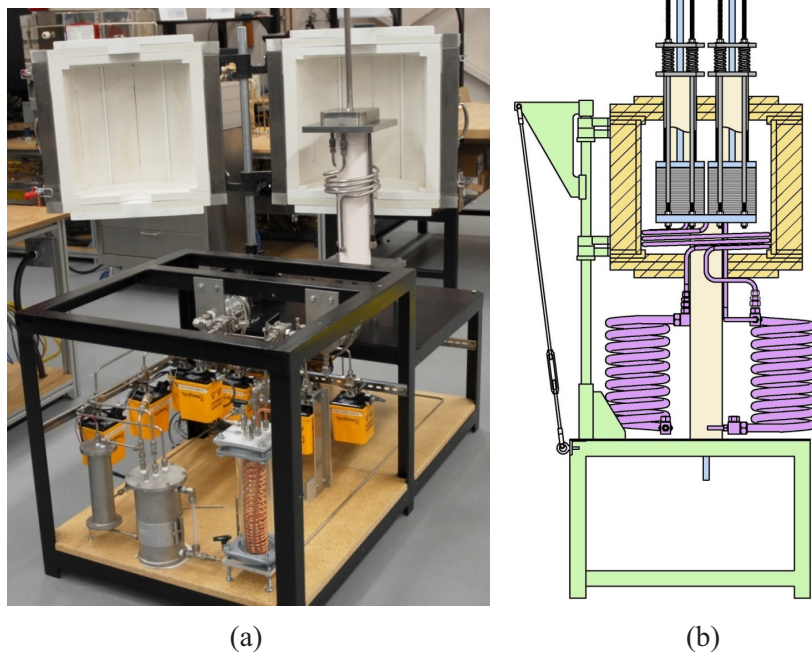
Figure 3-12. Test stand No. 6. (a) Existing configuration. (b) Cross-section showing double stack, heat recupators, and modified preheater coils.
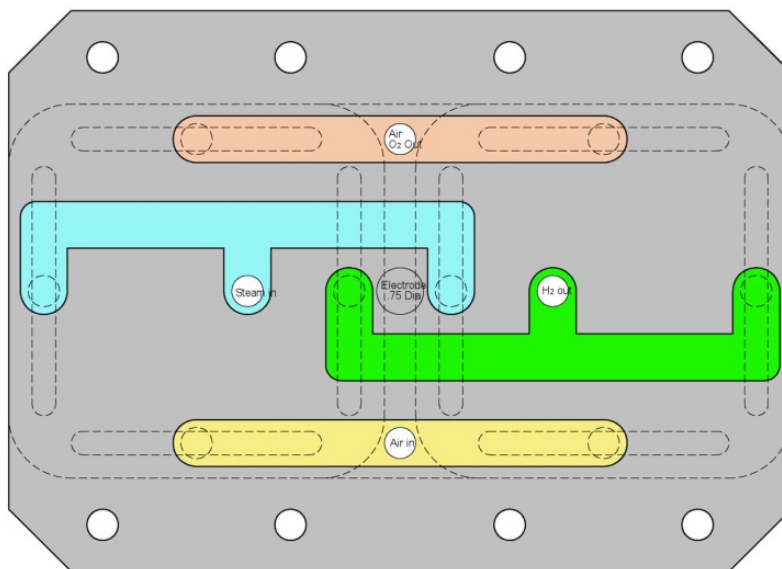
Figure 3-13. Base manifold/current collector plate for 4-kW testing.

3.2 Ceramatec, Incorporated, Button Cells and Stacks with Improved Air-side Electrodes

3.2.1 Button-Cell Testing

Two Ceramatec button cells were tested to evaluate the performance of the cells with a new air electrode. The button cells were operated in long-term tests in the electrolysis mode. The cell active area was 2.25 cm^2. Testing for the first cell started January 17, 2011; testing for the second cell started April 20, 2011. The operating conditions are listed in Table 3-1.

Table 3-1. Operating conditions during long-term tests of Ceramatec button cells.

Temperature (°C)	H$_2$ (sccm)	N$_2$ (sccm)	Air (sccm)	Dew Point (°C)	Current Density (A/cm^2)
850	50	200	0	70	0.25

Figure 3-14 presents the long-term performance of the first button cell in the electrolysis mode. The cell had been operated for almost 4000 hours and shows negative degradation (performance increasing). Current density and cell voltage histories are shown in Figure 3-14(a). It is seen from Figure 3-14(b) that ASR dropped from 2.5 to 1.3 Ω-cm^2 after 4000 hours of operation. This is by far the best button cell we have ever tested. However, identification of the mechanisms responsible for this behavior require further investigation.

(a)   (b)
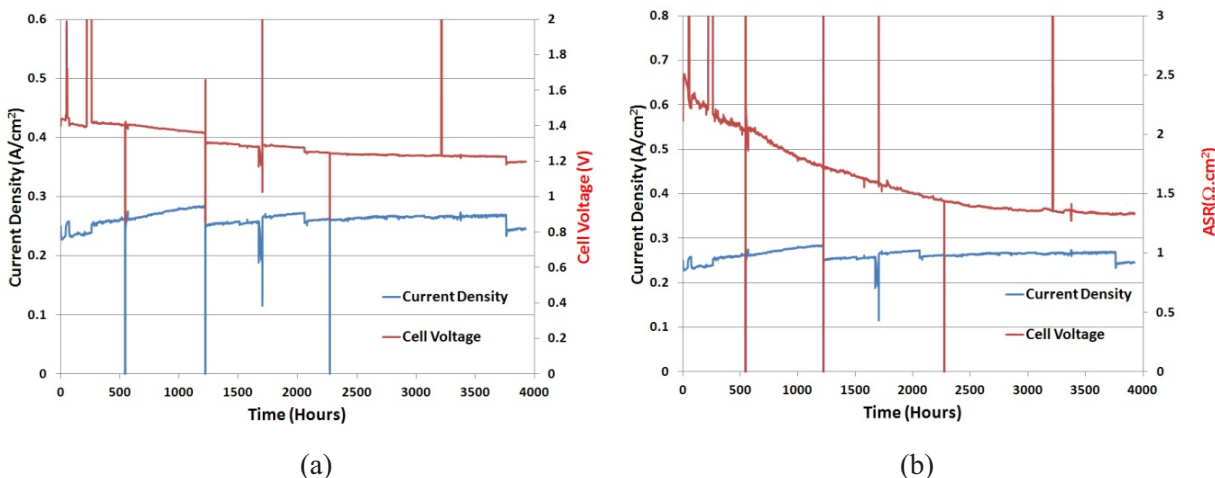
Figure 3-14. Ceramatec button cell No. 391 operated in electrolysis mode. (a) Current density and cell voltage histories. (b) Current density and ASR histories.

Figure 3-15 shows the long-term performance of the second button cell in the electrolysis mode. The cell had been operated for 1800 hours and shows 5.9%/khr degradation rate from 300 to 1300 hours. The ASR increased from 0.8 to 1.1 Ω-cm^2 when reaching 1300 hours. Although it didn't repeat the performance of the first cell, the overall ASR was much lower.
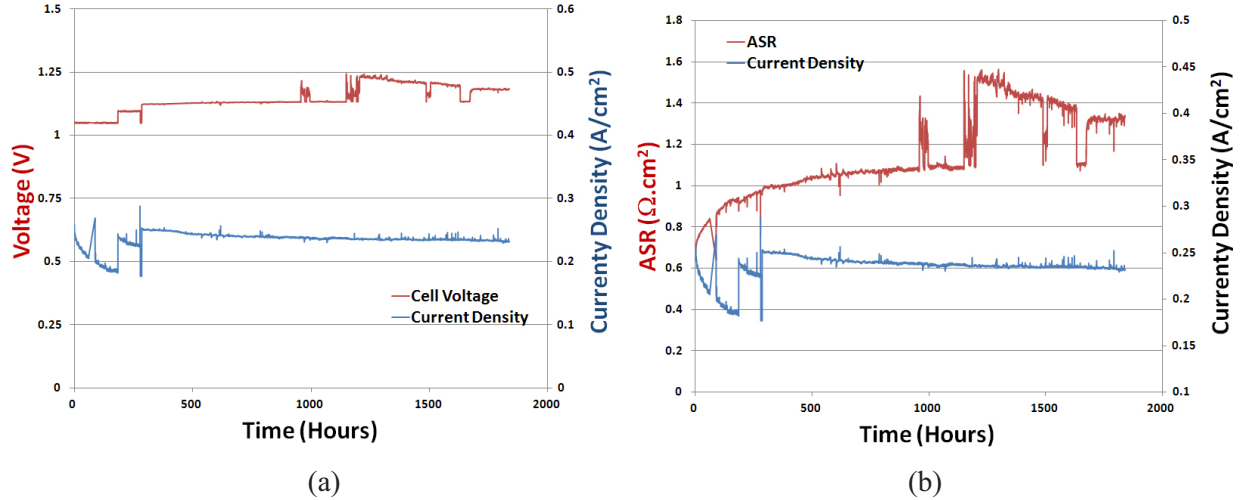
Figure 3-15. Ceramatec button cell No. 390 long-term operation in electrolysis mode. (a) Current density and cell voltage histories. (b) Current density and ASR histories.

The results of those two button-cell tests illustrate that novel air electrode material and enhanced bonding between electrolyte-electrode mitigate degradation in HTE.

3.2.2 Stack Testing

Three Ceramatec 10-cell stacks were tested to demonstrate mitigating degradation by improving air electrode materials and enhancing electrolyte-electrode bonding. Three stacks were tested from May 11, July 13, and September 13, 2011, respectively. The operating conditions are listed in Table 3-2.

Table 3-2. Operating conditions during long-term tests of Ceramatec 10-cell stacks.

Stack No.	Temperature (°C)	H_2 (sccm)	N_2 (sccm)	Air (sccm)	Dew Point (°C)	Current Density (A/cm^2)
1	800	1000	1000	5000	80	0.25, 0.317
2	800	1000	1000	5000	80	0.25
3	800	1000	1000	5000	80	0.25

Figure 3-16 represents the 1000-hour electrolysis test of stack No. 1. Constant current densities, 0.25 and 0.317 A/cm^2, were applied alternately during the long-term test to evaluate the effect of current density on degradation. Overall, the ASR increased from 1.25 to 1.48 Ω-cm^2. The degradation rate at the lower current density is 5.8%/khr, while at the higher current, density is 5.7%/khr. The ASR is lower at higher current density, which is consistent with the results during initial polarization scans. Figure 3-17 shows the intermediate voltages measured during the test. It is seen that all the units behaved similarly during the tests.
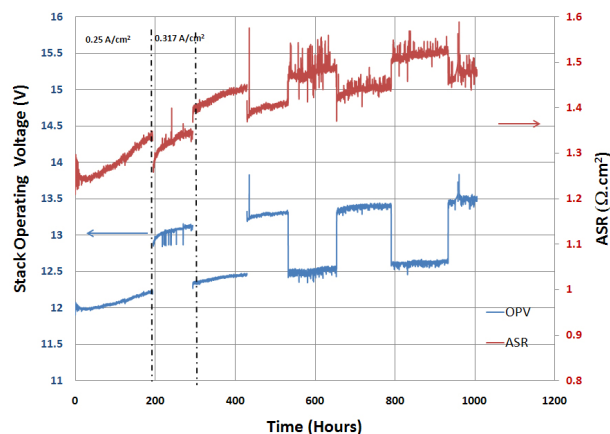
Figure 3-16. Ceramatec stack No. 1 1000-hour test with different current density applied alternately.
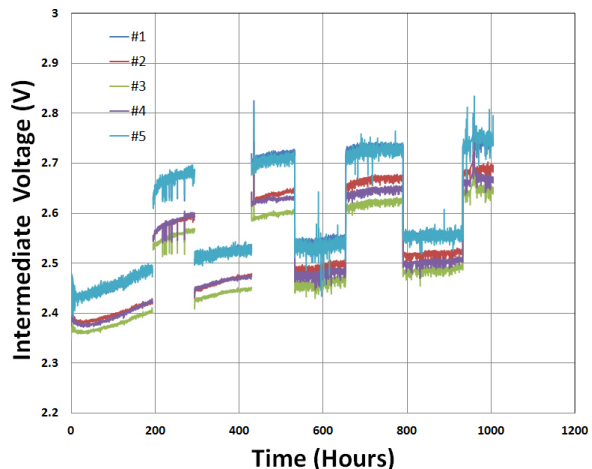
Figure 3-17. Intermediate voltages measured during test of stack No. 1.

Figure 3-18 represents the 1000-hour electrolysis test of stack No. 2. The stack was operated galvanostatically at 0.25 A/cm^2 during the long-term test. Overall, the ASR increased from 1.69 to 1.77 Ω-cm^2. The stack performance increased during the first 70 hours, which may be due to initial conditioning of the stack. Thereafter, the stack performance started degrading. Calculating from 70 hours to the end, the degradation rate is 8.1%/khr. The degradation increased a little compared to the first stack. Furthermore, the intermediate voltages shown in Figure 3-19 illustrate that some cells degrade faster than others. For example, intermediate No. 5 voltage degraded 11.3% over 1000 hours, while intermediate No. 1 voltage degraded 1.5% over 1000 hours.
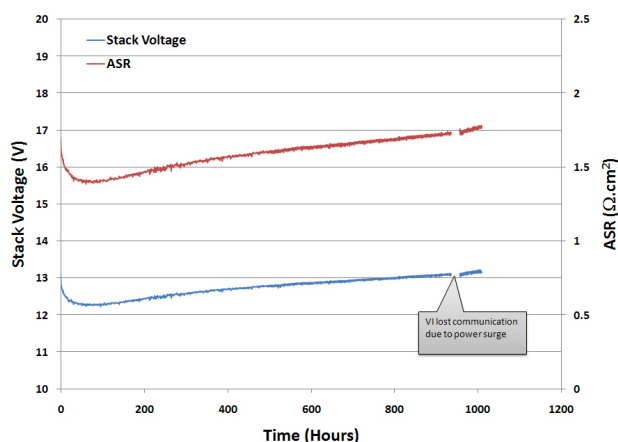
Figure 3-18. Ceramatec stack No. 2 1000-hour test.
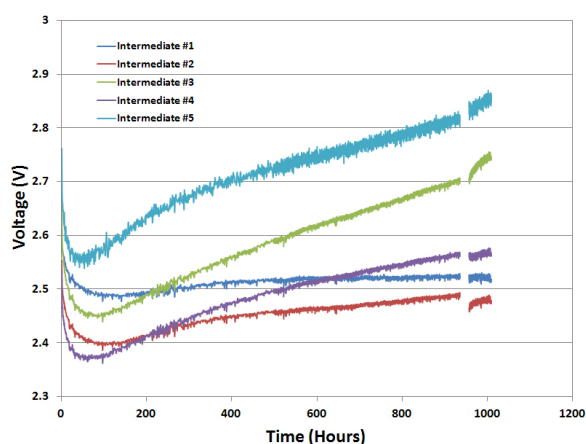
Figure 3-19. Intermediate voltages measured during test of stack No. 2.

55

Figure 3-20 represents the 1800-hour electrolysis test of stack No. 3 and the test is still running. The stack was operated galvanostatically at 0.25 A/cm^2 during the long-term test. The stack behaved totally differently with the two previous stack. The stack was degrading for the first 200 hours, but after then it started increasing performance. After 1600 hours of operation, the stack voltage became stabilized. Therefore, no degradation happened on this stack so far. No clue is available to explain why the performance increased until the post-test analysis is done. However, it may indicate a way to solve the problem of degradation. Furthermore, the intermediate voltages shown in Figure 3-21 illustrate the same trend of performance increase during the test.
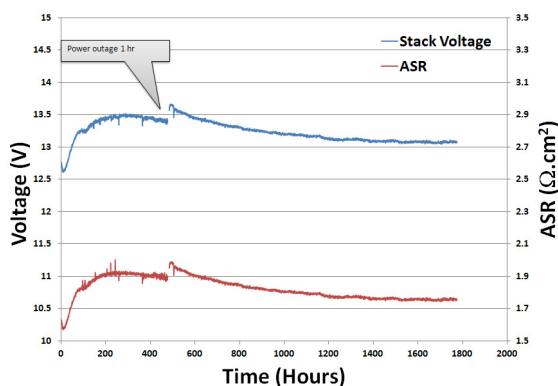
Figure 3-20. Ceramatec stack No. 3 1800-hour test.
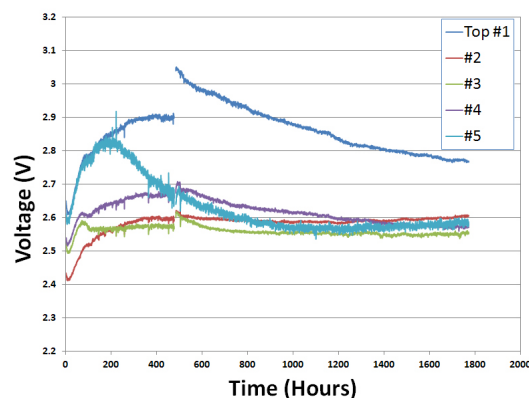
Figure 3-21. Intermediate voltages measured during test of stack No. 3.

3.3 National Aeronautics and Space Administration—Glenn Research Center Bi-electrode-supported Button Cells

3.3.1 Button-Cell Testing

Testing of a total of three cells from batch No. 1 and one cell from batch No. 3 of NASA—GRC 5- × 5-cm single cells was attempted in FY-11 using INL HTSE test stand No. 4 (Figure 3-22). The third cell from batch No. 1 was unfortunately damaged in shipping, thus only three of the 5- × 5-cm single cells were tested in FY-11. The single cells as supplied by NASA—GRC were previously reduced, thus heatup and startup of cell testing was simplified. The cells tested were operated at a temperature of 850°C for long-term testing in the electrolysis mode. Several stages of heatup and staged cell characterization were performed. Table 3-3 summarizes the test conditions adopted. The heatup profile for the furnace had a ramp rate of 2°C/min. A safe forming gas consisting of 95% nitrogen and 5% hydrogen was provided through the test section during the second stage of heatup (between 450 and 750°C) to prevent oxidation of the Ni test fixture components and re-oxidation of the cell steam hydrogen electrode. Once at 750°C, the gas flows were increased to allow for initial characterization of cell performance in the SOFC mode (see Figure 3-22). This initial characterization of the cell performance was determined through a dc-potential (V-I) sweep obtained with dry inlet conditions in the fuel cell mode via the use of the Amrel electronic load over the current density range of 0 to 0.5 A/cm^2. The nominal active area for the cells tested throughout this study was 16 cm^2. Having characterized SOFC performance at 750°C, this procedure was repeated at 800 and 850°C. Upon completion of dry SOFC characterization at 850°C, steam was introduced to the cell via the humidifier for SOFC and SOEC characterization from -0.5 A/cm^2 to +0.5 A/cm^2 for dew-point conditions of 25, 50, and 68°C. SOEC potential sweeps were facilitated through the operation of a Lambda GEN20-38 (20 V – 30 A) power supply controlled via the Labview™ based virtual instrument. The power supply was also used for provision of power during long-term SOEC operation.
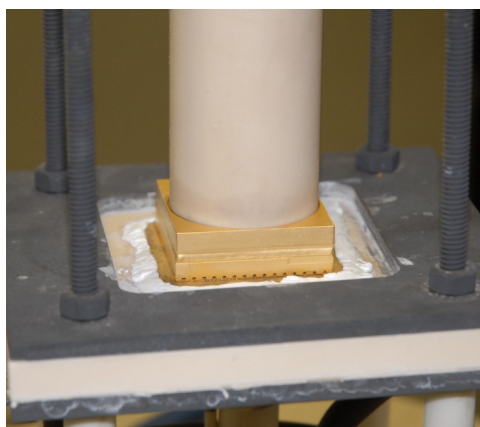
Figure 3-22. NASA—GRC 5- × 5-cm single cell installed and sealed in INL test stand No. 4.

Table 3-3. Heatup profile executed during testing of NASA—GRC 5- × 5-cm single cells.

Step	Temperature	Dew Point (°C)	H_2 Flow (sccm)	N_2 Flow (sccm)	Air-side Flow (sccm)
1	0 → 450 at 5°C/min	0.0	0.0	0.0	0.0
2	450 → 750 at 2°C/min	0	7.5	142.5	150.0
3	750 Hold for SOFC characterization	0	500.0	500.0	1000.0
4	750 → 800 at 2°C/min	0	500.0	500.0	1000.0
5	800 Hold for SOFC characterization	0	500.0	500.0	1000.0
6	800 → 850 at 2°C/min	0	500.0	500.0	1000.0
7	850 Hold for SOFC and SOEC characterization	0	500.0	500.0	1000.0
8	850 Hold for SOFC and SOEC characterization	25	500.0	500.0	1000.0
9	850 Hold for SOFC and SOEC characterization	50	500.0	500.0	1000.0
10	860 Hold for SOFC and SOEC characterization	68	500.0	500.0	1000.0
11	850 Long-term SOEC operation with mid-term and end SOEC/SOFC mode characterization	68	300.0	300.0	300.0

After the series of initial cell characterizations were performed, the gas flows were adjusted to provide equal inlet conditions of 33%mol steam, hydrogen, and nitrogen for steady state long-term testing in the SOEC mode. Once the gas flows and OCV had stabilized, a dc-potential sweep for SOFC and SOEC characterization from -0.5 A/cm^2 to +0.5 A/cm^2 was repeated before placing the cell into constant

current SOEC operation with a current density of 0.5 and 0.2 A/cm^2 for the first and second cells tested in this study, respectively. During cell test No. 1, the current density was reduced to 0.2 A/cm^2 after 86 hours when the ASR had increased by a factor of 2.62. The lowering of the current density was used to provide an initial estimate of the relationship between current density and degradation rate.

The two successful cell tests presented below were operated in the long-term SOEC mode for approximately 95 and 114 hours, respectively. Prior to the shutdown of cells held under the long-term test, final dc-potential sweeps were performed in both the SOFC and SOEC modes. After initial cell characterization was complete at the beginning of each test, the cells were placed into a long-term SOEC mode of operation. Figure 3-8 illustrates the ASRs and cell operating voltages as a function of time for each test. The cell in test No. 1 was operated at a current density of 0.5 A/cm^2 for the first 86 hours and lowered to 0.2 A/cm^2. The cell in test No. 2 was operated at 0.2 A/cm^2 throughout the test. Mid-term dc-potential sweeps were performed at approximately halfway through each test. These appear as vertical lines in data. The dc-potential sweep data acquired during initial cell characterization, at mid-term, and at the end of each test are plotted in Figure 3-9 and Figure 3-10 for tests No. 1 and No. 2, respectively.

The OCVs of the cells at each measurement stage can be determined through the examination of Figure 3-23 and Figure 3-24 on the respective y-axis intercepts (I = 0 A). Both cells behaved consistently during initial characterization. The dry OCV values at the peak operating temperature of 850°C in both cases were approximately 1.03 V. Similarly, when steam was introduced to the cells at 33%mol, both cells had an OCV of 0.911 V. The OCV values at the test termination points differed as anticipated due to the cell degradation process, the rate of which was driven by the test conditions.
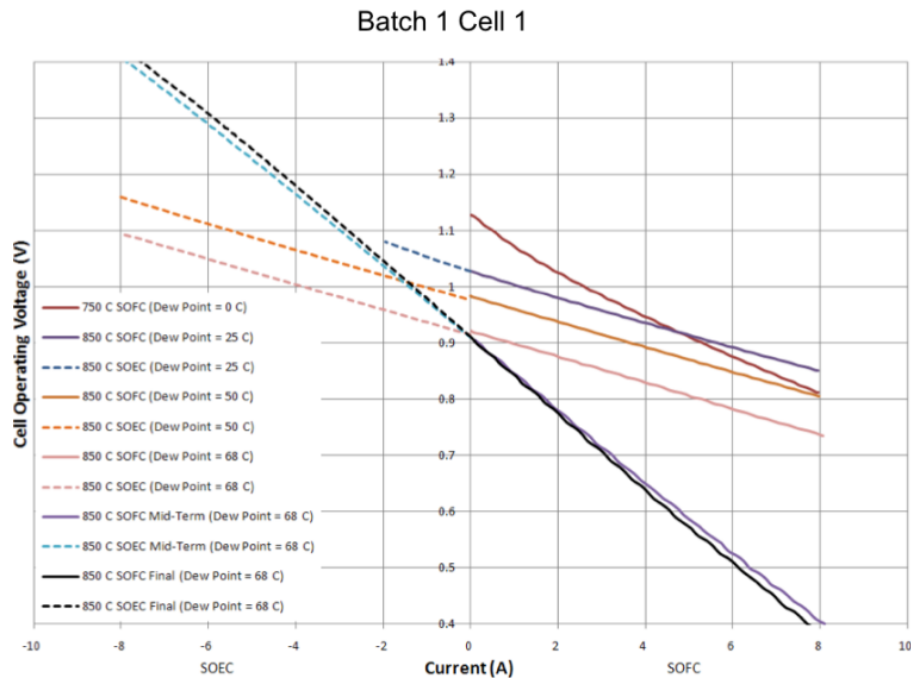
Figure 3-23. Batch No. 1, cell No. 1, dc-potential sweeps at initial, mid-term, and final stages of long-term SOEC operation; 9 hours separate mid-term and final sweeps.
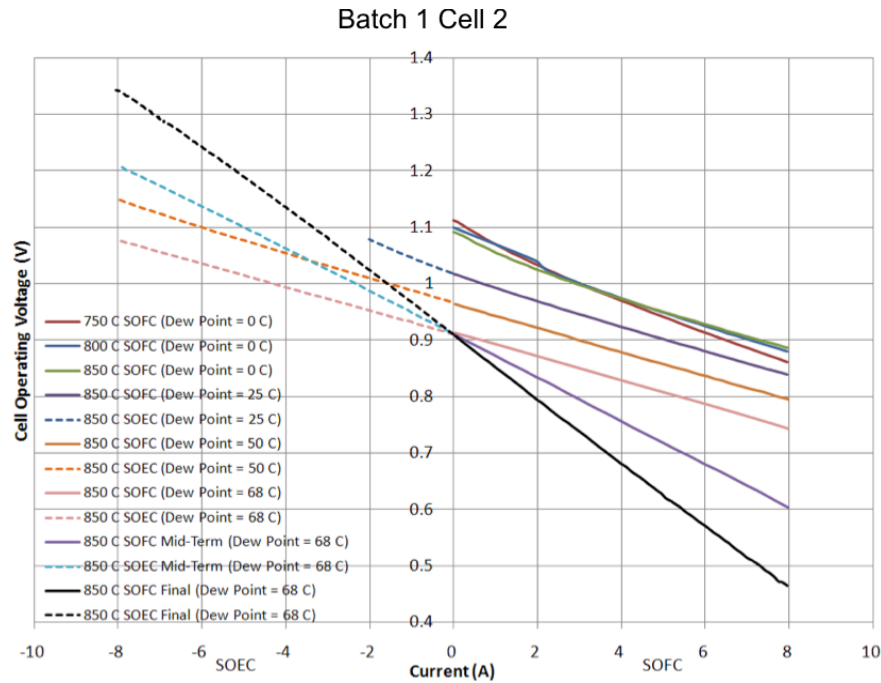
Figure 3-24. Batch No. 1, cell No. 2, dc-potential sweeps at initial, mid-term, and final stages of long-term SOEC operation; effect of operating temperature and inlet dew point upon cell performance in SOFC mode is demonstrated.

The initial cell characterizations illustrated through the dc-potential sweeps presented in Figure 3-23 and Figure 3-24 demonstrate the cells' expected responses to the changes in both operating temperature and steam content. Cell degradation is clearly exhibited in the dc-potential plots and the change in the gradients of each time dependant sweep is directly proportional to the increase in ASR.

Examination of the cell voltages in Figure 3-25 can yield estimates for the cell degradation rates. For the cell in test No. 1 while operated at a current density of 0.5 A/cm^2, the apparent cell degradation rate was approximately 323%/khr. When its current density was reduced to 0.2 A/cm^2 during the final 9 hours of test No. 1, the cell exhibited an apparent degradation rate of 109%/khr. The cell operated at 0.2 A/cm^2 throughout test No. 2 exhibited an apparent degradation rate of approximately 100%/khr. Thus, for the single cells tested from batch No. 1, there is a clear relationship between current density and cell degradation rates.

59
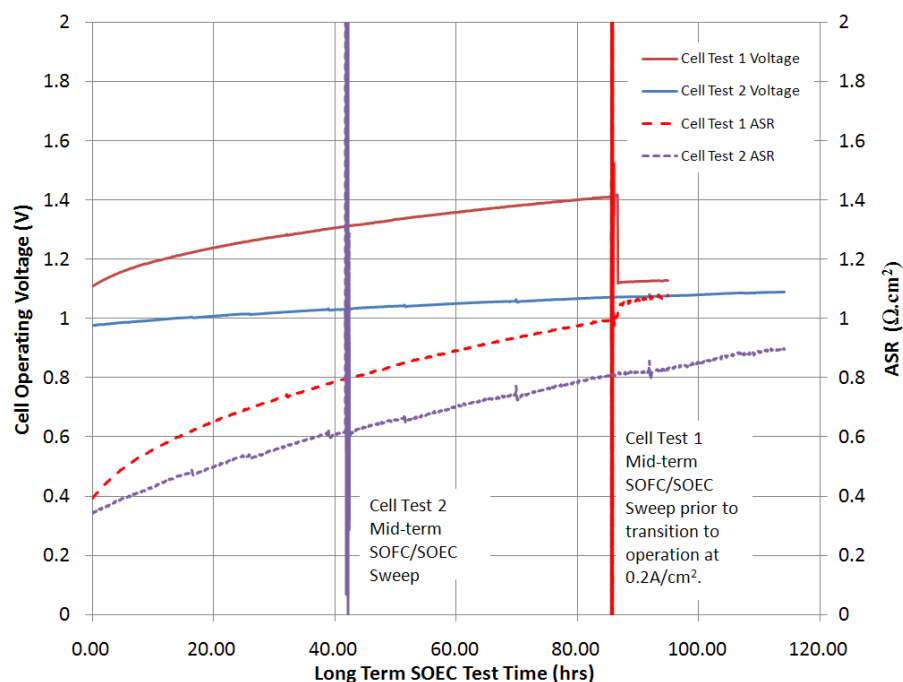
Figure 3-25. Long-term SOEC operating voltage and ASR data for batch No. 1 , cell No. 1 (test No. 1), and batch No. 1, cell No. 1 (test No. 2). Cell in test No. 1 was operated at current density of 0.5 A/cm² for first 86 hours and lowered to 0.2 A/cm². Cell in test No. 2 was operated at 0.2 A/cm² throughout the test. Mid-term dc-potential sweeps appear as vertical lines in data.[3]

Upon conclusion of the batch No. 1 cell tests, a single cell with a modified composition was received from NASA—GRC (batch No. 3, cell No. 1). This cell was installed in test stand No. 4 and heated to operating temperatures via the protocol outlined in Table 3-3. Unfortunately, no operating voltage/OCV was achieved with this cell, prompting its shutdown. The outlet dew-point conditions at temperature indicated that there was air ingress into the cell. Upon termination of the test, it was determined that the cell had cracked open during heatup.

Having performed testing of single cells, NASA—GRC provided INL with a prototype of its three-cell all-ceramic stack design for testing. This stack design features its own ceramic inlet manifolds for both the air and steam/H_2 sides (Figure 3-26, right). No outlet manifolds were provided. Using NASA—GRC's glass sealant, 15-in. long zirconia gas inlet tubes were bonded vertically into the top of the manifold. Given the manifold design of the stack, minor and temporary modifications to test stand No. 4 were required to provide an inlet gas supply to the stack and physically accommodate the stack in the test stand test fixture. Under this modification work, the normal test fixture steam/H_2 inlet line was disconnected from the outlet of the inlet dew-point can and a temporary stainless steel bellows tube was connected in its place. This temporary steam/H_2 line was connected at the top of the furnace to the corresponding zirconia inlet tube via a Swagelok compression fitting. Similarly, the normal air inlet tubing was connected to the air inlet manifold tube atop the furnace. A new inconel lower electrode (Figure 3-26, left) was fabricated to lift the stack above the normal single-cell recess in the test fixture such that the manifold could be accommodated. The new lower electrode was coated in Au for oxidation resistance and good electrical contact with the stack.

60

Figure 3-26. Left: Au-plated stack adaptor cathode plate. Right: NASA—GRC three-cell all-ceramic stack installed in INL test stand No. 4.

Once installed into the furnace, the stack was heated up to the maximum operating temperature of 850°C following the heatup process used for single cells and outlined in Table 3-3. Unfortunately, no OCV was recorded at 750, 800, or 850°C. Several attempts were made to alter the inlet gas flow composition to yield an OCV. Without the ability to monitor the outlet conditions in the stack, it was not possible to determine the problem without terminating the experiment. Upon opening the furnace, it was apparent that the manifold design had failed during heatup and thermal stresses in the manifold had caused its steam/H_2 inlet riser section to crack and move away from the main part of the manifold. This can be seen in Figure 3-27. While no test data were obtained for the NASA—GRC stack technology in FY-11, the INL HTSE Program has developed the testing capability for a further test at the beginning of FY-12.
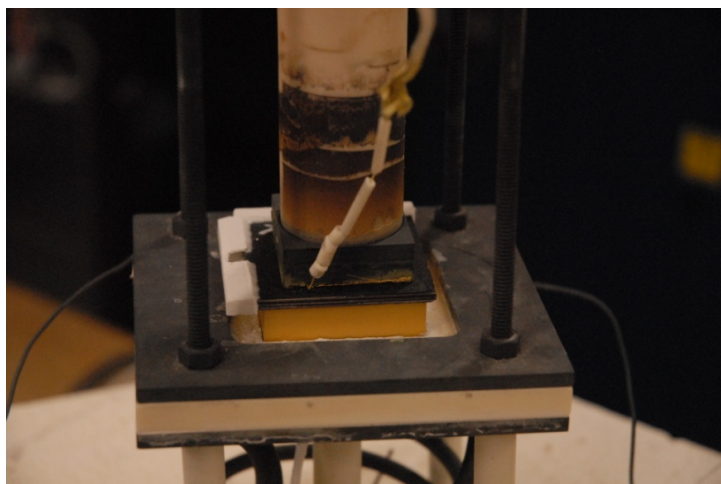
Figure 3-27. Prototype three-cell stack with failed zirconia steam/H_2 inlet manifold riser.

3.3.2 Summary and Future Work

In FY-11, the INL HTE Laboratory developed significant test infrastructure in support of NASA—GRC single-cell and three-cell stack performance analyses. An overview of the test apparatus is provided in Section 3.4.

The test data generated in FY-11 are representative of a first batch of NASA—GRC's prototypic 5- × 5-cm SOEC single cells. Clearly a significant relationship between the operational current density

and cell degradation rate is evident. While the performance of these cells was lower than anticipated, in-house testing at NASA—GRC has yielded higher performance and lower degradation rates with subsequent production batches of cells operated in the SOFC mode. At the time of writing, INL is currently completing the testing of three new 5- × 5-cm single cells. These cells featured modification to cell compositions and cell reduction techniques with the aim to decrease the cell degradation rate while allowing for higher operational current densities to be sustained. Detailed results from the testing of new batches of single cells will be presented in the FY-12 year-end report.

At the start of FY-12, NASA—GRC supplied INL with three 5- × 5-cm single cells and one 5- × 5-cm stack produced from batch No. 3 of their SOEC sets. At the time of writing, two of the three single cells have been successfully tested to the same test conditions presented above. A significant improvement in the overall degradation rate of the cells was noted over the cells tested in FY-11. Specifically, batch No. 3, cell No. 1, had a degradation rate of 54.5%/khr and batch No. 3, cell No. 2, had a degradation rate of 55.4%/khr. Batch No. 3, cell No. 3, will be operated in the fuel cell mode for long-term testing to determine cell performance in comparison to fuel cell performance measured at NASA—GRC. A repeat test of the NASA—GRC stack technology is to be performed in the first quarter of FY-12. While the material performance and durability still requires substantial development, overall it should be noted that NASA—GRC has made good progress with this novel cell and stack fabrication approach.

3.4   St. Gobain Single Cells and Stacks

3.4.1 Single-Cell Testing

3.4.1.1   Single-Cell Test Apparatus and Improvements

The electrode-supported cells tested in this study are supported by the porous 1.5-mm-thick steam-hydrogen electrode whose initial composition is NiO and YSZ, as described in Section 2.5. The NiO must be reduced to Ni metal for the electrode to become electronically conductive. This reduction process is accomplished by exposing the electrode to increasing levels of H_2 at 900°C, as indicated in Table 3-4.

Table 3-4. Cell electrode reduction procedure.

Step	Hold Time (min)	H_2 Flow Rate (sccm)	Dew-Point Temperature (T_{dp}) (°C)	H_2O Flow Rate (sccm)	N_2 Flow Rate (sccm)	Air Flow Rate (sccm)	Cell Temperature (T_{cell}) (°C)	Mole Fraction of Steam (y_{H2O})
0 (heatup)	N/A	0	Bypass	0	500	500	1°C/min	0
1	7.5	80	Bypass	0	500	580	900	0
2	7.5	160	Bypass	0	500	660	900	0
3	7.5	160	22	20.8	500	660	900	0.031
4	5	320	22	25.9	500	820	900	0.031
5	5	500	22	23.7	250	750	900	0.031
6	5	500	22	15.8	0	500	900	0.031

The initial heatup of the cell (Step 0) is performed under inert gas at a heatup rate of 1°C/min to 900°C. The cell is then exposed to varying nitrogen-hydrogen-steam gas mixtures for the time durations indicated in Table 3-4. The steam was introduced by bubbling the nitrogen-H_2 mixture through a room-temperature water bath (humidifier). The corresponding steam flow rates can be calculated based on the nitrogen and hydrogen flow rates and bath temperature. These calculated steam flow rate values are listed in Table 3-4. The steam/hydrogen electrode of the reduced cell is silver/gray in color.

3.4.1.2   Single-Cell Test Procedure and Analysis

This section describes how test conditions are to be determined. The nominal active area for the cells in this study is 16 cm². The maximum current density is usually set such that the maximum cell voltage is near the thermal neutral voltage (V_{tn} = 1.287 V at 800°C). Once the current density and cell area are known, the total cell current is known ($I = I \times A_{cell}$) and the molar hydrogen production rate can be determined directly from Faraday's law:

$$Q_{M,H_2,prod} = \frac{I}{2F}.$$
(3-1)

This molar value can be converted to a standard volumetric flow rate (e.g., sccm) by dividing it by the standard-state molar density, ρ_M = 44.615 mol/m³.

A desired value for maximum fraction of steam utilization can then be specified. Depending on the objective of the test, this value could range from 0.2 to 0.9. Low values of steam utilization generally yield better cell performance in the electrolysis mode. High values can cause localized steam starvation and result in lower cell performance. Analysis of large-scale systems has indicated that overall system performance drops off for steam utilization values below approximately 0.5, but is fairly flat above that value.[4] Once the desired steam utilization is specified, the required inlet steam flow rate can be determined from:

$$Q_{H_2O,i} = \frac{Q_{H_2,prod}}{U_{H_2O}}$$
(3-2)

Since steam is introduced (in this case) using a humidifier, the steam flow rate depends on both the inlet dew-point temperature, which is approximately the same as the humidifier bath temperature, and flow rates of nitrogen and hydrogen. So the inlet dew-point temperature must be specified. INL typically uses a value of 50 to 70°C for single-cell testing.

For testing in the electrolysis mode, a reasonably high inlet dew-point temperature is required, typically 60 to 70°C. Once the inlet dew-point temperature is specified, the corresponding inlet mole fraction of steam is given by:

$$y_{H_2O,i} = \frac{P_{sat}(T_{dpi})}{P_T}$$
(3-3)

where $P_{sat}(T_{dpi})$ is the vapor pressure of steam at the specified inlet dew-point temperature, obtained from an appropriate correlation such as the Antoine equation.

The total required gas flow of nitrogen plus hydrogen can then be obtained from:

$$Q_{gas,i} = Q_{H_2O,i} \frac{1 - y_{H_2O,i}}{y_{H_2O,i}}$$
(3-4)

The inlet flow rate of hydrogen can be determined by specifying the desired inlet mole fraction of hydrogen, typically 0.1 to 0.2. Inlet hydrogen is required to maintain reducing conditions on the Ni cermet material. The respective flow rates of hydrogen and nitrogen are then obtained from:

$$Q_{H_2,i} = \frac{y_{H_2,i}}{y_{H_2O,i}} Q_{H_2O,i} \quad \text{and}$$
(3-5)

$$Q_{N_2} = Q_{gas} - Q_{H_2,i}$$
(3-6)

Air is typically used on the oxygen side of the cell as a sweep gas to prevent buildup of pure oxygen. The flow rate of air is scaled with respect to the oxygen production rate of:

$$Q_{O_2,prod} = Q_{H_2,prod} / 2$$
(3-7)

as follows:

$$Q_{air} = \frac{N_{O_2 prod} Q_{O_2,prod}}{y_{O_2,air}}$$
(3-8)

where N_{O2prod} is a factor indicating the number of oxygen production equivalents desired in the sweep air and y_{O2}, air is the mole fraction of oxygen in the sweep gas ($y_{O2, air} = 0.21$). Typically, $N_{O2prod} = 1$, which yields an outlet sweep gas mole fraction of oxygen equal to 0.347.

Once the cell operating temperature is selected (typically 800°C), the test conditions are fully specified.

3.4.1.3   Single-Cell Testing

This section describes the performance of St. Gobain single electrode-supported cells operating in the fuel cell and electrolysis modes. These cells were originally developed by Forschungszentrum Jülich. The French ceramics firm St. Gobain has licensed the Jülich fuel cell technology and are now producing cells and stacks. Single cells with two different air electrodes, modified LSM and LSCF, were tested in FY-11. The cell specifications and operating conditions during long-term tests are listed in Table 3-5. These cells were optimized for fuel cell operation, but their performances in electrolysis were not well documented.

Table 3-5. Cell specifications and operating conditions for long-term testing.

Cell No.	Start Date (MM/DD/YY)	Temperature (°C)	H_2 (sccm)	N_2 (sccm)	Air (sccm)	Dew Point (°C)	Current Density (i) (A/cm^2)	Air Electrode
T30-170-10	01/03/11	800	500	500	1000	70	0.625	Modified LSM
T30-248-09	01/19/11	800, 900	500	500	1000	70	0.125	Modified LSM
14571	02/07/11	850	500	500	1000	70	0.5	LSCF
14572	03/02/11	850	500	500	1000	70	0.5	LSCF
14573	05/07/11	850	500	500	1000	70	0.5	LSCF
T34-136-03	08/04/11	850	500	500	1000	70	0.5	Modified LSM
T34-312-04	08/18/11	850	500	500	1000	60, 70	0.2,0.4	Modified LSM

Initial efforts on testing these single cells were not quite successful due to a corrosion issue associated with a Ag-Pd current collector, as described in Section 2.5. Stable performance in the fuel cell mode could not be obtained with the new apparatus with the original design. As shown in Figure 3-28, cell voltages were drifting down quickly, but it was not due strictly to the cell degradation. Severe inconel plate oxidation and a burned-out air electrode were observed after testing, as shown in Figure 3-29 and Figure 3-30.

(a)   (b)
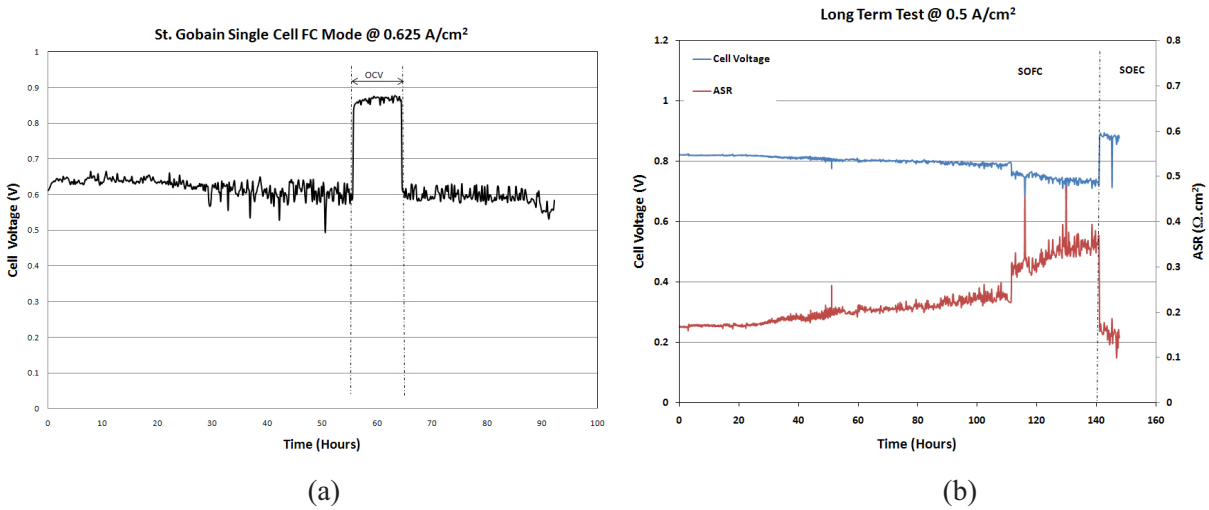
Figure 3-28. St. Gobain single cells tested in fuel cell mode. Top: No. T30-170-10; Bottom: No. 14572.
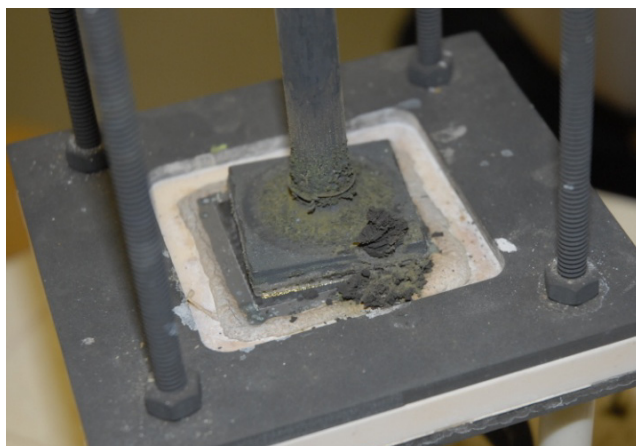
Figure 3-29. Corrosion of inconel air-side current collector due to interaction with Ag-Pd plate.
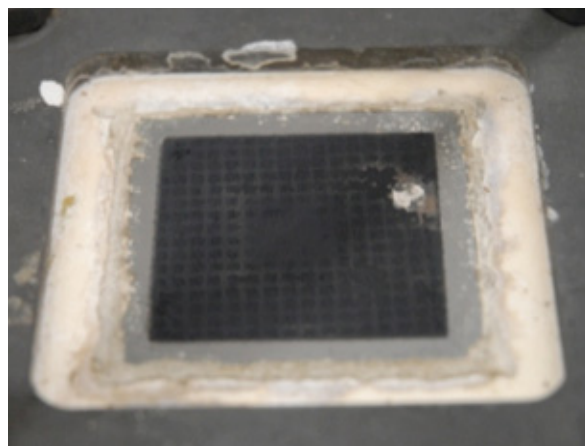
Figure 3-30. Damage to air electrode (upper right) due to corrosion of Ag-Pd current collector plate.

After implementing several improvements to the test apparatus, stable performance was obtained in the fuel cell mode for St. Gobain single cells and corrosion of the current collector was no longer observed. The final design of the apparatus was described in Section 2.5. This apparatus has now been used to test nine single cells and one three-cell stack without problems. Initial performance of St. Gobain single cells was characterized both in the fuel cell and electrolysis modes, as shown in Figure 3-31. Figure 3-31 shows the effect of steam content on the voltage-current density sweeps. The cells with LSCF air electrodes generally demonstrated better initial performance than those with modified LSM air electrodes. Initial ASR values for the modified LSM cells was typically 0.3 Ω-cm^2. Initial ASR values for the LSCF cells were typically 0.2 Ω-cm^2.

(a)   (b)
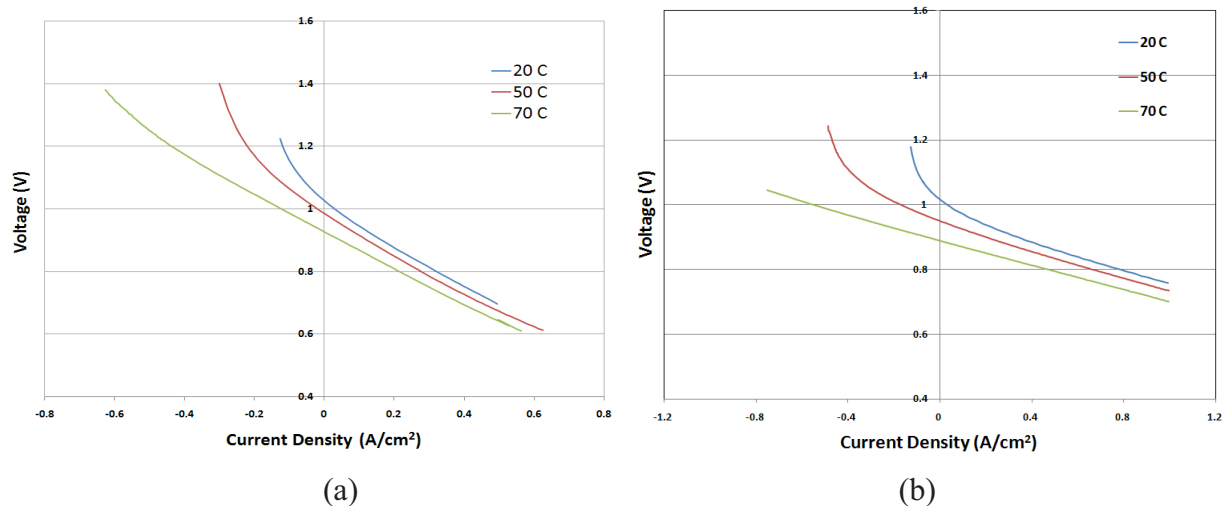
Figure 3-31. Typical voltage current sweeps of St. Gobain single cells. (a) Modified LSM No. T34-136-03. (b) LSCF No. 14573.

All the cells were operated in the fuel cell mode for over 100 hours to establish baseline performance. Operation was then switched to the electrolysis mode. The degradation rates between two modes can be compared. Figure 3-32 show the results of long-term test in both the modes from cell No. T34-136-03 with a modified LSM electrode and cell No. 14573 with an LSCF electrode. Cell No. T34-136-03 showed no degradation for 110 hours in the fuel cell mode, while cell No. 14573 showed only slight degradation

for 190 hours of operation in the fuel cell mode. However, after the cells were switched to the electrolysis mode, both cells exhibited rapid degradation.

(a) (b)
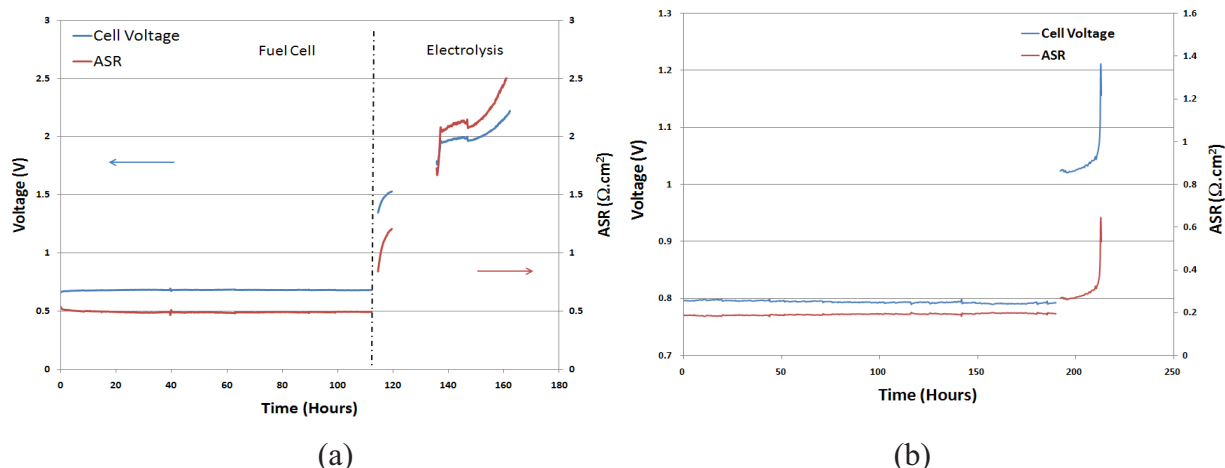
Figure 3-32. Long-term test in fuel cell and electrolysis modes. (a) Modified LSM No. T34-136-03. (b) LSCF No. 14573.

EIS was also used to diagnose the degradation mechanism during the long-term tests. Figure 3-33 shows the Nyquist plot of EIS measurements obtained at different times during the test. It can clearly be seen that after only 5 hours of operation in the electrolysis mode, the radius of the semi-circle at low frequency enlarged significantly, indicating significant electrochemical change on the electrode and/or electrolyte-electrode interface. Post-test photographs verify the findings obtained from impedance measurements. Figure 3-34 shows an example of nearly complete electrode-electrolyte delamination found after the test of cell No. T34-136-03.
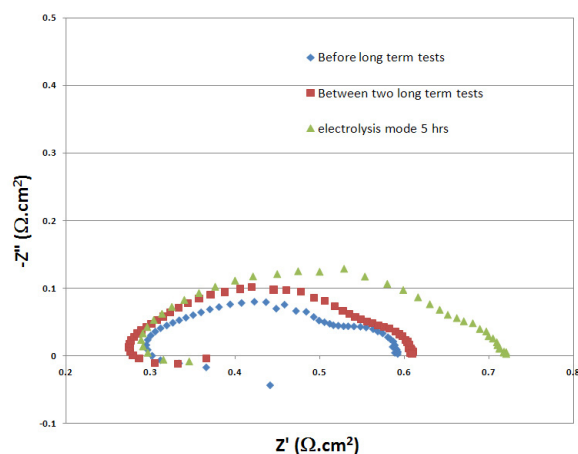
Figure 3-33. Nyquist plots of EIS measured during test of cell No. T34-136-03 with modified LSM.
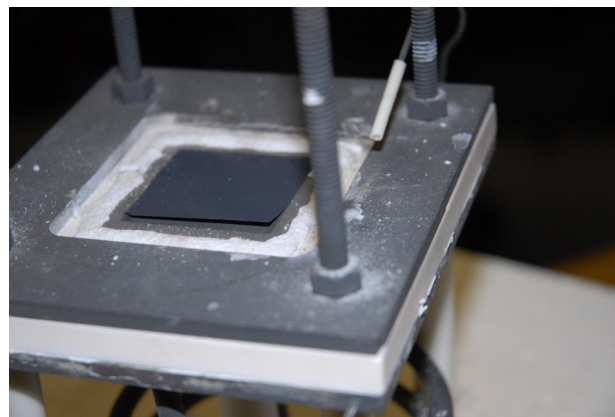
Figure 3-34. Electrode-electrolyte delamination found after test of cell No. T34-136-03 with modified LSM.

To further verify that the specific operating conditions were not the primary factors that resulted in rapid degradation of St. Gobain cells, cell No. T34-312-04 was operated at different conditions such as lower steam content and different current densities. As shown in Figure 3-35, the cell once again behaved well in the fuel cell mode with no degradation. However, it suffered from rapid degradation after being switched to the electrolysis mode.
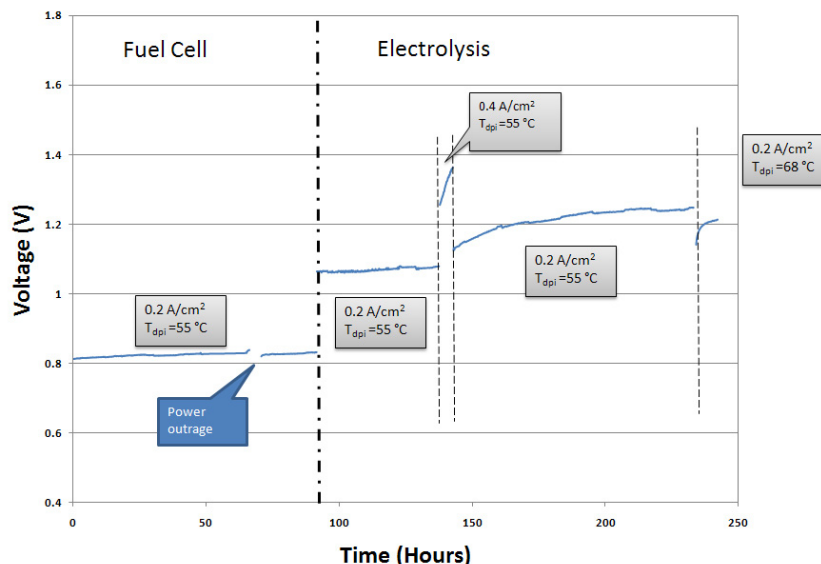
Figure 3-35. Long-term test at different conditions on cell No. T34-136-04 with modified LSM.

In summary, St. Gobain single cells have very stable performance in the fuel cell mode, but all the cells have rapid degradation in the electrolysis mode. Modification needs to be made to overcome delamination issue in electrolysis. It should be noted that these cells were provided to INL at no cost and that they have not been optimized in any way for the electrolysis mode.

3.4.1.4   Single-Cell Testing Summary and Conclusions

Initial performance characterization of St. Gobain Ni cermet-supported cells operating in both the fuel cell and electrolysis modes has been completed. Results indicate excellent initial performance in both modes of operation, with an initial ASR value of approximately 0.2 to 0.3 Ω-cm^2 in both modes for the case of high steam content. ASR values were shown to increase with reduced steam content in both modes of operation. Power densities are most favorable for low steam content in the fuel cell mode and high steam content in the electrolysis mode. Impedance spectra exhibit well defined low-frequency and high-frequency arcs for these cells. Long-duration tests indicate significantly higher degradation rates in the electrolysis mode compared to the fuel cell mode.

3.4.2 Short Stack Testing

INL submitted obtained a three-cell short stack from St. Gobain for testing in the electrolysis mode. A detailed description of the stack was provided in Section 2.5.2. This stack was also tested in test stand No. 6 using the MSRI end plates and compression apparatus. However, the gas flow configuration for this stack is counter-flow, so the steam hydrogen and air flow inlets are located on opposite sides of the stack. Therefore, to be able to use the MSRI end plates, a flow adapter plate (Figure 3-36) was needed to channel the steam/hydrogen and air flows from the cross-flow inlets to the counter-flow inlets. The flow adapter plate by itself is shown in Figure 3-36(a). Figure 3-36(b) shows the adapter plate and the stack in place between the two MSRI end plates. The St. Gobain stack also uses a U-flow arrangement with the flow inlets and outlets both located on the bottom side of the stack, so only a single adapter plate was needed.

(a)   (b)
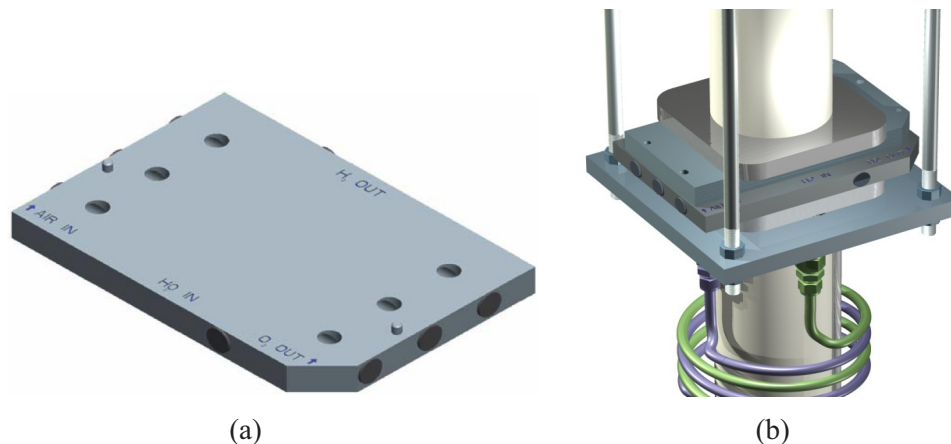
Figure 3-36. Flow adapter plate for testing of St. Gobain stack with counter-current flow. (a) Flow adapter plate. (b) Flow adapter plate and stack in place between two MSRI end plates.

Instead of using spring loading for stack compression, dead weights made of carbon steel were used to apply a constant mechanical compression force to the stack during the tests. The total load applied on the stack was 17.306 kg. Figure 3-37 shows a St. Gobain stack before and after assembly at INL. Testing of two St. Gobain three-cell short stacks at INL was conducted from November 1, 2010, to March 7, 2011. Results of the first test were inconclusive since poor cell-interconnect contact was achieved.

represents the cell reduction procedure used for the St. Gobain stacks. Operating conditions used for stack testing are listed in Table 3-7.
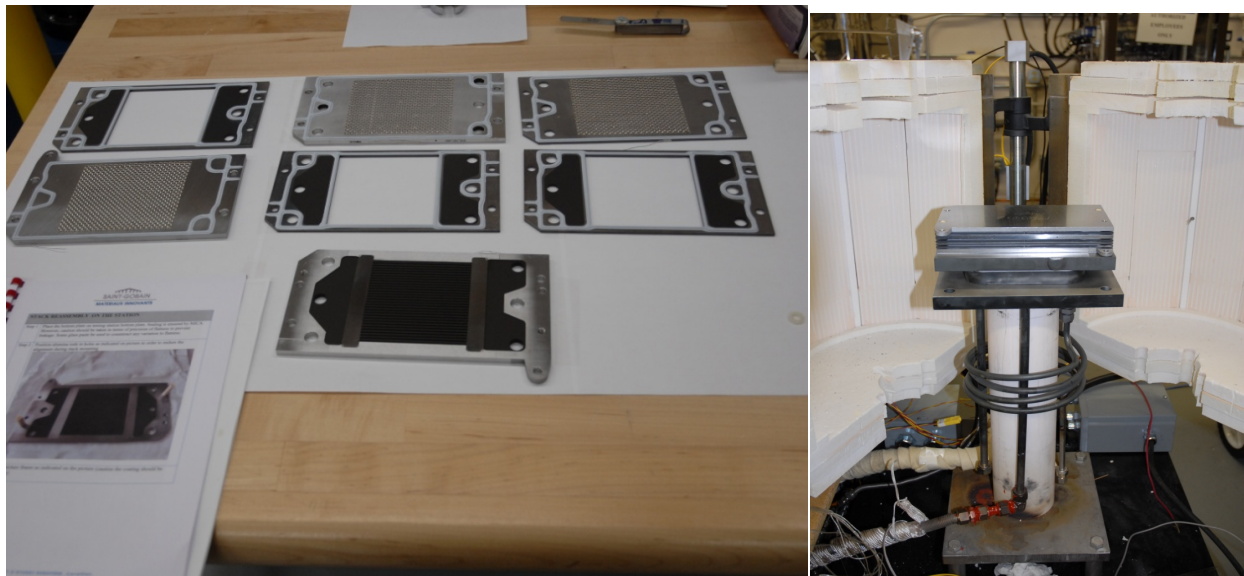
Figure 3-37. St. Gobain stack before and after assembling

69

Table 3-6. Stack reduction procedure.

Step	Hold Time (min)	H_2 Flow Rate (slpm)	Dew-Point Temperature (T_{dp}) (°C)	N_2 Flow Rate (sccm)	Air Flow Rate (slpm)	Stack Temperature (T_{stack}) (°C)
0	60	0.243	Bypass	4.86	5.1	800
1	45	0.486	Bypass	4.86	5.35	800
2	30	0.972	Bypass	4.86	5.83	800
3	20	1.94	Bypass	4.13	7.29	800
4	10	3.89	Bypass	2.19	9.72	800
5	5	5	Bypass	0	10	800
6	5	5	43	0	10	800

Table 3-7. Operating conditions for St. Gobain stack testing.

Stack No.	Start Date (MM/DD/YY)	Temperature (°C)	H_2 (sccm)	N_2 (sccm)	Air (N_2) (sccm)	Inlet Dew-Point Temperature (T_{dpi}) (°C)	Current Density (i) (A/cm^2)
1	11/01/10	Failed at initial performance evaluation					
2	08/15/11	800	2500	2500	5000	70	0.2

Figure 3-38 shows the initial performance of stack No. 2. Initial stack performance characterization was determined through a series of dc-potential sweeps in both the fuel cell and electrolysis modes [Figure 3-38(a)]. Results of these sweeps indicated good initial performance, with ASR values near 1.0 Ω-cm^2 in the fuel cell mode [Figure 3-38(b)]. Long-term durability testing was performed first in the fuel cell mode for 250 hours, then in the electrolysis mode. Final stack performance characterization was again determined by a series of dc-potential sweeps at the same flow conditions as the initial sweeps in both the electrolysis and fuel cell modes. The initial voltage current curves were relatively linear between the fuel cell and electrolysis modes. The stack did not show starvation effect at lower steam content in electrolysis due to the abundant flow that was supplied to this three-cell short stack.

(a)   (b)
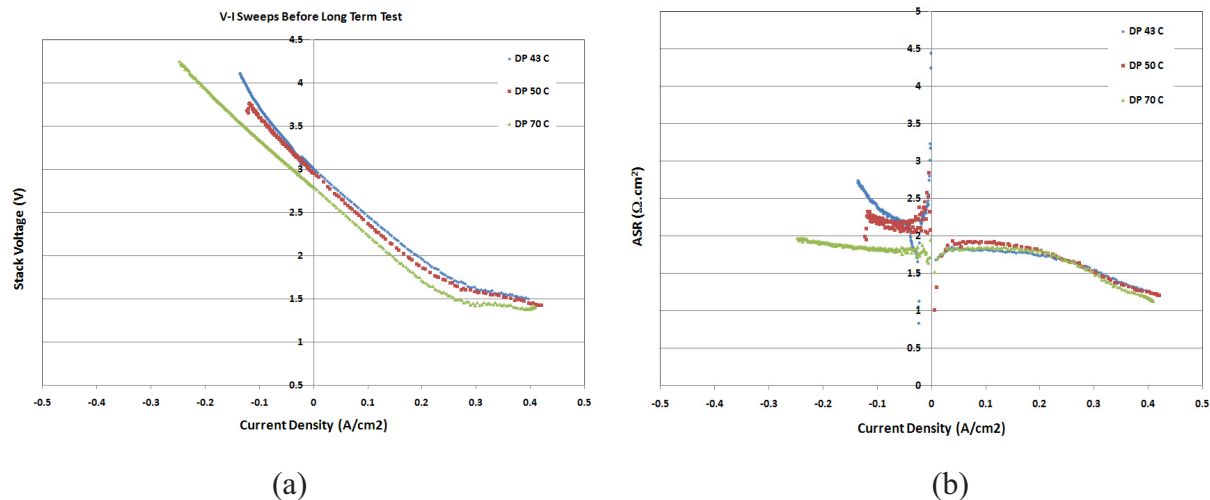
Figure 3-38. St. Gobain stack No. 2. (a) Initial voltage current sweeps. (b) Corresponding ASR values.

After the initial performance evaluation, the stack was operated in the fuel cell mode for 250 hours before being switched to the electrolysis mode. A summary of the long-term stack performance is provided in Figure 3-39 and Figure 3-40.

(a)   (b)
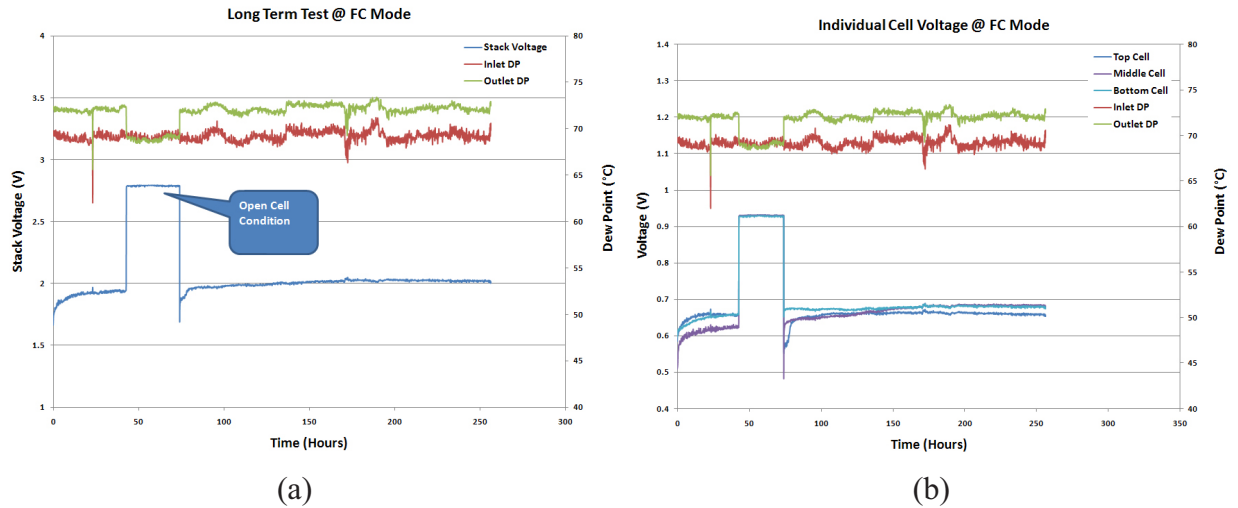
Figure 3-39. St. Gobain stack No. 2 operated in fuel cell mode. (a) Stack voltage. (b) Individual cell voltages.

(a)   (b)
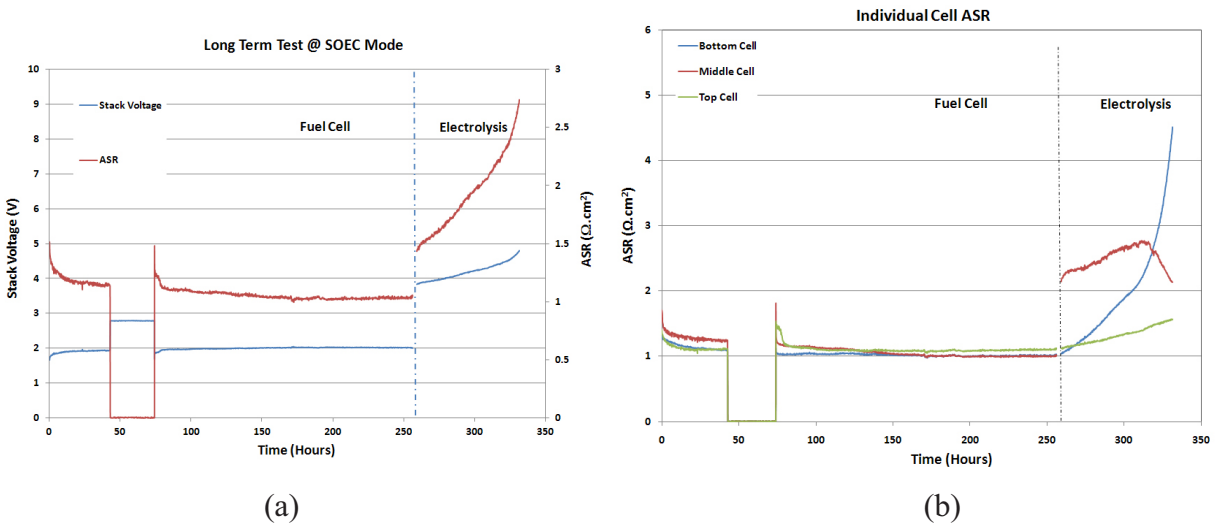
Figure 3-40. St. Gobain stack No. 2 long-term performance in fuel cell and electrolysis modes. (a) Stack voltage and ASR. (b) Individual cell ASR values.

Figure 3-40 provides a time history of the stack ASR. The ASR in the fuel cell mode actually improved (decreased) during the initial 40 hours of long-term operation. This initial performance improvement is associated with conditioning of the air-side LSM electrode. Stack performance was very stable in the fuel cell mode for 250 hours. There was a disruption in the current over a weekend due to a drop-out of the electronic load for unknown reasons. However, this disruption had no long-term effect on the performance of the stack. The ASR value recovered after the current disruption.

After 250 hours, stack operation was switched to the electrolysis mode. The switch resulted in an immediate increase in the stack ASR and subsequent rapid degradation. The degradation in the electrolysis mode was so rapid that the test was halted after approximately 330 hours. Rapid SOEC mode

71

degradation of cells with LSM air electrodes has been observed previously with single-cell tests, so the result is not unexpected.

In the electrolysis mode, the ASR increased from 1.5 to 2.7 Ω-cm^2 in just 75 hours. The test had to be shut down due to the rapid degradation in electrolysis. Figure 3-40 shows the stack performance and variations of the individual cell voltages during the whole test.

In summary, consistent with the single cells, St. Gobain stacks demonstrated stable performance in the fuel cell mode, but showed significant degradation in the electrolysis mode. Modification of the cell microstructure is needed to allow for stable operation in the electrolysis mode.

3.5 Materials and Systems Research, Incorporated, Single Cells and Stacks

3.5.1 Single-Cell Testing

A full description of the improved INL single-cell test apparatus was provided in Section 3.1.2. Two batches of electrode-supported single cells were provided by MSRI. Each 5- × 5-cm single cell has a 4- × 4-cm active area. The cell composition is Ni-YSZ/YSZ/LSCF with an optimized functional layer for electrolysis operation. The cells were tested in the new apparatus described in Section 3.1.2. Polarization scans were conducted by Amrel Eload and Lamda power supply. Two single cells from different batches were tested starting from June 1, 2011, and September 19, 2011, respectively. The operating conditions are listed in Table 3-8. Instead of just doing electrolysis, the cells were operated in the fuel cell mode for a while and then switched to the electrolysis mode. In that case, the degradation under two different modes can be compared. The cell that is operated both in the fuel cell and electrolysis modes is called reversible solid-oxide cell.

Table 3-8. Operating conditions for single-cell testing.

Cell No.	Temperature (°C)	H$_2$ (sccm)	N$_2$ (sccm)	Air (sccm)	Dew Point (°C)	Current Density (A/cm^2)
1	800	500	500	1000	70	0.5
2	800, 850	500	500	1000	80	0.2, 0.3, 0.4

Figure 3-41 shows the initial voltage current sweeps conducted for cell No. 1. The measurements were carried out at 800 and 850°C. Figure 3-41 clearly shows that steam starvation happens at higher current density in the electrolysis mode. The ASR at 850°C with the inlet dew point at 70°C is around 0.25 Ω-cm^2 in the electrolysis mode, which is much better compared to the electrolyte-supported cells.

(a)   (b)
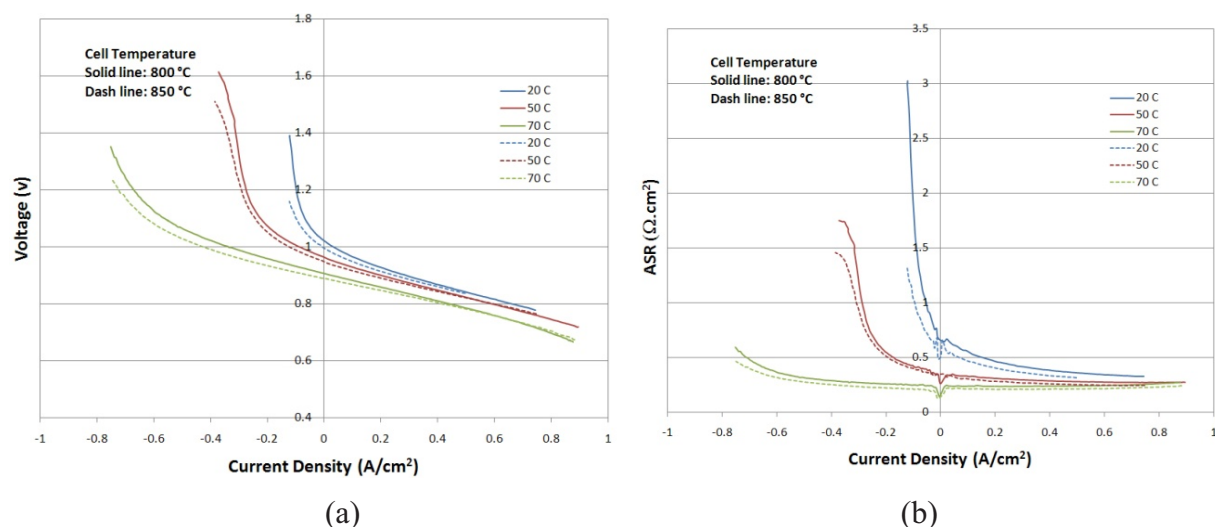
Figure 3-41. MSRI single-cell No. 1. (a) Voltage current sweeps. (b) Corresponding ASR.

Figure 3-42 represents the long-term test of cell No. 1 both in the fuel cell and electrolysis modes at 850°C. The cell was operated in the fuel cell mode at 0.5 A/cm^2 for about 110 hours, followed by 320 hours running at the same current density in the electrolysis mode. No obvious degradation was found during the fuel cell mode. After switching to the electrolysis mode, the cell started slightly degrading. The degradation rate is 4.25%/khr, which is very good at such high current density. A post-test photograph of cell No. 1, as shown in Figure 3-43, shows no sign of electrode-electrolyte delamination. (The broken upper corners occurred during removal of the cell from the test fixture.) Furthermore, the uniform criss-cross pattern on the air-side electrode indicates good cell contact with the current collector plate and Au mesh.
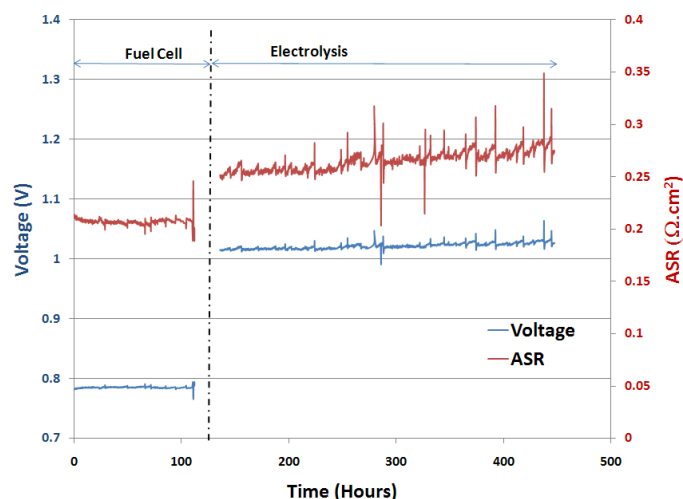
Figure 3-42. MSRI single-cell No. 1 long-term test in fuel cell and electrolysis modes.
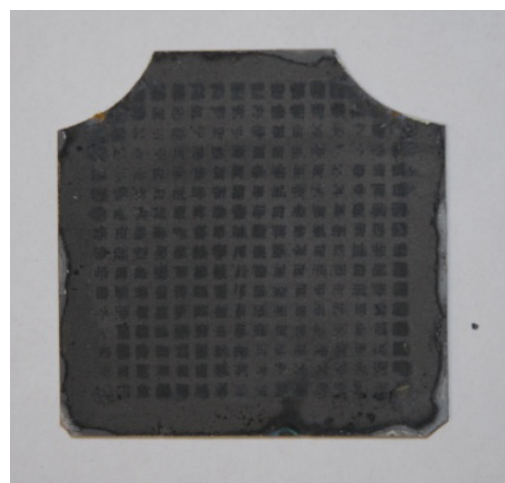
Figure 3-43. MSRI single-cell No. 1 post-test photograph.

To provide information of an optimized operating condition for MSRI stack testing in the future, a different long-term test was performed on cell No. 2. The cell was first operated in the fuel cell mode for about 100 hours, and then in the electrolysis mode it was operated at different current densities for about 200 hours. The effect of current density on degradation is illustrated in Figure 3-44. In the electrolysis mode, at 0.2 A/cm^2, the cell shows a degradation rate of 2.256%/khr; at 0.3 A/cm^2, the cell

shows a degradation rate of 4.75%/khr; and at 0.4 A/cm^2, the cell shows a degradation rate of 5.426%/khr. The test clearly demonstrates that the degradation rate increases as current density increases. To mitigate degradation, MSRI cells are better operated near 0.2 A/cm^2.
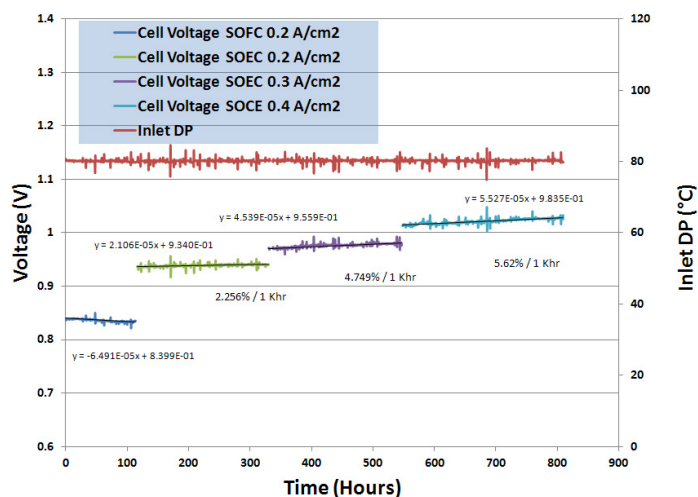
Figure 3-44. MSRI single-cell No. 2 long-term test in fuel cell and electrolysis modes.

In summary, generally MSRI electrode-supported single cells show much better stable performance in the electrolysis mode than the cells from other vendors. MSRI cells are optimized for electrolysis operation and have a much lower degradation rate.

3.5.2 Stack Testing

3.5.2.1 Test Apparatus

In 2010, a sixth test station was added to the bench-scale HTE testing capability at INL. This new test stand added significant additional capability to the INL HTE Laboratory. At the heart of the test stand is a vertically-mounted split-tube furnace that provides increased access to the electrolysis test articles without physically removing the furnace. The furnace has an electrical power rating up to 15 kW and can be operated at temperatures up to 1000ºC. It has an inside diameter of 16 in. and a height of 21 in. The vertical clamshell design provides easy access to the test fixture (inconel 625) that facilitates the supply of process gases and electrical power to stacks that are on test. The test fixture can be easily adapted to the requirements imposed by a variety of stack configurations.

The test stand includes a choice of three steam delivery systems, allowing a large range of gas flow rates and steam mole fractions to be delivered to the stack on test within the furnace (see Figure 3-2). Steam can be supplied to the test fixture using a traditional humidifier in which a carrier gas mixture is bubbled through a bath of deionized water that is maintained at a specified temperature using feedback control. The steam flow rate is determined by the temperature of the water bath and flow rate of the carrier gases composed of a controlled mixture of hydrogen and nitrogen. All piping downstream of the bubbler is heat-traced and insulated to prevent condensation.

The second steam generation method is through the use of a controlled evaporator and mixer (CEM) (Bronkhorst). The CEM is built around a liquid mass flow control valve, gas-liquid mixing device and heat exchanger in which heat is added to the mixture of fluids for evaporation. Deionized water and the carrier gas are supplied by separate mass flow controllers. Total evaporation of the water is achieved in the CEM. The piping downstream of the CEM to the furnace is also heat-traced and insulated to prevent

condensation. There are two complete CEM systems incorporated into the test stand. The smaller unit has a maximum water flow rate of 100 g/hr, maximum gas flow rate of 1 slpm, and maximum heater power of 150 W. The larger unit can provide up to 1000 g/hr of water and 100 slpm of gas flow with a 1-kW heater capacity.

The test fixture is based on a design developed at MSRI. It is capable of providing compressive force to the top of a stack while on test through either the addition of dead mass or via compression springs outside of the hot zone of the furnace. When testing stacks produced by MSRI, the compressive load was provided via springs. A total compression load of 181 kg (400 lb) was used. The compression load is transferred to the stack via an alumina tube and the upper electrode plate, as shown in Figure 3-45. Once the stack is in place on the lower portion of the test fixture, an alumina load transfer tube is installed atop the upper electrode, onto which compression springs with pusher plates are placed. Compression of the stack to the desired loading is achieved through the tightening of nuts on four threaded bars that stand in parallel to the load transfer tube and, fixed to the lower test fixture portion, run through the pusher plates. Upon achieving the desired compression of the springs and hence forced loading of the stack, the furnace may be closed and a heatup procedure executed. During heatup, the compression of the springs is monitored and carefully adjusted to maintain the prescribed load and compensate for thermal expansion of the threaded rods and compression of the compliant seals in the stack. A closeup photograph of the stack mounted on the test fixture is provided in Figure 3-46. A photograph of the stack installation in progress is provided in Figure 3-47.
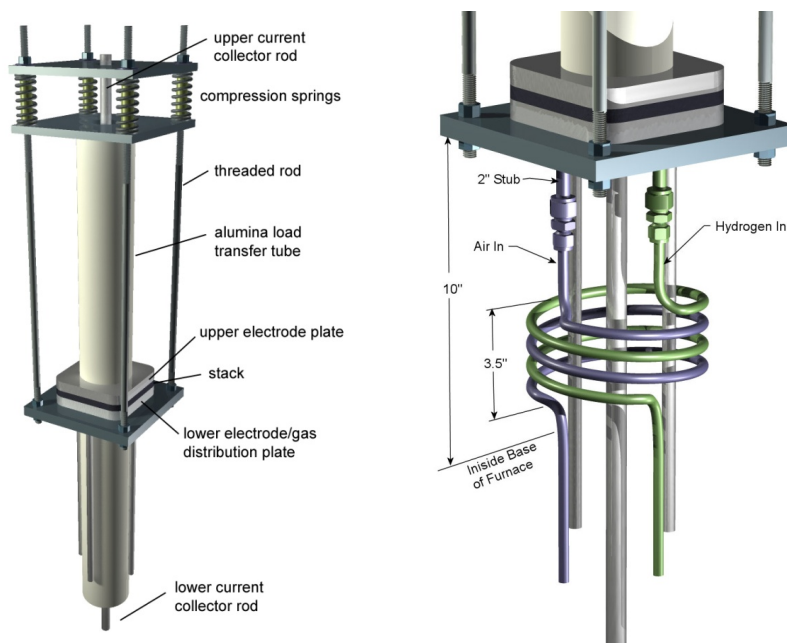
Figure 3-45. Test fixture details, test stand No. 6.

Figure 3-46. Five-cell MSRI SOEC stack mounted on test fixture.

Figure 3-47. Installation of five-cell MSRI SOEC stack in test stand No. 6.

A P&ID for the test stand used for these tests was provided in Figure 3-2. Remotely-controlled motor-operated valves are used to simplify the selection of the piping configuration for a given desired operating condition. If the humidifier is selected, a bypass option is available to provide dry gas to the stack during startup and cooldown. If the CEM is selected, either the small or large unit is selected. Also, a nitrogen purge of the liquid mass flow controllers is available when the CEM option is selected. Three additional valves provide on-off control of the air, deionized water, and condenser cooling water. Two nonmotorized three-way valves are included in the system to provide a stack bypass option.

Real-time test data are collected from in-line instrumentation using a multi-channel data acquisition unit (Agilent) that is interfaced to the system controller computer using a Labview™ based virtual instrument. A programmable dc power supply (Lambda™) was used to provide electrical power to a stack while operated in the steam electrolysis mode. A programmable electronic load (Amrel) is used as a power sink for operation of stacks in the fuel cell mode. Switching between the power supply and electronic load is facilitated by a network of electronic relays housed within a switching box. Both the electronic load and power supply are controlled through the Labview™ based virtual instrument, allowing for data acquisition and control of dc-potential sweeps for stack performance characterization.

3.5.2.2 Solid-oxide Electrolysis Cells and Stack

The solid-oxide cells used for this study have a square profile with outer dimensions of 15.2×15.2 cm and a cell active area of 100 cm^2. The cells incorporate a negative-electrode-supported multi-layer design with Ni-zirconia cermet negative electrodes, thin-film YSZ electrolytes, and multi-layer La ferrite-based positive electrodes. The Ni-zirconia electrode has a support layer thickness of 700 µm and graded functional layer with an overall thickness of 15 µm. The electrolyte thickness is 8 to 10 µm. The positive electrode also has a graded functional layer with a thickness of 20 µm and current collecting layer thickness of 50 µm.

The stack is internally manifolded with compliant seals. Treated metallic interconnects with integral flow channels separate the cells and electrode gases. The cells incorporate semi-elliptical cutout gas flow channels, four per side around the outer periphery of the cells, that mate with corresponding holes in the interconnect plates and compliant seals. The stack operates in cross-flow, with an inverted-U-shaped overall flow pattern such that the gas flow inlets and outlets are all located underneath the stack. Stack mechanical compression is accomplished by means of the custom spring-loaded test fixture described previously.

Installation of MSRI stacks within the test section is a relatively simple procedure. Correct alignment of the process gas (steam/H$_2$) and air inlets and outlets of the stack to the corresponding flow channels of the test section is most critical. Compliant gasket seals are placed underneath and atop the stack prior to

placement on the test fixture lower electrode/gas distribution plate. Contact aids are used to assist electrical contact between the stack and upper and lower fixture electrodes.

3.5.2.3   Test Results

A five-cell MSRI stack was installed in INL HTE Laboratory test stand No. 6 on January 10, 2011, and details of this test were reported.[5] The stack was maintained at a temperature of 800°C after a controlled heatup, seal curing, and cell reduction procedure (with a dry forming gas) were completed. Table 3-9 summarizes the heatup procedure used for the MSRI five-cell stack.

Table 3-9. Summary of MSRI stack heatup procedure and operating conditions.

Step	Temperature (°C)	Compressive Load (lb)	H_2 Flow Rate (slpm)	N_2 Flow Rate (slpm)	O_2-Side Flow Rate (slpm)
1	20 – 600 at 5°C/min	100	0.45	4.05	4.5 – N_2
2	600 – 830 at 5°C/min	400	0.45	4.05	4.5 – N_2
3	830, 30-min hold	400	0.45	4.05	4.5 – N_2
4	830 →800 at 5°C/min	400	0.45	4.05	4.5 – N_2
4	800, 1-hr hold	400	0.45	4.05	4.5 – N_2
4	800, 1-hr hold	400	1.2	4.8	6.0 – N_2
5	800, 1-hr hold	400	1.8	4.2	6.0 – N_2
6	800, long-term operation	400	2.5	2.5	4.1 – N_2

Once the seals were cured and cells of the stack were fully reduced, a stable OCV was achieved. Initial characterization of the cells and overall stack performance was determined through a series of dc-potential (V-I) sweeps obtained over a range of inlet conditions in both the fuel cell and electrolysis modes. Approximate inlet conditions of 0%mol, 50%mol, and 70%mol steam were examined for the influence of steam on the stack performance. These molar concentrations may be considered in terms of inlet dew-point temperatures of 0, 79.1, and 86.1°C, respectively. Upon completion of initial characterization, the stack was placed into long-term SOEC testing for 1000 hours of operation with a current density of 0.2 A/cm^2 (20-A total current) and inlet dew-point value of 86.1°C. After 1000 hours of testing, a final set of dc-potential sweeps were recorded.

Figure 3-48 illustrates a comparison of the initial V-I sweep data recorded on January 11, 2011, to the final sweeps after 1000 hours of testing in the electrolysis mode recorded on February 22, 2011. SOFC sweep 1, 1-11, was performed with only dry hydrogen flowing on the fuel side. The voltage current curve for this sweep exhibits significant curvature at low current density. This effect is associated with the high sensitivity of the Nernst potential to small changes in average steam concentration as cells begin to convert hydrogen to steam in the fuel cell mode. SOFC sweep 2, 1-11, and SOEC sweep 1, 1-11, were performed with 50% mole fraction steam. These sweeps exhibit nearly linear behavior that is continuous in the fuel cell and electrolysis modes. SOEC sweep 2, 1-11, was performed with 70% steam. Note that the open-cell (zero-current) potential decreases with higher steam content. This sweep shows nearly linear voltage current behavior with a slope that is parallel to SOEC sweep 1, 1-11.
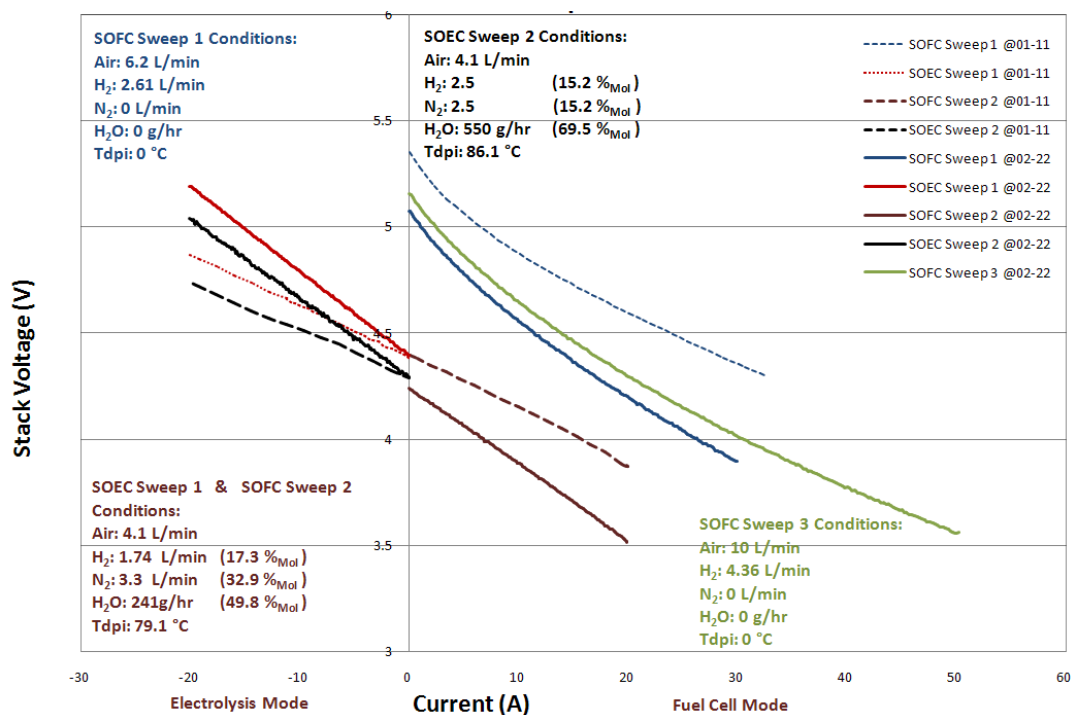
Figure 3-48. dc-potential SOEC and SOFC polarization curves for first MSRI stack tested at INL. Final results were obtained after 1000 hours of operation in steam electrolysis mode with current density of 0.2 A/cm².

Final voltage current sweeps were obtained after 1000 hours of operation in the SOEC mode. In all cases, the final sweeps have slightly steeper slopes than the corresponding initial sweeps, as expected, due to performance degradation.

Results from the 1000-hour INL test are presented in Figure 3-49 through Figure 3-51. Figure 3-49 shows the overall stack voltage and current for the 1000-hour test. The test was performed at a constant current of 20 A. Stack voltage increased from 4.58 to 5.047 V over the test duration, indicating a degradation rate of 10.2%/khr based on voltage. An expanded view of the stack voltage, along with the inlet and outlet dew-point values, is presented in Figure 3-50. The outlet dew-point values are approximately 3.5°C lower than the inlet values, which is consistent with the electrolytic conversion of steam to hydrogen at these gas flow rates and this amperage. The dew-point measurements allow for independent determination of the steam consumption/hydrogen production rate. Figure 3-50 indicates fluctuations in stack voltage that correlate with fluctuations in dew-point values observed during the first 800 hours of the test. These fluctuations were attributed to significant drops in facility water pressure that resulted in the reduction in steam production. These fluctuations in water pressure were rectified approximately 800 hours into the test through the installation of a booster pump downstream of the mains water supply, ahead of the water purification system.
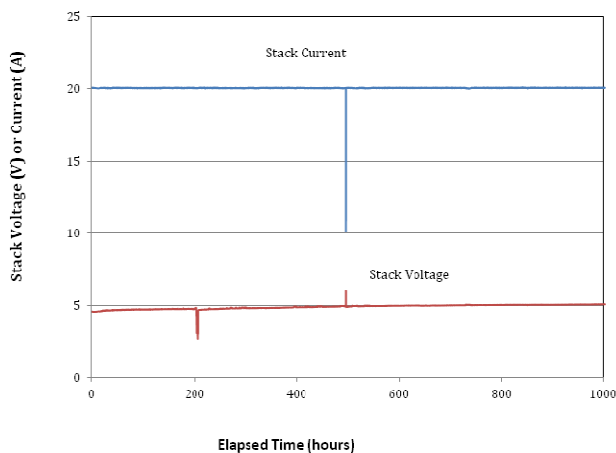
Figure 3-49. Stack voltage and current, long-term test.
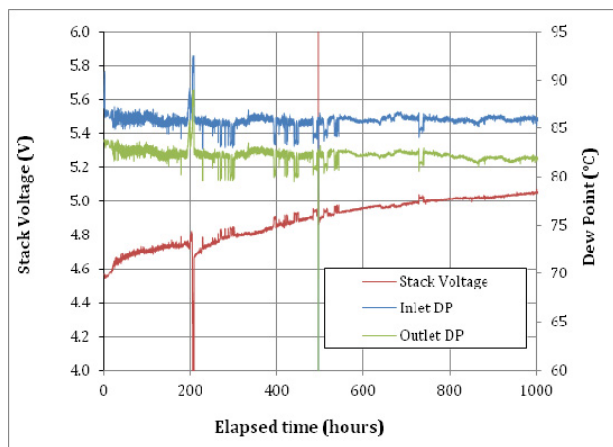
Figure 3-50. Stack voltage and dew-point temperatures, 1000-hour INL test.
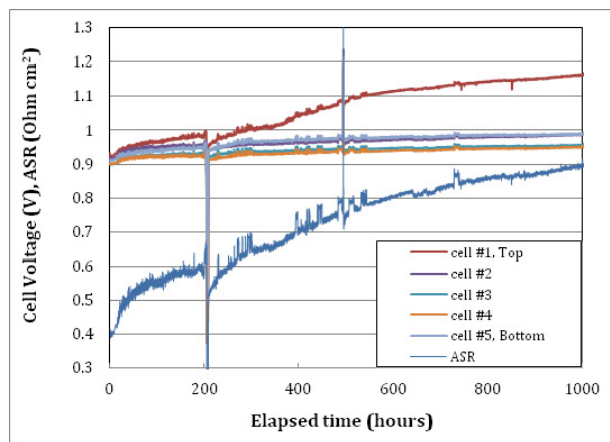
Figure 3-51. Individual cell voltages, long-term test, current density of 0.2 A/cm², and inlet steam molar concentration of 69.5%mol. The apparent stack ASR and its behavior as a function of time is also indicated.

Another notable artifact of a significant test anomaly is evident in Figure 3-49 and Figure 3-50 at approximately 210 hours when the gas generator partially failed to operate on a liquid nitrogen dewar used to supply N_2 to the test facility. The reduction in N_2 supply resulted in increased steam molar concentrations and hence a dramatic drop in SOEC operating voltage. This problem was rectified rapidly by switching the N_2 supply to a secondary nitrogen dewar.

Individual cell voltages recorded during the long-term test, along with the apparent ASR values (stack operating voltage minus stack OCV divided by current density), are presented in Figure 3-51. The individual cell voltages are very steady, except for the top cell, which increases dramatically during the long-term test. In fact, cell No. 1 degraded at a rate of approximately 24.1%/khr while cell No. 4 (the second from the bottom of the stack) exhibited the lowest degradation rate of only 3.28%/khr. Clearly the overall degradation of the stack was significantly influenced by the degradation of the uppermost cell. We are investigating the possible causes of the accelerated degradation of that cell. The initial stack ASR value was 0.41 Ω-cm². The stack ASR increased to 0.89 Ω-cm² by the end of the 1000-hour test.

A second five-cell short stack with advanced anode-supported cells was delivered to INL in August of 2011. Performance of this stack was excellent. After an initial conditioning period (approximately

79

70 hours), the degradation rate over the next 1000 hours was less than 3.0%/khr, based on voltage, with an increase in ASR value from 0.61 to 0.77 Ω–cm^2. Overall results are presented in Figure 3-52, which shows the overall stack voltage and current over 1000 hours. The stack was operated in the constant current mode. Degradation is represented by the increase in operating voltage. On the scale used in Figure 3-52, the increase in stack voltage over 1000 hours is not obvious. Figure 3-53 shows the stack voltage and ASR value over 1000 hours on an expanded scale. A linear regression fit is also shown for each. The fit for the voltage data indicates a degradation rate of 2.85%/khr over the time period from 100 to 1000 hours. Individual cell voltage histories are presented in Figure 3-54. Performance was nearly uniform over the five cells, but the top cell did exhibit a slightly higher voltage and degradation rate throughout the test.
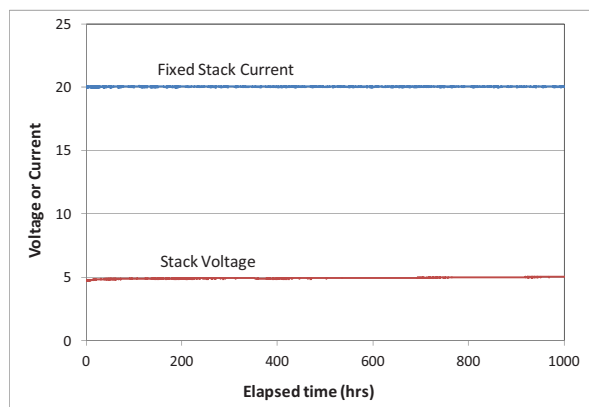
Figure 3-52. Overall results of long-term durability test, five-cell MSRI stack.
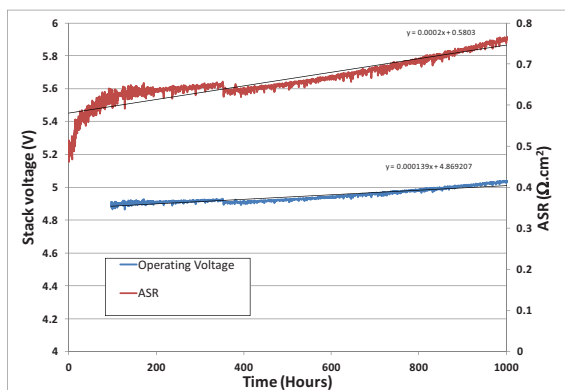
Figure 3-53. Results of long-term durability test, five-cell MSRI stack, expanded scale.
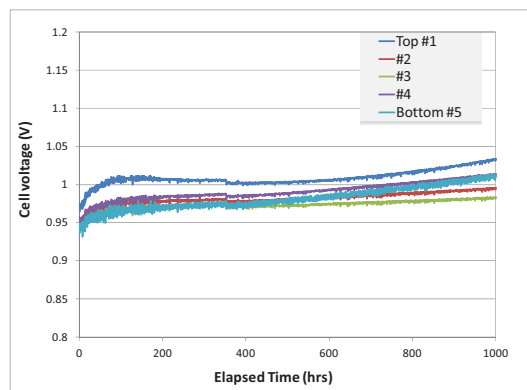
Figure 3-54. Results of long-term durability test, five-cell MSRI stack, individual cell voltages.

Long-term operation of this stack at a current of 20 A was continued to the 1100-hour mark, followed by an examination of the effect of increased current density on degradation rate.

Figure 3-55 and Figure 3-56 show the effect of increased current density on the degradation rate. At 1100 hours, the current density was increased from 0.2 to 0.38 A/cm^2, corresponding to the maximum current (38 A) supported by the power supply. The degradation rate at 0.38 A/cm^2 increased to 14.7%/khr. All the individual cells behaved similarly in this test, as shown in Figure 3-56. So the special treatment on the top cell significantly decreased the stack degradation.
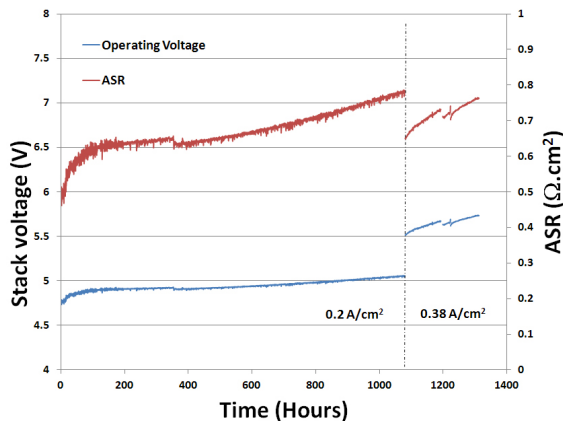
Figure 3-55. MSRI stack No. 3 long-term electrolysis test at 0.2 A/cm² and 0.38 A/cm².
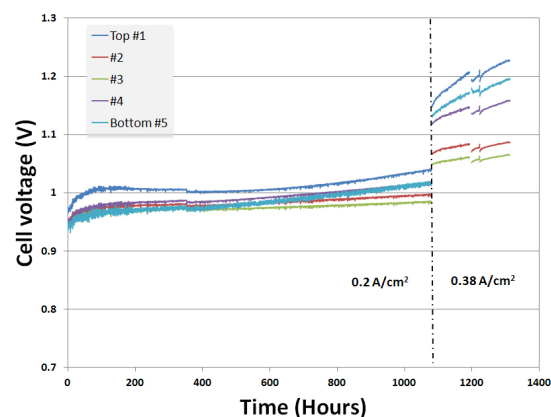
Figure 3-56. MSRI stack No. 3 long-term electrolysis test at 0.2 A/cm² and 0.38 A/cm².

A major INL HTSE Program milestone for FY-12 is "demonstration of HTE at large scale (4 kW or higher) for 1000 hours." To achieve this milestone, proven cell and stack technology, that has been successfully demonstrated at INL, should be used. Based on testing experience, MSRI has been identified as the supplier of the most promising cell/stack hardware for FY-12 large-scale demonstration. Preliminary tests will be conducted to verify performance of these larger format cells before large-scale testing is initiated. INL will work closely with MSRI to meet these objectives.

3.6   References

1   O'Brien, J. E., Stoots, C. M., Herring, J. S., McKellar, M. G., Hawkes, G.L., Harvego, E. A., Sohal, M. S., and Condie, K. G., "High Temperature Electrolysis for Hydrogen Production from Nuclear Energy – Technology Summary," INL/EXT-09-16140, May 18, 2009.

2   Herring, J. S., O'Brien, J. E., Stoots, C. M., and Hawkes, G. L., "Progress in High-Temperature Electrolysis for Hydrogen Production using Planar SOFC Technology," *International Journal of Hydrogen Energy*, Vol. 32, Issue 4, pp. 440–450, March 2007.

3   O'Brien, R.C., O'Brien, J.E., Stoots, C.M., Zhang, X., Farmer, S.C., Cable, T.L., Setlock, J.A., "Testing and performance analysis of NASA 5 cm by 5 cm bi-supported Solid Oxide Electrolysis Cells operated in both fuel cell and steam electrolysis modes," Proceedings of the 2011 ASME International Mechanical Engineering Conference and Exposition, Denver CO, November 2011.

4   O'Brien, J. E., McKellar, M. G., Harvego, E. A., and Stoots, C. M., "High-Temperature Electrolysis for Large-Scale Hydrogen and Syngas Production from Nuclear Energy – Summary of System Simulation and Economic Analyses," *International Journal of Hydrogen Energy*, Vol. 35, Issue 10, pp. 4808–4819, May 2010.

5   O'Brien, J. E., McKellar, M. G., Harvego, E. A., and Stoots, C. M., "High-Temperature Electrolysis for Large-Scale Hydrogen and Syngas Production from Nuclear Energy – Summary of System Simulation and Economic Analyses," *International Journal of Hydrogen Energy*, Vol. 35, Issue 10, pp. 4808–4819, May 2010.

4 DEGRADATION STUDIES—PHYSICAL EXAMINATIONS

4.1 Chemical and Structural Degradation Mechanisms—Massachusetts Institute of Technology

4.1.1 Introduction

The reversible solid-oxide cell is a promising technology for electricity production (SOFC), as well as for hydrogen and synthetic fuel production (SOEC).[1, 2] However, the high working temperature (above 800°C) induces a material degradation problem that deteriorates the cell performance severely.[3] Sr-doped La cobaltite, $La_{1-x}Sr_xCoO_{3-\delta}$ (LSC), a promising candidate as cathode/anode material for SOFCs/SOECs[4, 5, 6, 7] and anode bond layer material for SOECs[3, 8] showed different electrochemical performance when synthesized at different temperatures.[9] Furthermore, these LSC thin-film cathodes that are grown at lower temperatures (340 to 510°C) are significantly more stable than the high-temperature-grown (of nearly 630°C) ones that show severe degradation of oxygen reduction reaction (ORR) kinetics during thermal annealing at 600°C.[9] Annealing-induced degradation of surface chemistry can also detrimentally impact the electrolysis activity of the LSC-based anode materials.

Kubicek *et al.*[10] has shown that the surface cation chemistries of these LSC films, especially their Sr content, differ as a function of the deposition temperature. The structure of the LSC surfaces that have varying levels of Sr is important to understand because the activity of the surface can directly relate to the atomic structure that a given cation composition exists in.[11] In addition, it is essential to identify how the processing and functional conditions of temperature and oxygen chemical potential drive changes in the cation chemistry and structure on the surface, because those conditions can then be controlled to tune the surface activities in both SOECs and SOFCs. In this work, we present our findings on the following:

1. Effects of the synthesis and annealing temperatures and oxygen pressure on the surface cation chemistry of LSC thin films.

2. Possible atomic structures that these surface chemistries exist in.

3. Atomic-level mechanisms that drive the varying levels of cation segregation on the surfaces.

4. Relations of the resulting surface chemistry and structure to the electrochemical activity and stability.

The activation and deactivation of the oxygen evolution reaction (OER)/ORR kinetics can be in general described by the inherent electronic structure on a defect-free cathode/anode surface.[12, 13] However, the surface chemistry of the oxygen electrodes (SOEC anodes and SOFC cathodes) is complex associated with an anion sublattice and two cation sublattices, and the oxygen vacancies also play an important role on the surface activity. Furthermore, the surface of the oxygen electrodes is not static, the corresponding structure and surface chemistry (i.e., cation concentration and oxygen nonstoichiometry) are driven dynamically by the surrounding chemical environment, temperature, and oxygen partial pressure (Po_2).[14, 15, 16, 17, 18, 19, 20, 21] For example, on the surface of $La_{1-x}Sr_xMnO_3$, a widely studied perovskite-type oxide anode/cathode, the concentration of Sr-dopant cation was shown to increase with decreasing Po_2[14] and increasing temperature (greater than 500°C),[15] and the electron transfer ease (measured by tunneling conductance on the surface) was found to decrease with increasing Sr.[15] On another well-studied perovskite, $SrTiO_3$, the surface was drastically altered for both oxidizing (800 to 1000°C, 200 Torr O_2) and reducing conditions (1000°C, 10^{-8} Torr O_2) in comparison with the original stoichiometric surfaces.[22] While oxidizing conditions induced the formation of a Sr-rich Ruddlesden-Popper phase on the surface of $SrTiO_3$, reducing conditions caused the formation of Ti-rich phases such as titanium oxide and Ti_2O. The cation segregation is observed also on other oxide systems than perovskite oxides, such as the fluorite structured gadolina-doped ceria and YSZ.[23, 24, 25, 26, 27, 28]

These results in general have to be interpreted in terms of cation segregation, in some cases initiated on the perovskite lattice by simply replacing La by Sr to a larger extent than the bulk nominal Sr content, and in some cases followed by solid-state reactions at elevated temperatures, which cause the formation of new chemical phases on the surface and also influence the region underneath.

In general, a unified theory that explains the origin of the cation segregation on these complex oxide systems does not yet exist. However, the possible driving forces to segregation originate from the elastic and chemical interactions (the latter including electrostatic and polarization effects) of the dopant with the surrounding lattice. The specific mechanisms that manifest these interactions are related to the following:

1. Size mismatch between the dopant and host cations and the related elastic energy minimization by pushing the dopant to free surfaces or interfaces.[29, 30, 31, 32]

2. Space-charge theory that predicts the existence of interfacial segregation even without an ionic size mismatch[33] predominantly due to electrostatics.

3. Point defect interactions, such as the strong association of oxygen vacancies and dopant cations, that can drive the dopants to interfaces where vacancies are in abundance.[24]

Regardless of the specific driving mechanism, the segregating cation has to diffuse to the energetically preferred interface, and thus, such segregation is kinetically feasible typically at relatively high temperatures at which the cation mobility is significant. This point is of relevance to the LSC thin films that are deposited at the lower temperatures in this work, as will be discussed later in Section 4.2.3.4.

Upon Sr segregation on perovskite surfaces, as on LSC, the surface can evolve and form different atomic structures. In the simplest case, Sr replaces La on the surface[14, 34] while retaining a perovskite-terminated structure. Surface phase separations in the form of a separated oxide layer of SrO[3, 19] and Ruddlesden Popper phases, for example $(La,Sr)_2MnO_4$ on $(La,Sr)MnO_3$,[35] are also possible. The nucleation and growth of these three general forms of Sr-enriched phases are driven by the thermodynamic conditions of temperature and oxygen pressure. The activation or deactivation of OER/ORR kinetics has most often been connected to the Sr-enriched surface "composition," but not to the "structure" that the Sr enrichment can exist in. Furthermore, the transitions between such possible surface phases and their impact on the surface activity have not been shown directly and consistently. For example, even on the same electrode composition, $La_{0.6}Sr_{0.4}Co_{0.8}Fe_{0.2}O_{3-\delta}$, a commonly used oxygen electrode material, some studies have reported that the surface Sr species can block active surface sites[36] while others reported that the surface Sr enrichment due to cathodic polarization can activate the ORR kinetics.[9] Jiang et al.[18, 19] proposed that the SrO-enriched surfaces of $(La,Sr)MnO_3$ (LSM) blocks the ORR activity, but the cathodic polarization can dissolve the segregated SrO species back into the lattice and enhance the oxygen dissociative adsorption on the LSM surface. Contrary to this argument, very recently, Mutoro et al.[37] demonstrated that a small amount of secondary phase containing SrO deposited (not inherently segregated) onto LSC film surfaces can activate the electrode. Wagner et al.[38] also reported a strong enhancement of the rate for chemical surface exchange of oxygen on both undoped and Fe-doped $SrTiO_3$ thin single crystals coated with alkaline earth (Ca, Sr, Ba) oxide surface layers with physical vapor deposition. However, the physical origin behind these empirical observations is not understood. It is clear from the motivating evidence summarized above that the structure of surface Sr segregation, not only the composition, on oxygen electrodes is important in determining the OER/ORR activity; however, this is still an open question.

In this work, the purpose is to uncover the origin of the differences in the LSC electrode activity and stability induced by the synthesis and annealing temperatures. For this purpose, we systematically assessed the segregation of constituent cations, their bonding environments, and the heterogeneities of the surface microstructure and microchemistry arising from the cation segregation. The information on the

cation bonding states and the surface microstructure may connect the segregation to particular phase changes on the surface. Angle-resolved x-ray photoelectron spectroscopy was used for identifying the cation chemistry with a depth resolution from the surface. The lateral spatial distribution of cations on the nanoscale was investigated using nanoprobe auger electron spectroscopy (AES). A clear correlation of the cation segregation levels, Sr bonding environments and surface microstructures to the electrochemical activity and stability has been revealed. The inherent atomic structure of the LSC films was found to strongly affect the cation segregation tendencies near the surfaces. A structural change of the surface due to $SrO/Sr(OH)_2$-rich phase separation and the accompanying degradation of the LSC film defect chemistry and electronic structure near the surface were found responsible for the significant electrochemical deactivation of the LSC electrodes over time at elevated temperatures.

4.1.2 Experimental

The LSC films were deposited on single-crystalline (100)-oriented 5- × 5- × 0.5-mm YSZ substrates (9.5 mol% Y_2O_3, CrysTech GmbH, Germany) by pulsed laser deposition (PLD) with 50-ns laser pulses supplied by an excimer laser (Lambda Physics, COMPexPro 201) working at 248 nm and a pulse frequency of 5 Hz.[9,10] The provided fluence on the target surface was about 1.5 J cm^{-2}. A constant flow of oxygen was provided during the deposition at an oxygen pressure of 0.4 mbar. In this work, the measurements were performed on 200-nm-thick LSC films grown at 450 and 650°C, hereafter denoted as LSC_450°C and LSC_650°C, respectively, to represent the LSC films deposited at low and conventionally high temperatures.

A Veeco/Digital Instrument Nanoscope IV was used to perform tapping mode atomic force microscopy (AFM) for characterizing the surface morphology. A Physical Electronics Model 700 scanning nanoprobe AES is used to identify the surface cation content with the ability to detect lateral heterogeneities in cation compositions with high spatial resolution. Incident electrons of 10 keV and 10 nA were used for both SEM imaging and the auger electron excitation. The La *MNN*, Sr *LMM*, and Co *LMM* auger emissions were measured for quantifying the surface cation composition of the LSC films. The smoothing and differentiation of the AES spectra collected were carried out using the Savitsky-Golay algorithm.[3] Quantification of the AES differential spectra is performed using peak-to-peak intensities of the tight-scans of the noted emissions from the constituent cations. The sampling depth of these AES electrons are approximately 8.0 nm for Sr *LMM*, approximately 4.0 nm for La *MNN*, and approximately 4.5 nm for Co *LMM*. We used the standard sensitivity factors for the chemical quantification with AES, and the sensitivity factors for these emissions in the LSC films may vary from the provided standards. Therefore, rather than the absolute values of the surface chemical content, the qualitative trends should be taken into account in our AES results as a function of deposition and annealing temperatures in this study.

Angle-resolved x-ray photoelectron spectroscopy (XPS) is used to identify the cation chemistries with near-surface depth resolution on LSC films as a function of growth temperature and annealing time. The Omicron EA 125 hemispherical analyzer and Omicron DAR 400 Mg/Al dual anode nonmonochromated x-ray source were used for XPS measurements. The Sr 3*d*, La 4*d*, La 3*d*, and Co 2*p* photoelectron were analyzed. CasaXPS 2.3.15 software was used for spectral analysis and compositional quantification, Mg K-α x-ray (1253.6 eV) operated at 300 W was used in the XPS measurements reported here. While most samples were examined in their as-deposited or as-annealed conditions, when we attempted to compare the association of Sr with carbon and Co-oxidation state on the surface, the carbon contamination was removed from the surfaces of the air-exposed LSC films prior to the analysis. This was done by heating the samples in oxygen pressure of 5 × 10^{-5} mbar at 400°C for 1.5 hours in the ultra high-vacuum chamber. A resolution of approximately 1.0 eV at full width at half-maximum (FWHM) is attained. For the excitation energy of 1253.6 eV, the sampling depths of these photoelectrons at normal emission are approximately 6 nm for Sr 3*d* and La 4*d*, approximately 3 nm for La 3*d* and approximately 3 nm for Co 2*p*.[39]

The ratio of Sr/(Sr+La) was computed using the Sr $3d$ and La $4d$ emissions, La/Co was computed using the La $3d$ and Co $2p$ emissions, and both of these ratios were then used to compute the (Sr+La)/Co. By using photoelectrons with similar attenuation depths in the calculation of Sr/(Sr+La) and La/Co, possible quantitative errors caused by different attenuation depths was minimized. These spectra were measured at different emission angles, 0°, 60° and 80°, between the sample surface normal and the detector position. The measurements at larger emission angles are more surface sensitive than those at the small angles. At 60°, approximately 65% of the Sr $3d$ and La $4d$ signals, 90% of the La $3d$ signal, and 85% of the Co $2p$ signal emanate from the top 1 nm from the surface of the LSC films. To deduce differences in the chemical binding environment on LSC surfaces as a function of synthesis temperature and annealing time, the Sr $3d$, La $4d$, and Co $2p$ spectra were analyzed. Because the dominant segregating species was found to be Sr, particular attention was given to the analysis of the Sr $3d$ photoelectron spectrum.

4.1.3 Results

4.1.3.1 Surface Microstructure of As-prepared $La_{1-x}Sr_xCoO_{3-\delta}$ (LSC) Films

The LSC film morphology depends on the PLD growth temperature as shown in the AFM images of LSC_450°C and LSC_650°C (Figure 4-1). An evident observation is the increase of grain size from 450 to 650°C on the basis of nucleation theory.[40] The microstructure of the LSC_650°C films is nonuniform. The root-mean square roughnesses of these two films increase from 1.5 ± 0.3 nm on LSC_450°C to 6.0 ± 1.2 nm on LSC_650°C with some protruding grains on the film. We will show in the next section that the surface chemistry of both LSC_450°C and LSC_650°C are actually uniform despite the nonuniform microstructure of the as-prepared LSC_650°C surface.

| (a) | (b) |
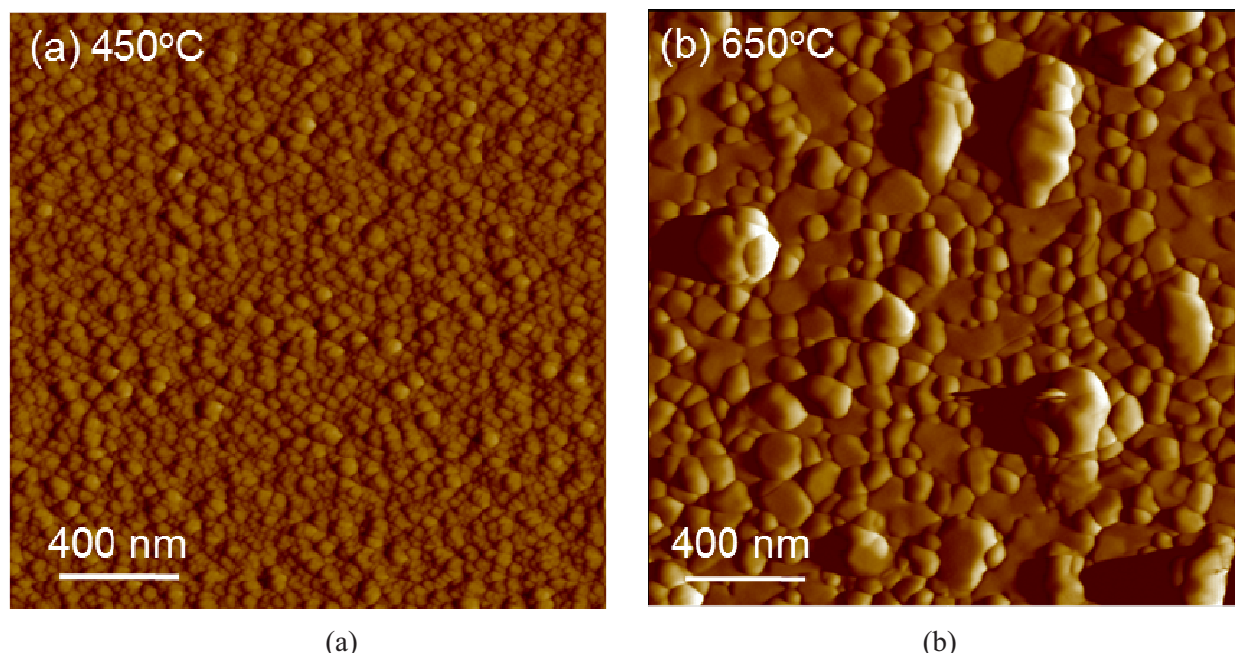
Figure 4-1. AFM images. (a) LSC_450°C with smooth and uniform microstructure. (b) LSC_650°C with varying sizes and shapes of grains on surface.

4.1.3.2 Surface Cation Chemistry of As-prepared $La_{1-x}Sr_xCoO_{3-\delta}$ (LSC) Films

The major difference in the surface chemistry of the LSC films as a function of their deposition temperature is the varying levels of Sr content on/near their surfaces. As shown in Figure 4-2, on

LSC_450°C, the Sr/(La+Sr) ratio is close to the bulk nominal value of 0.4, while for LSC_650°C, it is about 0.55, higher than nominal, suggesting Sr enrichment on the surface. Furthermore, as seen from the angle-resolved analysis of Sr/(Sr+La) from 0 to 60 degrees, LSC_450°C has a uniform Sr distribution as a function of depth in the near-surface region. LSC_650°C, on the other hand, has more Sr enrichment on the very surface, with an evident increase of Sr/(Sr+La) from 0 to 60 degrees. Both films, however, have A-site rich surfaces with a (Sr+La)/Co of 1.45 to 1.50 at an emission angle of 60 degrees, suggesting a mixed termination of A- and B-site cations on the surface of both the LSC_450°C and LSC_650°C films. The bulk composition of these films was measured by inductively coupled plasma-optical emission spectrometry, and was found very close to the nominal values (fractions of La, Sr, and Co as approximately 0.3, 0.2, and 0.5).[10] This confirms that the surface compositions found by XPS to be rich in A-site cations are related to inherent surface segregation, and are not an artifact of film growth by PLD.
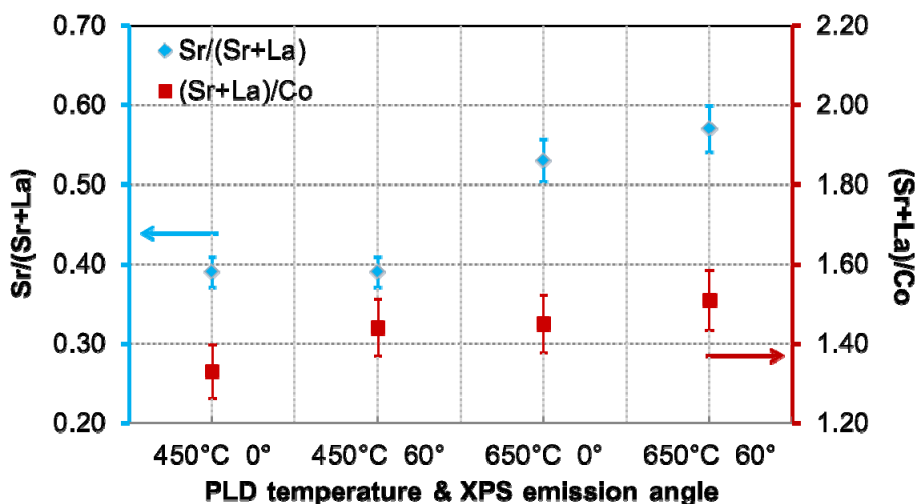
Figure 4-2. Sr/(Sr+La) and (Sr+La)/Co ratios on LSC_450ºC and LSC_650ºC, deduced from the x-ray photoelectron spectroscopy measurements at emission angles of 0 and 60 degrees.

The La $3d$, La $4d$, and Co $2p$ spectra exhibited almost the same signature on LSC_450°C and LSC_650°C at different emission angles, suggesting similar chemical bonding states of La and Co in these two samples. However, Sr $3d$ spectra showed evident differences as a function of emission angle on LSC_650°C. Because the dominant segregating species is Sr on the as-prepared state of the LSC_650°C films, particular attention was given to the analysis of the Sr $3d$ photoelectron spectrum in the rest of this report. The Sr $3d$ peak was deconvoluted to two main contributions. The Sr $3d$ doublet separation and area ratio were constrained to 1.7 eV and 1 : 0.66, respectively. The contributions to the Sr $3d$ photoelectron spectrum were found to arise from the perovskite lattice-bound Sr ($Sr_{lattice}$) at the lower binding energies (131.6 eV $\pm$ 0.2 eV for $3d_{5/2}$ and 133.3 $\pm$ 0.2 eV for $3d_{3/2}$), and from the surface-bound Sr ($Sr_{surface}$) at the higher binding energies (133.6 eV $\pm$ 0.2 eV for $3d_{5/2}$ and 135.3 $\pm$ 0.2 eV for $3d_{3/2}$). $Sr_{surface}$ is attributed to the Sr chemical environment on the surface of the LSC films because of its growing contribution at larger emission angles, as shown in Figure 4-3. The FWHM varied from 1.3 eV for $Sr_{lattice}$ to 2.0 eV for $Sr_{surface}$. We turn our attention to the chemical environment of $Sr_{surface}$ on the Sr-enriched surfaces of the LSC films, and assess whether this $Sr_{surface}$ could be attributed to the formation of species such as $SrCO_3$, SrO, and $Sr(OH)_2$.[41, 42, 43]

As shown in Figure 4-3(a), the LSC_450°C and LSC_650°C films exhibited different characteristics in the Sr $3d$ photoelectron spectra. Here, since there is almost no carbon (less than 2%) left on the surface upon cleaning the samples in the analysis chamber, $Sr_{surface}$, which constitutes a large fraction of the total Sr signal, cannot originate from $SrCO_3$. Furthermore, the Sr in the SrO structure and Sr in LSC lattice

have very similar binding energies[42] beyond the resolution limit of this experiment configuration. Therefore, the $Sr_{surface}$ is most likely originating from $Sr(OH)_2$ that may form either on the Sr of the perovskite lattice, or on the Sr of a separated SrO phase, or from the formation of the $Sr(OH)_2$ phase on/from SrO, and in all three cases the bonding environment includes a Sr-OH signature. Even though LSC_450°C surface is stoichiometric, the existence of $Sr_{surface}$ on LSC_450°C suggests the reactive nature of LSC surface with water to form Sr-OH bonds, as in the $Sr(OH)_2$ species. Given that the (Sr+La)/Co on both the LSC_450°C and LSC_650°C surfaces is 1.45 to 1.5, and a particle-free surface microstructure, we believe the $Sr_{surface}$ related to $Sr(OH)_2$ species is predominantly on the perovskite lattice on the as-prepared states of these LSC films. The $Sr_{surface}$ component of the Sr $3d$ exists to a larger extent on the LSC_650°C film surface ($Sr_{surface}/Sr_{lattice} = 1.56$) compared to that on LSC_450°C ($Sr_{surface}/Sr_{lattice} = 0.87$) [Figure 4-3(b)], and it increases significantly with increased emission angles on LSC_650°C. On the other hand, the emission angle dependence of the $Sr_{surface}/Sr_{lattice}$ on LSC_450ºC is much smaller. The enhanced presence of the $Sr_{surface}$ on LSC_650ºC is consistent with the enhanced Sr segregation on the surface (Figure 4-2) driven by the growth temperature. Later we will see that the relative contribution of this $Sr_{surface}$ component can also be used to deduce separation of SrO-rich phases upon annealing of the LSC films.

(a)   (b)
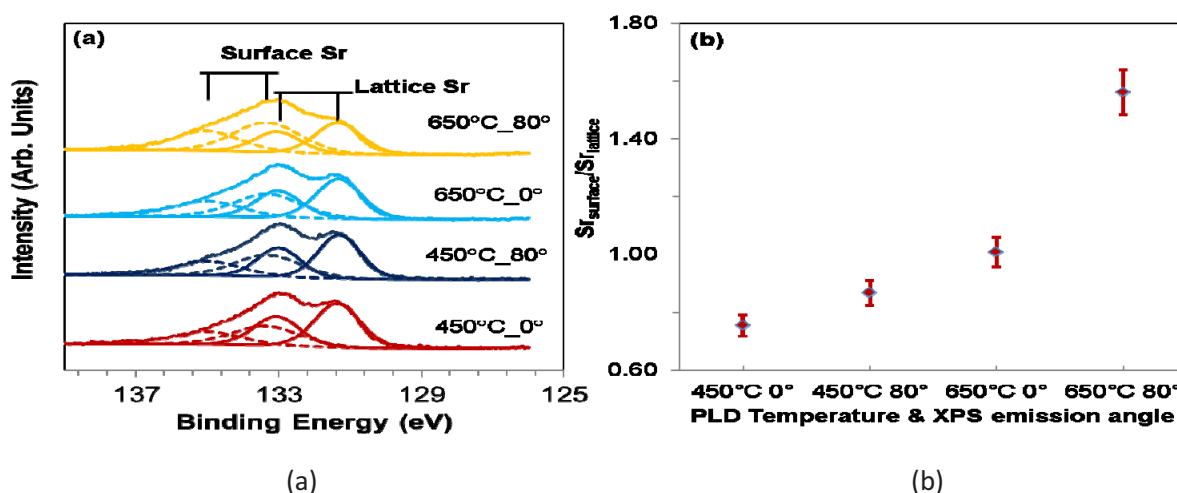
Figure 4-3. $Sr_{surface}$ attributed to Sr chemical environment on surface of LSC films because of its growing contribution at larger emission angles. (a) Sr $3d$ region of photoelectron spectra. (b) $Sr_{surface}/Sr_{lattice}$ ratio on LSC_450°C and LSC_650°C at emission angles of 0 and 80 degrees. Sr $3d$ spectra in (a) are normalized to show same highest intensity.

The depth resolution of the XPS analysis was complemented by the lateral resolution of our AES analysis to deduce whether any chemical heterogeneity is present on the surfaces of both LSC_450°C and LSC_650°C in their as-prepared states. AES nano-probe analysis was performed on five to six different regions on each sample. As exemplified in Figure 4-4, both film surfaces had spatially uniform distribution of the constituent cations in their as-prepared states. The Sr/(La+Sr) from AES point analysis is approximately 0.4 on LSC_450°C, close to its bulk nominal, and is around 0.55 on LSC_650°C, both consistent with the corresponding XPS analysis. The high (Sr+La)/Co values of 4 to 5 should only be considered in a qualitative comparison between the samples as a function of processing conditions because of the uncertainty of sensitivity factors used in this quantification. Instead, the (Sr+La)/Co from XPS are quantitatively more representative of the native surface because of the consistency of the kinetic energies of the emissions used in the compositional analysis. Even though the LSC_650°C film exhibited different grain sizes as shown in Figure 4-1, the laterally resolved AES proved similar surface chemistries on these different grains (shown in the table of Figure 4-4). This suggests that the variation on grain size and height may arise only from the different crystallographic orientations of the LSC grains compared to

the rest of the film, and secondary phases that are rich in Sr do not exist in a spatially heterogeneous form on LSC_650°C in its as-prepared state.

<center>(a)   (b)</center>

Area	LSC_450°C		LSC_650°C	
	Sr/(Sr+La)	(Sr+La)/Co	Sr/(Sr+La)	(Sr+La)/Co
1	0.39	4.43	0.55	4.86
2	0.41	4.43	0.58	4.62
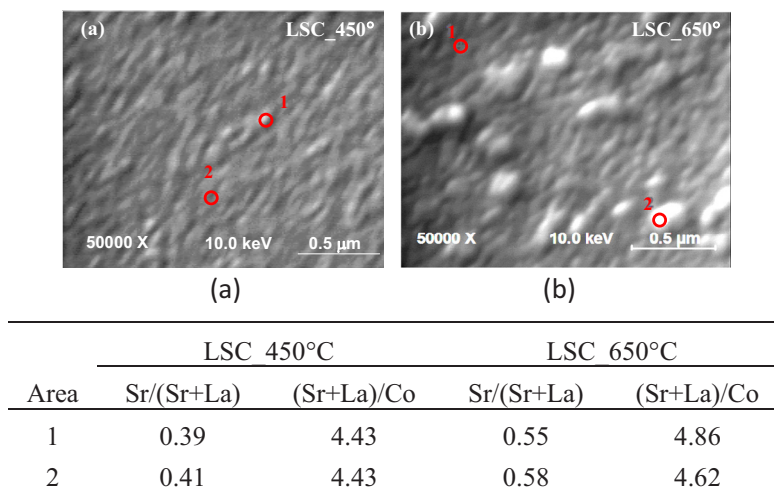
Figure 4-4. SEM image and AES point analysis on (a) LSC_450°C and (b) LSC_650°C. AES analysis showed similar chemical composition of the grains with different sizes on LSC_650°C.

  Both XPS and AES showed that the as-prepared LSC_450°C has uniform stroichiometric Sr content on the A-site, and smaller amount of Sr$_{surface}$ species in comparison to the as-prepared LSC_650°C surface. The lack of a Sr-rich surface on LSC_450°C arises likely from the kinetic limitations to cation out-diffusion at the low temperatures of its deposition, even though in theory Sr enrichment is energetically favored on these surfaces.[34, 44] Because of the laterally uniform surface cation chemistry detected by AES, and the (Sr+La)/Co ratio of 1.3 to 1.4 deduced from the XPS analysis, we believe the Sr$_{surface}$ on these as-prepared LSC films is arising from Sr(OH)$_2$ species that form on the Sr sites of the perovskite LSC surface instead of a separated SrO phase. Both the Sr/(Sr+La) and the relative presence of Sr(OH)$_2$ signature in the total Sr $3d$ signal are more enhanced on LSC_650°C. The larger presence of Sr compared to bulk nominal is consistent with the recent results from secondary ion mass spectroscopy[10] on samples equivalent to these LSC_650°C. The stoichiometric cation chemistry as reflected with a nominal Sr content, along with a smaller amount of Sr(OH)$_2$ species on the surface, can contribute to the higher oxygen reduction activity of LSC_450°C than the LSC_650°C observed by Januschewsky et al.[9] The hydroxyl species, which form when the electrodes are subjected to humidity in air during electrochemical testing, could block the catalytically active oxygen vacancy sites at the electrode surface and deteriorate the activity. A severe degradation of cathodes of similar composition as those here was reported by Hjalmarsson et al.[45] when electrochemical tests were performed in humidified air as compared to dry air.

4.1.3.3   *Surface Microstructure and Cation Segregation Induced by Thermal Annealing*

  We reported previously that the 200-nm-thick LSC films deposited at 340 to 510°C are not only more active than the LSC films of the same thickness deposited at a higher temperature (i.e., 650°C), they are also much more stable and exhibit relatively little degradation electrochemically over time at elevated temperatures.[9] To identify the chemical mechanism behind the different degradation behavior of the LSC films represented here by LSC_450°C and LSC_650°C, the samples were annealed at 600°C in air for 1, 3, and 72 hours, and subsequently subjected to XPS and AES analysis. Annealing these films at 600°C induces rougher surfaces for both films, with the root mean square roughness increased to 2.5 ± 0.5 nm for LSC_450°C and 9.0 ± 1.5 nm for LSC_650°C after 72 hours.

<center>88</center>

LSC_450°C has uniform surface morphology with increased grain size after annealing for 72 hours [Figure 4-5(a)]. The first hour of annealing induces more Sr and La on the surface [Figure 4-5(b)]. The Sr segregation level on LSC_450°C after 1 hour is about the same as that on the as-prepared LSC_650°C. The concurrent increase of Sr/(Sr+La) [Figure 4-5(b)] and the (Sr+La)/Co [Figure 4-5(c)] without an evident formation of secondary particles on the granular film surface suggests the separation and coverage of the LSC surface with a thin Sr-rich phase layer on LSC_450°C. Annealing time longer than 1 hour did not induce significantly higher Sr enrichment, as evidenced with the almost constant Sr/(Sr+La) ratio and a small increase of La/Co. The seemingly constant Sr content after 1 hour of annealing may be because the Sr content reaches its equilibrium state in the top 3 nm of XPS sampling depth for the 60-degree emission angle. Even though the total depth of the Sr enrichment layer may increase with annealing time, and thus contribute to a continuous degradation of electrochemical performance, we could not detect more Sr near the surface beyond the sampling depth of the XPS emissions used.
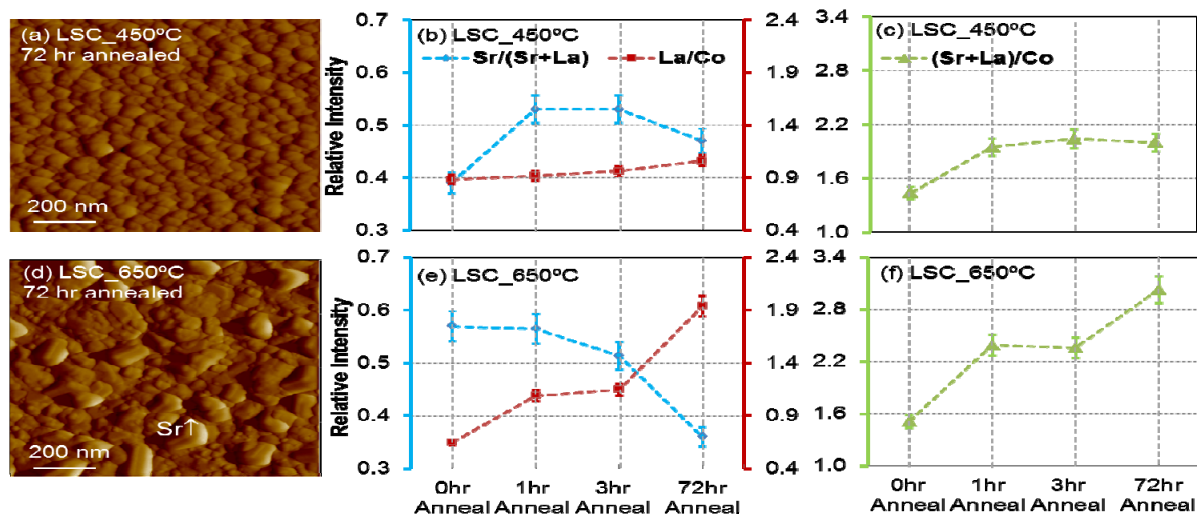
Figure 4-5. AFM images of (a) LSC_450°C and (c) LSC_650°C after annealing for 72 hours at 600°C in air. Cation ratios of Sr/(Sr+La), La/Co, and (Sr+La)/Co deduced from x-ray photoelectron spectroscopy at the emission angle of 60 degrees on LSC_450°C (b and c) and LSC_650°C (e and f) after annealing for 1, 3, and 72 hours at 600°C in air.

The LSC_650°C surface, too, exhibits a sharp increase in (Sr+La)/Co accompanied by an increase also in La/Co after 1 hour of annealing, while no change is found on the Sr/(La+Sr). Beyond the first hour, the La/Co and (Sr+La)/Co continue to increase with annealing time [Figure 4-5(e) and (f)], suggesting the depletion of Co on the surface. Furthermore, the Sr/(Sr+La) was found to "seemingly" decrease. We recall that LSC_650°C exhibits large sized and faceted crystals after annealing at 600°C for 72 hours [Figure 4-5(d)]. The apparent decrease of the Sr/(Sr+La) from XPS analysis, together with the surface morphology shown in Figure 4-5(d), may actually imply the separation and clustering of an Sr-rich phase (e.g., SrO) on the surface. This is because the local clustering of such Sr-enriched phase into particles can result in the depletion of the Sr in the near-surface areas of the film without the Sr-enriched particles, and the height of these large particles [20 to 40 nm from the height profile of AFM image in Figure 4-5(d)] is far beyond the sampling depth of XPS Sr $3d$ signal. Therefore, the clustering of Sr-rich particles actually would reduce the total Sr $3d$ emission that can be detected from them compared to the geometry where the same amount of Sr-rich phase is spread thinly on the LSC surface. This hypothesis will be further discussed in the following spatially resolved AES analysis. The main apparent difference between the surface cation composition of these LSC_450°C and LSC_650°C films as a function of time at 600°C is in the (Sr+La)/Co and La/Co ratios, which shows that less Co is left exposed on LSC_650°C compared to that on LSC_450°C.

The lateral uniformity of cation chemistry was investigated by performing AES point analysis and high-resolution mapping on both LSC_450°C and LSC_650°C after annealing for 3 and 72 hours. As its uniform surface morphology indicated [Figure 4-5(a)], LSC_450°C exhibited a laterally uniform surface cation composition, despite the cation segregation on/near the surface detected by angle-resolved XPS. However, a significantly heterogeneous cation chemistry was found laterally on LSC_650°C especially after 72 hours, differing from the larger particles to the smaller grains of the film shown in Figure 4-6(a). The AES elemental mapping with nanoscale resolution, combined with SEM, provides a detailed view of the lateral distribution of the constituent cations, La, Sr, and Co, on the LSC_650°C surface after 72 hours. It is evident from these AES elemental maps [Figure 4-6(b), (c), and (d)] that the particles on the LSC_650°C surface are Sr-rich with significantly lower La and Co contents. The lateral size of these chemical inhomogeneities is several hundred nanometers, consistent with the secondary particle/crystallite sizes shown in the AFM image of the same surface in Figure 4-6(d). On the basis of AES point analysis, we note that the Sr/(Sr+La) (approximately 0.46) and (Sr+La)/Co (approximately 4.34) on the particle-free parts of the film on the 72-hour annealed LSC_650°C is close to the near-stoichiometric surface of LSC_450°C in its as-prepared state. This shows that the particle-free region on the film became more stoichiometric upon separation of the secondary phase particles. To deduce the composition of the secondary phase particles, we use as a reference point the stoichiometric film composition with Sr:La:Co of 4:6:10 and the AES emission intensity ratios of the elements on the particles to those on the film (approximately 4:1 for the Sr signal, 5:1 for the La signal, and 3:1 for the Co signal from the intensity scale bars). From this, an Sr:La:Co ratio of approximately 16:1:3 (as a maximum) was estimated on the particles. Since a single-phase compound in equilibrium with this stoichiometry does not exist, this result suggests that these particles are made largely of SrO and/or $Sr(OH)_2$, accompanied by smaller amounts of La oxide, Co oxide, or La-Co oxide in them. In comparison to the uniform lateral distribution of cation chemistry on the as-prepared LSC_650°C [Figure 4-6(c)], upon annealing in air the separation of SrO-rich phases out of the perovskite phase near the surface is evident, while no net increase in Sr content was detected near the surface at these annealing conditions with XPS. The enhanced Sr segregation on LSC_650°C in its as-deposited condition may gradually induce SrO phase separation during thermal annealing in air, which eventually forms hydroxides. The higher oxygen pressure in air during this annealing compared to the PLD-deposition conditions may be one reason that thermodynamically favors the formation of secondary phase SrO-rich crystallites on the surface of the perovskite LSC. Such clustering of a SrO-rich phase did not occur on LSC_450°C, likely because of the poorly crystalline state of the film, which may not drive as much Sr to the surface (this will be discussed later).
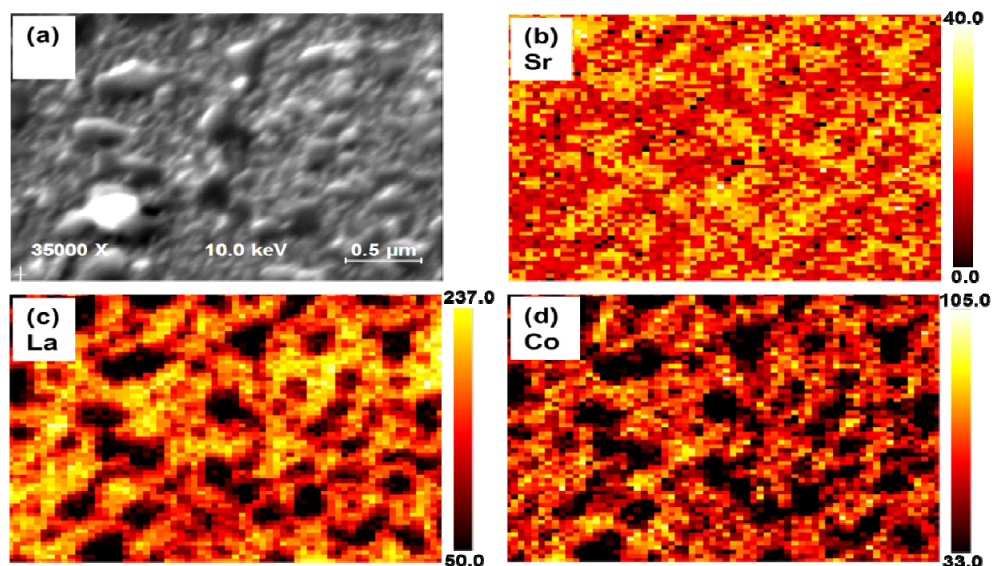
Figure 4-6. SEM image (a) and elemental maps for Sr (b), La (c), and Co (d) on LSC_650°C after annealing for 72 hours at 600°C in air. Scale bars show signal intensity, and are not a direct measure of cation content. Large particles in (a) are Sr-rich associated with low contents of La and Co.

The separation of Sr-rich phases was further confirmed by the changes in the Sr $3d$ chemical environment detected by XPS measurements on the annealed LSC_650°C surface. As shown in Figure 4-7(a) and Figure 4-7(b), the intensity of the $Sr_{surface}$ peaks increases relative to the intensity of $Sr_{lattice}$ peaks during annealing. Upon 3 and 72 hours of annealing, the $Sr_{surface}$ peaks became dominant, very different from that of the as-prepared film.[a] The changes of Sr $3d$ signature indicated different bonding states for Sr on the surface. This supports the hypothesis that, during annealing, the Sr enrichment on the perovskite structure surface may evolve to form secondary phase separation (e.g., in the form of SrO-rich phase separation). It is known that the SrO and other alkaline earth metal oxides are very reactive to water (in the form of humidity in air, for example) and form –OH species on the surface.[42, 46] Thus, here the separated SrO–rich phase may induce enhanced formation of the $Sr(OH)_2$ as the $Sr_{surface}$ species observed in XPS. $Sr(OH)_2$ in air is stable up to 1000°C before forming anhydrous SrO.[47] Therefore, this separated surface phase is expected to remain as $Sr(OH)_2$ at least on the top surface layer of these particles in ambient air at 600°C. In contrast, although the annealing induces more $Sr_{surface}$ species also on LSC_450°C, the corresponding change in the Sr $3d$ signature is not nearly as drastic as on LSC_650°C after 72 hours. Actually no change was observed in $Sr_{surface}/Sr_{lattice}$ from 3 to 72 hours on LSC_450°C. This result implies that the Sr-related restructuring is not as significant on LSC_450°C and likely more uniform, consistent with the rather smooth surface morphology (deduced from AFM) and uniform surface cation composition distribution (deduced from AES point analysis) after 72 hours of annealing. SrO is known to be a large-band-gap insulator and SrO and $Sr(OH)_2$ are not expected to facilitate electron transfer in OER/ORR.[48] The observed partial blockage of the active sites, as Co, and reduction of active surface area on LSC_650°C surface with such SrO-rich particles may be one contributor to the significant deactivation of their surface oxygen exchange kinetics during annealing.

---

[a]   Although the energy separation of the two sets of Sr peaks ($Sr_{surface}$ and $Sr_{lattice}$) became larger for the 3- and 72-hour annealed states, we used the same fitting parameters for the purpose of a consistent comparison of all states.
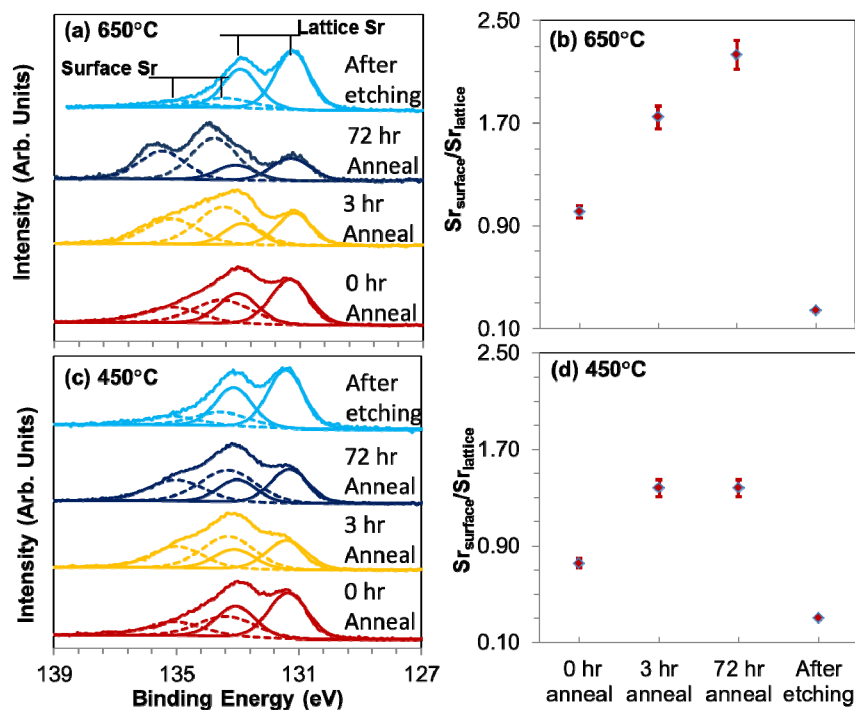
Figure 4-7. Sr 3*d* **region of photoelectron spectra and Sr$_{surface}$/Sr$_{lattice}$ ratio on LSC_650°C (a) and (b), and LSC_450°C (c) and (d), in their as-prepared (0-hour-annealed), 3-hour-annealed, 72-hour-annealed, and chemical-etched states. Sr 3***d* **spectra in (a) and (c) are normalized to show same highest intensity.**

HCl etching (0.14 mol/l for 10 s) of the 72-hour-annealed LSC_650°C and LSC_450°C removes the surface particles and segregation layer, and induces a uniform and nearly stoichiometric Sr/(Sr+La) of approximately 0.4 and (Sr+La)/Co of approximately 1.6 (from XPS) on both specimens. In addition, Sr$_{surface}$ peak intensities are found to decrease significantly after HCl etching [Figure 4-7(a) and Figure 4-7(c)]. The combined XPS and AES results show the removal of the Sr segregation layer and separated SrO/Sr(OH)$_2$-rich particles, and the exposure of a more stoichiometric LSC surface upon chemical etching.

It is worth paying attention to the changes in the binding environment of Co on the surface because this information can provide indications to the state of vacancies and electron transfer properties of the LSC surface, both of which are important in determining the surface oxygen exchange activity on the LSC films. The evolution of the Co 2p photoelectron spectra on the LSC_650°C surface as a function of annealing time is shown in Figure 4-8. The evolution of the Co 2p spectra on LSC_450°C upon annealing is qualitatively similar to the one shown in Figure 4-8. In the as-prepared state, there is a weak Co^{2+} satellite peak[49, 50] at around 786 eV. This suggests that a small amount of Co^{2+} coexisted with Co^{3+}/Co^{4+} in the near-surface region of LSC. (We note that Co^{3+} and Co^{4+} are indistinguishable from the main peaks of Co 2p photoelectron spectra, while both states are expected to exist on/in LSC at elevated temperatures). Upon annealing to 3 and 72 hours, we have shown above that a SrO-rich phase or layer forms on the LSC film surfaces, which shows separation of the Sr out of the LSC lattice upon annealing. Coincident with this process, a more dominant satellite peak feature arises at around 790 eV that is characteristic of a mixed Co^{2+} and Co^{3+} state as in Co$_3$O$_4$.[49] The more pronounced satellite feature of Co$_3$O$_4$ with thermal annealing suggests increased amount of Co^{3+} in the near-surface lattice of LSC upon Sr segregation in the form of SrO/Sr(OH)$_2$ separation. Furthermore, the FWHM of the Co 2$p_{3/2}$ main peak decreases upon annealing, and is found as approximately 2.6, approximately 2.2, and approximately 1.8 eV for the as-prepared, 3-hour-annealed, and 72-hour-annealed states, respectively. The decreased FWHM also

suggests more Co^{3+} and less Co^{2+} on the surface with annealing time, since the multiple splitting causes extensive broadening in the Co^{2+} $2p$ spectra.[39] Even though CoO has a single type of Co (octahedral Co^{2+}), its $2p_{3/2}$ is broader than that of Co_3O_4 that has two types of Co (tetrahedral Co^{2+} and octahedral Co^{3+}). The reduced amount of Co^{2+} and increased amount of Co^{3+} in the near-surface lattice of LSC have implications on the surface oxygen reduction activity through two possible mechanisms. First, the change in the oxidation state from Co^{2+} to Co^{3+} may be charge-compensated on the oxygen sublattice by accomodating a smaller amount of oxygen vacancies on the LSC surface. Second, the oxidation of Co^{2+} to Co^{3+} results in the decrease of electron density effectively in the conduction band of LSC surface, and based on a recent model by Jung and Tuller, this can have detrimental influence on the electron transfer to surface oxygen in the reduction process.[51] While both of these mechanisms can contribute to the degradation of the LSC surface activity in OER/ORR, along with the partial coverage of the surface with $SrO/Sr(OH)_2$-related blocking particles discussed above, we believe the decrease in the availability of electrons in the conduction band of LSC surface is a more detrimental factor.
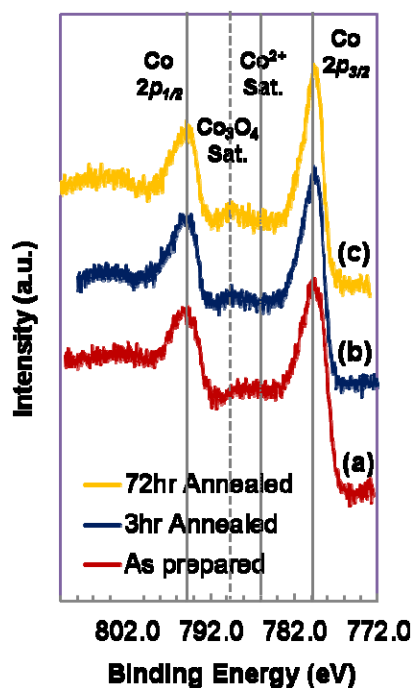
Figure 4-8. Co 2p region of the photoelectron spectra in as-prepared, 3-hour-annealed, and 72-hour-annealed states for LSC_650°C. Solid lines indicate main peak positions, dashed line indicates energy position of Co₃O₄ satellite peak, and dotted line indicates energy position of Co²⁺ satellite peak. Co 2p spectra show enhanced formation of Co³⁺ and decrease of Co²⁺ contribution upon annealing LSC_650°C in air at 600°C.

4.1.3.4   Relation of Surface Cation Chemistry to Electrochemical Activity and Stability of LSC Films

We noted in our motivation of this work that the relation of cation chemistry and surface structure to the electrochemical activity and stability of LSC thin-film electrodes has not yet been defined and understood in a complete form.[9, 10] The following three major findings from this work contribute to close this gap. The mechanisms governing the activity and stability of the LSC films deposited at low temperatures (represented by LSC_450°C) and those deposited at high temperatures (represented by LSC_650°C) are discussed in these three points, accompanied by the schematic illustration in Figure 4-9(a).

93
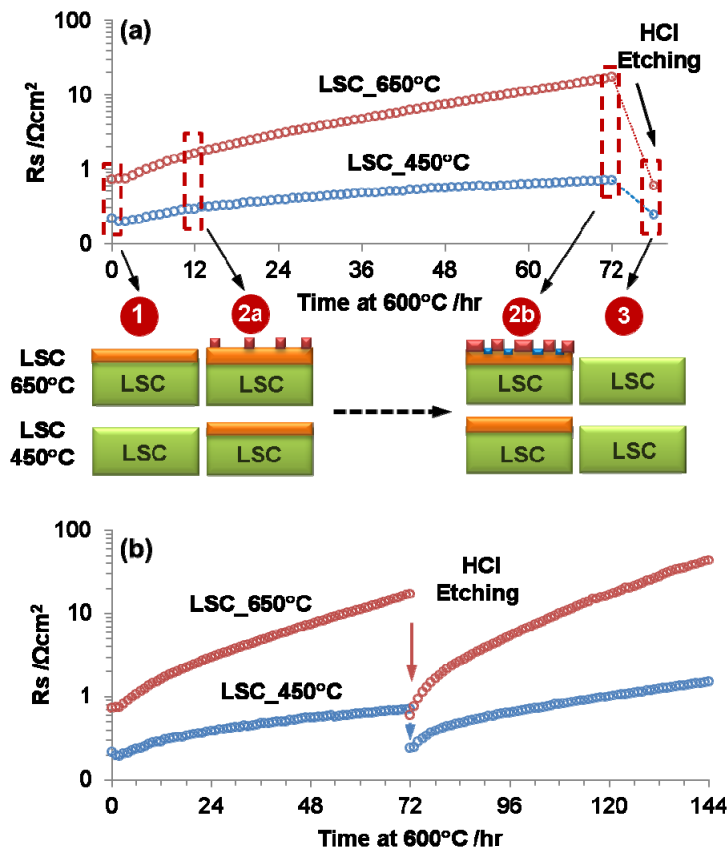
Figure 4-9. (a) Surface polarization resistance, Rs, of LSC_650°C and LSC_450°C measured by impedance spectroscopy[10] at 600°C in air and likely mechanisms that govern differences between activity and stability of these LSC films. Schematic drawing 1-3 marked the critical points correlating the surface chemistry to the electrochemical activity, as explained in the text. The green box denotes LSC bulk with a stoichiometric cation content, orange box denotes Sr enrichment in the perovskite structure, red boxes denote separated SrO-rich phases, and the blue boxes denote the particle free region with relatively reduced Sr content around SrO-rich particles. The drawing size of particles and LSC films thickness are not to scale. (b) Surface polarization resistance Rs of LSC_650°C and LSC_450°C measured at 600°C in air before and after HCl etching. After etching, LSC_650°C degrades much faster than LSC_450°C, qualitatively similar to the case in the first 72 hours of annealing before etching.

The more stoichiometric Sr/(La+Sr) and (Sr+La)/Co (also recently noted by Kubicek *et al.*[10]), the relatively small amount of $Sr(OH)_2$ environment on the surface, and the more uniform depth distribution of constituent cations may all contribute to the higher electrochemical performance of LSC_450°C than LSC_650°C in the as-prepared states. This is the case, despite the evidence that both of these LSC film surfaces are terminated by both the A- and B-site cations in a comparable way [Figure 4-2, (Sr+La)/Co], a mixed termination of the perovskite phase on the surface. The lack of a Sr-rich surface on the as-prepared state of LSC_450°C arises likely from the kinetic limitations to cation out-diffusion at the low temperatures of its deposition. At temperatures lower than 500°C, cations can be assumed immobile in the perovskite lattice.[52] The higher activity of a more stoichiometric Sr content on the LSC surface is interesting, because a higher Sr content on LSC is presumed typically to induce more oxygen vacancies as active sites on the surface. The reason for this behavior opposite to the conventional understanding of LSC surface warrants more research at the molecular and electronic structure level on such surfaces.

94

The reason for the severe time-dependent degradation of LSC_650°C during annealing at 600°C is likely governed by the phase separation of a SrO/Sr(OH)$_2$-rich structure out of the originally Sr-rich LSC phase [approximately La$_{0.4}$Sr$_{0.6}$CoO$_3$ from Figure 4-2 and Figure 4-4(a)] surface, forming a chemically heterogeneous ''skin.'' However, for LSC_450°C, since a discernable heterogeneous SrO phase separation and clustering was not found, the gradual degradation might arise from either the formation of Sr$_{surface}$ species (e.g., Sr(OH)$_2$), which block surface activity, and/or from the separation of a thin and uniformly distributed SrO layer formation accompanied by a continuous growth of the Sr-segregation depth beyond the XPS and AES sampling depths from the surface. We note that the time constant of Sr enrichment on the perovksite phase LSC surface, likely limited by cation diffusion, is on the order of less than approximately 1 hour at 600°C, shown in Figure 4-5 for LSC_450°C. This is faster than the nucleation and growth of new SrO/Sr(OH)$_2$-related phases that is nonuniformly distributed in the form of particles on the surface. There are three ways that this new surface microstructure and microchemistry can degrade the activity of the LSC_650°C films. First is the partial coverage of the LSC surface by the blocking particles, as the electronically insulating behavior of SrO is known.[53] However, from Figure 4-6, this coverage amounts up to about 50% of the apparent surface area, while the degradation of the ORR activity of LSC_650°C was shown to be two orders of magnitude increase in ASR over 72 hours of annealing at 600°C.[9] Therefore, the partial blockage of the active surface with inactive phases do not explain the significant degradation of LSC_650°C and we believe there must be a chemical reason for such significant degradation, apart from but related to such SrO/Sr(OH)$_2$-rich particles. Therefore, second, we noted that this heterogeneously-distributed phase separation actually leads to a lower level of Sr in the near-surface region of the particle-free parts of the LSC surface (as shown by our XPS and AES analysis). Reduction of the Sr level in near-surface lattice of LSC may be charge-compensated on the oxygen sublattice by decreasing the amount of oxygen vacancies on/near the LSC surface[54, 55, 56] Loss of oxygen vacancies, known as active sites for adsorption and dissociation of oxygen[57] can result in the degraded oxygen reduction kinetics on the surface. Third, and likely more importantly, a change in the oxidation state of Co from Co^{2+} to Co^{3+} was found concurrently with the SrO/Sr(OH)$_2$-phase separation out of the LSC lattice. The oxidation of Co^{2+} to Co^{3+} results effectively in the decrease of electrons as minority carriers in the conduction band of LSC surface, and can have detrimental influence on the electron transfer to oxygen in the reduction process.[52] These three major reasons can be responsible for the serious degradation of the ORR/OER activity of the LSC films at 600°C,[9, 10] represented by the annealing of LSC_650°C in this work. On the other hand, the LSC films deposited at low temperatures, represented by LSC_450°C in this work, are much more stable over time, and we believe this is because of only a thin layer of SrO/Sr(OH)$_2$-rich phase separation uniformly distributed on their surface rather than the significant and nonuniform separation found on LSC_650°C.

The recovery of the electrochemical activity after chemical etching of both LSC_450°C and LSC_650°C is because of the exposure of a stoichiometric and compositionally uniform LSC surface upon removal of the Sr segregation layer [removal of the Sr$_{surface}$ species (i.e., the separated Sr(OH)$_2$/SrO particles or layer)]. After chemical etching, both samples showed relative degradation behaviors similar to those before etching [Figure 4-9(b)], where LSC_650°C degraded much faster than LSC_450°C despite the fact that they both have similar chemical compositions and Sr bonding states after HCl etching (Figure 4-7). Therefore, the different degradation rates here are more likely related to the different structure/crystallinity among the two films and not to their initial surface chemistries. The poor crystallinity of LSC_450°C has a role in suppressing significant Sr segregation and the accompanying degradation of OER/ORR activity as discussed next.

It is important to note that the poorly crystalline state of the LSC_450°C film may actually govern the relative stability of surface chemistry and OER/ORR activity reported here at elevated temperatures. The level of disorder ranging from amorphous to fully crystalline states (dependent on the thin-film preparation method) is known to impact the bulk electrical properties of the SOFC-related materials.[58, 59]

In this work, the crystallinity of the LSC films is shown uniquely to have an impact on the evolution of LSC surface cation chemistry. We mentioned in the background of this work that the cation segregation on the oxide surfaces has its origins in the elastic and chemical/electrostatic interactions that the dopant has with the lattice. The smaller extent of Sr segregation on LSC_450°C can result from the degree of crystal disorder, which suppresses Sr-rich phase separation by accommodating the Sr cations inside the bulk lattice more easily. From the elastic strain energy point-of-view, the less dense poorly crystalline LSC_450°C can have more open space (defect sites, vacancies, nano-pores, dislocations, and their strain fields) in the lattice and this permits the larger size cation (i.e., Sr) to stay in the bulk rather than being driven strongly to the surface. A complete suppression of long-range phase separation in the amorphous phase, contrary to the crystal where decomposition is the ground state of the material system, was also shown for semiconductor alloys and explained on the basis of strain energy.[60] It is also possible that the disorder in LSC_450°C accommodates more oxygen vacancies in the bulk, and this can electrostatically attract the Sr cations more to the bulk compared to the fully crystalline state. Because of such more favorable elastic and electrostatic interactions of Sr in the bulk, we believe that the inherently disordered crystal structure of LSC_450°C actually governs the high activity and stability of the LSC surface in OER/ORR kinetics by suppressing the extensive segregation and phase separation on the surface.

4.1.4 Conclusions

This study elucidated the mechanisms that govern the differences in the OER/ORR activity and stability of LSC films induced by the thermodynamic conditions in synthesis (PLD) and annealing. XPS and AES were used to systematically assess the segregation of surface cations, their chemical bonding environments, and the changes in surface microstructure and microchemistry. We have shown that both the initial surface composition (Sr content and binding environment) of the perovskite LSC phase, and the micro-structural and micro-chemical transformations from the perovskite to secondary SrO-rich phases are directly or indirectly correlated to the electrochemical activity and stability of LSC films. The nearly stoichiometric and uniform depth distribution of constituent cations, accompanied by the relative smaller amount of hydroxide species, correlate to the higher electrochemical activity on LSC_450°C than on LSC_650°C in the as-prepared states. Upon annealing LSC_650°C in air at 600°C up to 72 hours, a structural change of the surface in the form of $SrO/Sr(OH)_2$-rich phase separation with approximately 100- to 200-nm large crystallites takes place on the initially Sr-rich LSC phase surface. The partial blockage of the surface with these phase-separated particles and the degradation of the LSC near-surface defect chemistry and electronic structure were found responsible for the severe time-dependent degradation of LSC_650°C. The oxidation of Co^{2+} to Co^{3+}, concurrent with Sr-rich phase separation, results effectively in the decrease of electrons in the conduction band of LSC surface, and can detrimentally influence the electron transfer to oxygen in the reduction process. On the other hand, the gradual and milder degradation of the LSC_450°C electrode upon annealing is not associated with severe and nonuniform surface phase separation, and rather may arise from either the enhanced formation of $Sr(OH)_2$ as $Sr_{surface}$ species and/or the gradual growth of a thin and uniformly distributed SrO-segregation layer. The full recovery of the very high electrochemical activity of both LSC_450°C and LSC_650°C after the (etching-induced) exposure of a renewed stoichiometric LSC surface testifies the favorable role of a stoichiometric cation chemistry on the OER/ORR kinetics of the perovskite structured LSC. The poorly crystalline atomic structure of the LSC deposited at low temperatures (LSC_450°C) prohibits the extensive segregation and phase separation of cations on the surface, and thus inherently governs the high activity and stability of the LSC surface in OER/ORR kinetics. A deep understanding of the relation of thermodynamic and kinetic driving forces (temperature, Po_2, electrochemical potential), as well as the material atomic structure (disorder, lattice strain) to the surface cation and anion chemistry, as demonstrated in part here but also in a broader range of materials, is essential for advancing our ability to tailor the electrochemical performance of both SOEC anodes and SOFC cathodes.

4.1.5 Acknowledgements

4.2   Mechanistic Evaluation of Degradation Processes in Solid-oxide Electrolysis Cells—University of Connecticut

4.2.1 Program Objective

The overall objective of the program is to elucidate the mechanisms of performance degradation observed in the HTSE cells. The specific focus during the reporting period has been to investigate the root cause of the observed delamination of the air electrode (anode) at the electrode/electrolyte interface in SOECs. Literature review and communications with cell fabricators indicate that Cr evaporation form stack components and balance of plant materials remain one of the major concerns for the long-term electrode deactivation and performance degradation. The possibility of using a conducting ceramic coating as a Cr blocking layer for mitigating the degradation due to Cr poisoning of the air electrode has also been evaluated.

4.2.2 First Quarter Fiscal Year 2011

4.2.2.1   Accomplishments

1. Ten electrochemical tests with air-electrode half-cells were performed, which exhibited marked differences in their long-term behavior. The tests with air electrodes comprised of pure LSM, LSM-YSZ composite, and pure LSCF compositions, and their long-term performance, delamination patterns, and chemical changes at the interfaces were analyzed.

2. Two novel hypotheses were proposed related to the chemical changes leading to anomalous shrinkage behavior or phase change in the nonstoichiometric LSM cathodes when exposed to high P_{O_2}. Select perovskite compositions were identified, which are being synthesized to validate the proposed hypotheses.

3. To reduce the variation in the long-term electrochemical testing, a new test setup was designed and assembled. The test setup uses a well-controlled vertical loading mechanism to keep the electrodes under constant load for reproducible electrochemical results.

4.2.2.2   Experimental

Degradation at the oxygen electrode-electrolyte interface was studied using half-cells, with the air electrode material on both sides of the electrolyte. This allows for simplification of the experiments because air is flowed on both sides of the cell, without any gas-tight high-temperature sealing requirements. As voltage is applied, oxygen ions are pumped through the cell, and the cell electrochemical behavior is monitored over several days. Cells were fabricated from YSZ electrolyte substrates obtained from ENrG Incorporated, Buffalo, NY. Electrode paste from Nextech Materials was subsequently screen printed on both sides of the YSZ disc using a semi-automated screen printer with 105 mesh screen, then sintered in air for 2 hours at various temperatures. Materials and sintering temperatures are listed in Table 4-1.

Table 4-1. Electrolyte and electrode materials used.

Material	Composition	Sintering Temperature (°C)
YSZ	$(ZrO2)0.92(Y2O3)0.08$	N/A
LSM	$La_{0.8}Sr_{0.2}MnO_{3-x}$	1200
LSM-YSZ	50wt% LSM, 50wt% YSZ	1200
LSCF	$(La_{0.6}Sr_{0.4})0.995(Co_{0.2}Fe_{0.8})O_{3-x}$	1000

Ag or Au mesh current collectors were attached to each electrode using Ag or Au paste. In the initial test setup, each cell was placed on top of an alumina tube inside a furnace and the Ag wires ran down the sides of the tube to beneath the furnace. Leads from a Bio-Logic VMP2 multi-channel potentiostat were attached for voltage application and impedance measurements during testing. Ag evaporation was noticed during post-test examination. As the evaporation of the current collection material may have detrimental effect on the cell performance and long-term stability, Au paste and mesh were used in the subsequent tests. To prevent the delamination of the Au mesh current collector, a new setup was designed and constructed, which applied a constant pressure on the electrodes during the entire testing period (Figure 4-10). A load of 300 to 500 g/cm^2 was applied to the SOEC button cells to assure that good electrical contact was maintained.[61] The current collection incorporated Au mesh with alumina plates with machined flow channels.
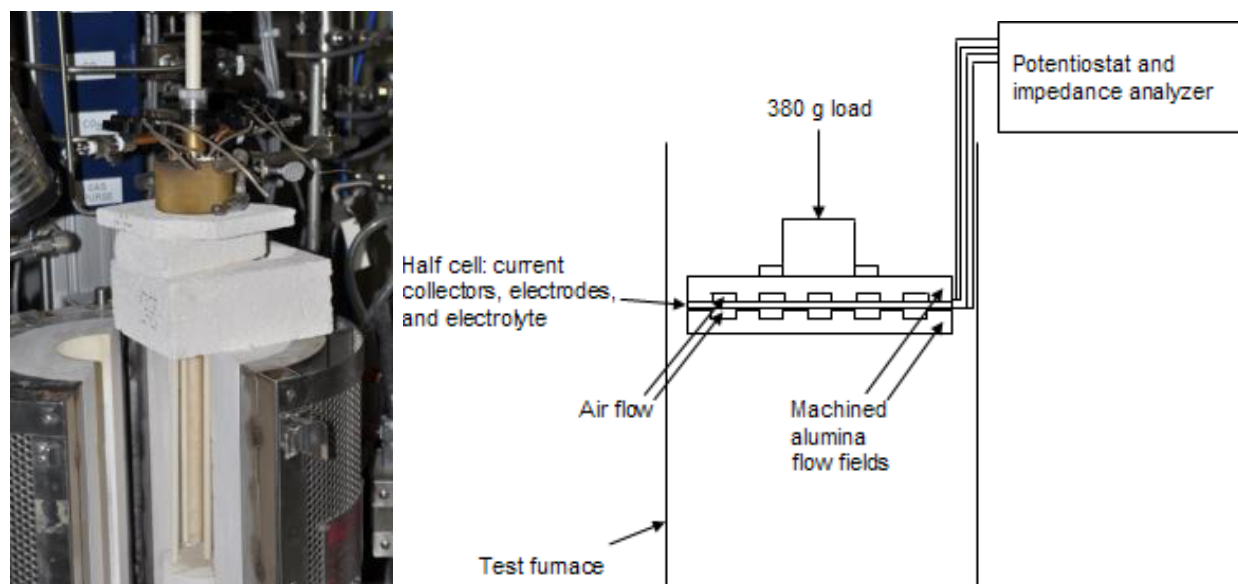
Figure 4-10. Half-cell between alumina plates (with flow channels) with alumina tube (center) applying pressure inside open furnace. Left: Photograph. Right: Schematic.

The cells were heated to the operating temperature of 840°C in flowing air. Using a potentiostat, a constant voltage was then applied for 100 hours and the cell current was monitored throughout the test. The electrochemical measurements were performed using a Bio-Logic VMP2 potentiostat. The half-cells were subjected to dc bias between 0 and 0.8 V while the electrode and electrolyte resistances were measured as a function of time by superimposing impedance spectroscopic measurements with 10-mV ac excitation voltage (Figure 4-11). Impedance measurements were taken at an interval of every 4 hours.
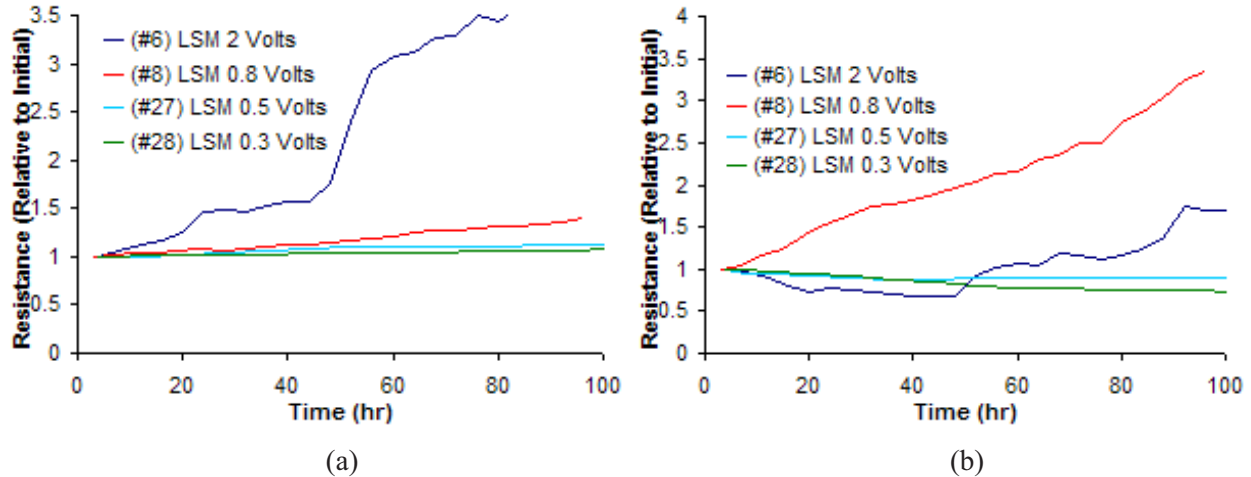
Figure 4-11. LSM electrolyte (a) and electrode (b) degradation comparison at different voltages cell-to-cell variation of electrode characteristics.

4.2.2.3   Results

The electrochemical tests with half-cells exhibited marked differences in their long-term behavior. Table 4-2 summarizes tests with LSM, LSM-YSZ, and LSCF electrodes that have been performed to-date with applied dc bias and the degree of delamination observed on the air-side electrode.

Table 4-2. Specifications for two experiments performed.

Cell No.	dc Bias (V)	Electrode Material	Maximum Current (A)	Degree of Delamination
5	0	LSM	0	None
28	0.3	LSM	0.30	None
27	0.5	LSM	0.91	None
8	0.8	LSM	1.11	None
4	0.8	LSM	1.27	Complete
14	0	LSM-YSZ	0	None
13	0.8	LSM-YSZ	2.00	None
24	0.5	LSCF	0.21	None
20	0.8	LSCF	1.43	Complete

As seen in Table 4-2, none of the three materials experienced anode delamination at dc biases less than 0.8 V. At 0.8 V, the LSM anode delaminated in only one of the two tests performed, and the LSCF anode delaminated in the single test performed. The LSM-YSZ anode did not delaminate under any testing conditions. In the cells for which delamination was observed, the anode had detached completely from the electrolyte. Resistance measurements using impedance spectroscopy are summarized in Figure 4-11. Resistances were plotted after normalizing to the first measurement, so R = 1 initially for all tests and the relative changes are plotted on the y-axis.

Figure 4-11 shows the LSM electrolyte (left) and electrode (right) resistances as a function of time and applied voltage. The rate of electrolyte degradation is directly related to the voltage in the range from 0.3 to 2 V. The rate of electrode degradation does not correlate as well with voltage, which is likely due to cell-to-cell variation of electrode characteristics.

Post-test microscopic examination revealed different microstructural features present on electrolyte surfaces. Figure 4-12 shows the electrolyte surface features developed under various conditions on cells tested with LSM electrodes. The initial electrolyte surface showed a typical dense equiaxed structure with localized isolated pores. Figure 4-12(a) represents the anode-side YSZ surface after applying 0.8 V for 100 hours. The YSZ surface in this case shows structural damage. Large pores have developed along the grain boundaries. There appear to be some "crater-like" features with surrounding small grains or particles. For comparison, the cathode surface of a 0.8-V cell is also shown Figure 4-12(b), which appears unaltered from the untested electrolyte surface under the electrode. An example of such a "finger print" at the LSM/YSZ interface after removing the cathode is also often seen in the SOFC literature.[62]

(a)   (b)
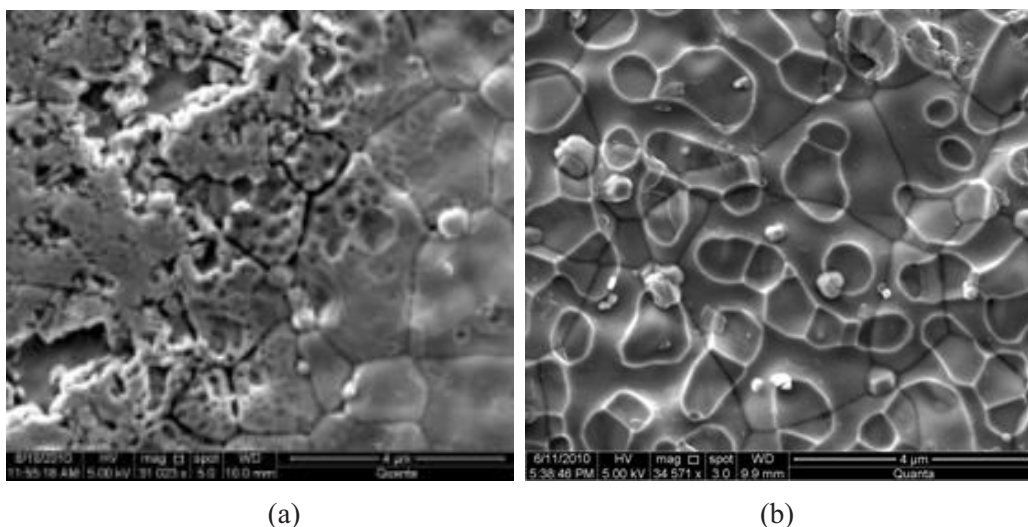
Figure 4-12. Comparison of electrolyte surface morphologies developed on LSM cells after etching with hydrochloric acid. (a) Surface in contact with anode after applying 0.8 V for 100 hours. (b) Surface in contact with cathode after applying 0.8 V for 100 hours.

4.2.2.4   *Summary and Future Work*

A correlation between anode delamination, morphology changes at the anode-electrolyte interface, and cell degradation rate has been established. However, more testing is needed to confirm the findings. Based on the testing completed to date, LSM and LSCF tend to delaminate when the applied potential is 0.8 V or higher. The mechanism of LSM delamination is hypothesized to be based on the oxygen pressure buildup at the anode-electrolyte interface and resulting chemical changes leading to anomalous shrinkage behavior or phase change in the LSM cathodes such as La-zirconate formation. The observed delamination in the LSCF is most probably due to interfacial reactions ($SrZrO_3$ formation), as well as thermal expansion mismatch.

To prevent reactions between LSCF and YSZ, a gadolinia-doped ceria interlayer will be used on future LSCF tests. This will be more representative of LSCF as used in solid-oxide cells over 800°C because the insulating reaction products severely degrade the performance of cells with no interlayer.[63]

The future work will incorporate novel approaches to study the oxygen electrode issues using a patterned microelectrode and in-situ environmental scanning electron microscope "micro-cell." In-situ experiments inside a high-temperature environmental scanning electron microscope will be designed to observe any contact morphology changes as a function of time. Our study will also employ a focused ion beam and an in-situ Omniprobe manipulator to fabricate a "micro-cell" for the electrical measurements. A "micro-cell" for simultaneous electrical and SEM observation will be comprised of small sections from the oxygen electrode/electrolyte interface, which will be cut using the focused ion beams.

To test the hypothesis that delamination may be due to anode lattice shrinkage and/or phase changes, the LSM composition with higher A-site substitution will be tested. The large A-site doping level is expected to suppress the oxygen excess behavior at high P_{O2}. It is also the intent to change a site dopant from Sr to Ca as higher Sr doping may result in the formation of insulating Sr-zirconate phase. Based on the published phase diagram, the Sr could be replaced with Ca while maintaining the desired perovskite phase.[64] A starting composition of $La_{0.5}Ca_{0.5}MnO_3$ (LCM50) will be synthesized and characterized for the air-electrode material. A suit of structural and electrochemical characterization will be used to evaluate the novel electrode composition, including x-ray diffraction (XRD), thermal expansion co-efficient, and electrochemical measurements of the total and partial conductivities as a function of various oxygen activities. The novel composition will also be tested as an air electrode in half-cell experiments using the same parameters as those already performed.

4.2.3 Second Quarter Fiscal Year 2011

4.2.3.1   Accomplishments

1. We have developed an accelerated testing methodology for the evaluation of electrode delamination and electrical performance degradation.

2. The LSM/YSZ/LSM degradation behavior at various dc load conditions has been examined and interface delamination has been analyzed for Vapplied greater than 0.3 V.

3. Our experimental study, for the first time, shows interface compound formation and morphological changes under SOEC operating conditions.

4. A novel hypothesis has been developed to explain the observed delamination pattern and performance degradation. A composition of perovskite, which maintains the hypostoichiometric composition at high P_{O2}, was identified as suitable composition to validate the hypothesis. A starting composition of $La_{0.5}Ca_{0.5}MnO_3$ was identified as promising candidate material as an air electrode for SOEC devices.

5. A variety of powder synthesis routes have been explored for the synthesis of phase pure and optimal high surface area La-Ca-manganite (LCM) powder. A chemical powder synthesis technique based on the citric acid was identified as a suitable route and the process has been scaled-up for the LCM powder preparation. LCM disks and bars have been successfully fabricated and sintered for physical and electrochemical characterization.

6. The physical, chemical, and electrochemical properties of the LCM compound have been measured using XRD, absorption surface area measurement technique (BET), thermogravimetric analysis, coefficient of thermal expansion (CTE), and electrical conductivity.

7. The first round of tests with $La_{0.5}Ca_{0.5}MnO_3$ half-cells has been completed. The $La_{0.5}Ca_{0.5}MnO_3$ half-cells also exhibited delamination; however, the mode of delamination appears to be different from the LSM cells. The cause of the observed different mode of delamination is the focus of our current study.

8. For the first time, we report the Cr evaporation behavior under the SOEC operating conditions. Our observations indicate Cr partial pressure under oxygen-rich SOEC operation conditions. The observations have been rationalized based on the thermochemical models and pertinent scale microstructure.

4.2.3.2   Background

Based on the observations from the limited long-term SOFC testing, the electrode delamination is considered as the largest contributor to cell performance degradation. The SOEC operating condition leads the delamination of the anode electrode from the electrolyte resulting in current constriction and increased ohmic loss.[65, 66, 67, 68, 69, 70, 71] This delamination is believed to be related to the evolution of oxygen at the air electrode-electrolyte interface in SOECs. Although exact reason for the origin of such delamination is not clear, a model for mechanical failure has been proposed related to the mismatch between the greater ability of zirconia to release oxygen and lesser ability of the electrode material such as LSM,[72] to conduct oxide ions away. The mismatch results from the difference in ionic conductivities of the electrolyte and air electrode materials. If this is the case, then any defect at the solid–solid interface between the two materials could serve as a nucleation point where oxygen could be released after the electron is transferred to the electrode. Under continuous operation, as more oxygen would be released into this defect, pressure would build up, and the defect would grow into a crack that would eventually cleave the perovskite–zirconia interface(s). When using a primarily electronic conducting air electrode such as LSM, oxygen can nucleate at defects on the air electrode-electrolyte interface and create high pressures in closed pores. The high oxygen pressure may cause enough interfacial tension to detach the air electrode from the electrolyte. With mixed conducting electrodes such as LSM-YSZ or LSCF, oxide ions can be conducted away from the interface as fast as they are supplied by the electrolyte, and oxygen pressure does not significantly build up.[73]

A novel hypotheses leading to "chemical failure" for the observed delamination has been proposed by the investigators, which is related to the chemical changes leading to anomalous shrinkage behavior or phase change in the LSM cathodes when exposed high P_{O_2}. The proposed model refers to the chemical changes in the LSM lattice in high P_{O_2} due to the well-known hyper stoichiometric behavior of $La_xSr_{1-x}MnO_3 + \delta$ which has an oxygen excess ($\delta > 0$).[74] This behavior results in metal ion vacancies and anomalous shrinkage of the lattice or phase change in the LSM cathodes. It is hypothesized that lattice shrinkage or phase change near the anode-electrolyte interface could cause local stresses and eventual anode detachment.[9]

To test the hypothesis that delamination may be due to anode lattice shrinkage and/or phase changes, the LSM composition with higher A-site substitution are being synthesized. The large A-site doping level is expected to suppress the oxygen excess behavior at high P_{O_2}. The experimental work progressed towards the fabrication, electrochemical testing and characterization of air electrode half-cells. The post-test microscopic and chemical analyses were performed to examine the delamination pattern and chemical changes.[75, 76]

4.2.3.3   Experimental

4.2.3.3.1 Half-cell Degradation Testing

The accelerated degradation experiments were continued using half-cell configurations. The half-cells were fabricated from YSZ electrolyte substrates procured from ENrG Incorporated, Buffalo, NY. Pure $La_{0.8}Sr_{0.2}MnO_{3-x}$ paste (Nextech Materials) was subsequently screen printed on both sides of the YSZ disc using a semi-automated screen printer with 105 mesh screen, then sintered at 1200°C in air for 2 hours. Ag mesh and wires for current collection were attached to each electrode using Ag paste. Each cell was placed on top of an alumina tube inside a furnace with Ag wires running down the sides of the tube to beneath the furnace. Leads from a Solartron Electrochemical Measurements System (Model 1287 and 1260) were attached for voltage application and impedance measurements during testing. The cells were heated to the operating temperature of 840°C in flowing air. Using the potentiostat, a constant voltage was then applied for 100 hours and the cell current was monitored throughout the test.

The electrochemical measurements were performed using the Solartron Electrochemical Measurement System (Model 1287 and 1260). The half-cells were subjected to dc bias (0 and 0.8 V) and electrode and electrolyte resistances as a function of time were measured by superimposing impedance spectroscopic measurements with 10-mV ac excitation voltage. The electrode resistance of the half-cell with 0.8-V dc bias showed drastic increase compared to the cell tested without bias. After cooldown, the anode (oxygen evolution electrode) of the 0.8-V bias cell was found completely delaminated and detached from the electrolyte. Electrolyte and electrode interfaces developed at both anodes and cathode electrodes were subsequently examined using a field emission scanning electron microscope. Electrolyte–electrode interfaces were examined after dissolution of the LSM electrode to understand the electrolyte surface morphology and XRD analysis was conducted to understand compound formation.

4.2.3.3.2 Perovskite Synthesis

The $La_{0.5}Ca_{0.5}MnO_3$ material was synthesized employing different synthetic methods such as solid-state, oxalic-adipic, and sol-gel (gelatin) methods, wherein manipulation of calcination temperatures and times, as well as the variation of chelating agents-metal cations ratio, are exploited as the tools of choice. Table 4-1 summarizes the various chemical routes that have been used to synthesize the LCM compound. The optimal particle size was found with the citric acid as the chelating agent (Figure 4-13). The $La_{0.5}Ca_{0.5}MnO_3$ material prepared by the citric acid method showed no impurities peaks (Figure 4-14).

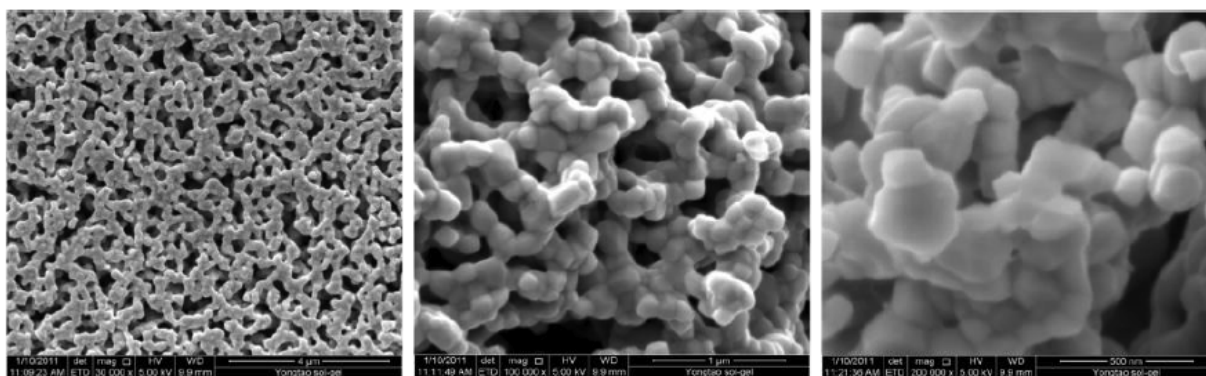**Figure 4-13. SEM micrographs of $La_{0.5}Ca_{0.5}MnO_3$ material synthesized using citric acid method at different magnifications.**

(a)   (b)
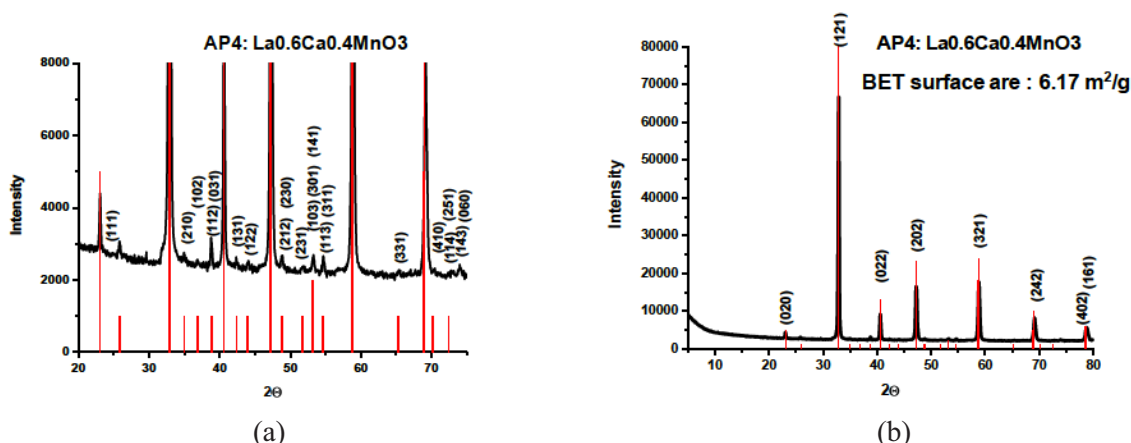
Figure 4-14. XRD pattern of $La_{0.5}Ca_{0.5}MnO_3$ synthesized using citric acid (AP4) method showing pure perovskite phase. (a) With expanded Y scale. (b) Overall XRD pattern.

4.2.3.3.3 Evaluation of Physical, Chemical and Electrochemical Properties of $La_{0.5}Ca_{0.5}MnO_3$ Material

The phase pure LCM powder was used to fabricate pellets and bars required for CTE and electrical conductivity measurements. The pellets were fabricated by pressing powder into an approximate die pressure of 3 MPa using the desktop electromotion press (MTI Corporation). The pellets were then placed in high purity alumina boats and completely covered with additional powder for protection from contamination during sintering. A firing schedule, which included 3°C/min ramp and 4 hours of dwell time at 1250°C, was used for sintering pallets. Crack-free dense samples were obtained after the sintering cycle and the conductivity specimens in the form of bars were cut from the pellet using a low-speed diamond saw (SYJ-160) (MTI Corporation).

4.2.3.3.4 Coefficient of Thermal Expansion Measurements

The CTE measurements were carried out in a Netzsch dilatometer (Model DIL 402 PC) in the temperature range of 25 to 1000°C. A pure alumina rod was used to generate the required reference file in the same temperature range.

4.2.3.3.5 Electrical Conductivity Measurements in Flowing Gas

Four shallow grooves were cut on the edges of each conductivity specimen and 5-mil Ag wires were wrapped around each groove and served as electrodes. Ag-conductive adhesive paste (Johnson Matthey, MA) was used to improve the contact between the sample and wires, thus reducing the contact resistance. The two outer leads were used to flow a steady dc current while the inner electrodes served as the voltage probes. The first set of measurements was performed in air upon heating from 600 to 800°C using steps of 25°C. At each temperature step, 30 minutes was allowed for temperature stabilization and equilibration in the gaseous atmosphere.

4.2.3.4 Results and Discussions

4.2.3.4.1 Synthesis of La-Ca-manganite (LCM) Perovskites

The selection of optimal synthesis technique for LCM powder production included two important parameters: BET surface area and powder morphology. As pallets and bars are required for the evaluation of the bulk properties of electrode material such as CTE and electrical conductivity, the powder morphology was found to be crucial for crack-free pallet fabrication. The foam-like powder morphology exhibited high BET surface area but often resulted into sample cracking during the sintering step, due to the large associated shrinkage. Among various synthesis techniques that were explored, only the citric acid method yielded high surface area, as well as appropriate particle morphology that could be utilized for pallet and bar fabrication.

4.2.3.4.2 Coefficient of Thermal Expansion Measurements

The expansion behavior for LCM bar (powder prepared from citric acid method) was studied and the coefficient of thermal expansion was determined as 12.8 ppm/°C over a range of 25 to 1000°C (Figure 4-15). The measured value of our 50% Ca-doped samples is higher than reported literature value for 30% Ca-doped sample of 10.4 ppm/°C.[19] As the CTE is expected to increase with the A-site dopant level, the higher measured CTE can be rationalized for our 50% Ca-doped samples. The air-electrode fabrication will undergo a high-temperature firing process; however, the small estimated difference in the CTE with the YSZ electrolyte of around approximately 2 ppm/°C is not expected to result into any electrode delamination.
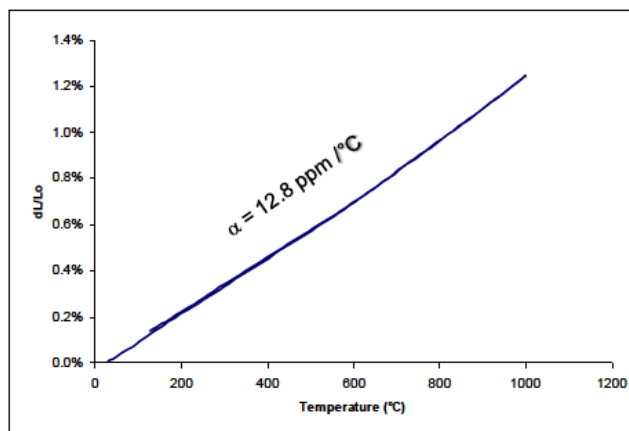
Figure 4-15. Thermal expansion behavior. La$_{0.5}$Ca$_{0.5}$MnO$_3$ material synthesized using in-house citrate process.

4.2.3.4.3 Electrical Conductivity Measurements

Figure 4-16 shows the measured electrical conductivity of in-house synthesized LCM as a function of temperature in the flowing air. The data for three other perovskite compositions from literature are also shown on the plot for comparison. The measured data for the La$_{0.5}$Ca$_{0.5}$MnO$_3$ perovsike is comparable to the literature data for La$_{0.7}$Ca$_{0.3}$MnO$_3$ and La$_{0.8}$Sr$_{0.2}$MnO$_3$. [21, 22] The measured value of 165 s/cm at 800°C is expected to be sufficient for a low spreading resistance of the air electrodes in SOEC devices.
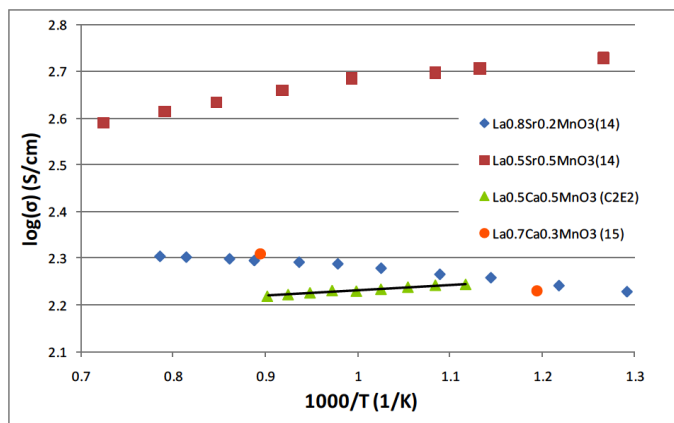
Figure 4-16. Electrical conductivity of La$_{0.5}$Ca$_{0.5}$MnO$_3$ material as function of temperature.

4.2.3.4.4 Half-cell Measurements Using La$_{0.5}$Ca$_{0.5}$MnO$_3$

LCM paste was formulated using binder V006 and solvent terpeniol (LCM powder: V006: terpeniol 54 w%: 30 w%: 16wt%) and approximately 1.0-cm diameter round electrodes were screen printed. The electrodes were sintered at 1250°C for 2 hours and Ag/Pd current collectors were applied. The long-term electrochemical testing was conducted for 100 hours at 850°C under 0.8- and 0.5-V bias conditions. Figure 4-17 shows results from two different long-term experiments. The top half of the graph shows results from a reproducibility test undertaken to study the test to test variation in the long-term electrochemical testing. All five LSM/YSZ/LSM cells were prepared and tested under identical conditions. Excellent reproducibility was exhibited by the cells as seen by the narrow spread of the long-term performance curves. The lower half of the graph shows performance from two LCM/YSZ/LCM cells that clearly show lower performance than LSM cells. At higher cell operating

voltages (simulating the accelerated testing), the degradation trend in these two groups of cells appears to be identical. Tests will be conducted at lower voltage to further differentiate the interface separation behavior.
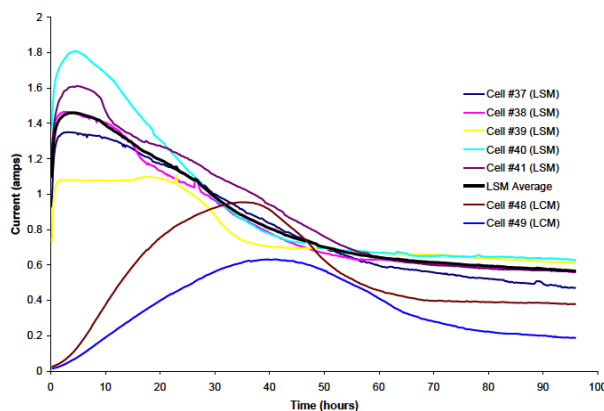
Figure 4-17. Five (5) LSM cells tested under 0.8-V conditions yield similar long-term degradation behavior. LSM20 cells exhibit superior performance and condition faster than LCM cells.

The post-test examination revealed delamination and separation of the LCM air electrodes as seen with LSM/YSZ cells. The SEM examination revealed a few "crater-like" features on the delaminated surfaces (Figure 4-18). The electrolyte surface in contact with the electrochemically active electrode showed surface deformation. The interface compound formation is postulated to be due to the presence of high dopant activity leading to the formation of reaction product. Lower dopant level followed by introduction of composite architecture is currently being developed to reduce the tendency for compound formation.
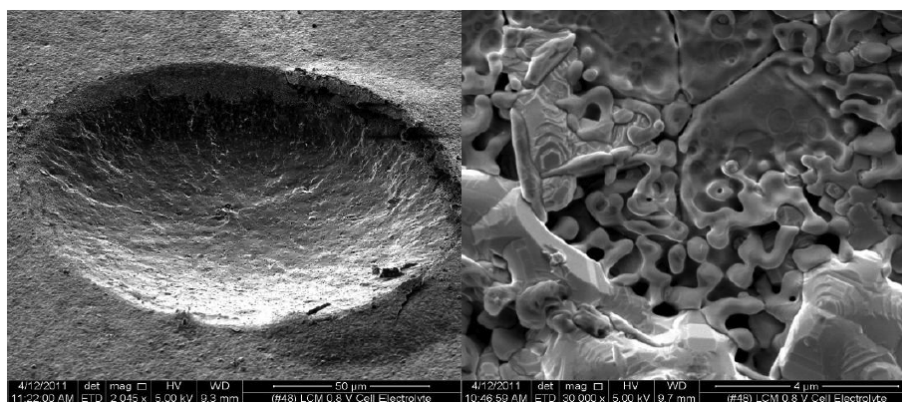
Figure 4-18. Left: Micrograph of areas on YSZ electrolyte spalled and formed crater near electrode-electrolyte interface. Right: Micrograph of electrolyte surface (near edge) contacting Ag- Pd contact paste also showed severe deformation.

A thin layer (1 μ) of Ca-zirconate was found in between the LCM electrode and YSZ electrolyte (Figure 4-19). The exact cause of the Ca-zirconate layer formation that appears to be causing the delamination is not known. Further investigation is required to understand the formation of the continuous thin Ca layer at the interface.
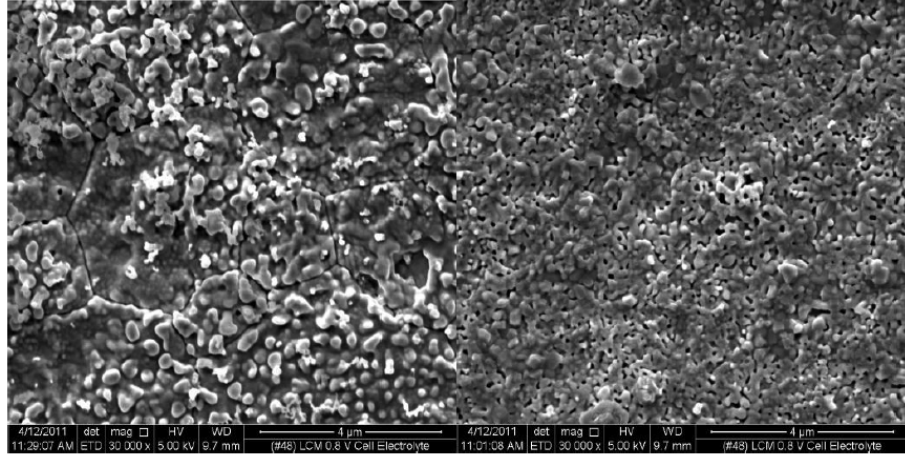
Figure 4-19. Left: Micrograph of left-over Ca-zirconate (other part peeled away with delaminated electrode). Right : Micrograph of Ca-zirconate covered area that stayed loosely adhered to electrolyte.

4.2.3.4.5 Measurements of Cr Evaporation Rate in Solid-oxide Electrolysis Cell Conditions

One of the major sources of degradation in SOEC devices has been found to be related to electrode poisoning due to Cr incorporation into the oxygen electrode and bonding layer materials. The overall degradation of the oxygen electrode is postulated to be a result of increased ohmic losses due to the formation of Cr containing phases and loss of electrochemical activity, as well as the coverage and loss of electrochemical reaction sites.

The overall process of Cr poisoning can be divided into Cr evaporation, transport, deposition, and poisoning. Both vaporization and condensation reactions are as follows:

Vaporation reaction: $Cr_2O_3(s) + H_2O(g) + O_2(g) = CrO_2(OH)_2$ (4-1)

$Cr_2O_3(s) + H_2O(g) + O_2(g) = CrO(OH)_2$ (4-2)

$Cr_2O_3(s) + O_2(g) = CrO_3(g)$ (4-3)

Condensation reaction: $CrO_2(OH)_2(g) = CrO_2(OH)_2(s)$ (4-4)

$CrO_2(OH)_2(g) = Cr_2O_3(s) + H_2O(g) + O_2(g)$ (4-5)
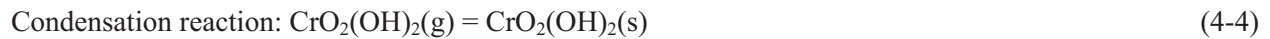
The total pressure of Cr species is expressed as: (4-6)

ΣP (total Cr containing species) $= p(CrO_3) + p(CrO_2(OH)_2) + p(CrO(OH)_2)$ (4-7)

The transpiration method has been commonly used in the measurements of Cr evaporation rate that is based on the principle that the volatile species formed over the heated sample are carried away by a constant gas flow and collected in a condenser. The masses of the transported elements are determined afterwards by quantitative chemical analysis such as inductively coupled plasma. The gaseous atmosphere around the air electrode during the operation of an SOEC device will be rich in oxygen as oxygen is produced at the air electrode during the operation of an SOEC device.

Two long-term Cr evaporation experiments (500 hours each) from SS310 (common austenitic stainless steel used in high-temperature application) has been completed in the SOEC oxygen-rich atmospheres: a) 50-50 O2-N2 (3% H_2O), and b) 90-10 O2-N2 (3% H_2O). The data are shown in Figure 4-20 that also includes the Cr evaporation rate for standard SOFC conditions. The measured high rates in the SOEC conditions agrees with the general trend reached using the thermo-chemical calculations (using HSC software).
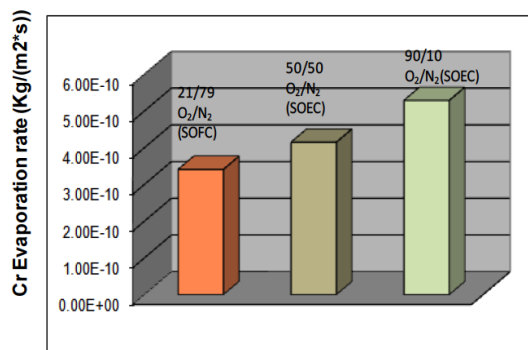
Figure 4-20. Cr evaporation rate from SS310 under different gaseous conditions.

4.2.3.5   Conclusions

1. A composition of perovskite with hypo-stoichiometric compositions at high P_{O2} was identified suitable to validate the hypothesis.

2. Various synthesis routes were explored for the synthesis of phase pure and optimal high surface area LCM powder. A chemical powder synthesis technique based on the citric acid was identified as a suitable route and the process was scaled-up for the LCM powder preparation.

3. LCM disks and bars were successfully fabricated and sintered for physical and electrochemical characterization.

4. The physical, chemical and electrochemical properties of the LCM compound were characterized using XRD, BET, thermogravimetric analysis, CTE, and electrical conductivity.

5. Electrochemical tests using "LCM half-cell" configurations show degradation of the electrode–electrolyte interface in the air electrode. Large crater formation in the electrolyte is observed.

4.2.4 Third and Fourth Quarters Fiscal Year 2011

4.2.4.1   Accomplishments

1. The Cr evaporation rate has been measured for the Mn-Co spinel-coated SS441 sample under realistic SOEC conditions. The coated sample exhibited X100 lower Cr evaporation rate compared to bare SS441.

2. Post-test examination of the Mn-Co spinel-coated sample has been completed. The growth in the mixed spinel (Mn-Co-Cr) layer at the interface has been observed.

3. A nano-composite LCM-gadolinium-doped ceria (GDC) powder has been synthesized and half-cells have been fabricated using the nano-composite powder. A number of 100-hour degradation tests have been completed. The cells exhibited low degradation and no delamination. Assessment of Ag as an air electrode for SOEC devices has been initiated. SOEC anode materials for higher performance are being further developed. Ag is currently being examined as a candidate material for establishing electrochemical processes and viability for low-temperature SOECs.

4.2.4.2   Reduction in Cr-poisoning-related Degradation in Solid-oxide Electrolysis Cells

One of the major sources of degradation in SOEC devices has been found to be related to electrode poisoning due to Cr incorporation into the oxygen electrode and bonding layer materials. The overall

degradation of the oxygen electrode is postulated to be a result of increased ohmic losses due to the formation of Cr containing phases and loss of electrochemical activity, as well as the coverage and loss of electrochemical reaction sites.

We have demonstrated 100× reduction in the Cr evaporation rate for the Mn-Co spinel-coated SS441 sample under realistic SOEC conditions (Figure 4-21). The transpiration method has been used in the measurements of the Cr evaporation rate, which is based on the principle that the volatile species formed over the heated sample are carried away by a constant gas flow and collected in a condenser. The masses of the transported elements are determined afterwards by quantitative chemical analysis such as inductively coupled plasma. The gaseous atmosphere around the air electrode during the operation of an SOEC device will be rich in oxygen as oxygen is produced at the air electrode during the operation of an SOEC.
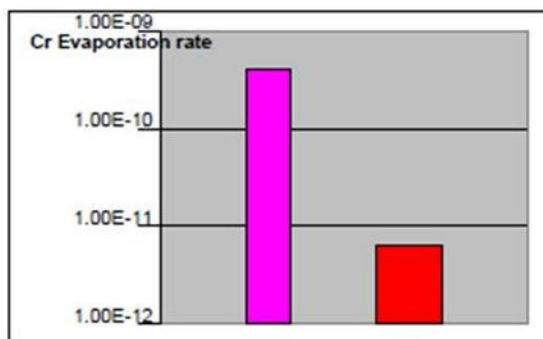
Figure 4-21. Measured Cr evaporation rate from bare SS441 and Mn-Co spinel coated SS 441 alloy at 850°C in 90%O$_2$ and 10% nitrogen gas bubbled through 3% water. (simulated SOEC conditions). A reduction of approximately 100 × in the evaporation rate has been observed.

Figure 4-22 and Figure 4-23 show surface and cross-sectional micrographs of the coated sample. There is some grain growth observed after the 500-hour-long evaporation test. Figure 4-3 shows energy dispersive x-ray spectroscopy line scans of the coated samples and growth in the mixed spinel (Mn-Co-Cr) layer at the interface was observed.
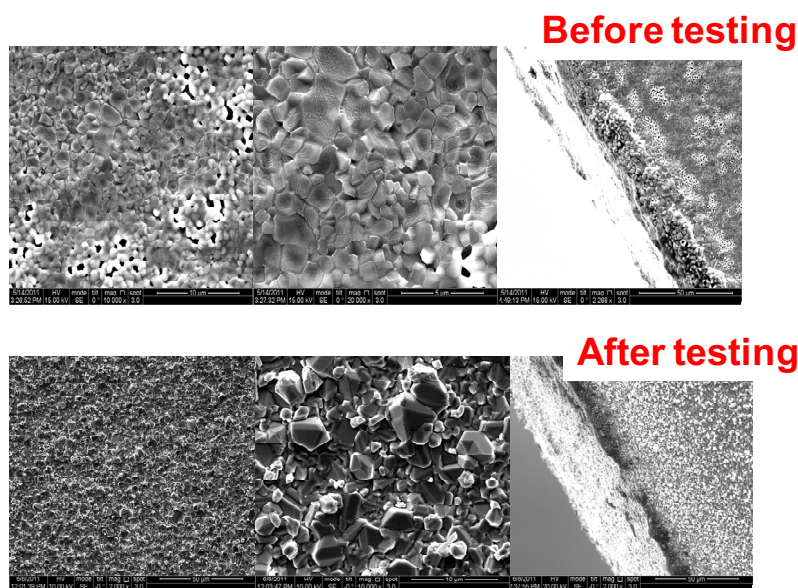
Figure 4-22. Before and after test surface and cross-sectional micrographs of Mn-Co coated sample.
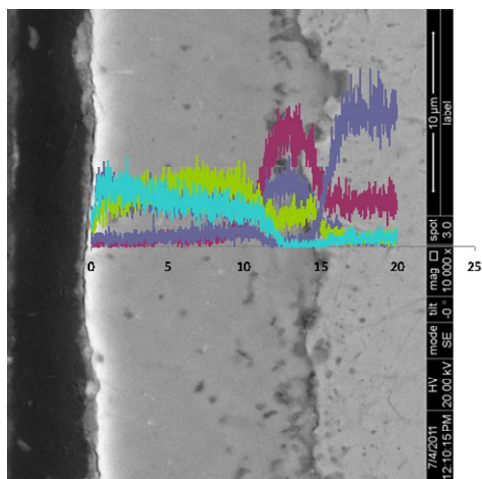
Before testing   **After testing**
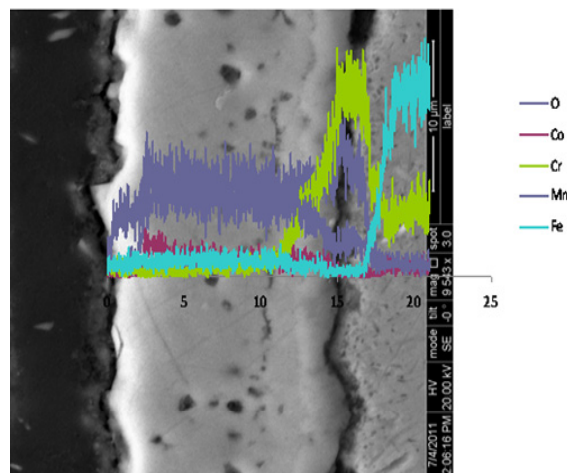
Figure 4-23. Energy dispersive x-ray spectroscopy line scan showing relative concentration of various elements in coating and adjacent area of alloy.

4.2.4.3   Electrode Materials and Electrochemical Testing

1. Synthesized and tested $La_{1-y}Sr_yMnO_{3-x}$, $La_{1-y}Sr_yFe_{1-z}Co_zO_{3-x}$, $La_{1-y}Ca_yMnO_{3-x}$, and nano-composite LCM-GDC. Electrodes under symmetric cell configuration. Long-term electrochemical performance has been measured

2. Measured physical and chemical properties: surface area, CTE, elemental composition, lattice structure, and electrical conductivity.

3. Devised a simplified symmetrical cell measurement to demonstrate that the air electrode of the SOEC that remains prone to delamination from the electrolyte surface and extensive degradation of the electrolyte bulk and interface occurs during oxygen evolution. A novel mechanism that LSM delamination is related to reactions at the anode-side LSM-YSZ interface, driven by high oxygen pressures to form La-zirconate and manganese dioxide, has been proposed. The interface becomes fragmented and weakened due to mismatch in thermal expansion coefficients and lattice volumes between the various compounds. This interfacial degradation is exacerbated by mechanical effects of the high oxygen pressure, causing gradual separation of the anode.[77, 78, 79, 80]

4. Nanocomposite of LCM50/GDC has shown significantly improved stability and performance relative to LSM (see Table 4-3).

Table 4-3. Summary of various groups of air electrode materials studied and their degradation behavior.

	$La_{0,8}Sr_{0,2}MnO_3$ (LSM)	$La_{0,8}Sr_{0,2}MnO_3$ (LCM50)	n-LCM50/GDC Composite
100-hour performance degradation	High	Very high	None
Electrode activation time	Low	High	Low
Delamination	Very severe	Severe	None
Reaction product formation	Pyrochiore	Pyrochiore	Pyrochiore

5. SOEC anode materials for higher performance are being further developed. Ag is currently being examined as a candidate material for establishing electrochemical processes and viability for low-temperature SOECs.

4.2.4.4   Conclusions

1. The Cr evaporation test on Mn-Co spinel-coated SS441 sample exhibited approximately 100× reduction in the Cr evaporation rate when compared to bare SS441.

2. The half-cells using nano-composite LCM-GDC powder have been fabricated. Three 100-hour degradation tests have been completed. The cells exhibited low degradation and no delamination. Detailed post-test examination of the cells is in progress.

3. Ag and Ag-Pd alloys will be evaluated for low-temperature SOEC application. Materials will be also used for developing a mechanistic understanding for delamination and interface morphological changes.

4.3   References

1 Jensen, S. H.; Larsen, P. H.; Mogensen, M. International Journal of Hydrogen Energy 2007, 32, 3253.

2 Hauch, A.; Ebbesen, S. D.; Jensen, S. H.; Mogensen, M. Journal of the Electrochemical Society 2008, 155, B1184.

3 Sharma, V. I.; Yildiz, B. Journal of the Electrochemical Society 2010, 157, B441.

4 Adler, S. B. Chem. Rev. 2004, 104, 4791.

5 Petrov, A. N.; Kononchuk, O. F.; Andreev, A. V.; Cherepanov, V. A.; Kofstad, P. Solid State Ion. 1995, 80, 189.

6 Kawada, T.; Yokokawa, H. Electrical Properties of Oxide Materials 1997, 125-, 187.

7 Jacobson, A. J. Chemistry of Materials 2009, 22, 660.

8 Mawdsley, J. R.; David Carter, J.; Jeremy Kropf, A.; Yildiz, B.; Maroni, V. A. International Journal of Hydrogen Energy 2009, 34, 4198.

9 Januschewsky, J.; Ahrens, M.; Opitz, A.; Kubel, F.; Fleig, J. Advanced Functional Materials 2009, 19, 3151.

10 Kubicek, M.; Limbeck, A.; Fromling, T.; Hutter, H.; Fleig, J. Journal of the Electrochemical Society 2011, 158, B727.

11 Montini, T.; Bevilacqua, M.; Fonda, E.; Casula, M. F.; Lee, S.; Tavagnacco, C.; Gorte, R. J.; Fornasiero, P. Chemistry of Materials 2009, 21, 1768.

12 Hammer, B.; Norskov, J. K. Nature 1995, 376, 238.

13 Abild-Pedersen, F.; Greeley, J.; Nørskov, J. Catal. Lett. 2005, 105, 9.

14 Fister, T. T.; Fong, D. D.; Eastman, J. A.; Baldo, P. M.; Highland, M. J.; Fuoss, P. H.; Balasubramaniam, K. R.; Meador, J. C.; Salvador, P. A. Appl. Phys. Lett. 2008, 93.

15 Katsiev, K.; Yildiz, B.; Balasubramaniam, K.; Salvador, P. A. Appl. Phys. Lett. 2009, 95.

16 Yildiz, B.; Myers, D. J.; Carter, J. D.; Chang, K.-C.; You, H. Advances in Solid Oxide Fuel Cells III: Ceramic and Engineering Science Proceedings; John Wiley & Sons, Inc., 2009.

17 Decorse, P.; Caboche, G.; Dufour, L.-C. Solid State Ion. 1999, 117, 161.

18 Wang, W.; Jiang, S. P. Solid State Ion. 2006, 177, 1361.

19 Jiang, S. Journal of Solid State Electrochemistry 2007, 11, 93.

20 Falcón, H.; Barbero, J. A.; Alonso, J. A.; Martínez-Lope, M. J.; Fierro, J. L. G. Chemistry of Materials 2002, 14, 2325.

21 Gomann, K.; Borchardt, G.; Schulz, M.; Gomann, A.; Maus-Friedrichs, W.; Lesage, B.; Kaitasov, O.; Hoffmann-Eifert, S.; Schneller, T. Physical Chemistry Chemical Physics 2005, 7, 2053.

22 Szot, K.; Speier, W. Phys. Rev. B 1999, 60, 5909.

23 Hughes, A. E.; Badwal, S. P. S. Solid State Ion. 1991, 46, 265.

24 Lee, H. B.; Prinz, F. B.; Cai, W. Acta Materialia 2010, 58, 2197.

25 Majumdar, D.; Chatterjee, D. X-ray photoelectron spectroscopic studies on yttria, zirconia, and yttria-stabilized zirconia; AIP, 1991; Vol. 70.

26 Ridder, M. d.; Welzenis, R. G. v.; Gon, A. W. D. v. d.; Brongersma, H. H.; Wulff, S.; Chu, W.-F.; Weppner, W. Subsurface segregation of yttria in yttria stabilized zirconia; AIP, 2002; Vol. 92.

27 Scanlon, P. J.; Bink, R. A. M.; van Berkel, F. P. F.; Christie, G. M.; van Ijzendoorn, L. J.; Brongersma, H. H.; van Welzenis, R. G. Solid State Ion. 1998, 112, 123.

28 Nowotny, J.; Sorrell, C. C.; Bak, T. Surf. Interface Anal. 2005, 37, 316.

29 Han, J. W.; Kitchin, J. R.; Sholl, D. S. Step decoration of chiral metal surfaces; AIP, 2009; Vol. 130.

30 Lussier, A.; Dvorak, J.; Stadler, S.; Holroyd, J.; Liberati, M.; Arenholz, E.; Ogale, S. B.; Wu, T.; Venkatesan, T.; Idzerda, Y. U. Thin Solid Films 2008, 516, 880.

31 Estrade, S.; Arbiol, J.; Peiro, F.; Infante, I. C.; Sanchez, F.; Fontcuberta, J.; de la Pena, F.; Walls, M.; Colliex, C. Appl. Phys. Lett. 2008, 93.

32 Estrade, S.; Rebled, J. M.; Arbiol, J.; Peiro, F.; Infante, I. C.; Herranz, G.; Sanchez, F.; Fontcuberta, J.; Cordoba, R.; Mendis, B. G.; Bleloch, A. L. Appl. Phys. Lett. 2009, 95.

33 Guo, X. Solid State Ion. 1995, 81, 235.

34 Jalili, H.; Han, J. W.; Kuru, Y.; Cai, Z.; Yildiz, B. J. Phys. Chem. Lett. 2011, 2, 7.

35 Dulli, H.; Dowben, P. A.; Liou, S. H.; Plummer, E. W. Phys. Rev. B 2000, 62, R14629.

36 Simner, S. P.; Anderson, M. D.; Engelhard, M. H.; Stevenson, J. W. Electrochemical and Solid-State Letters 2006, 9, A478.

37 Mutoro, E.; Crumlin, E. J.; Biegalski, M. D.; Christen, H. M.; Shao-Horn, Y. Energy & Environmental Science 2011.

38 Wagner, S. F.; Warnke, C.; Menesklou, W.; Argirusis, C.; Damjanović, T.; Borchardt, G.; Ivers-Tiffée, E. Solid State Ionics 2006, 177, 1607.

39 NIST Database 82, U.S. Department of Commerce 2001.

40 K. Byrappa, T. O. Crystal growth technology Springer, 2003.

41 Van der Heide, P. A. W. Surf. Interface Anal. 2002, 33, 414.

42 Dupin, J. C.; Gonbeau, D.; Vinatier, P.; Levasseur, A. Phys. Chem. Chem. Phys. 2000, 2, 1319.

43 Hudson, L. T.; Kurtz, R. L.; Robey, S. W.; Temple, D.; Stockbauer, R. L. Phys. Rev. B 1993, 47, 10832.

44 Piskunov, S.; Heifets, E.; Jacob, T.; Kotomin, E. A.; Ellis, D. E.; Spohr, E. Phys. Rev. B 2008, 78, 121406/1.

45 Hjalmarsson, P.; Søgaard, M.; Mogensen, M. Solid State Ion. 2008, 179, 1422.

46 Liu, P.; Kendelewicz, T.; Brown Jr, G. E.; Parks, G. A. Surface Science 1998, 412-413, 287.

47 Dinescu, R.; Preda, M. Journal of Thermal Analysis and Calorimetry 1973, 5, 465.

48 III/17B-22A-41B, C. A. a. e. o. t. v.; Madelung, O., Rössler, U., Schulz, M., Ed.; Vol. 41B: II-VI and I-VII Compounds; Semimagnetic Compounds.

49 Petitto, S. C.; Marsh, E. M.; Carson, G. A.; Langell, M. A. J. Mol. Catal. A-Chem. 2008, 281, 49.

50 Kim, J. G.; Pugmire, D. L.; Battaglia, D.; Langell, M. A. Appl. Surf. Sci. 2000, 165, 70.

51 Jung, W.; Tuller, H. L. Advanced Energy Materials 2011, n/a.

52 Horita, T.; Ishikawa, M.; Yamaji, K.; Sakai, N.; Yokokawa, H.; Dokiya, M. Solid State Ion. 1998, 108, 383.

53 S. Massidda, J. Y., and A. J. Freeman Physica (Amsterdam) 1988, 152C, 251.

54 Senarisrodriguez, M. A.; Goodenough, J. B. J. Solid State Chem. 1995, 118, 323.

55 Mineshige, A.; Kobune, M.; Fujii, S.; Ogumi, Z.; Inaba, M.; Yao, T.; Kikuchi, K. J. Solid State Chem. 1999, 142, 374.

56 Hueso, J. L.; Holgado, J. P.; Pereñíguez, R.; Mun, S.; Salmeron, M.; Caballero, A. J. Solid State Chem. 2010, 183, 27.

57 Mastrikov, Y. A.; Merkle, R.; Heifets, E.; Kotomin, E. A.; Maier, J. The Journal of Physical Chemistry C 2010, 114, 3017.

58 Tuller, H. L. Solid State Ion. 2000, 131, 143.

59 Rupp, J. L. M.; Scherrer, B.; Gauckler, L. J. PCCP Phys. Chem. Chem. Phys. 2010, 12, 11114.

60 Tzoumanekas, C.; Kelires, P. C. Journal of Non-Crystalline Solids 2000, 266-269, 670.

61 Introduction to Solid Oxide Fuel Cell Button Cell Testing. Washington, D.C.: US Fuel Cell Council's Solid Oxide Fuel Cells Focus Group, July 6, 2007.

62 Michael Keane, Atul Verma and Prabhakar Singh, Mechanistic Evaluation of Degradation Processes in Solid Oxide Electrolysis Cells (SOEC), Progress Report #1, June, 2010.

63 Kim, Wi-Heon et al. Intermediate temperature solid oxide fuel cell using (La,Sr)(Co,Fe)O3-based cathodes. Solid State Ionics 177 (2006) 3211–3216.

64 Yokokawa, Harumi et al. Recent Developments in Solid Oxide Fuel Cell Materials. Fuel Cells 1 [2] (2001) 117–131.

65 J. Herring, C. Stoots, J. O'Brien, J. Hartvigsen, G. Housley, AIChE Annual Meeting 2007, Salt Lake City, USA., 2007.

66 J. Herring, J. O'Brien, C. Stoots, G. Hawkes, J. Hartvigsen, and M. Shahnam, International Journal of Hydrogen Energy 32, 440–450, 2007.

67 J. Guan, N. Minh, B. Ramamurthi, J. Ruud, J. Hong, P. Riley, D. Weng, Final Technical Report to the U.S. Department of Energy; 2007.

68 C. Stoots, J. O'Brien, J. Hartvigsen, AIChE Annual Meeting, Salt Lake City, 2007.

69 J. Mawdsley, D. Carter, B. Yildiz, A. Call, A. Kropf, M. Ferrandon, D. Myers, V. Maroni, AIChE Annual Meeting, Salt Lake City, 2007.

70 D. Carter, J. Mawdsley, J. Kropf, V. Maroni, V. Sharma, and B. Yildiz, Workshop on the Stack Degradation, Fuel Cell Seminar, Phoenix, AZ, 2008.

71 P. Singh, L. R. Pederson, J. W. Stevenson, D. L. King, and G. L. McVay, Workshop on the Stack Degradation, Fuel Cell Seminar, Phoenix, AZ, 2008.

72 Huang, Wenhua et al. Measurement of partial oxygen ion conductivity of Sr-doped lanthanum manganite. Journal of Power Sources 173 (2007) 887–890.

73 Michael Keane, Atul Verma and Prabhakar Singh, Observations of Anode Delamination in Solid Oxide Electrolysis Cell, to be presented at 35th International Conference and Exposition on Advanced Ceramics and Composites, Daytona Beach, Florida, January, 23-28, 2011.

74 Nakamura, Keikichi. The defect chemistry of $La_{1-\Delta}MnO_{3+\delta}$. Journal of Solid State Chemistry 173 (2003) 299–308.

75 Michael Keane, Atul Verma and Prabhakar Singh, Mechanistic Evaluation of Degradation Processes in Solid Oxide Electrolysis Cells (SOEC) , Progress Report #1, June, 2010.

76 Michael Keane, Atul Verma and Prabhakar Singh, Mechanistic Evaluation of Degradation Processes in Solid Oxide Electrolysis Cells (SOEC) , Progress Report #2, December, 2010.

77 Michael Keane, Atul Verma and Prabhakar Singh, Mechanistic Evaluation of Degradation Processes in Solid Oxide Electrolysis Cells (SOEC) , Progress Report #1, June, 2010.

78 Michael Keane, Atul Verma and Prabhakar Singh, Mechanistic Evaluation of Degradation Processes in Solid Oxide Electrolysis Cells (SOEC) , Progress Report #2, December, 2010.

79 Michael Keane, Atul Verma and Prabhakar Singh, Mechanistic Evaluation of Degradation Processes in Solid Oxide Electrolysis Cells (SOEC) , Progress Report #3, June, 2011.

80 Michael Keane, Atul Verma and Prabhakar Singh, Observations of Anode Delamination in Solid Oxide Electrolysis Cell, to be presented at 35th International Conference and Exposition on Advanced Ceramics and Composites, Daytona Beach, Florida, January, 23–28, 2011.

5   COMPUTATIONAL FLUID DYNAMICS MODELING AND CODE VALIDATION

5.1   Three-Dimensional Computational Fluid Dynamics Electrochemical and Heat Transfer Model of Internally-Manifolded Solid-oxide Electrolysis Stack

5.1.1   Introduction

A three-dimensional (3-D) computational fluid dynamics (CFD) and electrochemical model has been created to model HTE cell performance and steam electrolysis in an internally-manifolded planar SOEC stack. This design is being evaluated experimentally at INL for hydrogen production from nuclear power and process heat. Mass, momentum, energy, and species conservation are numerically solved by means of the commercial CFD code FLUENT. An SOFC model adds the electrochemical reactions and loss mechanisms and computation of the electric field throughout the cell. The FLUENT SOFC user-defined subroutine was modified for this work to allow for operation in the SOEC mode. Model results provide detailed profiles of temperature, operating potential, steam-electrode gas composition, oxygen-electrode gas composition, current density, and hydrogen production over a range of stack operating conditions. Results will be presented for a five-cell stack configuration that simulates the geometry of five-cell stack tests performed at INL and MSRI. Results will also be presented for a single cell that simulates conditions in the middle of a large stack. Flow enters the stack from the bottom, distributes through the inlet plenum, flows across the cells, gathers in the outlet plenum, and flows downward making an upside-down U-shaped flow pattern. Flow and concentration variations exist downstream of the inlet holes. Predicted mean outlet hydrogen and steam concentrations vary linearly with current density, as expected. Contour plots of local electrolyte temperature, current density, and Nernst potential indicate the effects of heat transfer, reaction cooling/heating, and change in local gas composition.

Results are discussed for using this design in the electrolysis mode. Discussion of thermal neutral voltage, enthalpy of reaction, hydrogen production, cell thermal efficiency, cell electrical efficiency, and Gibbs free energy are discussed and reported herein.

A research program is under way at INL to simultaneously address the research and scale-up issues associated with the implementation of HTE for large-scale hydrogen production from nuclear energy.[1, 2] The research program includes both experimental work and CFD modeling aimed at performance characterization of electrolysis cells and stacks. Various stack configurations of electrolysis cells[3] have been analyzed showing the importance of flow distribution through large planar stacks. Previous models[4] also included consideration of externally-manifolded planar cross-flow designs. The INL research program also includes materials development tasks. In the present work, two 3-D CFD models have been created to analyze HTSE in a planar cross-flow internally-manifolded solid-oxide electrolysis stack. The first model represents a stack of five cells that simulates the geometry of five-cell stack tests performed at INL and MSRI. The second model is for a single-cell stack. Details of the model geometry are specific to cells fabricated by MSRI.[5] The MSRI cell is compared to experimental tests performed at INL.

5.1.2   Nomenclature

ASR area-specific resistance

E   voltage potential, V

F   Faraday constant, 96487 J/V-gmol

ΔG Gibbs free energy, J/gmol

ΔH	molar enthalpy of reaction, J/gmol
i	current density, A/m^2
I	current, A
j	electrons transferred per H2 molecule
$\dot{N}$	molar flow rate, gmol/s
P	pressure in stack, Pa
Q	external heat transfer, W
R	universal gas constant, J/gmol-K
T	temperature, K
V	voltage, volt
W	work, product of I*V, W
y	molar fraction

Greek Letters

| γ | molar exponent |
| η | efficiency |

Subscripts

act	activation overpotential
eff	effective
H2	Hydrogen gas
H2O	steam
max	maximum
o	open-cell
O2	Oxygen
R	reaction
ref	reference
std	standard pressure
tn	thermal neutral

5.1.3 Numerical Model and Discussion

The numerical models developed for this report are based on the geometry of a five-cell and single-cell SOEC stack designed and fabricated by MSRI and tested at INL. An illustration of the experiment test fixture is shown in Figure 5-1. Cells have a square profile with outer dimensions of 15.2 × 15.2 cm and a per-cell active area of 100 cm^2. The internally-manifolded stack is designed to operate in an upside-down U-shaped flow pattern, with the steam/H$_2$ mixture entering the inlet manifold on the bottom in the illustration in Figure 5-1. The cell operates in cross-flow where the steam/hydrogen flow direction is perpendicular to the air/oxygen flow.
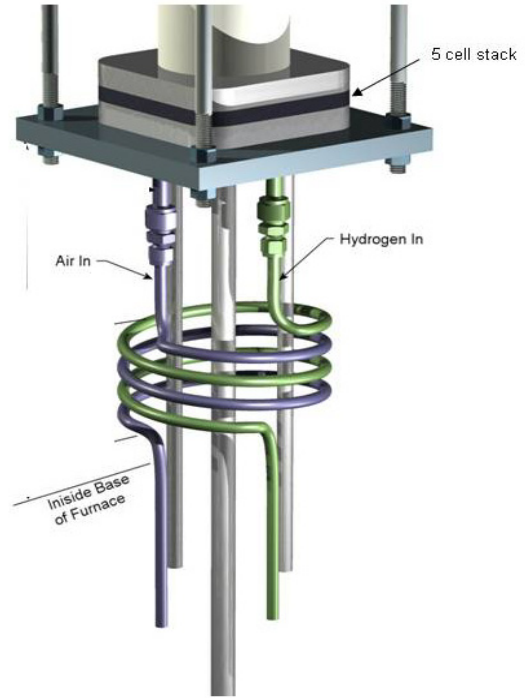
The numerical domain extends from the thick metal current collector plate on the bottom that is grounded, to the top of the upper metal current collector plate where the current is distributed. Table 5-1 depicts the layers that comprise a single cell. The typical cell repeat unit starts from the one-half thickness separator plate with various layers continuing up until the top as a one-half separator plate.

Figure 5-1. Experimental apparatus.

Table 5-1. Layers comprising repeat unit cell.

Stainless-steel separator plate (one-half thickness)

O_2 flow channel (grill)

O_2 mesh

O_2 electrode

O_2 functional layer

Electrolyte (no thickness)

H_2 functional layer

H_2 electrode

H_2 mesh

H_2 flow channel (grill)

Separator plate (one-half thickness)

The wire meshes shown in Table 5-1 serve as a method of ensuring good electrical contact between the grill and electrode and also allowing flow to distribute evenly.

The FLUENT SOFC module treats the electrolyte as a two-dimensional planar element. Therefore, the electrolyte in the model has a geometrical thickness of zero. On either side of the electrolyte are the electrodes that are created with 3-D elements. Therefore, the electrolyte/electrode assembly in the model is only as thick as the two electrodes. For this electrode-supported cell design, the missing electrolyte thickness is not significant, compared to the electrode thicknesses. The grills are modeled as an anisotropic porous media. The grills shown in Table 5-1 are described as a sheet of metal with several long slender slots cut through it that allow electrical current to be passed through and flow to be passed along the channels formed by the slots. The permeability of the square channels is calculated as $D_H^2/32$, where D_H is the hydraulic diameter. This calculation is independent of length and found by setting the pressure drop of laminar flow through a rectangular tube equal to that of a fluid in a Darcy porous media where $dP/dx = \mu u/k$, where μ is viscosity, u is velocity, and k is permeability. Reynolds numbers are very low, around 10.

The numerical grid used in this study includes a 60×60 mesh in the active cell area in the X and Y directions. Flow enters in the round tubes below the inlets and exits in the round tubes at the same height as the inlets. Each flow channel (current collector) has 10 numerical cells through its thickness, whereas each electrode has three elements through its thickness. Figure 5-2 shows a top view of the grid that is uniform in the Z direction. Grid refinement results[6] indicated good agreement with as rough as a 5×5 grid, whereas the grid for this model is 60×60 for the electrolyte area. The five-cell mesh has 3.45 million numerical cells and 3.75 million nodes. Figure 5-3 shows the mesh for the five-cell stack from a perspective view. The mesh shown in Figure 5-2 is protruded through the entire 3-D model.
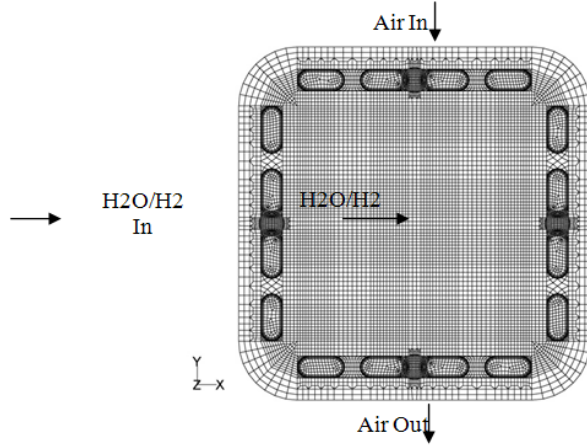
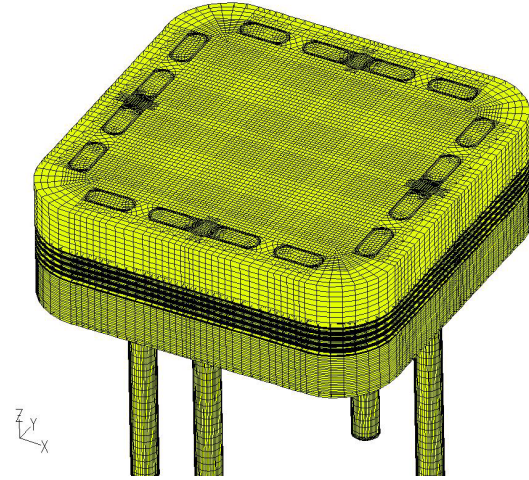**Figure 5-2. Surface mesh and flow directions.**

Figure 5-3. 3-D numerical grid.

Flow enters the domain in the steam/hydrogen inlet tube and air inlet tube at 1073 K. Each flow stream then enters a long slot plenum and is distributed through the four slot holes and then horizontally through the grills. Black body radiation to the oven is assumed for all external surfaces with an emissivity of the stainless steel specified at 0.4. This value is probably low since the surfaces all become oxidized and black in appearance. The mole fraction of hydrogen at the inlet is set at 0.50, while the steam mole fraction is set at 0.50. This set of conditions is termed "INL test," whereas MSRI suggested test conditions have the steam entering at 0.70 and hydrogen at 0.30 for mole fractions.

A voltage boundary condition of 0.0 was set on the bottom of the model and a current of -20.0 A was set on the top of the model. Details of the electrochemical model used in the FLUENT SOFC module are found in various publications from the author and in the manual itself.

Standard permeability values were specified for the electrodes along with typical values[7] for porosity and tortuosity.

In the electrolysis mode, the net heat flux to the stack is negative at low current densities, increasing to zero at the current density corresponding to the "thermal-neutral" voltage (1.287 V/cell), and positive at higher current densities. Assuming the process occurs at a specified temperature, the thermal-neutral voltage can be predicted from direct application of the First Law to the overall system:

$$Q - W = \dot{N}_{H2} \Delta H_R \tag{5-1}$$

Letting $Q = 0$ (no external heat transfer), $W=VI$, and noting that the electrical current is directly related to the molar production rate of hydrogen by

$$\dot{N}_{H2} = I / 2F \tag{5-2}$$

where F is the Faraday number (F = 96,487 J/V-gmol), yields:

$$V_{tn} = -\Delta H_R / 2F \tag{5-3}$$

Since the molar enthalpy of reaction, ΔH_R, is strictly a function of temperature (albeit a very weak function), the thermal-neutral voltage is also strictly a function of temperature, independent of cell ASR and gas compositions. The particular values of net cell heat flux at other operating voltages do however depend on cell ASR and gas compositions. The thermal-neutral voltage increases only slightly in

118

magnitude over the typical operating temperature range for steam electrolysis cells, from 1.287 V at 800°C to 1.292 V at 1000°C. Stack operation at or below the thermal-neutral voltage simplifies thermal management of the stack since excess air flow is not required. In fact, in the electrolysis mode, since oxygen is being produced, there is also no theoretical need for air flow to support the reaction at all. In a large-scale electrolysis plant, the pure oxygen produced by the process could be saved as a valuable commodity. Careful consideration must be given, however, to the choice of materials for containing pure oxygen at elevated temperatures. In addition, it may be desirable to sweep with air or some other gas to minimize the effects of any hydrogen leakage.

A thermal efficiency, η_t, can be defined for electrolysis cells, analogous to the fuel cell efficiency definition presented in textbooks on fuel cells. The thermal efficiency quantifies the heating value of the hydrogen produced by electrolysis per unit of electrical energy consumed in the stack. Based on this definition:

$$\eta_t = \frac{\Delta H_R \dot{N}_{H2}}{VI}$$

(5-4)

Eliminating the current I, the thermal efficiency can be expressed in terms of cell operating potential as:

$$\eta_t = \frac{\Delta H_R / 2F}{V} = \frac{V_{tn}}{V}.$$

(5-5)

The thermal efficiency for the fuel cell mode is the inverse of Eqn. (5). It should be noted that the value of the thermal efficiency defined in this manner for electrolysis can exceed 1.0. As an example, for the reversible stoichiometric case, the cell potential approaches reference open-cell value, $E_o = \Delta G_R / 2F$, yielding:

$$\eta_{t,\max} = \frac{\Delta H_R}{\Delta G_R}$$

(5-6)

which for steam electrolysis at 850°C is equal to 1.34. For cases with variable gas concentrations, the open-cell potential is given by the Nernst Equation, which for the hydrogen/oxygen/steam system takes the form:

$$E = E_o - \frac{RT}{jF} \ln \left[\left(\frac{y_{H2O}}{y_{H2} y_{O2}^{1/2}} \right) \left(\frac{P}{P_{std}} \right)^{-1/2} \right]$$

(5-7)

FLUENT calculates the activation over-potential by the following set of equations. The parameter i_{0ref} is set at 1e4 A/m^2 for the oxygen electrode and 1e8 A/m^2 for the hydrogen electrode.[6] FLUENT treats this effective current density as:

$$i_{0eff} = i_{0,ref} (Y_j)^\gamma$$

(5-8)

where (Y_j) is the mole fraction and γ is the concentration exponent set to 0.5. With i being the local current density, the activation potential for the cathode and anode can then be calculated as:

$$V_{act} = \frac{2RT}{jF} \sinh^{-1} \left(\frac{i}{i_{0eff}} \right)$$

(5-9)

5.1.4 Results

Results of the FLUENT simulations are presented in Figure 5-4 through Figure 5-17. Figure 5-4 shows the operating voltage versus current for two different sets of conditions. Experimental results will be compared in future publications. The first condition corresponds to the INL test condition with a steam inlet mole fraction of 0.5. The second condition is the MSRI-suggested setup with an inlet steam mole fraction of 0.7. In both cases, the remaining flow is hydrogen. A sweep of various currents was performed for both conditions from -20.0 to 5.0 A. This was done by performing a simulation for each current shown in Figure 5-4. The activation over-potential is very low for these planar cells as noted in previous articles by the author and experimenters at INL.[8] This is modeled by setting the exchange current density i_{0eff} to a large value of 1e8 in the model. Experimental sweeps also show linear behavior from the fuel cell to electrolysis modes, indicating very small activation over-potential.

Figure 5-5 shows a temperature contour plot of the outside of the cell at -20.0 A. The thick current collector top plate is cooler in the center due to the endothermicity of the reaction at -20.0 A. Some temperature smoothing has taken place between the cells and the top of the thick top plate, as the cells are cooler than the top of the plate at this condition (below thermal neutral). Black body radiation to the oven is assumed with an emissivity of 0.4 for all external surfaces. This is the only radiation heat transfer boundary condition in the model. The five cells are hotter than the thick stainless plates as they are insulated. Shown in Figure 5-6 are the temperature contours of a plane through one of the five electrolytes. Steam/hydrogen enters from the left and air/oxygen enters from the top. The top left corner is the most favorable region for the reaction to occur as it has the highest steam concentration and lowest oxygen concentration as shown in Eqn. (7).

Stack voltage contours are displayed in Figure 5-7 for the ground, five oxygen-side current collectors, and current tap on the top. The per cell voltage at -20.0 A is 5.20/5, or 1.04 V. To achieve thermal neutral conditions for this cell, a voltage of 5*1.287 V, or 6.435 V would be required. This would correspond to a large negative current according to Figure 5-4.
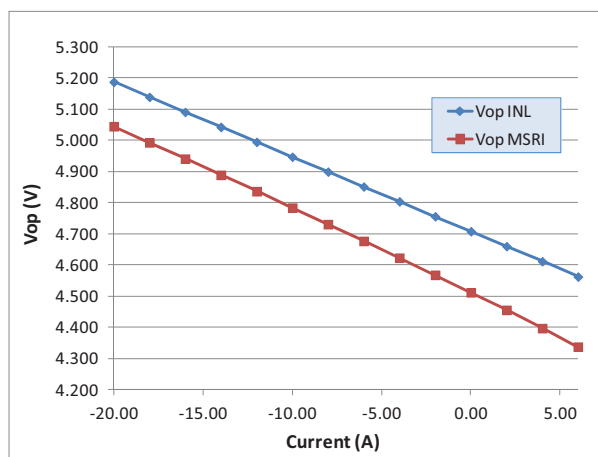

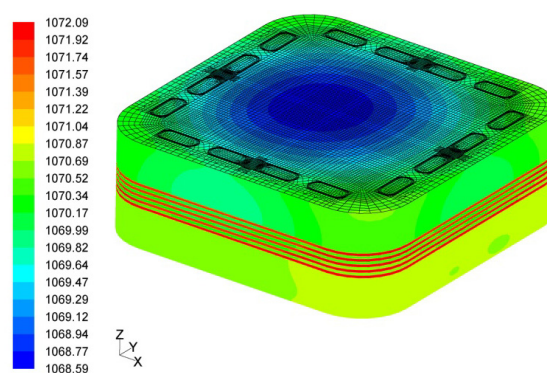**Figure 5-4. Operating voltage versus current for INL and MSRI test conditions.**

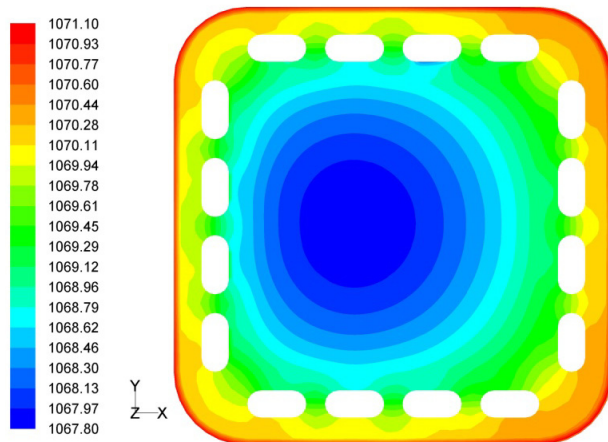**Figure 5-5. 3-D temperature contours (K) at -20.0 A.**

Figure 5-6. Temperature contours (K) on electrolyte plane at -20.0 A.
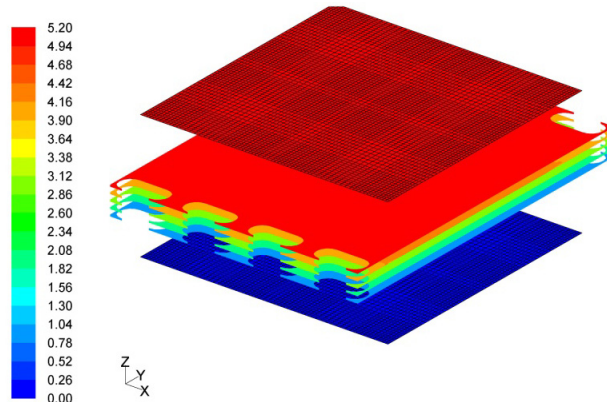

Figure 5-7. Voltage contours (V) at -20.0 A for ground, five separator plates, and current tap (on top).

Figure 5-8 shows the hydrogen mole fraction contours as the flow passes through the cells. A mole fraction of 0.50 for hydrogen and steam is imposed in the inlet stream. For this current of -20.0 A, a hydrogen mole fraction of 0.70 is achieved at the exit of the cells. This corresponds to a mole fraction varying from 0.50 for the steam down to 0.30 as shown in Figure 5-9. The interesting note about these contour plots are the waves that appear as the flow passes through the cell. The flow comes out of the four inlet plenum holes and disperses across the cell active area. The only path to disperse to the areas between the holes is through the sideways path of the wire mesh. The flow into this area between the holes is most notable at the inlet and outlet areas as this is where the flow is trying to get into and out of these areas. These contour plots also indicate that the flow is evenly distributed between the five cells on the steam/hydrogen side and the air/oxygen side. Parametric studies were performed on the x-y anisotropic permeability in the wire mesh. It is possible to impose such a small permeability in the wire mesh as to allow virtually no flow into this region, or to flow in very easily. A permeability of 1e-6 m^2 was input for the y and z directions for the wire mesh and 1e-4 m^2 for the x direction for the steam/hydrogen grill.
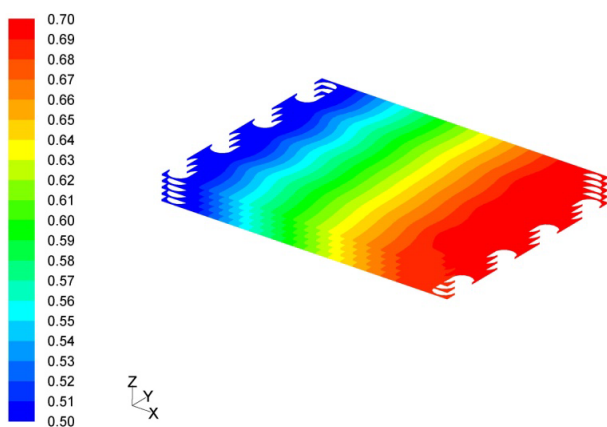

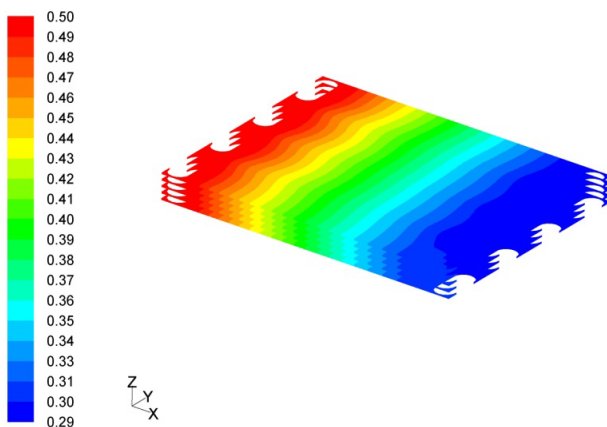**Figure 5-8. Hydrogen mole fraction for INL test conditions at -20.0 A.**

Figure 5-9. Steam mole fraction at -20.0 A for INL test conditions.

Figure 5-10 shows the mole fraction of the oxygen on the air/oxygen side. Air comes in with a mole fraction of 0.21 and exits around 0.26. The highest oxygen concentration is in the bottom left corner as the most favorable area for the reaction is the top left corner. As the air/oxygen flows across the cell, the oxygen concentration increases.

Pressure contours (gauge pressures) are plotted in Figure 5-11 and Figure 5-12 for the steam/hydrogen and air/oxygen current collectors, respectively. Again it is difficult for the flow to enter the dead regions between the inlet holes and also difficult to exit these dead regions near the exit holes thus causing the waviness evident in the pressure contours. The magnitudes of the pressures are very small across the cell, only 160 and 330 Pa.
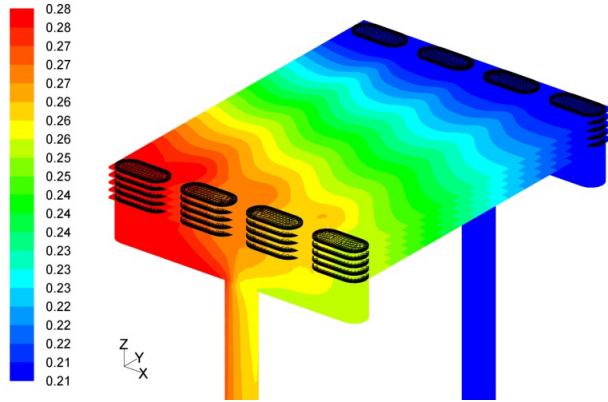

Figure 5-10. Oxygen mole fraction at -20.0 A with inlet and outlet tubes and plenums plotted.
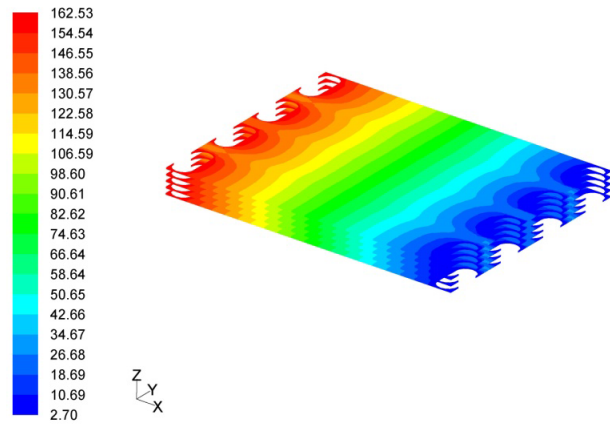

Figure 5-11. Pressure contours (Pa) on steam/hydrogen side at -20.0 A.

Velocity vectors are plotted in a zoomed-in view of the inlet holes with the wire mesh areas in Figure 5-13. The velocity vectors show the flow entering into the dead region between the holes. This view is from the center two holes as the inlet tube is impinging directly between the two holes with most of the flow directly in line with the inlet tube.
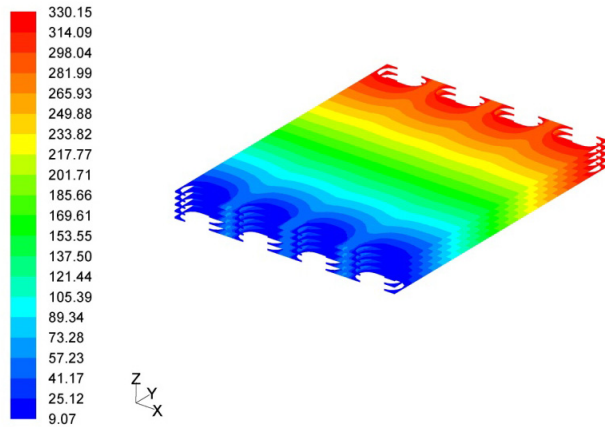

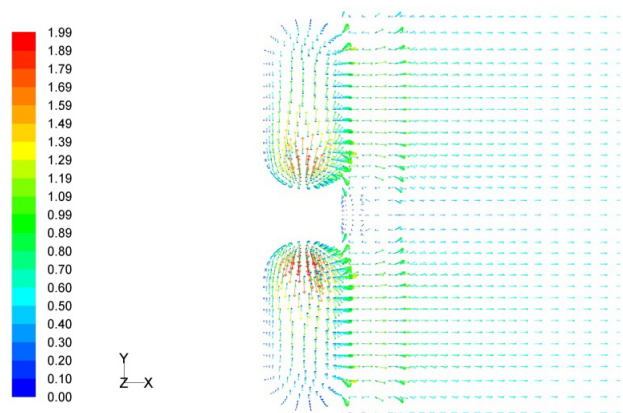**Figure 5-12. Pressure contours (Pa) on air/oxygen side at -20.0 A.**

Figure 5-13. Velocity vectors (m/s) in inlet holes and wire mesh on steam/hydrogen side at -20.0 A.

Figure 5-14 shows pathlines of the steam/hydrogen flowing through the inlet tubes, through the inlet plenum and inlet holes, then flowing across the cells, and gathering in the outlet holes, outlet plenum, and outlet tube. Figure 5-15 reveals a recirculation pattern of the pathlines in the inlet plenum before it flows through the cells.
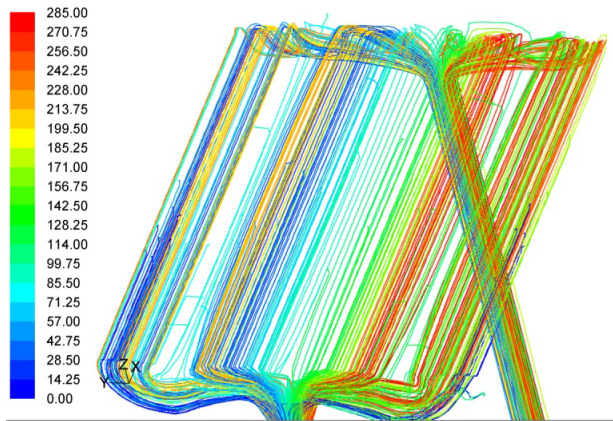
Figure 5-14. Pathlines through five-cell stack with inlet and outlet tubes and plenums plotted.
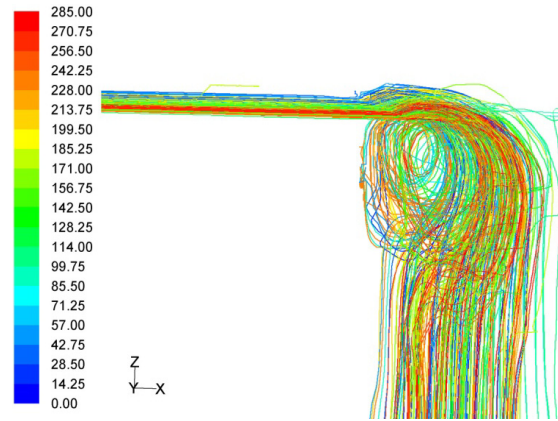
Figure 5-15. Pathlines showing recirculation in plenum before going through cells.

A current density contour plot is shown in Figure 5-16 on the electrolyte with the grid plotted for the inlet and outlet holes for the steam/hydrogen side for a current of -20.0 A. The largest current density occurs in the upper left corner as this is the most favorable region with the highest concentration of steam and lowest of oxygen. The waviness is also apparent in this view as the mole fractions of the steam/hydrogen dominate in the dead region downstream of the inlet holes.

Figure 5-17 shows the steam mole fraction for the INL test conditions for the single-cell model at -20.0 A. The waves also exist in this model and nearly identical results occur for the single-cell model. This fact that the results are the same for the single-cell and five-cell models indicates that a single-cell model is adequate for future work.
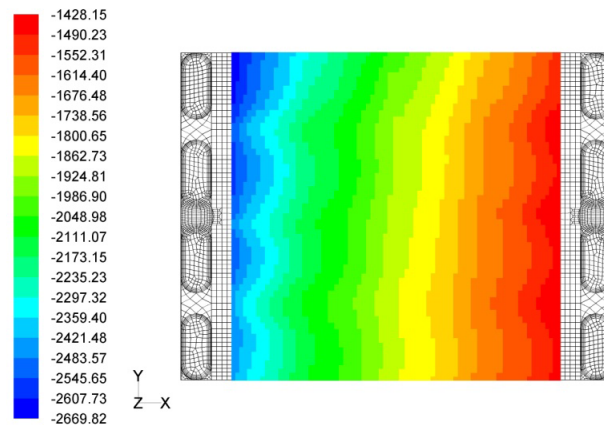

Figure 5-16. Current density (A/m^2) on electrolyte at 20.0 A.
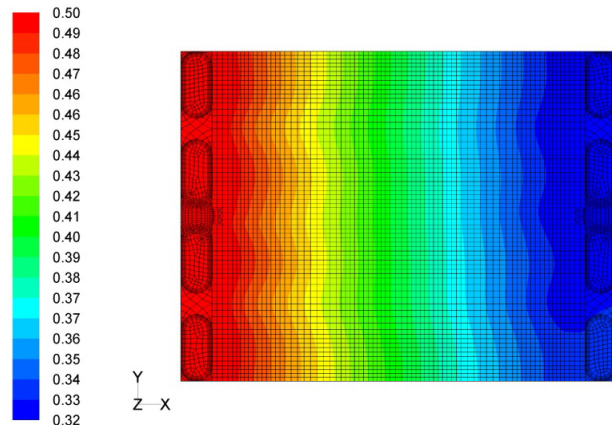
Figure 5-17. Steam mole fraction for single-cell model at -20.0 A.

Long inlet pipes and outlet pipes for the model were included to let the boundary layers develop. A velocity profile could have been used to simulate this developed boundary layer, but was not done so as to assure that the code calculated it as necessary.

5.1.5 Conclusions

A 3-D CFD, heat transfer, and electrochemistry model has been created and evaluated for a five-cell and single-cell stack designed from MSRI technology for an internally-manifolded electrolysis cell. A current sweep was evaluated showing a linear voltage versus current indicating small activation over-potential. A uniform flow distribution when comparing cell-to-cell flow was found for the five-cell stack. Dead regions of flow develop downstream of the area between the inlet holes and upstream of the outlet holes causing waves to appear in the contour plots of the mole fractions, pressure, and current density. Single-cell and five-cell results are nearly identical on a per cell basis showing that future calculations may be accurate with a single cell.

5.2   References

1   O'Brien, J. E., Stoots, C. M., Herring, J. S., and Hartvigsen, J. J., "Performance of Planar High-Temperature Electrolysis Stacks for Hydrogen Production from Nuclear Energy," *Nuclear Technology*, Vol. 158, pp. 118–131, May, 2007.

2   Herring, J. S., O'Brien, J. E., Stoots, C. M., and Hawkes, G. L., "Progress in High-Temperature Electrolysis for Hydrogen Production using Planar SOFC Technology," *International Journal of Hydrogen Energy*, Vol. 32, Issue 4, pp. 440–450, March 2007.

3   Hawkes, G. L., O'Brien, J. E., and Stoots, C. M., "3D CFD Model of a Multi-Cell High Temperature Electrolysis Stack," in review, *International Journal of Hydrogen Energy*, 2008.

4   Hawkes, G. L., O'Brien, J. E., Stoots, C. M., Herring, J. S., "CFD Model of a Planar Solid Oxide Electrolysis Cell for Hydrogen Production from Nuclear Energy," *Nuclear Technology*, Vol. 158, pp. 132–144, May, 2007.

5   http://www.msrihome.com/index.html

6   Hawkes, G. L., O'Brien, J. E., Stoots, C. M., Herring, J. S., and Jones, R. W., "CFD Model of a Planar Solid Oxide Electrolysis Cell: Base Case and Variations," paper # HT2007-32310, 2007 ASME-JSME Thermal Engineering Conference and Summer Heat Transfer Conference, July 8–12, 2007, Vancouver, BC, Canada.

7   Hawkes, G. L., O'Brien, J. E., "CFD Model of Electrode Supported Planar Solid Oxide Electrolysis Cells, paper no. 687d, AIChE Annual Mtg., Salt Lake City, UT, November 12–17, 2010.

8   Herring, J. S., O'Brien, J. E., Stoots, C. M., and Hawkes, G. L., "Progress in High-Temperature Electrolysis for Hydrogen Production using Planar SOFC Technology," International Journal of Hydrogen Energy, Vol. 32, Issue 4, pp. 440–450, March 2007.